

Electronic Transport in Helium Beam Modified Graphene and Ballistic Josephson Junctions

Nanda, Gaurav

DOI

[10.4233/uuid:342da318-4a11-4989-8c79-df0f0a11468f](https://doi.org/10.4233/uuid:342da318-4a11-4989-8c79-df0f0a11468f)

Publication date

2017

Document Version

Final published version

Citation (APA)

Nanda, G. (2017). *Electronic Transport in Helium Beam Modified Graphene and Ballistic Josephson Junctions*. [Dissertation (TU Delft), Delft University of Technology]. <https://doi.org/10.4233/uuid:342da318-4a11-4989-8c79-df0f0a11468f>

Important note

To cite this publication, please use the final published version (if applicable). Please check the document version above.

Copyright

Other than for strictly personal use, it is not permitted to download, forward or distribute the text or part of it, without the consent of the author(s) and/or copyright holder(s), unless the work is under an open content license such as Creative Commons.

Takedown policy

Please contact us and provide details if you believe this document breaches copyrights. We will remove access to the work immediately and investigate your claim.

**ELECTRONIC TRANSPORT IN HELIUM BEAM
MODIFIED GRAPHENE AND BALLISTIC JOSEPHSON
JUNCTIONS**

ELECTRONIC TRANSPORT IN HELIUM BEAM MODIFIED GRAPHENE AND BALLISTIC JOSEPHSON JUNCTIONS

Proefschrift

ter verkrijging van de graad van doctor
aan de Technische Universiteit Delft,
op gezag van de Rector Magnificus prof. ir. K.C.A.M. Luyben,
voorzitter van het College voor Promoties,
in het openbaar te verdedigen op dinsdag 16 mei 2017 om 15:00 uur

door

Gaurav NANDA

Master of Technology in Nanotechnology, Amity University, India
geboren te Hamirpur, India

Dit proefschrift is goedgekeurd door de

promotor: Prof. dr. ir. L.M.K. Vandersypen
copromotor: Dr. P.F.A. Alkemade

Samenstelling promotiecommissie:

Rector Magnificus	voorzitter
Prof. dr. ir. L.M.K. Vandersypen	promotor, Technische Universiteit Delft
Dr. P.F.A. Alkemade	copromotor, Technische Universiteit Delft

Onafhankelijke leden:

Prof. dr. H. W. Zandbergen	Technische Universiteit Delft
Prof. dr. C. Dekker	Technische Universiteit Delft
Prof. dr. C. Schönenberger	Universität Basel
Prof. dr. A. Götzhäuser	Universität Bielefeld
Prof. dr. ir. P. Kruit	Technische Universiteit Delft, reservelid

Overige leden:

Dr. ir. D. J. Maas	TNO Science and Industry
--------------------	--------------------------



This research is supported by the Dutch Technology Foundation STW, which is part of the Netherlands Organisation for Scientific Research (NWO) and partly funded by the Ministry of Economic Affairs (project number 12205)

Keywords: Helium ion microscopy, graphene, beam-induced deposition, ion-induced defects, graphene nanoribbons, Josephson junctions, and superconducting quantum interference devices (SQUIDS)

Printed by: Gildeprint

Front & Back: Edge-contacted graphene device exposed to a helium beam (front) and gate-tunable graphene SQUID (back)

Copyright © 2017 by Gaurav Nanda

Author email: gauravnanda18@gmail.com

Casimir PhD series, Delft-Leiden 2017-08

ISBN 978-90-8593-295-6

An electronic version of this dissertation is available at
<http://repository.tudelft.nl/>.

CONTENTS

1	Introduction	1
1.1	Motivation	1
1.2	Thesis objective and research questions	4
1.3	Outline of the thesis	4
	References	6
2	Graphene	9
2.1	Graphene	10
2.1.1	Graphene production	11
2.2	Electronic properties	12
2.3	Modification of electrical properties of graphene	15
2.3.1	Beam-induced modification and doping	15
2.3.2	Graphene nanoribbons	16
2.4	Introduction to superconductivity	17
2.4.1	Proximity-induced superconductivity	17
2.4.2	Josephson effect	19
2.4.3	Graphene-based Josephson junctions	20
2.4.4	Andreev reflection	20
2.4.5	Andreev bound states	21
	References	23
3	Helium Ion Microscopy	29
3.1	Helium ion microscopy: a brief review	30
3.1.1	Working principles	31
3.2	Beam-sample interaction	33
3.3	Applications of helium ion microscopy	37
3.3.1	Sample imaging	37
3.3.2	Helium ion beam lithography (HIBL)	37
3.3.3	Helium ion beam induced deposition	39
3.3.4	Helium ion milling	41
	References	44
4	Methods and Techniques	49
4.1	Fabrication of graphene devices	50
4.1.1	Sample cleaning	50
4.1.2	Exfoliation	50
4.1.3	Graphene identification	50
4.1.4	Boron nitride identification	51
4.2	Sample preparation	52
4.2.1	van der Waals pick-up technique	53

4.3	Characterization techniques	54
4.3.1	Atomic force microscopy	54
4.3.2	Raman spectroscopy	54
4.4	Contacting graphene	55
4.4.1	Electron beam lithography	56
4.4.2	Reactive ion etching	57
4.4.3	Electron beam evaporation	57
4.4.4	MoRe sputtering	57
4.4.5	Electrical measurements	58
	References	59
5	Modification of Encapsulated Graphene by HIM	61
5.1	Introduction	62
5.2	Sample preparation	62
5.3	Helium ion beam exposures	63
5.4	Defect study via Raman spectroscopy	64
5.4.1	Raman spectra of graphene	64
5.4.2	Defect dependence on the sample type	64
5.5	SRIM simulations	68
5.6	Electrical measurements	69
5.7	Discussion and conclusion	71
	References	72
6	Electronic Transport in Helium-Ion-Beam Etched Encapsulated Graphene Nanoribbons	79
6.1	Introduction	80
6.2	Results and discussion	81
6.2.1	Device milling and characterization	81
6.2.2	Low-temperature transport in GNRs	83
6.2.3	Model for defect induced transport in GNRs	85
6.3	Conclusion	87
	References	88
7	Helium ion beam induced growth of hammerhead AFM probes	93
7.1	Introduction	94
7.2	Experimental section	94
7.3	Hammerhead nano-needle fabrication	96
7.3.1	HeBID growth mechanism	96
7.3.2	Variation of needle diameter with ion dose	97
7.4	AFM measurements	100
7.5	Conclusion	101
	References	101
8	Ballistic Josephson junctions in edge-contacted graphene	105
8.1	Introduction	106
8.2	Results and discussion	107
8.3	Conclusion	111

8.4	Supplementary information	112
8.4.1	Tight-binding simulation	112
8.4.2	Current-voltage characteristics and temperature dependence	112
8.4.3	Fabry-Pérot interference in device D	112
8.4.4	Power spectral density from Fabry-Pérot oscillations	112
8.4.5	Effect of lead switching on magneto-transport	114
8.4.6	Anomalous Fraunhofer diffraction patterns	115
	References	115
9	Gate-tunable quantum interference devices of ballistic graphene	119
9.1	Introduction	120
9.2	Experimental section	120
9.3	SQUID operation	121
9.4	Conclusion	124
	References	124
10	Current-phase relation of ballistic graphene Josephson junctions	127
10.1	Introduction	127
10.2	Results and discussion	128
10.3	Conclusion	135
10.4	Supplementary information	136
10.4.1	Device fabrication	136
10.4.2	Ballistic transport in Dev2	136
10.4.3	Magnetic field to phase conversion	136
10.4.4	Eliminating inductance effects	138
10.4.5	Large asymmetry	138
10.4.6	Intermediate asymmetry	139
10.4.7	Estimating the loop inductance	139
10.4.8	RCSJ model	140
10.4.9	Tight-binding Bogoliubov-de Gennes calculations	143
10.4.10	Details of the theoretical model	143
10.4.11	Soft vs hard superconducting gap	146
10.4.12	Calculations using the side contact geometry	147
	References	148
11	Outlook	151
11.1	Summary of the studies in this thesis	152
11.1.1	Modification of graphene using HIM	152
11.1.2	Helium ion beam induced deposition	152
11.1.3	Graphene-based Josephson junctions	152
11.2	Future directions	153
11.2.1	Helium ion microscopy research	153
11.2.2	Graphene research	155
11.2.3	Technical challenges	157
	References	158

A	Device Fabrication Recipe	161
A.1	Si/SiO ₂ Cleaning	162
A.2	Bitmarkers	162
A.3	Contacting Graphene	163
A.3.1	Method 1.	163
A.3.2	Method 2 (etch fill).	164
A.4	Gate Dielectric	165
A.5	Top Gate	165
A.6	Device Bonding	165
	Summary	167
	Samenvatting	171
	Curriculum Vitæ	175
	List of Publications	177
	Acknowledgements	179

1

INTRODUCTION

The science of today is the technology of tomorrow.

Edward Teller

1.1. MOTIVATION

IT was late 1947 when William Shockley, John Bardeen, and Walter Brattain successfully demonstrated the first germanium-based transistor at Bell Laboratories[1]. In 1954, Texas Instruments started the first commercial production of junction transistors. Later on, in 1959 Richard Feynman introduced the world to the concept of nanotechnology. In his famous lecture "There's Plenty of Room at the Bottom" he laid the foundations of an era where things could be miniaturized[2]. The first demonstration of the transistor and the vision of Feynman led to the advancements of the technology, commonly named today "nanotechnology". The demonstration of the transistors gave birth to the silicon technology. This technology employs highly pure silicon to make transistors, which is an n-p-n structure using the grown-junction technique[3]. Because of the rapid growth of silicon-based research in the semiconductor industry, it became the preferred semiconductor material by the end of the 1950s. Then, as now, silicon has been the popular material choice for the semiconductor industries. However, silicon presents several long-term challenges, which were highlighted by G. E. Moore in 1965, and is since then commonly known as "Moore's Law"[4]. Which states that the number of transistors on an integrated circuit (IC) double every 18 months. Therefore, the need for smaller and faster electronics is physically limited by the capability of silicon. In the 1970s, Gallium arsenide (GaAs) became a potential material to replace silicon. But because of high material costs and the lack of a native oxide, GaAs has never supplanted silicon. This led to the continuous miniaturization of the silicon technology.

These advancements were strongly complemented by the inventions of optical lithog-

raphy, electron microscopy, and later ion microscopy in the 1970s. Other metrological tools such as the scanning tunneling microscope (STM), and the atomic force microscope (AFM) were developed in 1981 and 1982, respectively. Since the mid-1970s, lithographic tools became the heart of all semiconductor manufacturing components and their assembly. As the integrated circuits (ICs) are incorporated into more and more products, the quest for low-cost and high-performance devices continues to grow. To reduce cost and improve performance, the crucial process parameters such as material properties, defect profiles, linewidths and edge profiles need to be controlled carefully. In order to fulfill these demanding needs, semiconductor metrology became an integral part of semiconductor manufacturing process. Without the availabilities of metrological tools, it would have been impossible to improve the fast pacing semiconductor technology. In addition, focused ion beam (FIB) systems, developed almost 20 years ago, are still primarily used by large semiconductor manufacturers. Their main function is to patch or modify existing semiconductor devices. For example, in an integrated circuit, the gallium focused ion beam could be used to cut unwanted electrical connections, deposit conductive material, or to induce local doping. Therefore, to keep the semiconductor industry improving, the technological advancements in semiconductor materials, metrological tools, and the research on these need to continue.

Because of these advancements, science and technology have witnessed various scientific and technical breakthroughs in the last decade. Two relevant ones are the isolation of an atomically thin sheet of carbon, known as graphene in 2004[5], and the introduction of the helium ion microscope (HIM) in 2006[6]. Since then these became the center of the fundamental and applied research. This is apparent from the number of articles being published every year on graphene, see Figure 1.1. The number of HIM publications in 2016 is ~ 100 , far less than that of graphene.

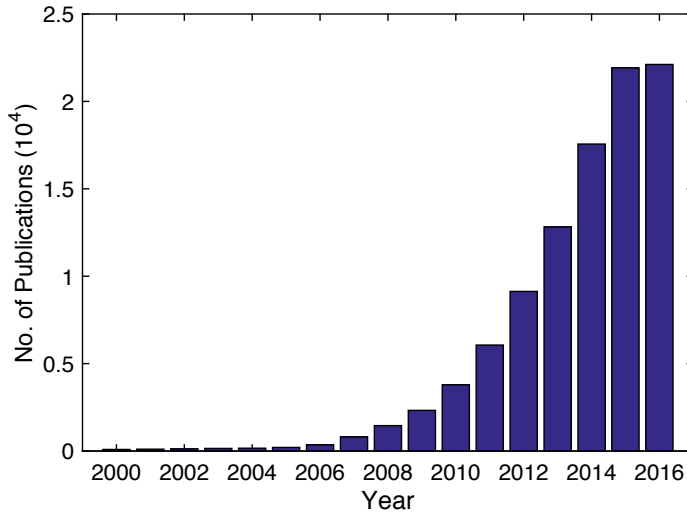


Figure 1.1: Number of publications on graphene from 2000 to December 2016. The number of publications are close to 22500. Source: Thomson Reuters Web of Science.

Graphene research has appeared in almost every field of science, such as biology, chemistry, physics, and material science. A graphene sheet is a million times thinner than a human hair, 200 times more resistant to breakage than steel[7], more conductive than copper, super transparent (97.7%)[8], and totally flexible[9]. Furthermore, graphene is impermeable to all gasses[10]. Graphene is a semimetal, unlike other semiconductors, and its charge carriers are described by a Dirac equation rather than the Schrödinger equation. This makes the electrons in graphene behave as massless fermions and gives graphene mobilities in excess of $10^6 \text{ V}^{-1} \text{ s}^{-1}$ [11]. Apart from high mobilities, the carrier density in graphene is gate tunable. By simple electrostatic gating, one can exploit the bipolar nature of the charge carriers in graphene.

From a basic physics point of view, graphene has led to interesting research on diverse topics, such as room temperature quantum Hall effect (QHE)[12], Klein tunneling[13], and proximity-induced superconductivity[14]. Of particular interest are the graphene-superconductor hybrid devices, which provide a novel platform for studying the proximity effect because of the gate tunable behavior and the unique electronic spectrum of graphene. However, the realization of such devices requires very high crystal quality of graphene and clean interfaces. Moreover, the superconductor-graphene contacts play a crucial role in determining how the Cooper pairs penetrate graphene. Therefore, it is essential to fabricate ultra clean graphene-superconductor hybrid devices and to study the supercurrent in a regime where the charge carriers ballistically travel, that means without random scattering from impurities and other imperfections. This realization could open up many new applications of graphene in science and technology. It has been proposed that high mobility graphene can be used to create new types of superconducting quantum devices for high-speed computing. It is generally expected that graphene could one day revolutionize electronics, energy, aerospace and biotechnology industry.

Although helium ion beam technology has by far not had the same impact as graphene, there is wide interest in using this technology for various application in physics, chemistry, material science, and biology. The technology was mainly developed for imaging and metrology applications, but it has now found its use for material modification and structuring at sub-10 nm scale. Moreover, the beam induced deposition capabilities of the helium ion microscope were explored for the deposition of platinum and tungsten by Chen *et al.*[15] and Kohama *et al.*[16], respectively. A nice review on helium ion beam deposition is reported by Alkemade *et al.*[17]. The authors reported the fabrication of a 36 nm wide PtC pillar with stationary exposure. However, because of the narrow interaction width of the helium beam in materials, one expects that narrower pillars must be achievable. This capability of the helium beam, to the best of my knowledge, is still unexplored. Other promising application of the helium beam is the modification and structuring of sensitive materials, such as graphene. There has been some, but limited, work on the combination of graphene and helium ion microscopy. Initial experiments by Lemme *et al.*[18] and Bell *et al.*[19] have outlined the potentials of the HIM in graphene research. The authors have shown that a focused helium beam can be used to make sub-10 nm structures in graphene. The capability to etch graphene with nanometer precision enables the fabrication of devices, such as graphene nanoribbons. However, the sub-10 nm nanoribbon devices made in graphene by HIM did not show any electrical conductance,

likely due to the beam induced damage and contamination. Although the use of HIM to etch graphene had already been demonstrated, detailed studies on the ion-material interaction, beam induced lateral damage extent, and the fabrication of functional devices were still lacking.

The idea to utilize the capabilities of helium ion microscopy and that of graphene gave birth to the primary motivation of this thesis.

1.2. THESIS OBJECTIVE AND RESEARCH QUESTIONS

It is clear from the previous section that graphene and the helium ion microscope form the two main ingredients of this thesis. The intended purpose of this thesis is to effectively explore the capabilities of each of the two ingredients individually and to combine them. Both ingredients offer a variety of interesting research themes dedicated, but not limited, to the various sub-fields of physics, material science, and biology. Although there are numerous interesting possibilities, we limit our research to a few of them. While the helium ion microscope is explored for its beam induced deposition and milling capabilities, proximity-induced superconductivity is explored in ballistic graphene. Not just that, the combination of graphene and helium ion microscopy is also studied, mainly for the modification of graphene and the fabrication of graphene nanoribbons.

In order to achieve the research objective, many research questions were raised and hopefully answered satisfactorily. This thesis will provide an explanation as to why these studies were conducted by addressing the following main research questions:

- Can we explain He^+ beam induced damage in graphene with a sole mechanism? What are the contributing factors? How does damage influence the charge transport?
- What are the limits of the helium ion beam induced deposition process?
- What influences the critical current in a ballistic graphene Josephson junction? What is the experimental signature?
- What is the importance of cleanliness of the graphene lattice and the metal-graphene interface to realize ballistic transport?
- Is the current-phase relation (CPR) in a ballistic graphene Josephson junction non-sinusoidal? How does the CPR behave as a function of gate-voltage and temperature in the ballistic limit?

1.3. OUTLINE OF THE THESIS

Chapter 2 gives an overview of the basic physical concepts of graphene and graphene devices, such as nanoribbons. The aim is to establish a basis for discussing the experimental results in the succeeding chapters. After an introduction, the electronic properties of graphene and the modification of graphene are discussed. The chapter ends with

a brief discussion on the proximity-induced superconductivity in graphene.

Chapter 3 describes the working principles of helium ion microscopy. Overviews of ion-matter interactions and various applications are also given.

Chapter 4 provides an overview of the experimental setups and the fabrication process of graphene devices that are used in the other chapters.

In **Chapter 5**, I discuss the changes in graphene as a function of the helium ion dose. In particular, I show that in graphene that is encapsulated between two hexagonal boron nitride (h-BN) layers, the built-up of helium beam damage is retarded and that beam induced contamination is absent. In **Chapter 6**, I used the helium beam to etch nanoribbons in encapsulated graphene, and in-situ electrical probes to determine the ion dose needed to isolate the graphene ribbons. The measured devices at 4 K show an energy gap opening in the narrowest ribbons.

Chapter 7 addresses the capabilities of a focused helium beam to grow hammerhead atomic force microscope (AFM) probes. We made nanoprobes with a radius below 10 nm and a hammerhead smaller than 35 nm. Moreover, we test the capabilities of the fabricated AFM probes for 2D metrology, in particular to measure sidewall angles and line-edge roughness of trenches and shark-fins in silicon.

Chapter 8 and 9 focuses on studies of hybrid graphene-superconductor devices. The Josephson junctions (JJs) studied in **Chapter 8** show well-defined transparent contacts of high-quality, thanks to the encapsulation of graphene in hexagonal boron nitride, which led to the observation of ballistic transport in graphene. The critical current in these Josephson junctions oscillates with the carrier density because of phase coherent interference of the electrons and the holes that carry the supercurrent caused by the formation of a Fabry-Pérot cavity. In **Chapter 9**, I study the electrical properties of a gate-tunable quantum interference device (SQUID) in graphene. The supercurrent in this device can be modulated via two individual gates and an applied magnetic field. By independently controlling the critical current of each graphene JJ, we can electrostatically tune the SQUID from a symmetric configuration to a highly-asymmetric one, where the critical current of one JJ is significantly larger than that of the other.

Chapter 10 of the thesis deals with an experimental and theoretical study of the current-phase relation (CPR) of graphene JJs embedded in a SQUID geometry. We show that the highly asymmetric configuration of these ballistic graphene JJs allows us to directly measure the current-phase relation (CPR), which has so far eluded experimental observation. At low temperatures (40 mK) we find the CPR to be forward skewed, thus deviating significantly from sinusoidal behavior. We show that this skewness varies with the Fermi energy and the temperature.

Finally, in **Chapter 11**, I discuss the current trends and future directions of the helium ion microscopy and graphene research.

REFERENCES

- [1] W. B. Shockley, J. Bardeen, and W. H. Brattain, *The nobel prize in physics*, (1986).
- [2] R. P. Feynman, *There's plenty of room at the bottom*, *Journal of Microelectromechanical Systems* **1**, 60 (1992).
- [3] M. Tanenbaum, L. B. Valdes, E. Buehler, and N. B. Hannay, *Silicon n-p-n grown junction transistors*, *Journal of Applied Physics* **26**, 686 (1955).
- [4] G. E. Moore, *Cramming more components onto integrated circuits (reprinted from electronics, 1965)*, *Proceedings of the IEEE* **86**, 82 (1998).
- [5] K. S. Novoselov, A. K. Geim, S. V. Morozov, D. Jiang, M. I. Katsnelson, I. V. Grigorieva, S. V. Dubonos, and A. A. Firsov, *Two-dimensional gas of massless dirac fermions in graphene*, *Nature* **438**, 197 (2005).
- [6] B. Ward, J. A. Notte, and N. Economou, *Helium ion microscope: a new tool for nanoscale microscopy and metrology*, *Journal of Vacuum Science & Technology B* **24**, 2871 (2006).
- [7] C. Lee, X. Wei, J. W. Kysar, and J. Hone, *Measurement of the elastic properties and intrinsic strength of monolayer graphene*, *Science* **321**, 385 (2008).
- [8] R. R. Nair, P. Blake, A. N. Grigorenko, K. S. Novoselov, T. J. Booth, T. Stauber, N. M. R. Peres, and A. K. Geim, *Fine structure constant defines visual transparency of graphene*, *Science* **320**, 1308 (2008).
- [9] S. Bae, H. Kim, Y. Lee, X. X. abd J. S. Park, Y. Zheng, J. Balakrishnan, T. Lei, H. R. Kim, Y. I. Song, Y. J. Kim, K. S. Kim, B. Özyilmaz, J. H. Ahn, B. H. Hong, and S. Iijima, *Roll-to-roll production of 30-inch graphene films for transparent electrodes*, *Nature Nanotechnology* **5**, 574 (2010).
- [10] J. S. Bunch, S. S. Verbridge, J. S. Alden, A. M. van der Zande, J. M. Parpia, H. G. Craighead, and P. L. McEuen, *Impermeable atomic membranes from graphene sheets*, *Nano Letters* **8**, 2458 (2008).
- [11] P. Neugebauer, M. Orlita, C. Faugeras, A. L. Barra, and M. Potemski, *How perfect can graphene be?* *Physical Review Letters* **103**, 136403 (2009).
- [12] K. S. Novoselov, Z. Jiang, Y. Zhang, S. V. Morozov, H. L. Stormer, U. Zeitler, J. C. Maan, G. S. Boebinger, and P. K. abd A. K. Geim, *Room-temperature quantum hall effect in graphene*, *Science* **315**, 1379 (2007).

- [13] A. F. Young and P. Kim, *Quantum interference and Klein tunnelling in graphene heterojunctions*, *Nature Physics* **5**, 222 (2009).
- [14] H. B. Heersche, P. Jarillo-Herrero, J. B. Oostinga, L. M. K. Vandersypen, and A. F. Morpurgo, *Bipolar supercurrent in graphene*, *Nature* **446**, 56 (2007).
- [15] P. Chen, E. van Veldhoven, C. A. Sanford, H. W. M. Salemink, D. J. Maas, D. A. Smith, P. D. Rack, and P. F. A. Alkemade, *Nanopillar growth by focused helium ion-beam-induced deposition*, *Nanotechnology* **21**, 455302 (2010).
- [16] K. Kohama, T. Iijima, M. Hayashida, and S. Ogawa, *Tungsten-based pillar deposition by helium ion microscope and beam-induced substrate damage*, *Journal of Vacuum Science & Technology B* **31**, 031802 (2013).
- [17] P. F. A. Alkemade and H. Miro, *Focused helium-ion-beam-induced deposition*, *Applied Physics A* **117**, 1727 (2014).
- [18] M. C. Lemme, D. C. Bell, J. R. Williams, L. A. Stern, B. W. H. Baugher, P. Jarillo-Herrero, and C. M. Marcus, *Etching of graphene devices with a helium ion beam*, *ACS Nano* **3**, 2674 (2009).
- [19] D. C. Bell, M. C. Lemme, L. A. Stern, J. R. Williams, and C. M. Marcus, *Precision cutting and patterning of graphene with helium ions*, *Nanotechnology* **20**, 455301 (2009).

2

GRAPHENE

This chapter provides a general overview of graphene, which is essential for the understanding of fabrication and working of devices studied in this thesis. The Dirac nature of charge carriers in graphene can be controlled by application of electric and magnetic fields, or by modifying graphene's lattice. The sub-goal of this chapter is to provide a broad overview of the properties of graphene, primarily focused on the experiments performed in this thesis. First, growth methods are briefly introduced, followed by a discussion of the electronic properties of graphene. An introduction to ion-induced modification and graphene nanoribbons is also provided. Towards the end of the chapter, induced superconductivity, the Josephson effect, and Andreev bound states in graphene will be discussed.

2.1. GRAPHENE

GRAPHENE is made of sp^2 hybridized carbon atoms arranged in a two-dimensional (2D) honeycomb lattice. Its extended honeycomb network forms the basic building block of other important allotropes; it can be wrapped to form fullerenes (0D), rolled to form nanotubes (1D), and can be stacked to form graphite (3D), see Figure 2.1. Graphene is undoubtedly emerging as one of the most promising nanomaterials because of its superb electrical[1], mechanical[2], and optical properties[3], which opens a way for its exploitation in a wide spectrum of applications. Although monolayer graphene had already been isolated in the 1960s[4], it took until 2004 before the first graphene-based field-effect transistor (FET) was made[5]. The carriers in graphene are described by a Dirac equation rather than the Schrödinger equation as for the most semiconducting materials, which opened the possibilities to explore intriguing new physics. Although graphene is predicted to create impact in almost every field of science, it suffers from several practical challenges. Graphene devices are usually made on a SiO_2 substrate. The carrier mobilities in such devices are limited by the scattering from charged impurities trapped in the substrate, surface roughness, and impurities from the resist and the environment[6]. Another possibility is to make suspended graphene devices. However, such devices cannot be incorporated into a complicated device architecture where a top-gate is required. Also, this does not prevent contamination that arises from resist residues.

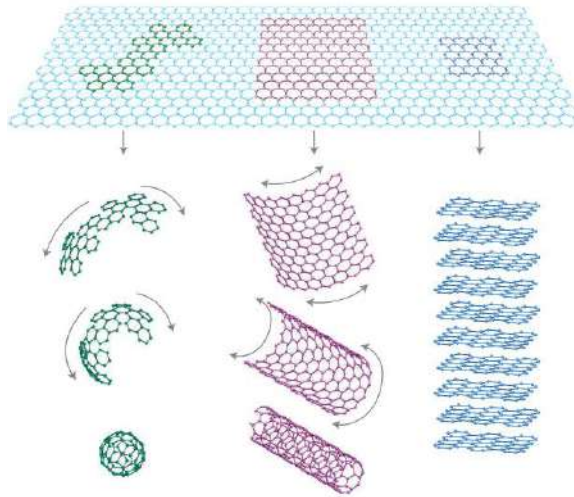


Figure 2.1: Shows a honeycomb lattice of carbon atoms, which can be transformed into fullerenes (0D), carbon nanotubes (1D), or a planar graphene sheet (2D). The Figure is taken from Ref.[7].

It has recently been shown that graphene encapsulated between atomically flat boron nitride (h-BN) sheets has enhanced carrier mobilities, reaching the limits of ballistic propagation at room temperature[8]. Graphene's gate-tunable behavior and its high mobility render it into a promising, novel component of future electronics. However, the

absence of a band gap in graphene prevents the possibility to turn off graphene FETs, which strongly limits their use in digital electronic circuits. A way to induce a bandgap is by patterning graphene into narrow stripes, so-called graphene nanoribbons (GNRs), where carrier confinement and edge effects introduce a band gap[9, 10]. GNRs are of particular interest as the geometry and physical or chemical termination of their edges may enable control over their electronic properties. This control may be exploited to improve the performance of graphene-based nanoribbon devices.

Apart from having many fascinating properties, graphene also provides a unique platform to study proximity-induced superconductivity. This type of superconductivity has been observed in graphene-based Josephson junctions by Heersche *et al.*[11]. The authors showed that the supercurrent in graphene can be carried by either electrons or by holes. In addition, a finite supercurrent can also flow at zero charge density. Since then, the critical currents in graphene are studied extensively as a function of junction geometry, temperature and applied gate voltage [11–15]. These exceptional electrical properties have opened up new avenues for the use of ballistic graphene in various sub-fields of solid-state physics.

2.1.1. GRAPHENE PRODUCTION

If you have ever written with a graphite pencil, you probably have spread multiple graphene sheets over your paper. Unfortunately, this method is uncontrollable and you are typically left with many sheets of varying thickness. For research and development, several production methods have been explored. Many new ways are regularly reported that improve the quality of material, decrease costs, and achieve larger areas. Since the inception of graphene research, the production of graphene can be classified into three main categories, namely mechanical exfoliation, epitaxial growth, and chemical vapor deposition. These three techniques are briefly discussed in the following subsections.

MECHANICAL EXFOLIATION

The most common method to produce graphene is the so-called "scotch-tape method", a mechanical exfoliation process that produces graphene sheets from graphite flakes by mechanical cleavage. By gently rubbing a freshly cleaved graphite crystal on an oxidized silicon wafer, numerous graphene flakes with varying thickness are transferred onto the wafer. Single or multilayer graphene flakes can easily be identified under an optical microscope because of thin film interference effects[16]. In fact, graphene flakes can be deposited on any substrate. First reported by Geim and Novoselov[5], mechanical exfoliation is the simplest method to produce graphene. This technique is probably the quickest process of obtaining a single graphene sheet but limits this fabrication scheme to devices for research purposes. We have only used mechanical exfoliation to make the devices reported in this thesis.

EPITAXIAL GROWTH

Epitaxial growth has the greatest potential for mass production of graphene. In this method, single layer or multilayer graphene is grown by sublimating Si atoms from a SiC substrate at high temperature. This is accomplished by heating a SiC wafer which results in the partial graphitization of the upper layer and in the formation of a graphene layer. This graphitization of the SiC (0001) plane was proposed already in 2002 by Charrier *et al.*[17]. Since then many groups around the world have optimized this growth technique. A very nice review of this growth technique has been reported by Tetlow *et al.*[18]. Recently, ballistic transport in epitaxially grown graphene nanoribbons has been demonstrated[19]. It is, however, difficult to control the number of layers and the grain sizes. Therefore, the use of this technique for graphene growth is limited mainly to research laboratories. In addition, the production cost associated with this technique is very high, which is now its bottleneck for mass production of graphene.

CHEMICAL VAPOR DEPOSITION (CVD)

An alternative to mechanical exfoliation and epitaxial growth is chemical vapor deposition (CVD)[20]. In CVD, a metal substrate such as copper is placed in a furnace and heated under high vacuum to around 1000 °C. This annealing results additionally in increased domain sizes. Next, a mixture of methane and hydrogen gas is passed through the furnace. The hydrogen catalyzes a reaction between methane and the surface of the metal substrate, causing carbon atoms from the adsorbed methane to be decomposed, resulting in a continuous graphene sheet. Copper is not the only substrate which can be used for graphene CVD; in fact, many transition metals are also suitable, such as nickel, cobalt, and platinum[20, 21]. The main differences between metal substrates come from differences in the metal's ability to adsorb carbon. In spite of the significant progress, there are a number of challenges, such as contamination-free graphene transfer, production of graphene with large and controlled grain size, cost-effectiveness, and control of the number of layers for commercial applications. We note that growing graphene directly on insulating substrates such as Si/SiO₂ and h-BN would help to overcome the quality degradation caused by the transfer process.

2.2. ELECTRONIC PROPERTIES

The band structure of graphene differs from the band structures of conventional semiconductors: in the former, the energy dispersion around the band edges is linear and in the latter quadratic[1]. The ground state configuration of the six electrons of an isolated carbon atom is $1s^2 2s^2 2p^2$, thus with four valence electrons. In graphene, three of which undergo sp^2 hybridizations and form in-plane σ bonds to three neighboring carbon atoms. These localized electrons have low energy and therefore, they do not contribute to the electronic transport. The fourth electron in the out-of-plane p_z orbital of each carbon atom binds with a similar electron in the p_z orbital of a neighboring carbon atom, leading to the formation of a half-filled delocalized π bond. The p_z electrons have higher energy and are responsible for the electronic transport in graphene. The carbon

atoms in graphene organize themselves into a hexagonal lattice, which forms a triangular lattice with two atoms per unit cell, see Figure 2.2. The lattice vectors can be written as:

$$\vec{a}_1 = \frac{a_0}{2}(3, \sqrt{3}), \quad \vec{a}_2 = \frac{a_0}{2}(3, -\sqrt{3}) \quad (2.1)$$

where $a_0=0.142$ nm is the C-C distance. The reciprocal-lattice vectors are:

$$\vec{b}_1 = \frac{2\pi}{3a_0}(1, \sqrt{3}), \quad \vec{b}_2 = \frac{2\pi}{3a_0}(1, -\sqrt{3}) \quad (2.2)$$

The three nearest-neighbor vectors in real space are:

$$\delta_1 = \frac{a_0}{2}(-1, \sqrt{3}), \quad \delta_2 = \frac{a_0}{2}(-1, -\sqrt{3}), \quad \delta_3 = a_0(1, 0) \quad (2.3)$$

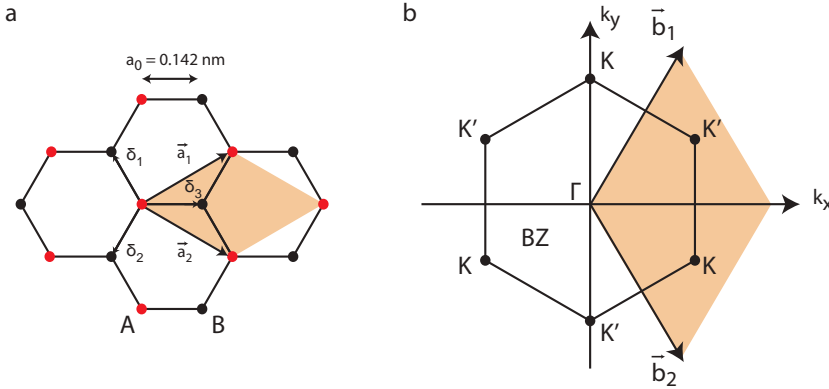


Figure 2.2: (a) The honeycomb lattice of graphene is divided into two triangular sublattices A and B, shown here in red and black. The unit cell is made of unit cell vectors \vec{a}_1 , \vec{a}_2 , and the three nearest-neighbor directions δ_1 , δ_2 , δ_3 with the inter-atomic distance of $a_0 = 0.142$ nm, (b) The reciprocal-lattice vectors \vec{b}_1 , \vec{b}_2 . The six K and K' points represent the first Brillouin zone.

Figure 2.2 shows graphene's hexagonal lattice divided into two interpenetrating triangular lattices, the lattice vectors \vec{a}_1 , \vec{a}_2 , the reciprocal lattice vectors \vec{b}_1 , \vec{b}_2 , and the three nearest-neighbor directions. The energy band structure of graphene was obtained by P. R. Wallace[22] using tight-binding calculations. The energy bands are:

$$E_{\pm}(k) = \pm t \sqrt{3 + f(k)} - t' f(k) \quad (2.4)$$

$$f(k) = 2 \cos(\sqrt{3} k_y a_0) + 4 \cos\left(\frac{\sqrt{3}}{2} k_y a_0\right) \cos\left(\frac{3}{2} k_x a_0\right) \quad (2.5)$$

where t is the hopping energy between nearest neighbor (~ 2.8 eV), and t' is the hopping energy between next-nearest neighbors (≤ 0.1 eV). The plus sign is referred to the π^* band (conduction band) and the minus sign is referred to the π band (valence band). The two points K and K' at the corners of the graphene Brillouin zone BZ are of importance for the physics of graphene, see Figure 2.2. Since for low energies, electrons in graphene can be described as massless Dirac fermions, the cones at the K and K' points are called Dirac cones. Their position in momentum space are:

$$K = \left(\frac{2\pi}{3a_0}, \frac{2\pi}{3\sqrt{3}a_0} \right), K' = \left(\frac{2\pi}{3a_0}, -\frac{2\pi}{3\sqrt{3}a_0} \right) \quad (2.6)$$

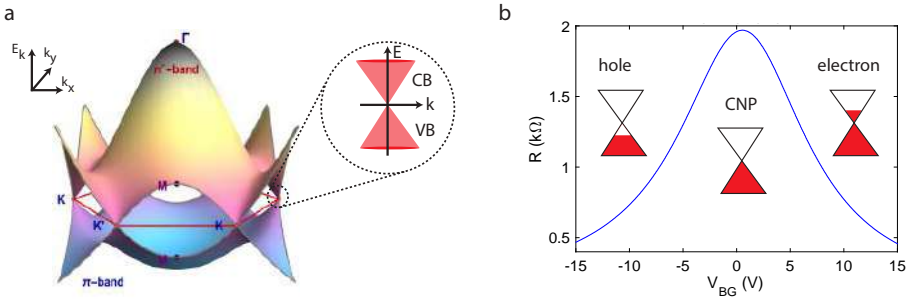


Figure 2.3: (a) The electronic dispersion of the π bands in the Brillouin zone of graphene. The dispersion relation of electrons (holes) at low energies is linear and can be described by cones around the K and K' points, (b) Four probe resistance R as a function of the gate voltage at room temperature. The inset shows the Dirac cone for different Fermi level positions.

When Equation 2.4 is expanded around K with $k = K + q$, a linear dispersion is obtained:

$$E(q) \approx v_f q + O\left[\left(\frac{q}{K}\right)^2\right] \quad (2.7)$$

where $v_f = \frac{\sqrt{3}ta}{2\hbar}$ is the Fermi velocity. Since a is the lattice constant of graphene ($a = \sqrt{3}a_0 = 0.246$ nm), $v_f \approx 1 \times 10^6$ m s $^{-1}$. Hence, graphene is a semimetal with an unusual linear dispersion relation. The band structure of graphene for low energies at K and K' points can be described by 2D Dirac equation for massless fermions (Weyl equation) as:

$$H\Psi = v_f \sigma \cdot \hat{p} \Psi \quad (2.8)$$

where $\hat{p} = -i\hbar\nabla$ is the momentum operator, $\sigma = (\sigma_x, \sigma_y)$ are the Pauli matrices. The Fermi level is located at the intersection of the cones for undoped graphene. The point where the two bands meet is called the charge neutrality point or the Dirac point. In graphene, the Fermi level can be shifted by means of a gate electrode. Depending on the polarity of the applied field, it can be shifted either into the hole or into the electron regime. It is of prime interest that charge carriers in graphene move without scattering,

which can be measured in terms of the carrier mobility. If the mean free path (l_{mfp}) is less than the junction length (L), the transport is diffusive. However, in a ballistic limit, $l_{mfp} > L$. The mobility (μ) can be calculated as $\sigma = n.e.\mu$, where e is the elementary charge, σ the conductivity, and n is the density of charge carriers. The carrier density can be calculated as:

$$n = \frac{\epsilon_r \epsilon_0}{e d} V_g \quad (2.9)$$

where V_g is the gate voltage, d is the thickness of the dielectric, and ϵ_r is the dielectric constant. A low-temperature mobility of $230,000 \text{ cm}^2\text{V}^{-1}\text{s}^{-1}$ has been reported for suspended graphene devices[23].

2.3. MODIFICATION OF ELECTRICAL PROPERTIES OF GRAPHENE

Graphene is a unique material that has potential applications in high-speed next generation electronics. However, its practical use is inhibited by the absence of a bandgap. Numerous efforts have been made to alter its electronic band structure in order to induce a bandgap. Some of the methods include plasma-assisted chemical modification[24], ultraviolet (UV) irradiation[25], electrically gated bilayer graphene[26], ion beam induced modification[27], etching of graphene into nanoribbons[10], and doping through chemical interactions with underlying substrate and strain caused by bending of graphene[28]. Although there are many methods by which the electronic properties of graphene can be modified, I limit my discussion to ion beam induced modification and etching of graphene into nanoribbons, which are both relevant to this thesis.

2.3.1. BEAM-INDUCED MODIFICATION AND DOPING

It has already been shown that the controlled exposure by charged particle beams, such as gallium, helium, and argon, modifies the electronic properties of graphene[27, 29, 30]. However, efficient use of ion beams to optimize the sheet modification of graphene requires detailed microscopic knowledge of damage production mechanisms and types of defects created by the energetic ions in the material. Focused ions beams can be used to modify the electronic properties by embedding defects in graphene at low-density. This modifies the transport properties via sparsely distributed local potential modulations. Nakaharai *et al.*[29] have shown that this modification can also lead to the opening of the bandgap due to strong localization of carriers at the defect sites. In addition, they found an on/off current ratio of 100 at room temperature. Recently, Moktadir *et al.*[31] reported that by adjusting the defect concentration, an insulating behavior is achieved for n-type conduction whilst a metallic behavior is achieved for p-type conduction. This is a consequence of the Fermi level pinning at the Dirac point induced by oxygen groups acting as charge traps. Guo *et al.*[32] studied the evolution of graphene following N^+ irradiation at different fluences using Raman spectroscopy. The authors showed that the ion-induced defects that are introduced in the plane after irradiation, are restored after

annealing in N_2 or NH_3 . The n-type doping in graphene was confirmed by the source-drain conductance and back-gate voltage sweeps in the measurement. Such nitrogen doping can lead to a finite bandgap in graphene[33]. However, understanding of the interaction between energetic particles and graphene is needed to optimize the electronic properties of graphene. Another study[34] has shown that the low-energy implantation of boron and nitrogen can also lead to effective doping of the graphene. This method of low-energy ion implantation offers an alternative to chemical doping in graphene. The physical mechanism for the introduction of defects and subsequent hetero dopant (boron or nitrogen) atoms into the graphene in a controllable way will be a promising route to tailor the properties of graphene for device applications. This will be discussed later in Chapter 5.

2.3.2. GRAPHENE NANORIBBONS

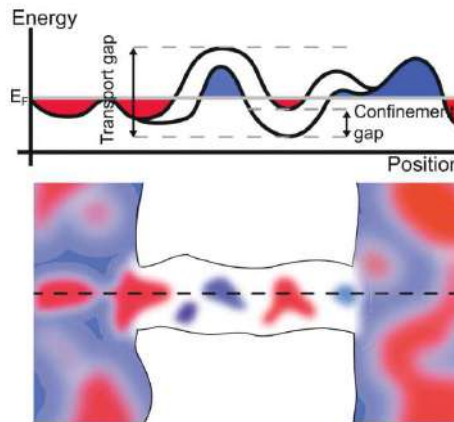


Figure 2.4: A cartoon showing a nanoribbon made of graphene. When the Fermi level is close to the charge neutrality point, quantum dots are formed due to potential inhomogeneities and a confinement gap is observed. Electron or hole puddles are depicted by blue and red regions, respectively. The conductance is not suppressed when the Fermi level is outside the gap region. The Figure is taken from Ref.[35].

The electronic properties of graphene nanoribbons (GNRs) differ from those of a 2D sheet due to a nanoribbon's finite width. The conductance of graphene nanoribbon devices at low temperatures ($\sim 4K$) is typically suppressed orders of magnitude below e^2/h for a large range of Fermi energies[9, 10]. GNRs can have two ideal edge configurations, namely "armchair" and "zigzag". Theoretical studies based on tight-binding approximations predict that GNRs are metallic or semiconducting depending on the crystallographic direction[1, 36]. In particular, zigzag GNRs are always metallic, while armchairs can be either metallic or semiconducting. The bandgap decreases with increasing ribbon width for the semiconducting GNRs. According to density functional theory calculations, both types of edges have energy gaps E_{gap} equals to α/W , where α ranges between 0.2-1.5 eV nm, and W is the GNR width[37]. In their review paper, Bischoff *et al.*[38] noted that a stern distinction has to be made between a *source-drain gap*—*i.e.*, the suppression of conductance in a limited source-drain voltage range— and a *trans-*

port gap — *i.e.*, the suppression in a limited gate voltage range. The semiconducting behavior in GNRs arises from the quantum confinement and the disorder induced by the edges. A narrow etched ribbon is likely to have a single or a few quantum dots (QDs) along the length of the ribbon, which leads to the formation of well-separated Coulomb diamonds[9, 10]. However, multiple QDs can also be formed in parallel or series, possibly leading to the overlap of multiple QDs. The source-drain gap can be interpreted as the charging energy of the largest quantum dot (QD) and is expressed as E_{gap} [38, 39]. The source-drain gap and the transport gap typically increases with decreasing ribbon width. Also, it is known that the gap is greatly influenced by the presence of disorder in the graphene nanoribbons (GNRs)[38, 40]. Coulomb blockade in disordered systems can explain the observed transport through GNRs. In contrast, Evaldsson *et al.*[41] inferred that not Coulomb blockade but Anderson-type localization, induced by edge disorder, is responsible for the energy gap in plasma-etched GNRs. The disorder along the edge of the ribbon leads to localized states caused by Anderson-type localization[41]. In practice, it is, however, hard to control the edge roughness of etched ribbons.

Many researchers have tried to fabricate GNRs with perfect edges using plasma etching[9, 10, 35, 38], chemical synthesis[42–44], electron beam etching[45–47], and ion beam etching [27, 48–51]. It is not straightforward, however, to make near-defect-free nanoribbons using the aforementioned techniques and, hence, it remains unclear how much the conductance and the presence of a gap are affected by edge effects, quantum confinement, and disorder[38]. Since the helium ion beam is of particular interest to this thesis, the technique of ion beam etching will be explained in more detail in Chapter 3.

2.4. INTRODUCTION TO SUPERCONDUCTIVITY

2.4.1. PROXIMITY-INDUCED SUPERCONDUCTIVITY

When a superconductor is cooled below its critical temperature, it loses its resistance and attains a superconducting state. In this state, the current can flow without any dissipation of energy. The phenomenon of superconductivity is explained by Bardeen-Cooper-Schrieffer (BCS) theory in terms of Bose-Einstein condensation. According to the BCS theory, large numbers of Cooper pairs occupy the ground state of a system, without exchanging energy with the environment[54]. A Cooper pair is a pair of electrons with opposite momentum. In 1956 Cooper found that a weak attraction can bind pairs of electrons into a bound state. It is worth mentioning that these Cooper pairs can easily break due to thermal fluctuations, so only at low temperatures, a sizable fraction of electrons pair up. The condensate is described by a macroscopic wavefunction as:

$$\Psi = |\Psi|e^{i\phi} \quad (2.10)$$

where $|\Psi|$ is the amplitude of the wavefunction, and ϕ its phase. When two superconducting leads are coupled via a weak link, the supercurrent can flow from one lead to the other due to the propagation of Cooper pairs from the superconductor to the weak link. This phenomenon is called proximity-induced superconductivity. The weak link can be

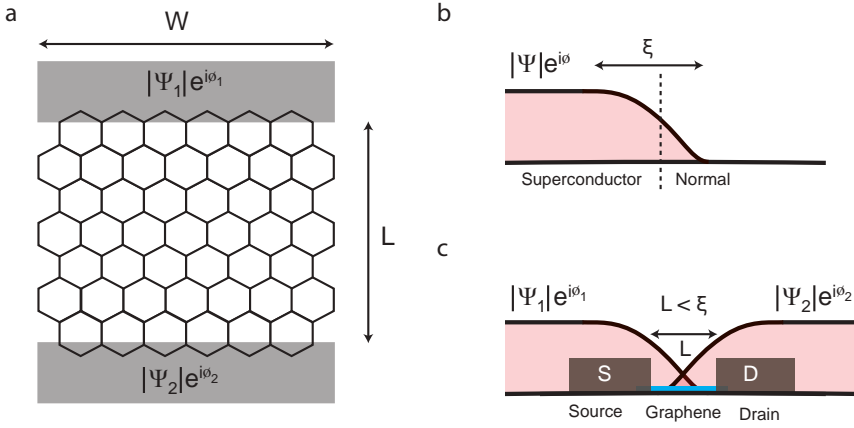


Figure 2.5: (a) Graphene is connected with two superconductors with wavefunctions Ψ_1 and Ψ_2 , (b) The wavefunction Ψ decays as the Cooper pairs enter the normal metal. The length scale over which it decays is the coherence length ξ , (c) When two superconductors are connected to a graphene weak link, the Cooper pairs can tunnel through the graphene sheet, leading to supercurrent in dc measurements. A necessary condition for supercurrent to flow through the weak link is that $\xi \gg L$, where L is the junction length. Figure adapted from Ref. [52, 53].

a metal, an insulator, or a semiconductor. This effect manifests itself as a non-dissipative dc current flowing through the weak link at zero voltage. It was first predicted from the BCS theory in 1962 by B. D. Josephson [55]. When a weak link, also called a Josephson junction (JJ), is connected to a superconductor, the correlations from the superconductor is picked up by the electrons in the weak link. This proximity effect leads to the modification of the local density of states (DOS) in the JJ, resulting in a phase-dependent energy gap around the Fermi energy, also known as mini-gap [56]. The size of the mini-gap depends on the timescale, τ . This timescale τ , which is the time taken by an electron to reach the superconductor, is characterized by the Thouless energy: $E_{Th} \simeq \hbar/\tau$ [53]. The Thouless energy for a ballistic system is:

$$E_{Th,b} = \hbar v_f / \xi = 2\Delta \quad (2.11)$$

where Δ is the proximity induced gap and ξ is the superconducting coherence length, also known as the length scale along which correlations are picked up. Here, ξ is described as: $\xi = \xi_b = \frac{\hbar v_f}{2\Delta}$. In a diffusive system, the Thouless energy is defined as:

$$E_{Th,d} = \hbar D / L^2 \quad (2.12)$$

where D is the diffusion constant, and ξ is described as: $\xi = \xi_d = \frac{\sqrt{\hbar D}}{2\Delta}$

2.4.2. JOSEPHSON EFFECT

The most basic phenomenon in the field of superconductivity is the Josephson effect, where a current can flow at zero voltage between two superconductors separated by a non-superconducting material. The only condition of this effect is that the Cooper pairs in the two superconductors are weakly coupled to each other. The standard Josephson junction (JJ) consists of two superconducting electrodes separated by an insulator, commonly called as SIS junctions. The current in these SIS junctions flow via quantum-mechanical tunneling through the insulating barrier. Another category of JJs is the SNS junctions, where the two superconductors are separated by a normal metal. The Cooper pairs diffuse from the superconductor into the normal metal over a characteristic length ξ . A finite supercurrent can flow only if the two superconducting wavefunctions overlap, as seen in Figure 2.5. A variety of materials has been explored as the normal metal between the two superconductors since the 1960s[57]. Of particular interest to this thesis is graphene, which has been explored for the past decade. In SGS system, the coupling strength between the superconductor and graphene can be controlled via the carrier concentration by means of a gate electrode. When two superconductor wavefunctions are linked by a graphene weak link, the current contains a supercurrent component I_s , which is independent of the voltage V across the superconducting electrodes. This supercurrent is determined by the phase difference between the two superconductors: $\Delta\phi = \phi_1 - \phi_2$, where ϕ_1 and ϕ_2 are the phases of the macroscopic Ginzburg-Landau[58] wavefunctions Ψ according to Equation 2.10. The current-phase relation (CPR) $I_s(\phi)$ can have a simple sinusoidal form, as demonstrated by Josephson in 1962[55]:

$$I_s = I_c \sin(\Delta\phi) \quad (2.13)$$

This is a simple form of the current-phase relation, where I_c is the critical current, which is the maximum supercurrent that flows between the two leads. Equation 2.13 holds true not only for simple superconductor-insulator-superconductor (SIS) junctions but also for superconductor-normal metal-superconductor (SNS) junctions. The general properties of the CPR, independent of the junction's material, are: (i) $I_s(\phi)$ should be a 2π periodic function such that $I_s(\phi) = I_s(\phi + 2\pi)$, (ii) The sign of the phase difference must change with changing the direction of the supercurrent flow, $I_s(\phi) = -I_s(-\phi)$, (iii) In the absence of a phase difference, $\phi=0$, there should be zero supercurrent, $I_s(2\pi n)=0$, where $n = 0, 1, 2, \dots$, (iv) Finally, the supercurrent should be zero at $\phi = \pi n$: $I_s(\pi n)=0$. Therefore, $I_s(\phi)$ lies only in the interval $0 < \pi < \phi$. The current-phase relation of a Josephson junction is peculiar in nature and can deviate from a simple sinusoidal form [59]. The general form of the CPR is written as:

$$I_s = \sum_{n=1}^{\infty} I_c^n \sin(n\Delta\phi) \quad (2.14)$$

where the I_c^n coefficients are the amplitudes of the various harmonics in the CPR.

2.4.3. GRAPHENE-BASED JOSEPHSON JUNCTIONS

Graphene-superconductor hybrid devices employ a graphene sheet connected to superconducting contacts, thus forming a SGS junction. These devices can either be in a short junction limit or in a long junction limit. Here, the SGS junctions are characterized by the quasiparticle mean free path l and the superconducting coherence length ξ (both of the normal metal region) in junctions that are either short (length $L < \xi$) or long ($L > \xi$). These junctions are either ballistic ($l > L$) or diffusive ($l < L$). The striking feature of these devices lies in the fact that the junction is gate-tunable, which features both a high electronic mobility and a large Fermi velocity[60]. The first graphene-based Josephson junction was reported by Heersche *et al.*[11]. The authors showed the dual nature of the charge carriers with non-zero supercurrent at the charge neutrality point. This work was followed by many others, mainly looking into the junction's critical current as a function of geometry, gate voltage, and temperature[61]. These studies were, however, limited because of diffusive transport and poorly defined interfaces. In a condition where the graphene-superconductor interfaces are well defined and combined with the high-quality of graphene, one can observe ballistic propagation of the charge carriers. Ballistic propagation of the charge carriers and electrostatic control of the carrier density can reveal features qualitatively different from the conventional SNS junction behavior. However, supercurrent transport through ballistic graphene has not been experimentally realized, mainly because of the technical limitations on the device-fabrication side.

Recently, however, significant technological progress has been made in improving the quality of graphene by encapsulation in hexagonal boron nitride (h-BN)[6, 8]. Moreover, one-dimensional electrical contacts to encapsulated graphene are demonstrated, which ensure the graphene-metal interfaces to be transparent. Now, the challenge is to contact this high-quality graphene to a superconductor while maintaining the transparency. It would, of course, be very interesting to study the dynamics of the critical current and its scaling with the channel length in the ballistic regime. We, for the first time, made these edge-contacted SGS junctions by contacting graphene to a molybdenum-rhenium superconductor. The fabrication process is outlined in Chapter 4 and the experimental observations are reported in Chapter 8.

2.4.4. ANDREEV REFLECTION

When a normal metal is connected to a superconductor, electronic transport through the metal/superconductor interface is governed by Andreev reflection. A. F. Andreev showed in 1964 that an electron from the normal metal can be transferred into the superconductor[62]. But this can only occur if an electron with momentum \vec{k} and group velocity \vec{v} with an energy $eV > \Delta$ above the Fermi energy (E_f) pairs up with another electron with momentum $-\vec{k}$, but with the same group velocity \vec{v} inside the normal metal, forming a Cooper pair. This process can be described as the reflection of a hole-like quasiparticle, having an inverted momentum \vec{k} and a group velocity $-\vec{v}$, thus moving away from the superconductor. For a normal metal-superconductor interface, the momentum along the boundary must be conserved. Thus the incidence angle of an incoming electron, θ_{inc} , and the reflection angle of a hole, θ_{ref} , obey a simple relation $p_e \sin \theta_{inc} =$

$p_h \sin \theta_{iref}$, where p_e and p_h are the total momentum of the electron and the hole, respectively[63]. The reflected hole remains in the conduction band of the normal metal, and therefore carries the opposite sign of the mass of the electron. To conserve the momentum, the hole reflects back along a path of the incident electron with $\theta_{inc} \approx -\theta_{ref}$, exhibiting perfect retroreflection[63]. The condition for retroreflection is satisfied when $eV < \Delta < E_f$. This process is schematically shown in Figure 2.6.

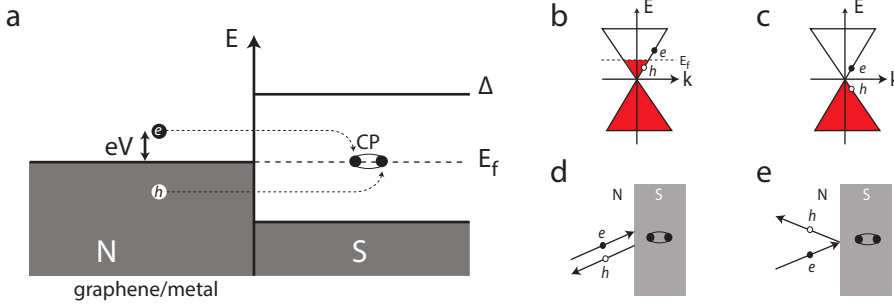


Figure 2.6: (a) Illustration of a NS junction composed of graphene and superconductor. The black and white circles represent the electrons and holes, respectively. Andreev reflection is a process where an electron from the conduction band with a total energy of eV is reflected as a hole with an energy $-eV$, forming a Cooper pair in the superconductor, (b) Linear band dispersion of graphene at higher densities, (c) Band dispersion at zero carrier density or zero doping, (d) For large densities, the electron at incident angle θ from the normal metal produces a Cooper pair in the superconductor and a retroreflected hole in the conduction band of the normal metal. This process is called retro-reflection, (e) For undoped graphene the hole undergoes an interband transition into the valence band, resulting in specular reflection. This phenomenon, only observable in undoped graphene, has been demonstrated recently by Efetov *et al.*[63]. This figure is inspired by Ref.[52, 63].

However, in the limit when $E_f < \Delta$, which is the case for undoped graphene¹, the reflected hole appears in the valence band rather than in the conduction band. This is called specular Andreev reflection[64]. The reflected hole now has the same mass sign as the incident electron, and therefore, because of momentum conservation, travels in the same direction along the interface, where $\theta_{inc} = \theta_{ref}$. The condition for specular Andreev reflection is satisfied when $\Delta > eV > E_f$.

2.4.5. ANDREEV BOUND STATES

The supercurrent in a SNS junction is mainly transmitted by discrete entangled electron-hole states confined to the normal metal, called Andreev bound states (ABS). In other words, Andreev reflections happen continuously on both interfaces in a SNS junctions, where the electron (hole) impinging on the surface of the superconductor will be reflected as hole (electron). This leads to a coherent circulation of electrons in one direction and holes in the other. The schematic of such a process is shown in Figure 2.7. The

¹Predicted to be observable when the normal metal in the N/SC junction consists of a zero-gap semiconductor and the Fermi energy is tuned close to the charge neutrality point.

total phase change is the phase picked up during Andreev reflection (AR) and during the electron/hole motion[65]. The phase which is picked up during AR can be derived from the Bogoliubov de-Gennes equation. The resonance condition is:

$$2\pi m = -2\arccos\left(\frac{E}{\Delta}\right) \pm (\phi_1 - \phi_2) + k_f L \frac{E}{E_f} \quad (2.15)$$

where m is the total number of ABS states in a junction of length L , ϕ_1 and ϕ_2 are the phases of the superconducting condensates in the two superconductors, and \pm corresponds to the two directions of the electron-hole pair.

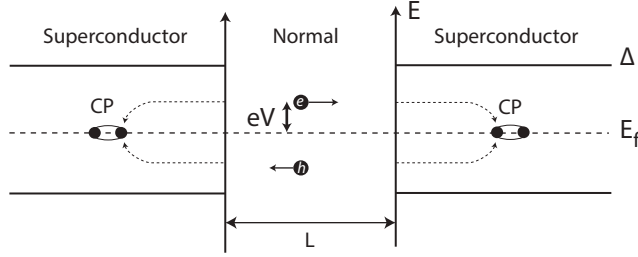


Figure 2.7: Shows a schematic of two superconducting leads with a normal region (graphene) between them. Successive Andreev reflections occur at the interfaces, resulting in the formation of Andreev bound state (ABS) in the normal metal. In each half cycle, one Cooper pair with charge $2e$ is transferred from one superconductor to the other. This leads to the formation of discrete resonant states of entangled $e-h$ pairs confined between the superconductors. This figure is adapted from Ref. [65].

A populated ABS carries a supercurrent $(2e/\hbar)(\frac{\delta E_n}{\delta \phi})$, which is phase dependent. The total phase dependent energy is the sum of all ABS as:

$$E(\phi) = \sum_n E_n(\phi) = \Delta \sum_n \sqrt{1 - T_n \sin^2(\phi/2)} \quad (2.16)$$

Where T_n is the transmission. The supercurrent in a junction is:

$$I(\phi) = \frac{e\Delta}{2\hbar} \sum_n \frac{T_n \sin(\phi)}{\sqrt{1 - T_n \sin^2(\phi/2)}} \quad (2.17)$$

The maximum supercurrent is achieved at $\phi = \pi/2$. The Josephson effect in these junctions is defined in terms of the current-phase relation. In junctions with small T_n (tunnel junctions with $T_n \ll 1$), the current-phase relation is sinusoidal[59, 66]. However, for junctions with a large transmission (in quantum point contacts with $T_n \lesssim 1$), the current-phase relation deviates strongly from the sinusoidal one[67–70]. A non-sinusoidal CPR has previously been measured in many systems, such as graphene[71], topological insulators[72] and quantum point contacts[67, 69]. This will be discussed later in Chapter 10 where we found that the CPR of graphene-based Josephson junctions deviates from a simple sinusoidal form.

REFERENCES

- [1] A. H. C. Neto, F. Guinea, N. M. R. Peres, K. S. Novoselov, and A. K. Geim, *The electronic properties of graphene*, *Reviews of Modern Physics* **81**, 109 (2009).
- [2] I. W. Frank, D. M. Tanenbaum, A. M. van der Zande, and P. L. McEuen, *Mechanical properties of suspended graphene sheets*, *Journal of Vacuum Science & Technology B* **25**, 2558 (2007).
- [3] R. R. Nair, P. Blake, A. N. Grigorenko, K. S. Novoselov, T. J. Booth, T. Stauber, N. M. R. Peres, and A. K. Geim, *Fine structure constant defines visual transparency of graphene*, *Science* **320**, 1308 (2007).
- [4] H. P. Boehm, A. Clauss, G. O. Fischer, and U. Hofmann, *Dünnste kohlenstoff-folien*, *Zeitschrift für Naturforschung* **17b**, 150 (1962).
- [5] K. S. Novoselov, A. K. Geim, S. V. Morozov, D. Jiang, M. I. Katsnelson, I. V. Grigorieva, S. V. Dubonos, and A. A. Firsov, *Two-dimensional gas of massless Dirac fermions in graphene*, *Nature* **438**, 197 (2005).
- [6] C. R. Dean, A. F. Young, I. Meric, C. Lee, L. Wang, S. Sorgenfrei, K. Watanabe, T. Taniguchi, P. Kim, K. L. Shepard, and J. Hone, *Boron nitride substrates for high quality graphene electronics*, *Nature Nanotechnology* **5**, 722 (2010).
- [7] A. K. Geim and K. S. Novoselov, *The rise of graphene*, *Nature Materials* **6**, 183 (2007).
- [8] L. Wang, I. Meric, P. Y. Huang, Q. Gao, Y. Gao, H. Tran, T. Taniguchi, K. Watanabe, L. M. Campos, D. A. Muller, J. Guo, P. Kim, J. Hone, K. L. Shepard, and C. R. Dean, *One-dimensional electrical contact to a two-dimensional material*, *Science* **342**, 614 (2013).
- [9] C. Stampfer, J. Güttinger, S. Hellmüller, F. Molitor, K. Ensslin, and T. Ihn, *Energy gaps in etched graphene nanoribbons*, *Physical Review Letters* **102**, 056403 (2009).
- [10] M. Y. Han, B. Özyilmaz, Y. Zhang, and P. Kim, *Energy band-gap engineering of graphene nanoribbons*, *Physical Review Letters* **98**, 206805 (2007).
- [11] H. B. Heersche, P. Jarillo-Herrero, J. B. Oostinga, L. M. K. Vandersypen, and A. F. Morpurgo, *Bipolar supercurrent in graphene*, *Nature* **446**, 56 (2007).
- [12] M. Titov and C. W. J. Beenakker, *Josephson effect in ballistic graphene*, *Physical Review B* **74**, 041401 (2006).
- [13] C. T. Ke, I. V. Borzenets, A. W. Draelos, F. Amet, Y. Bomze, G. Jones, M. Craciun, S. Russo, M. Yamamoto, S. Tarucha, and G. Finkelstein, *Critical current scaling in long diffusive graphene-based Josephson junctions*, *Nano Letters* **16** (8), 4788 (2016).
- [14] M. B. Shalom, M. J. Zhu, V. I. Fal'ko, A. Mishchenko, A. V. Kretinin, K. S. Novoselov, C. R. Woods, K. Watanabe, T. Taniguchi, A. K. Geim, and J. R. Prance, *Quantum oscillations of the critical current and high-field superconducting proximity in ballistic graphene*, *Nature Physics* **12**, 318–322 (2016).

- [15] V. E. Calado, S. Goswami, G. Nanda, M. Diez, A. R. Akhmerov, K. Watanabe, T. M. K. T. Taniguchi, and L. M. K. Vandersypen, *Ballistic Josephson junctions in edge-contacted graphene*, *Nature Nanotechnology* **10**, 761 (2015).
- [16] P. Blake, E. W. Hill, A. H. C. Neto, K. S. Novoselov, D. Jiang, R. Yang, T. J. Booth, and A. K. Geim, *Making graphene visible*, *Applied Physics Letters* **91**, 063124 (2007).
- [17] A. Charrier, A. Coati, T. Argunova, F. Thibaudau, Y. Garreau, R. Pinchaux, I. Forbeaux, J. M. Debever, M. Sauvage-Simkin, and J. M. Themlin, *Solid-state decomposition of silicon carbide for growing ultra-thin heteroepitaxial graphite films*, *Applied Physics Letters* **92**, 2479 (2002).
- [18] H. Tetlow, J. P. de Boer, I. J. Ford, D. D. Vvedensky, J. Coraux, and L. Kantorovich, *Growth of epitaxial graphene: Theory and experiment*, *Physics Reports* **542**, 195 (2014).
- [19] J. Baringhaus, M. Ruan, F. Edler, A. Tejada, M. Sicot, A. Taleb-Ibrahimi, A. P. Li, Z. Jiang, E. H. Conrad, C. Berger, C. Tegenkamp, and W. A. de Heer, *Exceptional ballistic transport in epitaxial graphene nanoribbons*, *Nature* **506**, 349 (2014).
- [20] H. Wang and G. Yu, *Direct cvd graphene growth on semiconductors and dielectrics for transfer-free device fabrication*, *Advanced Materials* **28**, 4956 (2016).
- [21] H. Ago, Y. Ito, N. Mizuta, K. Yoshida, B. Hu, C. M. Orofeo, M. Tsuji, K. Ikeda, and S. Mizuno, *Epitaxial chemical vapor deposition growth of single-layer graphene over cobalt film crystallized on sapphire*, *ACS Nano* **4**, 7407 (2010).
- [22] P. R. Wallace, *The band theory of graphite*, *Physical Review* **71**, 622 (1947).
- [23] K. I. Bolotin, K. J. Sikes, Z. Jiang, M. Klima, G. Fudenberg, J. Hone, P. Kim, and H. L. Stormer, *Ultrahigh electron mobility in suspended graphene*, *Solid State Communications* **146**, 351 (2008).
- [24] M. M. Jung, W. Song, D. S. Jung, S. S. Lee, S. Sun, C.-Y. Park, and K.-S. Ann, *Tuning the electrical properties of graphene via nitrogen plasma-assisted chemical modification*, *Journal of Nanoscience and Nanotechnology* **16**, 2756 (2016).
- [25] Z. Xu, Z. Ao, D. Chu, and S. Li, *UV irradiation induced reversible graphene band gap behaviors*, *J. Mater. Chem. C* **4**, 8459 (2016).
- [26] Y. Zhang, T.-T. Tang, C. Girit, Z. Hao, M. C. Martin, A. Zettl, M. F. Crommie, Y. R. Shen, and E. Wang, *Direct observation of a widely tunable bandgap in bilayer graphene*, *Solid State Communications* **459**, 820 (2009).
- [27] A. N. Abbas, G. Liu, B. Liu, L. Zhang, H. Liu, D. Ohlberg, W. Wu, and C. Zhou, *Patterning, characterization, and chemical sensing applications of graphene nanoribbon arrays down to 5 nm using helium ion beam lithography*, *ACS Nano* **8**, 1538 (2014).

- [28] J.-K. Lee, S. Yamazaki, H. Yun, J. Park, G. P. Kennedy, G.-T. Kim, O. Pietzsch, R. Wiesendanger, S. Lee, S. Hong, U. Dettlaff-Weglikowska, and S. Roth, *Modification of electrical properties of graphene by substrate-induced nanomodulation*, Nano Letters **13**, 3494 (2013).
- [29] S. Nakaharai, T. Iijima, S. Ogawa, S. Suzuki, S. L. Li, K. Tsukagoshi, S. Sato, and N. Yokoyama, *Conduction tuning of graphene based on defect-induced localization*, ACS Nano **7**, 5694 (2013).
- [30] B. S. Archanjo, A. P. M. Barboza, B. R. A. Neves, L. M. Malard, E. H. M. Ferreira, J. C. Brant, E. S. Alves, F. Plentz, V. Carozo, and B. Fragneaud, *The use of a Ga⁺ focused ion beam to modify graphene for device applications*, Nanotechnology **23**, 255305 (2012).
- [31] Z. Moktadir, S. Hang, and H. Mizuta, *Defect-induced Fermi level pinning and suppression of ambipolar behaviour in graphene*, Carbon **93**, 325 (2015).
- [32] B. Guo, Q. Liu, E. Chen, H. Zhu, L. Fang, and J. R. Gong, *Controllable n-doping of graphene*, Nano Letters **10**, 4975 (2010).
- [33] P. Rani and V. K. Jindal, *Designing band gap of graphene by B and N dopant atoms*, RSC Advances **3**, 802 (2013).
- [34] P. Willke, J. A. Amani, A. Sinterhauf, S. Thakur, T. Kotzott, T. Druga, S. Weikert, K. Maiti, H. Hofsässs, and M. Wenderoth, *Doping of graphene by low-energy ion beam implantation: Structural, electronic, and transport properties*, Nano Letters **15**, 5110 (2015).
- [35] P. Gallagher, K. Todd, and D. Goldhaber-Gordon, *Disorder-induced gap behavior in graphene nanoribbons*, Physical Review B **81**, 115409 (2010).
- [36] K. Nakada, M. Fujita, G. Dresselhaus, and M. S. Dresselhaus, *Edge state in graphene ribbons: nanometer size effect and edge shape dependence*, Physical Review B **54**, 7954 (1996).
- [37] V. Barone, O. Hod, and G. E. Scuseria, *Electronic structure and stability of semiconducting graphene nanoribbons*, Nano Letters **6**, 2748 (2006).
- [38] D. Bischoff, A. Varlet, P. Simonet, M. Eich, H. C. Overweg, T. Ihn, and K. Ensslin, *Localized charge carriers in graphene nanodevices*, Applied Physics Reviews **2**, 031301 (2015).
- [39] F. Sols, F. Guinea, and A. H. C. Neto, *Coulomb blockade in graphene nanoribbons*, Physical Review Letters **99**, 166803 (2007).
- [40] F. Molitor, A. Jacobsen, C. Stampfer, J. Güttinger, T. Ihn, and K. Ensslin, *Transport gap in side-gated graphene constrictions*, Phys. Rev. B **79**, 075426 (2009).
- [41] M. Evaldsson, I. V. Zozoulenko, H. Xu, and T. Heinzel, *Edge-disorder-induced anderson localization and conduction gap in graphene nanoribbons*, Physical Review B **78**, 161407 (2008).

- [42] X. Li, X. Wang, L. Zhang, S. Lee, and H. Dai, *Chemically derived, ultrasmooth graphene nanoribbon semiconductors*, Science **319**, 1229 (2008).
- [43] T. Shimizu, J. Haruyama, D. C. Marcano, D. V. Kosynkin, J. M. Tour, K. Hirose, and K. Suenaga, *Large intrinsic energy bandgaps in annealed nanotube-derived graphene nanoribbons*, Nature Nanotechnology **6**, 45 (2011).
- [44] D. V. Kosynkin, A. L. Higginbotham, A. Sinitskii, J. R. Lomeda, A. Dimiev, B. K. Price, and J. M. Tour, *Longitudinal unzipping of carbon nanotubes to form graphene nanoribbons*, Nature **458**, 872 (2009).
- [45] B. Sommer, J. Sonntag, A. Ganczarczyk, D. Braam, G. Prinz, A. Lorke, and M. Geller, *Electron-beam induced nano-etching of suspended graphene*, Scientific Reports **5**, 7781 (2015).
- [46] Q. Wang, R. Kitaura, S. Suzuki, Y. Miyauchi, K. Matsuda, Y. Yamamoto, S. Arai, and H. Shinohara, *Fabrication and in situ transmission electron microscope characterization of free-standing graphene nanoribbon devices*, ACS Nano **10**, 1475 (2016).
- [47] J. A. Rodríguez-Manzo, Z. J. Qi, A. Crook, J. H. Ahn, A. T. C. Johnson, and M. Drndić, *In situ transmission electron microscopy modulation of transport in graphene nanoribbons*, ACS Nano **10**, 4004 (2016).
- [48] D. Pickard and L. Scipioni, *Graphene nano-ribbon patterning in the orion plus*, Zeiss Application Note (2009).
- [49] M. C. Lemme, D. C. Bell, J. R. Williams, L. A. Stern, B. W. H. Baugher, P. Jarillo-Herrero, and C. M. Marcus, *Etching of graphene devices with a helium ion beam*, ACS Nano **3**, 2674 (2009).
- [50] Y. Zhang, C. Hui, R. Sun, K. Li, K. He, X. Ma, and F. Liu, *A large-area 15 nm graphene nanoribbon array patterned by a focused ion beam*, Nanotechnology **25**, 135301 (2014).
- [51] D. C. Bell, M. C. Lemme, L. A. Stern, J. R. Williams, and C. M. Marcus, *Precision cutting and patterning of graphene with helium ions*, Nanotechnology **20**, 455301 (2009).
- [52] V. E. Calado, *Graphene nanodevices*, PhD Thesis, Technische Universiteit Delft (2013).
- [53] H. Keijzers, *Josephson effects in carbon nanotube mechanical resonators and graphene*, PhD Thesis, Technische Universiteit Delft (2012).
- [54] J. Bardeen, L. N. Cooper, and J. R. Schrieffer, *Theory of superconductivity*, Physical Review **108**, 1175 (1957).
- [55] B. Josephson, *Possible new effects in superconductive tunneling*, Physics Letters **1**, 251 (1962).

- [56] J. Reutlinger, L. Glazman, Y. V. Nazarov, and W. Belzig, *Secondary "smile"-gap in the density of states of a diffusive Josephson junction for a wide range of contact types*, Physical Review B **90**, 014521 (2014).
- [57] K. K. Likharev, *Superconducting weak links*, Review of Modern Physics **51**, 101 (1979).
- [58] V. L. Ginzburg and L. D. Landau, *On the theory of superconductivity*, Zh. Eksp. Teor. Fiz. **20**, 1064 (1950).
- [59] A. A. Golubov, M. Y. Kupriyanov, and E. Il'ichev, *The current-phase relation in Josephson junctions*, Reviews of Modern Physics **76**, 411 (2004).
- [60] D. C. Elias, R. V. Gorbachev, A. S. Mayorov, S. V. Morozov, A. A. Zhukov, P. Blake, L. A. Ponomarenko, I. V. Grigorieva, K. S. Novoselov, F. Guinea, and A. K. Geim, *Dirac cones reshaped by interaction effects in suspended graphene*, Nature Physics **7**, 701 (2011).
- [61] X. Du, I. Skachko, and E. Y. Andrei, *Josephson current and multiple Andreev reflections in graphene SNS junctions*, Physical Review B **77**, 184507 (2008).
- [62] A. F. Andreev, *Thermal conductivity of the intermediate state of superconductors*, Soviet Physics—JETP **19**, 1228 (1964).
- [63] D. K. Efetov, L. Wang, C. Handschin, K. B. Efetov, J. Shuang, R. Cava, T. Taniguchi, K. Watanabe, J. Hone, C. R. Dean, and P. Kim, *Specular interband Andreev reflections at van der Waals interfaces between graphene and NbSe₂*, Nature Physics **12**, 328 (2016).
- [64] C. W. J. Beenakker, *Specular Andreev reflection in graphene*, Physical Review Letters **97**, 067007 (2006).
- [65] J.-D. Pillet, C. H. L. Quay, P. Morfin, C. Bena, A. L. Yeyati, and P. Joyez, *Andreev bound states in supercurrent-carrying carbon nanotubes revealed*, Nature Physics **6**, 965 (2010).
- [66] A. Furusaki and M. Tsukada, *Current-carrying states in Josephson junctions*, Physical Review B **43**, 10164 (1991).
- [67] C. W. J. Beenakker and H. van Houten, *Josephson current through a superconducting quantum point contact shorter than the coherence length*, Physical Review Letters **66**, 3056 (1991).
- [68] A. M. Black-Schaffer and J. Linder, *Strongly anharmonic current-phase relation in ballistic graphene Josephson junctions*, Physical Review B **82**, 184522 (2010).
- [69] M. L. D. Rocca, M. Chauvin, B. Huard, H. Pothier, D. Esteve, and C. Urbina, *Measurement of the current-phase relation of superconducting atomic contacts*, Physical Review Letters **99**, 127005 (2007).

- [70] I. Hagymási, A. Kormányos, and J. Cserti, *Josephson current in ballistic superconductor-graphene systems*, *Physical Review B* **82**, 134516 (2010).
- [71] C. D. English, D. R. Hamilton, C. Chialvo, I. C. Moraru, N. Mason, and D. J. V. Harlingen, *Observation of non-sinusoidal current-phase relation in graphene Josephson junctions*, *Physical Review B* **94**, 115435 (2016).
- [72] I. Sochnikov, L. Maier, C. A. Watson, J. R. Kirtley, C. Gould, G. Tkachov, E. M. Hankiewicz, C. Brüne, H. Buhmann, L. W. Molenkamp, and K. A. Moler, *Nonsinusoidal current-phase relationship in Josephson junctions from the 3d topological insulator HgTe*, *Physical Review Letters* **114**, 066801 (2015).

3

HELIUM ION MICROSCOPY

This chapter provides a general introduction to helium ion microscopy (HIM). After a brief introduction, ion-matter interaction is discussed for imaging and nanofabrication. I will try to give an overview of applications of helium ion microscopy that make use of the sub-nanometer probe size of the HIM. The sub-nanometer resolution of the beam provides a unique opportunity to study the modification of materials at the nanoscale. Although, HIM has potential applications in many fields, such as biology, plasmonics, electronics, and material science we limit our discussion to milling and beam induced deposition.

3.1. HELIUM ION MICROSCOPY: A BRIEF REVIEW

THE ability of glass to bend light has been known for over 2000 years. The first microscope ever used was a simple magnifying glass, which had power typically between 6x and 10x. But it was not until the late 17th century before the first real microscope was used by Antonie van Leeuwenhoek, a Dutch scientist and one of the pioneers of microscopy. Since then there have been tremendous advancements in the microscopy field. Numerous microscopy techniques have been introduced, such as optical microscopy, electron microscopy, and ion microscopy, which are now being used on a daily basis in science and technology. In 1878, Ernst Abbe proved that the smallest detail that can ever be resolved optically is of the order of a few tens of nanometers, which is limited by the wavelength of light[1]. The resolution of the microscopy is further improved after the formulation of the dual nature of electrons by Louis de Broglie in 1924 [2]. The smaller the object we want to see, the higher the energy and the shorter the wavelength we need to use. The wavelength of an electron is typically smaller than the shortest wavelength of visible light. Consequently, an electron beam can be used to image features smaller than 1 nm. The first electron microscope was invented by M. Knoll and E. Ruska[3], where the resolution was limited only by diffraction of the electrons. A scanning electron microscope (SEM) is nowadays a widely used instrument for imaging and material characterization. The smallest feature that can be resolved is limited by the diameter of the beam of electrons on the sample surface. This limits the capabilities of a scanning electron beam to image the sample with sub-nm resolution. According to Young and Fresnel[4], the size of the smallest spot in any optical system is limited by diffraction and is given by:

$$\delta \approx \frac{\lambda}{\alpha} \quad (3.1)$$

Here, δ is the minimum feature that can be resolved in an image, λ is the wavelength of the probing particles, which for electrons in SEMs is 0.01 nm, and α is the beam convergence angle. The maximum value of α is limited to $\pi/2$ radians. However, practical values of α are well below 1 mrad, resulting in poorer resolution, but also in a larger large depth of field[5]. The interaction of a focused charged particle beam with a sample surface has been extensively studied for imaging and nanofabrication since the 1960s[6]. It is only since liquid metal ion sources (LMIS) employing gallium were introduced in the 1970s [8, 9], focused beams are used for nanofabrication. Furthermore, a variety of other microscopy techniques, such as atomic force microscopy, and scanning tunneling microscopy have been developed in the recent decades.

About a decade ago, in 2007, a new kind of field ion microscope, employing helium ions was commercialized[10]. After the market introduction, the helium ion microscope (HIM) has been extensively used for imaging and nanofabrication. Helium ion microscopy unites the advantages of scanning electron microscopy (SEM) and focused ion beam (FIB) and overcomes some of their limitations. In particular, it makes it possible to image insulating samples, such as biological materials, without the need of a conductive coating.

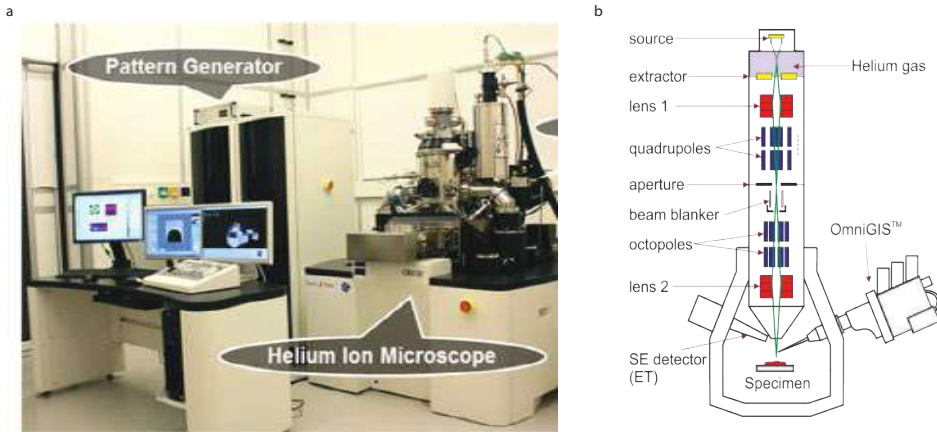


Figure 3.1: (a) Picture of the helium ion microscope (HIM) at TNO Delft. The microscope is equipped with an Omniprobe gas injection system (not visible) and Raith pattern generator. The picture is adapted from Ref.[11], (b) The schematic representation of the ion beam column. Image courtesy: Stuart Boden, University of Southampton.

The HIM is a surface imaging tool which scans a focused beam of helium ions across a surface to produce an image. It is similar to a scanning electron microscope (SEM). Since helium ions are $7,300\times$ heavier than electrons, the wavelength is shorter than that of an electron. Therefore, diffraction effects are negligible in helium ion microscopy, and HIM is able to produce a smaller probe size compared to even the best SEM. This leads to a small interaction volume of the beam in the bombarded material, and therefore high resolution imaging[5]. Note that high doses of helium beam can cause sputtering of the material and, therefore, can modify the surface morphology. Therefore, one has to be careful during sample imaging with HIM. The sub-nanometer helium beam can also be used for fine patterning of nanostructures. As a result, the helium ion microscope has been used as a nanofabrication tool for various applications. Recent examples include nano-structuring of graphene[12–14], direct writing of patterns in gold[15, 16], lithography[17, 18], and helium ion beam induced deposition (HeIBID)[11, 19].

3.1.1. WORKING PRINCIPLES

The basic principle of the helium ion microscope can be linked to the field ion microscope (FIM) developed by Müller and Tsong in the 1960s[20]. A FIM provides atomic-resolution imaging of a sample surface by introducing a noble gas, such as helium, in the vicinity of a positively charged sharp needle. The atoms of the gas are ionised very close to the tip surface and subsequently accelerated away by the intense electric field, forming an image onto a phosphor screen. Similarly, the ionization and acceleration of helium atoms are achieved in a Gas Field Ion Source (GFIS). Although, GFIS have been investigated for a long time [21, 22], only recently a stable ion source with high brightness has been realized [5, 10].

The main characteristic of the microscope is the nature of the beam interactions with the sample. These interactions produce the secondary electrons (SEs) that provide the image information. The source of a HIM consists of a tungsten needle with an atomically sharpened tip, which is biased at a positive voltage with respect to an extraction electrode. This needle is cooled to cryogenic temperature (~ 70 K) and a helium gas is introduced into the vicinity of the needle. The tip of the source contains three atoms, called a trimer, which is the most stable atomic configuration. Using Scanning Field Ion Microscopy (SFIM), the apex of the tip can be monitored and sharpened using high fields that can ultimately remove weakly bound atoms from the apex. An SFIM image of the trimer is shown in Figure 3.2a. The white region at the center contains three atoms. The emission from one of these ions is selected which behaves as a single atom emitter with high brightness of $\sim 1 \times 10^9$ A cm $^{-2}$ sr $^{-1}$ [10]. The schematic of the ionization process is shown in Figure 3.2b. At the very tip of the needle, the electric field strength is sufficiently high to cause field ionization of helium atoms, which are then accelerated away from the needle. This ion beam is then transmitted through an optical column towards the sample surface.

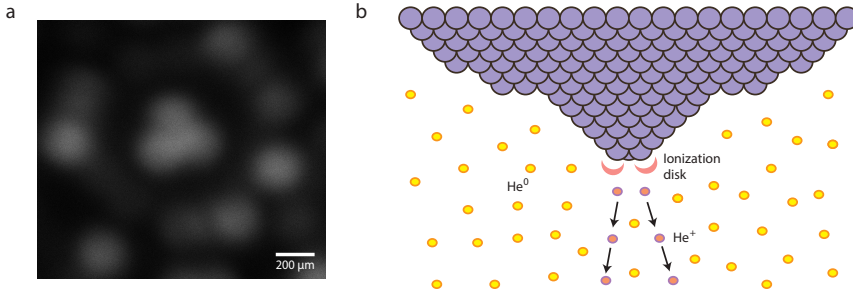


Figure 3.2: (a) Shows a Scanning Field Ion Microscopy (SFIM) image of the source. The three bright circles at the center are the three atoms at the very apex of the tip. The atoms of the next crystal plane are also visible as a ring of the inner atoms, (b) shows the ionization of the helium atoms at the very apex. The tip is sharpened to have only three atoms, a trimer, at the apex, which is the most stable configuration.

The column of the helium ion microscope consists of a deflection system and two electrostatic lenses. The first lens or the condenser lens images the source to a cross-over inside the column. The second lens or the objective lens images the cross-over onto the specimen plane [23]. The column can produce a focused probe with a spot size of about 0.25 nm [10]. The probe current and probe size can be modulated with apertures. The calculated beam diameter is often cited as the d_p of the probe and is defined as [23]:

$$d_p = \sqrt{((d_A^4 + d_S^4)^{1.3/4} + d_I^{1.3})^{2/1.3} + d_C^2} \quad (3.2)$$

where d_A is the contribution due to diffraction, d_S is the contribution due to spherical aberration, d_C the contribution due to chromatic aberration, and d_I is the natural size of the source image on the sample surface. Because all helium ions are extracted from one atom, the helium ion beam has an ultra-narrow energy distribution. This provides low

chromatic aberrations and, thus, a very high spatial resolution. Moreover, the helium ions have a negligible de Broglie wavelength: 1.4×10^{-4} nm for a 10 keV and 0.080 pm for a 30 keV He^+ beam [23, 24]. As a result, the helium ions follow nearly radial paths from the source and appear to originate from a point source. Hence, the probe size of the focused He^+ beam on a sample is limited by the aberrations of the beam focusing optics. The reported value for the virtual source is ≤ 0.25 nm. The so-called point source is characterized in terms of its angular intensity which is defined as the current emitted per solid angle. For HIM, the measured angular intensity is $0.5\text{-}1 \mu\text{A sr}^{-1}$ and the energy spread $0.25\text{-}0.5$ eV [23]. The ion beam energy in a commercial HIM can be varied between 10 keV and 40 keV.

3.2. BEAM-SAMPLE INTERACTION

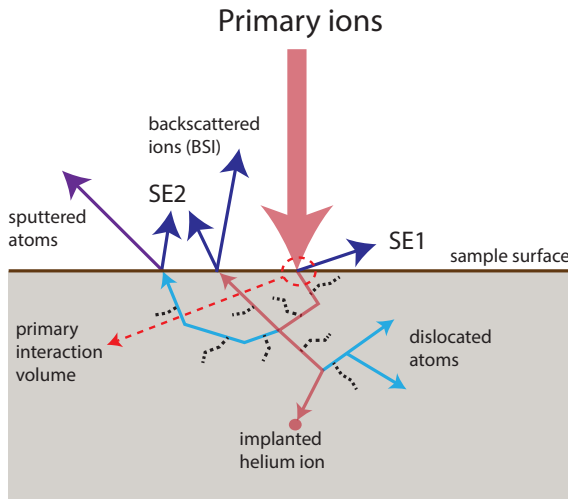


Figure 3.3: Shows an example of a primary ion trajectory with secondary electron (SE) emission and dislocated and sputtered atoms.

The understanding of helium beam-sample interaction is important for the experiments performed in Chapters 5 and 6. As a He^+ ion enters a solid with high energy, it undergoes multiple collisions with the atoms of the solid, generating excited electrons and gradually losing its energy along the way. The energy transfer process leads to multiple processes, as shown in Figure 3.3. The incident ions transfer kinetic energy and momentum to the target atoms. The ion-atom interactions can be elastic or inelastic. The inelastic interactions comprise transfer of energy to the electrons in the solid. If that happens when the ion is still close to the surface, it may result in the emission of secondary electrons or SE1s. These SEs have energies less than 50 eV. The elastic interactions comprise the transfer of momentum and energy of the ions to the target atoms. When a displaced

atom leaves the target material, it is called a sputtered atom.

Following the first collision, most incident ions collide more often and travel until they come to a stop. After a sequence of collision events, some of these ions may end-up close to the surface again, emitting secondary electrons (called SE2s) and maybe sputtered target atoms. The interaction volume is the total region in a solid where the beam interacts before it eventually comes to a stop. Monte Carlo simulation programs can be used to calculate the interaction volumes for electron and ion (helium and gallium) beams. Figure 3.4 presents Monte Carlo results of a 1 keV electron beam, a 30 keV gallium beam, and a 30 keV helium beam interacting with a silicon target. CASINO[25] is used for an electron beam and SRIM[26] for the ion beams. The helium beam in the first few tens of nanometers of the material scatters far less than an electron beam, and hence, remains better focused, see Figure 3.4. The electrons that are generated at depth z have a probability $P_{esc}(z)$ to escape to the vacuum. It is given by[23]:

$$P_{esc}(z) = C \exp(-z/\lambda) \quad (3.3)$$

where C is a constant and λ is the effective escape depth for SEs, which is for 5-100 eV electrons in most solids between 1 and 10 nm.

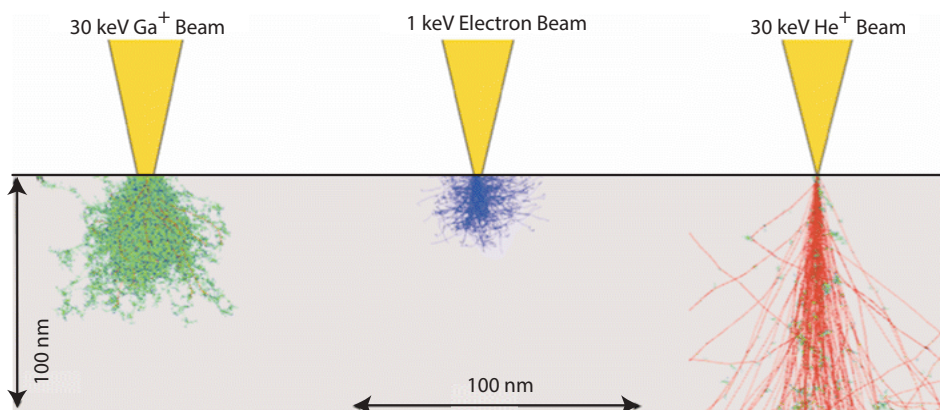


Figure 3.4: Comparison of interaction volumes for 30 keV Ga^+ , 1 keV electrons, and 30 keV He^+ in silicon. The interaction volume for the helium beam close to the surface is much narrower than that of the electron beam or the gallium beam. Taken from the Ref.[27]

Since the helium mass is much larger than the electron mass, the helium ion maintains much better its original direction. Initially, the energy loss of the incident ions is dominated by inelastic, or electronic, collisions. This phase is called the electronic loss regime[6]. In a nuclear collision, the ion scatters elastically from the nucleus of an atom. At a later stage, nuclear collisions start to dominate. In this regime, the ions scatter over large angles and the interaction volume broadens. In each nuclear collision, the ion transfers a small part of its energy to the target atom. If the incident particle has energy E and transfers energy T to the target atom, the ratio T/E is given by[6]:

$$\frac{T}{E} = \left(\frac{4M_1M_2}{(M_1 + M_2)^2} \right) \sin^2 \frac{\theta}{2} \quad (3.4)$$

where θ is the scattering angle, M_1 and M_2 are the mass of the projectile and the target atom, respectively. If T is smaller than the lattice binding energy, $E_{binding}$, it cannot displace the target atom. However, if $T > E_{binding}$, the target atom is knocked out (recoiled) of its lattice position. An energetic recoil atom can also initiate a collision cascade, leading to the generation of more recoils and SEs. The collision cascades determine to a large extent the interaction volume. The interaction volume of the helium ion beam is much narrower than that of the electron beam, especially in the first few nanometers. This means that the SEs generated by the ion beam will be localized much more to the area directly around the beam impact point on the specimen, allowing for more surface detail to be resolved in a helium ion microscope as compared to an electron microscope.

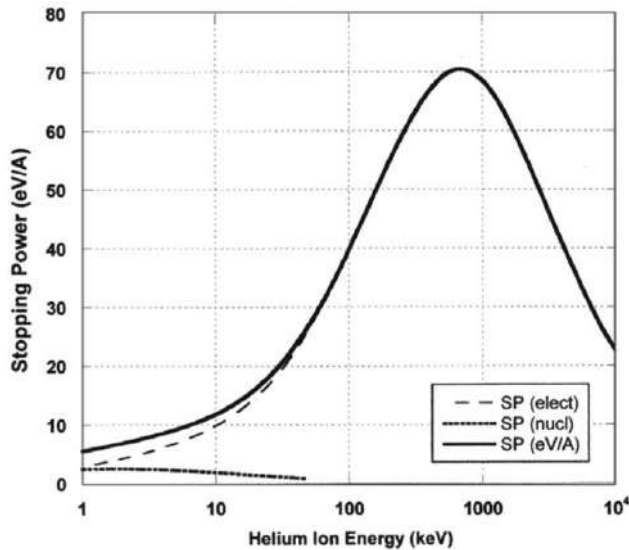


Figure 3.5: Shows the stopping power of helium ions in silicon. This figure is taken from Ref.[23].

Figure 3.5 shows the electronic, nuclear, and total stopping power of helium ions for silicon. Near 1 keV the electronic and nuclear stopping powers are comparable. But above 20 keV, the stopping power is almost exclusively determined by electronic collisions. The nuclear stopping power for an ion with energy E_o is calculated as[23]:

$$S_n(E_o) = \frac{8.462 \times 10^{-15} Z_1 Z_2 M_1 S_n(\epsilon)}{(M_1 + M_2)(Z_1^{0.23} + Z_2^{0.23})} (eV cm^2) atom^{-1} \quad (3.5)$$

where Z_1 and Z_2 are the atomic numbers of the projectile and the target atom, respectively. ϵ is the reduced energy and is defined as:

$$\epsilon = \frac{32.53 M_2 E}{Z_1 Z_2 (M_1 + M_2) (Z_1^{0.23} + Z_2^{0.23})} \quad (3.6)$$

The helium ions cause less sub-surface damage than gallium ions. However, high doses of helium ions could induce damage at the end of the stopping range. The implantation of helium has a dramatic influence on crystalline samples, leading to the formation of nanobubbles filled with helium[28]. At low beam energies, the bubbles form close to the surface and trapped helium can easily escape by out-diffusion, accelerated by the presence of defects. It is speculated that amorphous materials are less prone to bubble formation as the out-diffusion of helium from those materials is rather easy. In bulk silicon, the initial density reduction of the silicon is caused by the beam induced knock-out events. This leads to the amorphization of the single-crystalline silicon[23]. As the ion dose is further increased, the density of the material in the ion beam interaction region continues to decrease due to the subsurface implantation of helium that coalesces into nano-bubbles[23]. The nano-bubble formation in the substrate can have severe consequences on the device performance.

In addition, helium ions can also induce chemical change to polymers, such as resists, a process commonly known as ion beam lithography. In conventional electron beam lithography, the secondary electrons with energies between 2 and 50 eV contribute to the distribution of energy in the resist. This chemical change influences the solubility of the resist, which enables the exclusive removal of the exposed or the non-exposed areas of resist by immersion in a solvent. In helium ion beam lithography, primary beam, recoil atoms, phonons, surface or volume plasmons, and the SEs contribute to the distribution of the energy and the chemical change in the resist. However, the contributions from the phonons and surface or volume plasmons are minimal[23]. In lithography, the so-called point-spread function (PSF) describes the exposure of the resist; it combines the physical processes mentioned above and the resist development process described below. The PSF is the spatial distribution of the effective exposure dose. As mentioned before, helium ions scatter less than electrons, and therefore, their PSF is correspondingly narrower than electron or heavy ion's PSFs. A very nice discussion of these contributing factors to resolution in lithography with electron and helium ion beams is given by Ramachandra *et al.*[29]. In an elastic collision between a 30 keV He⁺ and a stationary electron, the He⁺ will transfer a maximum energy of ~16 eV to the electron[17]. For example, the energy of a Si-H bond in a common resist hydrogen silsesquioxane (HSQ), is ~3 eV. So, the SEs generated by the primary beam have enough energy to break bonds and thus help crosslink HSQ and make it less soluble. After the exposure, an organic or inorganic solution is used to wash away the unexposed regions, a process commonly known as development. The general mathematical expression of the PSF, involving the sum of two Gaussian terms, can be written as[23]:

$$PSF(r) = A \left[\frac{1}{\alpha^2} \exp\left(-\frac{r^2}{\alpha^2}\right) + \frac{\eta}{\beta^2} \exp\left(-\frac{r^2}{\beta^2}\right) \right] \quad (3.7)$$

where A is a normalisation constant, α is the forward scattering range, β is the backscattering range, r is the radial distance from the primary beam incidence site, and η is the

relative intensity ratio of backscattering to forward scattering. Detailed study of the PSF is crucial to improving the resolution of the lithography process.

3.3. APPLICATIONS OF HELIUM ION MICROSCOPY

Thanks to its sub-nanometer probe size, a focused helium beam has been used to modify the physical and chemical properties of materials. A few examples include modification of graphene[12–14], patterning of gold[15, 16], ion-induced growth of nanostructures[11, 19] and ion beam lithography of resists[17, 18]. Some of these potential uses of the microscope are discussed briefly in the following subsections.

3.3.1. SAMPLE IMAGING

The incoming ions interact with atoms in the sample. These interactions form the basis of signals that contain information about the sample's outermost layers. The helium ion microscope provides an image of a sample surface by scanning the focused ion beam in a raster fashion over the surface. The imaging employs the detection of the secondary electrons emitted into the vacuum. As mentioned above, the energies of these SEs are of the order of a few eV[6]. An Everhard-Thornley (ET) detector is used to collect the SEs emitted from the surface. A positively biased Faraday cage is typically positioned in front of the ET detector to attract the negatively charged SEs. In the detector, the electrons are accelerated by a voltage applied on the scintillator. These accelerated electrons are then converted to photons on a phosphor screen surface. These photons then travel through a photomultiplier tube for amplification. The photomultiplier produces an output signal that is related to the total number of electrons collected from the sample surface[30]. The schematic of such a process is shown in Figure 3.6.

The intensity in the secondary electron images is proportional to the number of detected secondary electrons emitted from the surface of the sample. The main advantage of helium ion microscopy is that insulating samples can be imaged without any metal coating, which ensures accurate imaging of critical surface details.

3.3.2. HELIUM ION BEAM LITHOGRAPHY (HIBL)

Another use of the helium ion microscope is for lithography. Ion beam lithography, a process of producing patterns with a focused ion beam, is very similar to electron beam lithography. Ion beams generate secondary electrons more efficiently than electron beams[31]. Therefore, the required ion dose for the resist activation is smaller than the required electron dose. Sub-10 nm resolution has been demonstrated with gallium ions in poly(methylmethacrylate) (PMMA) and hydrogen silsesquioxane (HSQ) already 25 years ago[32, 33]. However, because of the higher mass of gallium ions¹, the penetration range is shallower. This limits the resist thickness to be about 50 nm in the case of 30 keV gallium ions[31]. Because the mass of helium ions is approximately 7000 times larger

¹Mass of a gallium ion is 126,000 times higher than that of an electron[6].

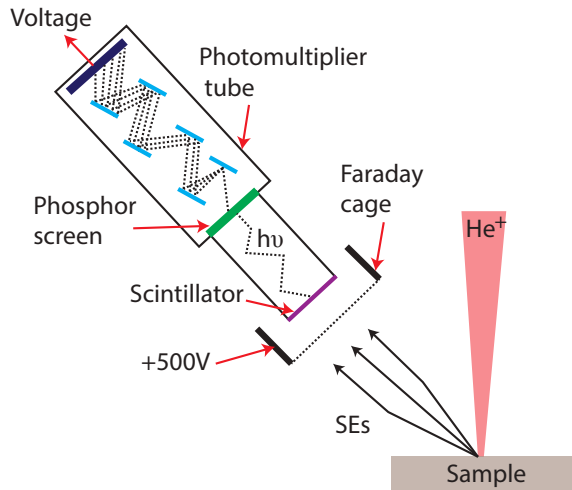


Figure 3.6: Working of an Everhart-Thornley (ET) detector. The incoming beam generates SEs from the sample surface. The Faraday cage is kept at a positive potential to attract the electrons. The signal from the scintillator is then amplified by a photomultiplier.

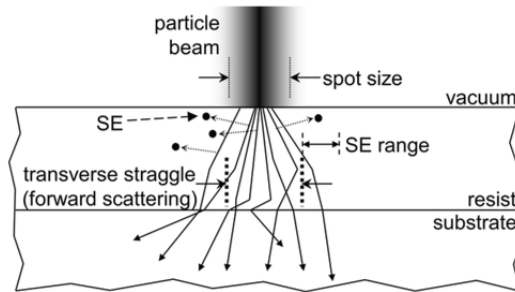


Figure 3.7: Illustration of the interaction of a focused helium beam with a resist. The range of the SEs in the resist limits the resolution. The backscattering of incident particles is ignored in this figure, which could also lead to the additional exposure of the resist. The figure is taken from Ref. [17].

than the electron mass, the lateral straggle of a focused helium ion beam is smaller than that of a focused electron beam at the same energy [10]. Since helium ions scatter less than electrons, the He^+ point spread function (PSF)² should be correspondingly narrower than electron PSFs. This is the reason why helium ion beam lithography shows reduced proximity effects compared to e-beam lithography. Although helium ion beam lithography suffers little from scattering and reduced proximity effects, the potential everyday use of this technology for nanofabrication is limited by the low brightness of the

²PSF is defined as the energy density profile deposited in point exposure.

source. However, HIBL is still in its infancy and needs further development. Sub-10 nm patterning in PMMA and hydrogen silsesquioxane (HSQ) with a helium ion beam has been demonstrated by Sidorkin *et al.*[18] and Winston *et al.*[17]. A pattern resolution below 10 nm is also reported in a fullerene-derived molecular resist[34]. In addition, neon ion lithography has also been investigated by Winston *et al.*[35]. Furthermore, it is recently reported that there are similarities in the resist activation response to a helium beam and extreme-ultraviolet (EUV) photons[36, 37]. Hence, helium ion lithography can be used as a pre-screening method for optimization of chemically amplified resists for EUV lithography.

3.3.3. HELIUM ION BEAM INDUCED DEPOSITION

The primary advantage of using a helium ion beam is that the interacting width of the helium ion beam is intrinsically smaller than that of a scanning electron beam or a gallium FIB at the same accelerating voltage. Hence, the important characteristic of helium ion beam induced deposition (HeBID) is the high spatial precision at which materials can be grown, without any noticeable overspray or proximity effects.³ This is the reason why HIM has the potential to go beyond what is possible with Ga⁺ focused ion beam in nanoscale device fabrication. The use of a focused helium beam with an integrated gas injection system for nanofabrication was explored for controlled deposition of tungsten[39] and platinum[19] nanostructures.

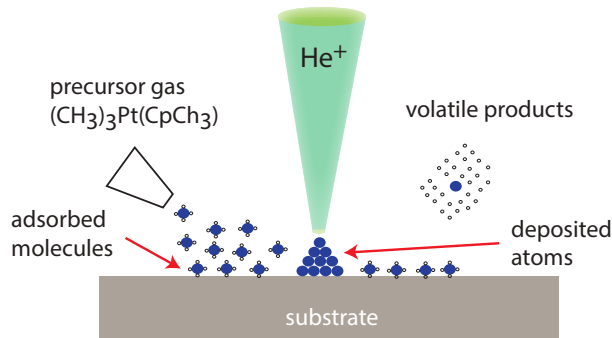


Figure 3.8: A schematic representation of the ion beam induced deposition process (IBID). The picture is adapted from the Ref. [24].

The IBID+EBID process is based on the dissociation of a molecular precursor that is adsorbed on a sample surface and which is constantly replenished by a gas-supply system. The gas-supply system consists of a precursor reservoir that is often heated. A fine nozzle is coupled to the gas-supply system. Before the deposition, the nozzle is inserted to

³The proximity effects for a He^+ beam are lower than that of a gallium beam or an electron beam[38].

a distance of $\sim 180 - 250 \mu\text{m}$ from the substrate surface, see Figure 3.9a. The deposition of a material is the result of the interaction between the incident beam, the substrate, and the chemical precursor. The adsorbed precursor molecules are dissociated by the primary beam and the energetic particles produced by this beam, such as backscattered and secondary electrons, or displaced atoms. The total deposition rate $R(r)$ can be expressed by[40]:

$$R(r) = Vn(r)\sigma f(r) \quad (3.8)$$

where $n(r)$ is the number of adsorbed molecules, σ is the dissociation cross section, V is the volume of the deposited molecule, and $f(r)$ is the ion flux distribution. Equation 3.8 proves that the yield of the HeBID depends on the product of $n(r)$ and σ . It is, however, not known whether or not the precursor molecules are dissociated only by secondary electrons. Likely, both primary and secondary particles (electrons, ions, and atoms) contribute to different aspects of He^+ beam induced deposition.

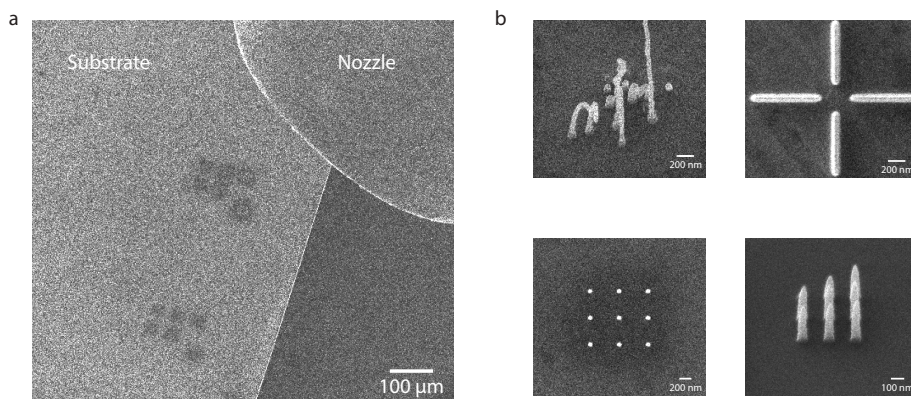


Figure 3.9: (a) Helium ion microscope (HIM) image of the tip of the nozzle and the substrate. The needle is inserted $150-180 \mu\text{m}$ away from the sample, (b) Shows a few examples of nanostructures grown by HeBID and subsequently imaged by HIM.

A schematic of the deposition process is shown in Figure 3.8. Precursor molecules are supplied by a gas-injection system and physisorbed on the sample surface. Only if proximity effects are negligible the adsorbed precursor molecules are dissociated within the focus of He^+ beam, followed by desorption of volatile products. A few examples of He^+ beam induced deposition of platinum nanostructures are shown in Figure 3.9b.

HEBID OF AFM PROBES

An atomic force microscope (AFM) is a high-resolution microscope by which one can measure the morphology of a three-dimensional surface by tracing a fine probe with a sharp tip apex. In order to enable the measurement of deep trenches and concave-convex surfaces, the AFM probe needs to have a high aspect ratio shape and a modified head[41]. Depending on the application, a customized tip-head is usually needed. Various attempts have been made to grow and to shrink the size of these probes by electron

beam induced deposition (EBID) followed by plasma etching[42]. However, EBID with a stationary electron beam usually gives relatively thick needles due to the scattering of primary and secondary electrons (SEs) in the growing material[19].

Another possibility is to use helium beam induced deposition (HeBID) to grow these probes. The main advantage of a He^+ beam over the electron beam is that the interaction width of the helium ions is smaller than that for an electron beam, or a gallium focused ion beam (Ga-FIB), at the same acceleration voltage[13]. Using a stationary He^+ beam, Chen *et al.*[19] fabricated 36-nm wide PtC nanopillars. These high aspect ratio nanopillars can be grown on existing AFM probes. Moreover, the tips narrower than 36 nm are needed. The growth of narrow AFM tips with the helium beam will be discussed in Chapter 7.

3.3.4. HELIUM ION MILLING

The helium ion beam can be used to remove material by direct sputtering of surface atoms. The HIM can generate a smaller beam as compared to a Ga^+ FIB and therefore is capable of higher resolution patterning. However, the sputter rate in case of HeFIB is much lower compared to Ga-FIB, as helium ions have a much lower mass. The low mass of helium ions and lower milling rates make this technique suitable for the controlled milling of sub-10 nm features. Helium ion milling (HIM) has been applied successfully to the structuring of a variety of systems such as monolayers of graphene for nanoelectronic applications[12, 14], and thin SiN[43], magnetic spin valves[44], Josephson junctions[45]. We utilize the milling capabilities of HIM to modify graphene encapsulated in boron nitride layers. This will be discussed in Chapters 5 and 6.

FABRICATION OF NANOPORES

Another use of this technology is for the fabrication of nanopores in thin membranes. These nanopores can be used for water filtration[46], separation of gasses[47], and biomolecular detection[43, 48]. A precise control over the lateral dimension of the nanopore is essential to realize all these applications. Solid-state nanopores have been extensively investigated for biomolecule detection in the past decade. Applications targeting the detection of biomolecules employ a silicon chip supporting a silicon nitride (SiN) or graphene membrane. The thickness of the SiN membrane varies between 20 and 50 nm. For the detection, a single nanopore is drilled in the silicon chip with the membrane. This chip is then positioned between two reservoirs of an electrolyte solution in a flow cell[43, 49]. Under the application of a voltage across the SiN membrane, a strong electric field is created at the pore, leading to a steady ionic current through it. As the ions or DNA molecules translocate through the pore, the current changes[43, 48]. This technique and instruments can potentially be used to read the individual base pairs of the DNA[48]. Various methods have been adopted for making nanopores in these membranes, such as transmission electron microscope (TEM), ion beam etching, and dielectric breakdown[50]. It is, however, difficult to control the size and dimensions of the pores using ion beam etching and dielectric breakdown. TEM, on the other hand, gives a very precise lateral control, but the throughput is extremely low, which limits its usage

in high volume manufacturing. A focused helium beam offers more flexibility concerning the speed and lateral control of the dimensions. This technique has been used to make nanopores in SiN down to 3.8 nm in SiN membranes and 2.9 nm in graphene[51].

Figure 3.10b shows ~ 6 nm nanopores in a thin SiN membrane made with HIM and subsequently imaged with TEM. Gold lines are created on the membrane to avoid charging and to be used for focusing the beam. Once satisfactorily focused, the beam was first blanked and then moved to the center of the membrane. The pattern generator exposed $5 \times 5 \text{ nm}^2$ areas with a dose of 7×10^{18} ions cm^{-2} . The membrane thickness used in this work was ~ 20 nm.

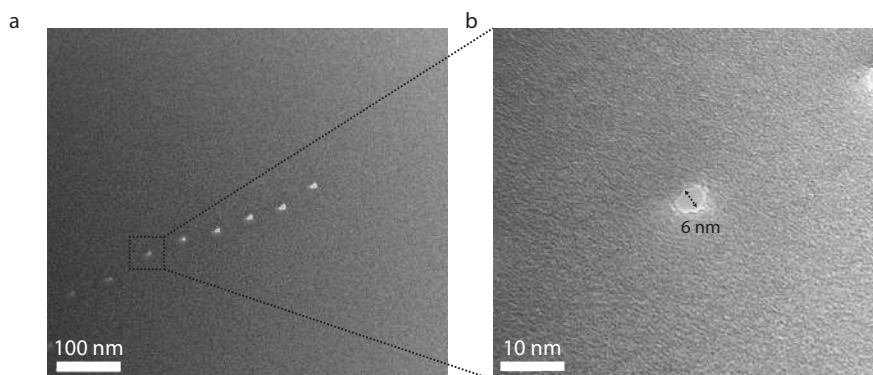


Figure 3.10: (a) Transmission electron microscope (TEM) image of the SiN membrane with pores milled by the helium beam, (b) A blow-up image of one of the pores.

MILLING OF GOLD

Focused helium ion beam is also a versatile method for obtaining a variety of plasmonic devices by carving nanostructures in gold thin films. A gold or silver metal nanostructure is typically used to study the optical phenomena related to the electromagnetic response of metal nanostructures[15, 16, 52]. The free electrons in the metal can be excited by the electric component of light, resulting in collective oscillations of the plasma of the free electrons. To study this effect, a nanoantenna is made of two closely spaced and optically coupled metal nanoparticles, such as gold. They can be used to focus optical fields to the subdiffraction-limited gap region between the individual metal nanostructures, as a consequence the optical field there can be very intense[53, 54]. Helium ion beam milling has successfully been used by Wang *et al.*[15] for milling partial nanogaps in gold, where part of the material in the gap was removed from the sides to obtain a thin conducting bridge of controlled dimensions. The authors were able to control the milling at the 1 nm level. Melli *et al.*[16] have reported that the quality factor of the Ga-FIB resonators in gold is 60% lower compared to helium ion milled plasmonic resonators.

We have fabricated metal bowtie antennas with precisely controlled shapes using a combination of e-beam lithography and helium ion beam milling. This is a novel device,

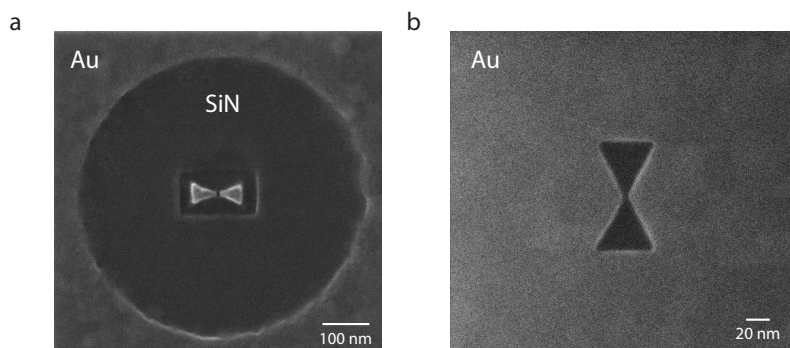


Figure 3.11: (a) HIM image of a plasmonic bowtie antenna carved in a 30 nm gold film on a suspended 50 nm SiN membrane, (b) HIM image of an inverted bowtie antenna showing the resolution of the microscope. The gap in the middle is between 2 and 5 nm.

which combines a plasmonic bowtie nanoantenna with a sub-10 nm diameter solid-state nanopore drilled at the center of the bowtie antenna. The plasmonic nanoantenna acts as a nano-detector, where the variations in the local optical intensity modulate the plasmonic heating, which can be measured electrically through changes in the ionic conductance of the nanopore[52, 53]. The optical heating is a consequence of the strong interaction of light and metal nanoparticles through excitation of plasmons. Figure 3.11 shows the patterning of bowtie antennas using a focused helium beam. Here we use a dose of 3×10^{18} ions cm^{-2} to fabricate a bowtie antenna in a ~ 30 nm thin film of gold. Because the forward sputtering during the Au milling leads to the thinning of underlying membrane, the thickness of the underlying SiN membrane is kept at ~ 50 nm. In the final step, a ~ 6 nm pore is drilled in the opening of the bowtie antenna.

MILLING OF GRAPHENE

A focused helium ion beam can also be used to perform direct milling of graphene. The first experiments to structure graphene with a helium ion beam were performed by Lemme *et al.*[55] and Bell *et al.*[56] in 2009. The advantages of the helium beam compared to the focused gallium ion beam include its small probe size and the ability to mill sensitive materials at low sputter rates[56]. For graphene on a 285 nm SiO_2 /silicon substrate, SRIM/TRIM simulations show that 99.6% of the ions pass directly through the graphene without displacing a C atom. Instead, the majority of the ion energy is deposited deep in the silicon substrate. At high ion doses, the implanted helium ions coalesce to form a bubble. Although trapping of helium ions in the sample is expected, the doses required to mill graphene are below the threshold required to form bubbles. The direct milling capabilities of helium ions were utilized by Lemme *et al.*[55] and Kalhor *et al.*[12] for the milling of sub-10 nm features in graphene, see Figure 3.12. However, their experiments revealed that the sub-10 nm devices milled in graphene had lost their electrical properties. Despite the narrow interaction volume, the rest of the graphene was severely damaged because of beam-related proximity effects. Other possible detrimental

mechanisms include beam induced carbon deposition and sputtering of graphene via backscattered ions. Dangling C bonds in graphene react readily with hydrocarbons from the environment, which further damages the crystalline structure of graphene. These various defect processes are speculated to damage graphene lattice and to reduce the conductivity. However, the individual role of each process is difficult to quantify.

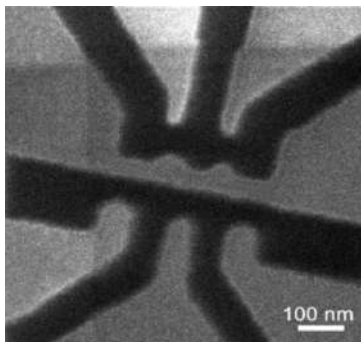


Figure 3.12: Helium ion micrograph of a sub-10 nm graphene double-quantum dot fabricated by helium ion beam milling. The milled graphene areas are shown in black. The figure is taken from Ref.[12].

In order to make graphene devices with a focused helium beam, one needs to understand the role of the detrimental side processes and to be able to mitigate them. One possible way is by protecting graphene against the environment, which can be achieved by encapsulation. The benefit of this encapsulation will be studied in Chapter 5. Furthermore, it will be interesting to investigate the effect of encapsulation on the charge transport properties of graphene, which will be studied in Chapter 6. So far, the lateral damage caused by the helium ion beam to graphene has not been studied in sufficient detail. This will also be studied in detail in Chapter 6.

REFERENCES

- [1] E. Abbe, *Die optischen hilfsmittel der mikroskopie*, Reports on scientific instruments at the London international exhibition , 383 (1878).
- [2] L. de Broglie, *Recherches sur la théorie des quanta*, Ann. Phys. **10**, 22 (1925).
- [3] M. Knoll and E. Ruska, *Das elektronenmikroskop*, Z. Physik **78**, 318 (1932).
- [4] D. C. Joy, *Helium ion microscopy: Principles and applications*, Springer (2013).
- [5] G. Hlawacek, V. Veligura, R. van Gastel, and B. Poelsema, *Helium ion microscopy*, Journal of Vacuum Science & Technology B **32**, 020801 (2014).
- [6] D. Cohen-Tanugi and N. Yao, *Superior imaging resolution in scanning helium-ion microscopy: A look at beam-sample interactions*, Journal of Applied Physics **104**, 063504 (2008).

- [7] D. C. Joy and C. S. Joy, *Low voltage scanning electron microscopy*, Micron **27**, 247 (1996).
- [8] J. Orloff and L. Swanson, *Study of a field-ionization source for microprobe applications*, Journal of Vacuum Science & Technology B **12**, 1209 (1975).
- [9] R. Seliger, J. W. Ward, V. Wang, and R. L. Kubena, *A high-intensity scanning ion probe with submicrometer spot size*, Applied Physics Letters **34**, 310 (1979).
- [10] R. Hill, J. Notte, and B. Ward, *The ALIS He ion source and its application to high resolution microscopy*, Proceedings of the Seventh International Conference on Charged Particle Optics **1**, 135 (2008).
- [11] P. F. A. Alkemade, E. M. Koster, E. van Veldhoven, and D. J. Maas, *Imaging and nanofabrication with the helium ion microscope of the van Leeuwenhoek laboratory in Delft*, Scanning **34**, 90 (2012).
- [12] N. Kalhor, S. A. Boden, and H. Mizuta, *Sub-10 nm patterning by focused He-ion beam milling for fabrication of downscaled graphene nano devices*, Microelectronic Engineering **114**, 70 (2014).
- [13] D. C. Bell, M. C. Lemme, L. A. Stern, and C. M. Marcus, *Precision material modification and patterning with he ions*, Journal of Vacuum Science & Technology B **27**, 2755 (2009).
- [14] A. N. Abbas, G. Liu, B. Liu, L. Zhang, H. Liu, D. Ohlberg, W. Wu, and C. Zhou, *Patterning, characterization, and chemical sensing applications of graphene nanoribbon arrays down to 5 nm using helium ion beam lithography*, ACS Nano **8**, 1538 (2014).
- [15] Y. Wang, M. Abb, S. A. Boden, J. Aizpurua, C. H. de Groot, and O. L. Muskens, *Ultra-fast nonlinear control of progressively loaded, single plasmonic nanoantennas fabricated using helium ion milling*, Nano Letters **13**, 5647 (2013).
- [16] M. Melli, A. Polyakov, D. G. D. C. Huynh, L. Scipioni, W. Bao, D. F. Ogletree, P. J. Schuck, S. Cabrini, and A. Weber-Bargioni, *Reaching the theoretical resonance quality factor limit in coaxial plasmonic nanoresonators fabricated by helium ion lithography*, Nano Letters **13**, 2687 (2013).
- [17] D. Winston, B. M. Cord, B. Ming, D. C. Bell, W. F. DiNatale, L. A. Stern, A. E. Vldar, M. T. Postek, M. K. Mondol, J. K. W. Yang, and K. K. Berggren, *Scanning-helium-ion-beam lithography with hydrogen silsesquioxane resist*, Journal of Vacuum Science & Technology B **27**, 2702 (2009).
- [18] V. Sidorkin, E. van Veldhoven, E. van der Drift, P. Alkemade, H. Salemink, and D. Maas, *Sub-10-nm nanolithography with a scanning helium beam*, Journal of Vacuum Science & Technology B **27**, L18 (2009).

- [19] P. Chen, E. van Veldhoven, C. A. Sanford, H. W. M. Salemink, D. J. Maas, D. A. Smith, P. D. Rack, and P. F. A. Alkemade, *Nanopillar growth by focused helium ion-beam-induced deposition*, *Nanotechnology* **21**, 455302 (2010).
- [20] E. W. Müller and T. T. Tsong, *Field ion microscopy principles and applications*, Elsevier New York (1969).
- [21] J. H. Orloff and L. W. Swanson, *Angular intensity of a gasphase field ionization source*, *Journal of Applied Physics* **50**, 6026 (1979).
- [22] K. Horiuchi, T. Itakura, and H. Ishikawa, *Emission characteristics and stability of a helium field ion source*, *Journal of Vacuum Science & Technology B* **6**, 937 (1988).
- [23] G. Hlawacek and A. Golzhauser, *Helium ion microscopy*, Springer International Publishing (2017).
- [24] P. Chen, *Three-dimensional nanostructures fabricated by ion-beam-induced deposition*, PhD Thesis, Technische Universiteit Delft (2010).
- [25] D. D. D, A. R. Couture, D. Joly, X. Tastet, V. Aimez, and R. Gauvin, *Casino v2.42: a fast and easy-to-use modeling tool for scanning electron microscopy and microanalysis users*, *Scanning* **29**, 92 (2007).
- [26] J. F. Ziegler, J. P. Biersack, and M. D. Ziegler, *SRIM-the stopping and range of ions in matter*, Chester, MD:SRIM co. (2008).
- [27] J. Notte, B. Ward, N. Economou, R. Hill, R. Percival, L. Farkas, and S. McVey, *An introduction to the helium ion microscope*, *AIP Conference Proceedings* **931**, 489 (2007).
- [28] V. Veligura, G. Hlawacek, R. P. Berkelaar, R. van Gastel, H. J. W. Zandvliet, and B. Poelsema, *Digging gold: keV He⁺ ion interaction with Au*, *Beilstein Journal of Nanotechnology* **4**, 453 (2013).
- [29] R. Ramachandra, B. Griffin, and D. Joy, *A model of secondary electron imaging in the helium ion scanning microscope*, *Ultramicroscopy* **109**, 748 (2009).
- [30] H. Guo, J. Gao, N. Ishida, M. Xu, and D. Fujita, *Characterization of two-dimensional hexagonal boron nitride using scanning electron and scanning helium ion microscopy*, *Applied Physics Letters* **104**, 031607 (2014).
- [31] A. Joshi-Imre and S. Bauerdick, *Direct-write ion beam lithography*, *Journal of Nanotechnology* **170415** (2014).
- [32] R. L. Kubena, J. W. Ward, F. P. Stratton, R. J. Joyce, and G. M. Atkinson, *A low magnification focused ion beam system with 8 nm spot size*, *Journal of Vacuum Science & Technology B* **9**, 3079 (1991).
- [33] L. Bruchhaus, S. Bauerdick, L. Peto, U. Barth, A. Rudzinski, and J. Mussmann, *High resolution and high density ion beam lithography employing HSQ resist*, *Microelectronic Engineering* **97**, 48 (2012).

- [34] X. Shi, P. Prewett, E. Huq, D. M. Bagnall, A. P. G. Robinson, and S. A. Boden, *Helium ion beam lithography on fullerene molecular resists for sub-10 nm patterning*, *Microelectronic Engineering* **155**, 74 (2015).
- [35] D. Winston, V. R. Manfrinato, S. M. Nicaise, L. L. Cheong, H. Duan, D. Ferranti, J. Marshman, S. McVey, L. Stern, J. N. J., and K. K. Berggren, *Neon ion beam lithography (NIBL)*, *Nano Letters* **11**, 4343 (2011).
- [36] N. Kalhor, W. Mulckhuysen, P. Alkemade, and D. Maas, *Impact of pixel-dose optimization on pattern fidelity for helium ion beam lithography on EUV resist*, *Proc. of SPIE* **9425** (2015).
- [37] D. Maas, E. van Veldhoven, A. van Langen-Suurling, P. F. Alkemade, S. Wuister, R. Hoefnagels, C. Verspaget, J. Meessen, and T. Fliervoet, *Evaluation of EUV resist performance below 20-nm cd using helium ion lithography*, *Proceedings of SPIE* **9048** (2014).
- [38] P. F. A. Alkemade and H. Miro, *Focused helium-ion-beam-induced deposition*, *Applied Physics A* **117**, 1727 (2014).
- [39] K. Kohama, T. Iijima, M. Hayashida, and S. Ogawa, *Tungsten-based pillar deposition by helium ion microscope and beam-induced substrate damage*, *Journal of Vacuum Science & Technology B* **31**, 031802 (2013).
- [40] I. Utke, P. Hoffmann, and J. Melngailis, *Gas-assisted focused electron beam and ion beam processing and fabrication*, *Journal of Vacuum Science & Technology B* **26**, 1197 (2008).
- [41] J. Foucher, P. Filippov, C. Penzkofer, B. Irmer, and S. W. Schmidt, *Manufacturing and advanced characterization of sub-25 nm diameter CD-AFM probes with sub-10 nm tip edges radius*, *Proceedings of SPIE* **8681**, 86811I (2013).
- [42] M. Wendel, H. Lorenz, and J. P. Kotthaus, *Sharpened electron beam deposited tips for high resolution atomic force microscope lithography and imaging*, *Applied Physics Letters* **67**, 25 (1995).
- [43] J. Yang, D. C. Ferranti, L. A. Stern, C. A. Sanford, J. Huang, Z. Ren, L. C. Qin, and A. R. Hall, *Rapid and precise scanning helium ion microscope milling of solid-state nanopores for biomolecule detection*, *Nanotechnology* **22**, 285310 (2011).
- [44] Y. Wang, S. A. Boden, D. M. Bagnall, H. N. Rutt, and C. H. de Groot, *Helium ion beam milling to create a nano-structured domain wall magnetoresistance spin valve*, *Nanotechnology* **23**, 395302 (2012).
- [45] S. A. Cybart, E. Y. Cho, T. J. Wong, B. H. Wehlin, M. K. Ma, C. Huynh, and R. C. Dynes, *Nano Josephson superconducting tunnel junctions in $\text{YBa}_2\text{Cu}_3\text{O}_{7-\delta}$ directly patterned with a focused helium ion beam*, *Nature Nanotechnology* **10**, 598 (2015).
- [46] M. Heiranian, A. B. Farimani, and N. R. Aluru, *Water desalination with a single-layer mos2 nanopore*, *Nature Communications* **6**, 8616 (2015).

- [47] K. Celebi, J. Buchheim, R. M. Wyss, A. Droudian, P. Gasser, I. Shorubalko, J.-I. Kye, C. Lee, and H. G. Park, *Ultimate permeation across atomically thin porous graphene*, *Science* **344**, 289 (2014).
- [48] S. J. Heerema and C. Dekker, *Graphene nanodevices for DNA sequencing*, *Nature Nanotechnology* **11**, 127–136 (2016).
- [49] F. Sawafta, A. T. Carlsen, and A. R. Hall, *Membrane thickness dependence of nanopore formation with a focused helium ion beam*, *Sensors* **14**, 8150 (2014).
- [50] H. Kwok, K. Briggs, and V. Tabard-Cossa, *Nanopore fabrication by controlled dielectric breakdown*, *PLoS ONE* **9**, e92880 (2014).
- [51] D. Emmrich, A. Beyer, A. Nadzeyka, S. Bauerdick, J. C. Meyer, J. Kotakoski, and A. Götzhäuser, *Nanopore fabrication and characterization by helium ion microscopy*, *Applied Physics Letters* **108**, 163103 (2016).
- [52] M. P. Jonsson and C. Dekker, *Plasmonic nanopore for electrical profiling of optical intensity landscapes*, *Nano Letters* **13**, 1029 (2013).
- [53] F. Nicoli, D. Verschueren, M. Klein, C. Dekker, and M. P. Jonsson, *DNA translocations through solid-state plasmonic nanopores*, *Nano Letters* **14**, 16917 (2014).
- [54] A. Kinkhabwala, Z. Yu, S. Fan, Y. Avlasevich, K. Müllen, and W. E. Moerner, *Large single-molecule fluorescence enhancements produced by a bowtie nanoantenna*, *Nature Photonics* **3**, 654 (2009).
- [55] M. C. Lemme, D. C. Bell, J. R. Williams, L. A. Stern, B. W. H. Baugher, P. Jarillo-Herrero, and C. M. Marcus, *Etching of graphene devices with a helium ion beam*, *ACS Nano* **3**, 2674 (2009).
- [56] D. C. Bell, M. C. Lemme, L. A. Stern, J. R. Williams, and C. M. Marcus, *Precision cutting and patterning of graphene with helium ions*, *Nanotechnology* **20**, 455301 (2009).

4

METHODS AND TECHNIQUES

The fabrication of graphene devices studied in this thesis is complicated and requires several parameters to be optimized individually. The process involves various techniques which are required to fabricate and characterize the devices. In this chapter, I describe the general approach used to fabricate graphene-based devices. Some experiments, however, were conducted using slightly different conditions; they are described separately in the corresponding chapters. The main focus in this chapter will be on the quantitative description of the techniques rather than on the details of the processes. I have included details of process flow separately in Appendix A.

4.1. FABRICATION OF GRAPHENE DEVICES

The fabrication of hexagonal boron nitride (h-BN) encapsulated graphene devices is a five-step process: (i) graphene and h-BN exfoliation, (ii) stacking of graphene and h-BN flakes, (iii) e-beam lithography, (iv) reactive ion etching, and (v) metal evaporation or sputtering. These processes are discussed one by one in the following subsections.

4.1.1. SAMPLE CLEANING

The exceptional transport properties of graphene are badly influenced by resist residues and adsorption of contaminations[1]. These residues are introduced on the surface of graphene during sample preparation, when for example, the use of resist (PMMA) for lithography is used. Therefore, to preserve the pristine nature of graphene, the surface of the sample needs to be cleaned. Before the transfer of graphene and h-BN flakes, the Si/SiO₂ substrates are cleaned with acetone and isopropyl alcohol (IPA), followed by a nitric acid (HNO₃) treatment. The cleaned substrates are then kept in a desiccator until use. Before the exfoliation, Si/SiO₂ substrates are exposed to a short oxygen plasma treatment. This step is important to remove any organic impurities adsorbed on the surface.

4.1.2. EXFOLIATION

Exfoliation is a process of splitting layered materials into separate thin sheets with the use of mechanical, electrostatic, or electromagnetic forces. In this thesis, we focus on the exfoliation by micromechanical cleavage of highly oriented pyrolytic graphite (HOPG) and h-BN crystals. In this process, the layered material (graphene or h-BN) is peeled off from a bulk crystal using an adhesive tape (SWT 20+ Nitto Dekko Corp.). After peeling, many flakes of the material remain glued onto the tape. Extensive rubbing of the tape with flakes against flat surfaces give rise to single and multiple atomic layers of layered material on the substrate. This was firstly demonstrated by Novoselov *et al.*[2], achieving single layer graphene. Recently flakes with size $>500 \mu\text{m}$ have been produced by this method[3].

4.1.3. GRAPHENE IDENTIFICATION

The micromechanical cleavage of HOPG (NGS naturgraphit GmbH) to a Si/SiO₂ substrate is carried out without any control of the final locations of the flakes on the substrate. The density of single-layer graphene flakes is extremely low; only a couple of usable¹ single-layer flakes are usually obtained on the substrate. The efficient identification and selection of the flakes rely on the optical microscopy. Graphene can be easily detected optically on silicon dioxide with a thickness of 90 nm and 285 nm, thanks to the light interference in the SiO₂. the modulation by the presence of graphene layers[4].

¹Only flakes with size $>10 \mu\text{m}$ are selected for making devices.

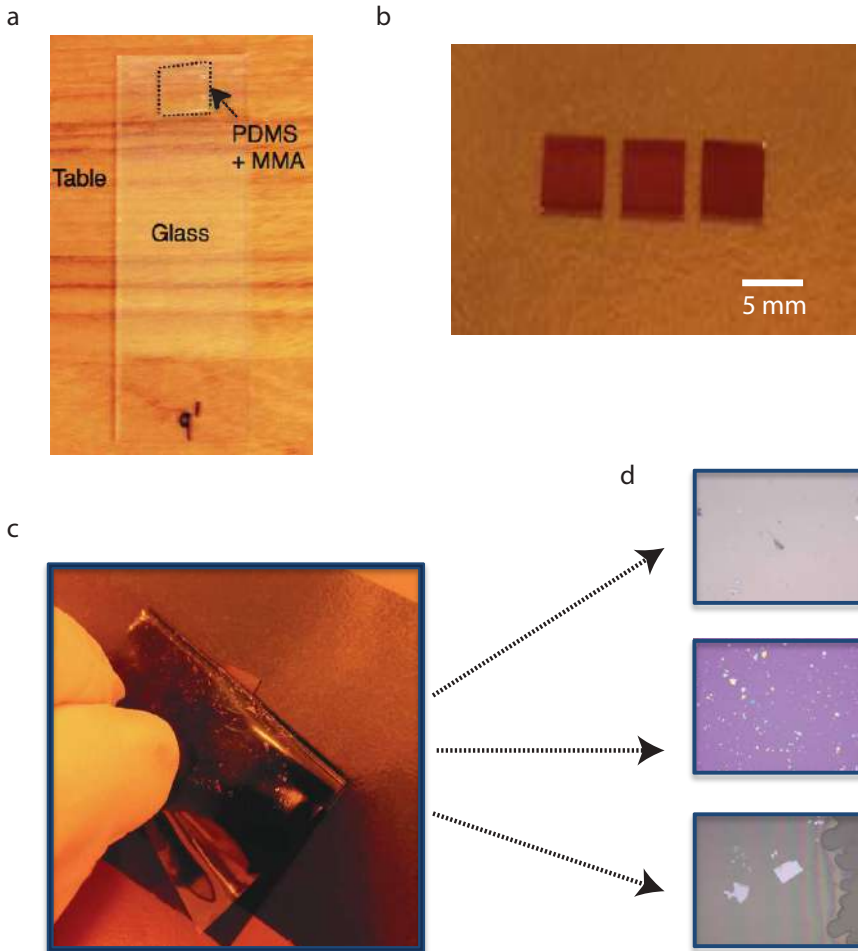


Figure 4.1: (a) A $2 \times 2 \text{ cm}^2$ PDMS film covered with a resist on the glass slide, (b) $6 \times 6 \text{ mm}^2$ diced silicon chips with $\sim 285 \text{ nm}$ oxide are used for the exfoliation and the final device fabrication, (c) Shows the exfoliation process, where the blue Nitto tape is pressed and subsequently peeled off the silicon chip, (d) Shows the optical microscope images of the exfoliated graphene on silicon (upper), h-BN on silicon (middle), and h-BN on glass (lower).

Figure 4.1d (upper) shows the clear contrast between the silicon dioxide and the single-layer graphene flakes.

4.1.4. BORON NITRIDE IDENTIFICATION

Hexagonal boron nitride (h-BN) is the inorganic analogue of graphene having a comparable layered structure. A single layer of h-BN is very similar to graphene having a hexagonal backbone where the carbon atoms are replaced atomically by boron and ni-

trogen atoms. h-BN and graphite have the identical interlayer distance ≈ 0.3 nm. However, unlike graphene, h-BN is an insulator because of the difference in electronegativity between boron and the nitrogen atoms[5]. In h-BN, the π electrons tend to localize around the nitrogen atomic centers, thus forming an insulating material. Hexagonal boron nitride (h-BN) has been used extensively as a substrate in electronic studies of graphene in the recent years[6, 7]. The h-BN shields the graphene from charged impurities and provides a smooth substrate, opening up the possibility to obtain clean devices with high mobilities.

Since h-BN shares the mechanical strength and thermal conductivity properties with graphite, the h-BN is exfoliated in the same manner as graphene from a h-BN crystal. In our study, the h-BN flakes are micromechanically exfoliated onto Si/SiO₂ wafers with a 285 nm oxide. The h-BN crystals employed have been prepared in the group of K. Watanabe[8]. We employ a combination of optical microscopy and atomic force microscopy to identify the uniformity and the thickness of the exfoliated flakes. For device fabrication, we keep the thickness of the bottom BN to be >10 nm, so the roughness of the SiO₂ substrate does not affect graphene. The thickness is optically checked, thanks to the light interference effects. Flakes with different thickness show different colors under an optical microscope; for instance, 10-20 nm thick flakes are dark blue, and 20-50 nm thick flakes are light blue. These reported thicknesses are established using AFM.

4

4.2. SAMPLE PREPARATION

The boron nitride-graphene-boron nitride stack is prepared by temperature aided van der Waals pick-up technique. The setup of this technique is shown in Figure 4.2. A similar setup without a temperature controller is reported by Ref.[9].

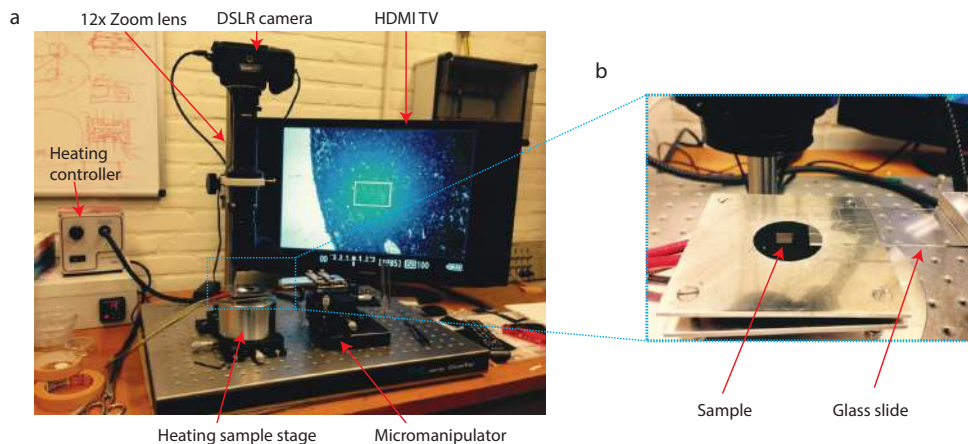


Figure 4.2: (a) Picture of the transfer setup, (b) A close image of the sample stage. A silicon sample is glued to the stage using double-sided carbon tape. The temperature of the stage is monitored by a thermocouple. There is enough space between the lens of the camera and the sample holder so that the glass slide can be moved freely.

4.2.1. VAN DER WAALS PICK-UP TECHNIQUE

Graphene and h-BN flakes are prepared by micro-mechanical exfoliation of HOPG and h-BN crystals. Graphene and h-BN are exfoliated onto 90 nm and 285 nm oxidized silicon samples, respectively. Single-layer graphene flakes are selected optically and their thicknesses are verified by Raman spectroscopy. Exfoliated graphene flakes that show a Raman defect (D) peak are discarded. Next, h-BN is exfoliated onto a glass slide covered by a 1-cm² viscoelastic PDMS and a spun-coated MMA/MAA layer. This glass slide with the h-BN flakes is then mounted on the micro-manipulator of the optical microscope. Subsequently, one h-BN flake on the glass is precisely aligned above the target graphene flake and the two flakes are then brought into contact. After a contact time of about 10 seconds, the glass slide is released smoothly such that the graphene flake sticks to the h-BN flake on the glass. During the pickup, the target substrate is heated to 90 °C to facilitate delamination of the graphene from the SiO₂. Finally, the graphene/h-BN stack is transferred from the glass to another h-BN flake, exfoliated onto a 285 nm thermal oxide at 70 °C. Depending on the substrate temperature, either pick-up or transfer can be realized. Figure 4.3 shows the transfer steps. The BN-graphene-BN stack is patterned using standard e-beam lithography in which the intended graphene geometry is defined via a PMMA/hydrogen-silsesquioxane (HSQ) mask. The final device is shaped via another e-beam lithography and reactive ion etching which are discussed in the following subsections.

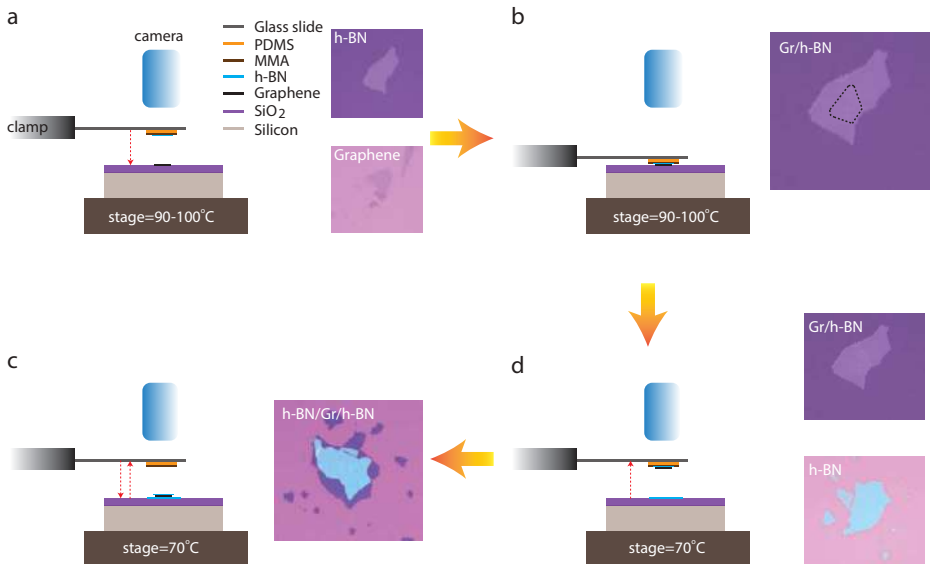


Figure 4.3: A schematic representation of the van der Waals pick-up process. (a) A glass slide with h-BN flake is mounted under the microscope and graphene sample is glued on the sample stage with heater, (b) The graphene flake is picked up by the h-BN flake on the glass slide, (c) A second sample with h-BN flakes is glued to the sample stage, (d) The h-BN/Graphene flake is transferred onto the new h-BN flake on the substrate. This way the graphene is sandwiched between two h-BN flakes.

4.3. CHARACTERIZATION TECHNIQUES

The atomic force microscopy (AFM) and Raman spectroscopy are used to characterize the BN-graphene-BN stacks. While we use the atomic force microscopy primarily to determine the thickness and uniformity of the stack, Raman spectroscopy is used to determine the number of graphene layers. Raman spectroscopy is also used to characterize the defects in single layer graphene.

4.3.1. ATOMIC FORCE MICROSCOPY

Atomic force microscopy (AFM) is used to determine the thickness, uniformity, and cleanliness of the graphene and the h-BN flakes. We use Bruker FastScan AFM. Figure 4.4 shows the AFM image of the BN-graphene-BN stack. The van der Waals pick-up method usually leaves a few bubbles at the graphene-BN interface. We use the AFM to locate a clean area in the stack. Once the exact dimensions of the clean areas in graphene flake is known, e-beam lithography is used to shape the device. Figure 4.4a shows the 2D AFM image of the typical stack and 4.4b shows the final device made after shaping the stack.

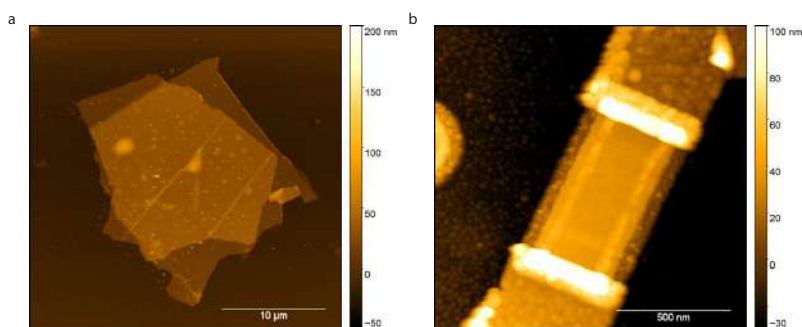


Figure 4.4: (a) Shows the AFM image of the final BN-graphene-BN stack. Tens of small bubbles can be clearly seen. These bubbles are due to the trapping of air and hydrocarbons at the interface during the transfer process. Clean sections without bubbles are used to make devices, (b) An AFM image showing the encapsulated graphene device.

4.3.2. RAMAN SPECTROSCOPY

Raman spectroscopy is a powerful technique for identifying the number of layers, detecting local doping levels, probing the nature of defects, and studying electron-phonon coupling in graphene[10–14]. We perform Raman spectroscopy measurements in air at room temperature with a Renishaw inVia Raman microscope. This spectrometer is equipped with a 514.3 nm (2.41 eV) laser with a spot size of about 350 nm. A 100x objective is used for the spectroscopy measurements. The laser power is kept well below 1 mW to avoid sample heating.

The main features in the Raman spectrum of graphene are D, G, D', and 2D peak, which

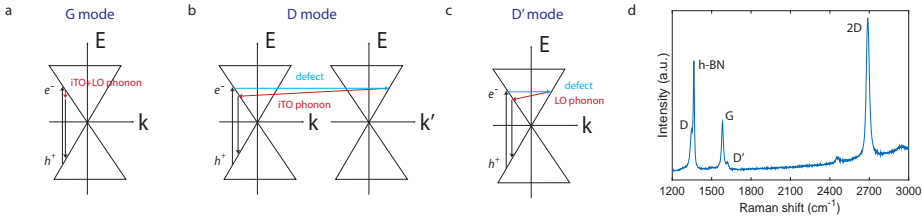


Figure 4.5: (a) Raman scattering process for the G peak, (b) Intervalley scattering process for the D peak, (c) Intravalley scattering process for the D' peak. The figure is adapted from Ref. [15], (d) Raman spectrum of the defected BN-encapsulated graphene, showing G, D, D', h-BN, and 2D peaks.

lie at 1345, 1580, 1620, and 2680 cm^{-1} , respectively. The G peak is due to the doubly degenerate E_{2g} , in-plane transverse optic (iTO) and longitudinal optic (LO), phonons at the Brillouin zone center Γ [13, 15]. The E_{2g} phonon requires in-plane stretching of the C-C bond in graphitic materials and is common to all sp^2 carbon materials. Figure 4.5a shows the three-step process of the G peak in graphene: (i) excitation of an electron/hole pair due to photon absorption, (ii) emission of a phonon due to relaxation of the electron or the hole, and (iii) emission of a photon due to electron/hole recombination.

The D peak arising from the iTO phonon mode near the K points in the Brillouin zone and is absent in the pristine graphene. The D peak is only activated by structural defects by a second-order Raman scattering process through the intervalley double resonance (DR). The absence of a D peak reveals high crystallinity of the sample. The corresponding double resonance Raman scattering is a four-step process [13, 15]: (i) laser-induced excitation of an electron/hole pair, (ii) inelastic electron-phonon scattering, (iii) elastic defect scattering, and (iv) photon emission due to electron/hole recombination. The DR condition is met when the energy is conserved in all these steps.

If there are some randomly distributed impurities or surface charges in the graphene, the G peak at 1583 cm^{-1} splits and a new peak, which is a shoulder to the G peak, appears at 1620 cm^{-1} . This shoulder to the G peak is called D' peak. The main cause of the appearance of the D' peak that the localized vibrational modes of the impurities can interact with the extended phonon modes of graphene [13, 16]. Consequently, the intravalley scattering of the longitudinal optic phonons with a small wavevector lead to the D' peak in the Raman spectrum [14, 15]. The 2D peak is the second order of the D peak and it involves two iTO phonons of opposite momentum. Therefore, it is always observed even in the absence of defects. The frequency of the 2D peak is twice that of the D peak. The shape of the 2D peak and the intensity ratio between the G peak and the 2D peak are used to identify single-layer graphene. A schematic explanation of the origin of G, D, and D' peaks is shown in Figure 4.5a.

4.4. CONTACTING GRAPHENE

The graphene is contacted using electron-beam lithography, etching, and metal evaporation or sputtering. The entire process is shown in Figure 4.6, where 4.6a shows the

fabrication process for the two-terminal devices and 4.6b the process for the superconducting quantum interference devices (SQUIDs) with a top gate electrode. These SQUID devices are used in Chapters 9 and 10.

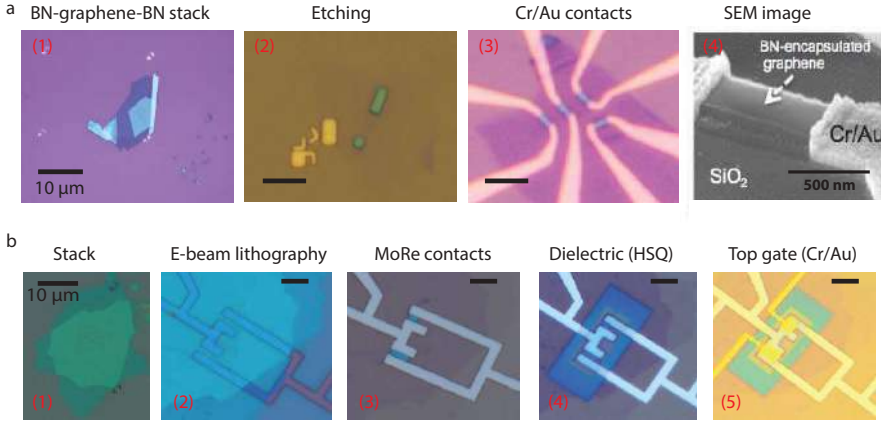


Figure 4.6: The cleanroom fabrication process for the graphene device. (a) Shows the process flow for a two-terminal device: (1) shows the BN-graphene-BN stack, (2) shows the stack after e-beam lithography and plasma etching, (3) after Cr/Au evaporation, and (4) shows the SEM image of the final device. The scalebar is $10\ \mu\text{m}$ in (2) and (3), (b) Shows the process flow for the SQUID device: (1) shows the BN-graphene-BN stack, (2) shows the stack after e-beam lithography development, (3) after MoRe sputtering and shaping of the stack, (4) after the top gate dielectric, and (5) after the Cr/Au top gate evaporation. The scalebar is $10\ \mu\text{m}$ in (1-5).

4.4.1. ELECTRON BEAM LITHOGRAPHY

Electron beam lithography (EBL) is perhaps the most important step in any nanofabrication process. E-beam lithography is a process in which a substrate with a thin layer of an electron sensitive resist is exposed to a high energy electron beam, typically 100 keV. This technique can easily produce sub-10 nm features[17]. We use the EBPG 5200 of Raith for the e-beam lithography. This instrument is capable of exposing areas as large as a 200 mm wafer with sub-8 nm features. The EBL process begins by spin-coating a substrate with a thin layer of sensitive resist. The lithographic resists can be sub-divided into two main categories: positive resists and negative resists. In the case of a positive resist, the exposed parts of the resist are removed with an appropriate developer. Positive resists are mainly used for lift-off. In case of a negative resist, only the exposed parts remain after the action of the developer. These resists are usually not very sensitive to etchants, and therefore, often used as a protective layer during etching.

In the work presented in this thesis, a bilayer polymethyl methacrylate (PMMA), a common positive resist, is used. Two types of PMMA, namely 495K A4 and 950K A3, are chosen on basis of their sensitivity to the electron beam. Since the underlying PMMA 495K A4 is more sensitive than PMMA 950K A3 above, an undercut is formed that eases the lift-off process. This bilayer resist is exposed with an electron dose of $1200\ \mu\text{C cm}^{-2}$ and the development is done in MIBK/IPA (1:3) solution for 90 seconds, see Figure 4.6b(2).

Hydrogen silsesquioxane (HSQ) is used as a negative resist, mainly to protect and shape the BN-graphene-BN stack. The HSQ is exposed to a dose between 500 and 1000 $\mu\text{C cm}^{-2}$. The exact recipe of this process is given in Appendix A.

4.4.2. REACTIVE ION ETCHING

Reactive ion etching (RIE) is a process which uses a chemically reactive plasma to remove material from a sample surface. The desired gas or mixture of gases is injected into the process chamber via a gas inlet in the top electrode. The plasma is generated under low pressure by a RF powered electromagnetic field. The sample is placed on a quartz cover plate to avoid re-deposition of electrode material. Very high plasma densities can be achieved, then the etch profiles tend to be more isotropic. For the devices in this thesis, we require a bar of encapsulated graphene, see Figure 4.6a(2). We use a PMMA/HSQ mask and shape BN-graphene-BN stack by reactive ion etching in a 20 ml min^{-1} O_2 plasma during 1 min (Leybold-Heraeus, 60 W, 50 μbar) and subsequently in a 40/4 ml min^{-1} $\text{CHF}_3 / \text{O}_2$ plasma also during 1 min (60 W, 80 μbar). After the etching, only the area covered by the mask remains. Finally, we remove the PMMA/HSQ mask by placing the sample in an acetone bath overnight, see Figure 4.6a(2),b(3).

4.4.3. ELECTRON BEAM EVAPORATION

We use electron beam evaporation (EBE) for the metallization step. After the e-beam lithography and development of the resist, the sample is placed in an e-beam metal evaporator (Temescal). An intense electron beam is generated from a filament and steered via electric and magnetic fields to strike source material (*e.g.* pellets of Au or Cr) and vaporize it within a vacuum environment. Our contacts consist of a 5/75 nm Cr/Au bilayer. The Cr is used as a sticking layer. In the final lift-off step, the unwanted metal is removed along with the resist via immersing the sample in a hot acetone bath (55°C) for about 5-6 hours. The final device after the EBL is shown in Figure 4.6a(3).

4.4.4. MORE SPUTTERING

We use molybdenum-rhenium alloy ($\text{Mo}_{60}\text{Re}_{40}$) as a superconductor to make Josephson junction contacts with graphene. MoRe is chosen because it makes highly transparent contacts with carbon materials[18]. It had been used to make contact with graphene in a high quality-factor superconducting optomechanical device[19]. The another advantage of MoRe is that its oxide is also a superconductor. Depending on the alloying ratio and deposition temperature, the transition temperature (T_c) of MoRe is between 8 K and 13 K.

MoRe is deposited by a sputtering process using a d.c. plasma with a power of 100 W in an argon atmosphere. In our studies, the sputtering is carried out in a high vacuum system with background pressure $< 2 \times 10^{-8}$ Torr at a rate of 11 nm min^{-1} during 7 min. Lift-off is completed in hot acetone ($T = 54^\circ\text{C}$) for about 3-4 hours. A second lithography step defines the intended graphene geometry in a covering PMMA/HSQ layer. This step

is completed by the same etch as described in the reactive ion etching section. The final device after the MoRe sputtering is shown in Figure 4.6b(3).

4.4.5. ELECTRICAL MEASUREMENTS

Standard d.c. techniques are used for the electrical measurements. The current-voltage curves and gate voltage sweeps are obtained initially at room temperature to test the quality of the fabricated device. For MoRe contacts we see that the charge neutrality point (CNP) of the graphene has been shifted to a slightly negative gate voltage. This is attributed to contact-induced doping of graphene. The devices with high contact resistance and a broad CNP are not suitable for the low-temperature measurements; only the devices with low contact resistance and low doping are selected. The selected sample is then glued to a chip carrier using silver paint. Next, bonds of aluminium wires are made to the contacts using an ultrasonic bonding machine (West-Bond).

4

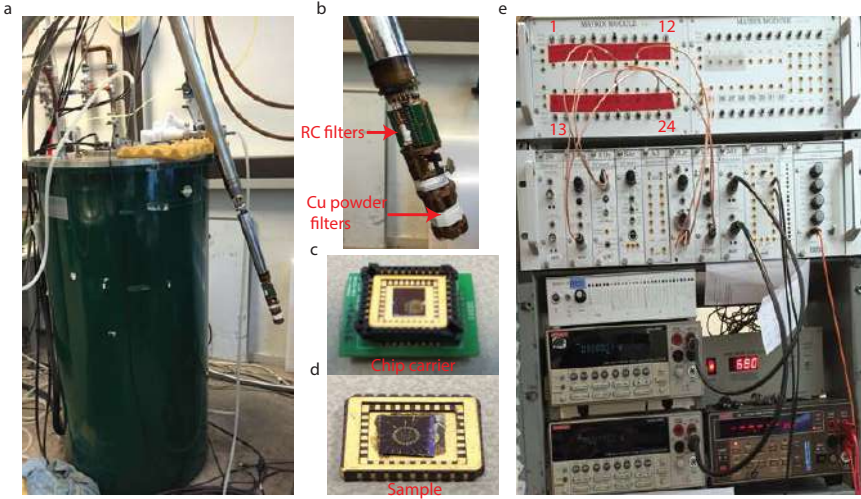


Figure 4.7: (a) A photograph of the dilution fridge of the low-temperature setup, (b) Shows the cold finger into which the chip is inserted. The cold finger has RC filter and Cu powder filters for the low noise measurements, (c) Photograph of the chip carrier, (d) Photograph of the sample mounted on the chip carrier. The sample is bonded to the carrier using the aluminum wires, (e) IVVI racks, which are built in-house at Delft.

Low-temperature d.c. measurements are performed in a Leiden Cryogenics MCK-50 3He/4He dilution fridge. This set-up can reach to a base temperature of 40 mK. The sample is loaded in the cold finger and pumped to a vacuum of $\approx 1 \times 10^{-4}$ mbar. The sample holder has 24 wires. The wires from the sample holder are connected to RC filters (10 kHz-500 MHz), and then to copper powder filters (10 MHz->40 GHz)[20]. The wires pass a π -filter that filters from 10 MHz to 10 GHz. The resistance of each wire is 2.53 k Ω . Of course for two-terminal measurements, 5.06 k Ω should be corrected for this wire resistance. The d.c. currents and voltages are applied and probed with home-built battery operated IVVI racks to minimize interference and noise from the environment[20].

These IVVI racks are developed in-house and can be added or removed depending on the kind of measurements. The setup is also equipped with a superconducting magnet coil that can sustain fields up to 12 T. Figure 4.7 shows the setup of the low-temperature electrical measurement system.

REFERENCES

- [1] G. B. Barin, Y. Song, I. de F. Gimenez, A. G. S. Filho, L. S. Barreto, and J. Konga, *Optimized graphene transfer: Influence of polymethylmethacrylate (PMMA) layer concentration and baking time on graphene final performance*, Carbon **84**, 82 (2015).
- [2] K. S. Novoselov, A. K. Geim, S. V. Morozov, D. Jiang, M. I. Katsnelson, I. V. Grigorieva, S. V. Dubonos, and A. A. Firsov, *Two-dimensional gas of massless Dirac fermions in graphene*, Nature **438**, 197 (2005).
- [3] Y. Huang, E. Sutter, N. N. Shi, J. Zheng, T. Yang, D. Englund, H. J. Gao, and P. Sutter, *Reliable exfoliation of large-area high-quality flakes of graphene and other two-dimensional materials*, ACS Nano **9**, 10612 (2015).
- [4] P. Blake, E. W. Hill, A. H. C. Neto, K. S. Novoselov, D. Jiang, R. Yang, T. J. Booth, and A. K. Geim, *Making graphene visible*, Applied Physics Letters **91**, 063124 (2007).
- [5] O. Hod, *Graphite and hexagonal boron-nitride have the same interlayer distance. why?* Journal of Chemical Theory and Computation **8**, 1360 (2012).
- [6] L. Wang, I. Meric, P. Y. Huang, Q. Gao, Y. Gao, H. Tran, T. Taniguchi, K. Watanabe, L. M. Campos, D. A. Muller, J. Guo, P. Kim, J. Hone, K. L. Shepard, and C. R. Dean, *One-dimensional electrical contact to a two-dimensional material*, Science **342**, 614 (2013).
- [7] C. R. Dean, A. F. Young, I. Meric, C. Lee, L. Wang, S. Sorgenfrei, K. Watanabe, T. Taniguchi, P. Kim, K. L. Shepard, and J. Hone, *Boron nitride substrates for high quality graphene electronics*, Nature Nanotechnology **5**, 722 (2010).
- [8] T. Taniguchi and K. Watanabe, *Synthesis of high-purity boron nitride single crystals under high pressure by using Ba-BN solvent*, Journal of Crystal Growth **303**, 525 (2007).
- [9] A. Castellanos-Gomez, M. Buscema, R. Molenaar, V. Singh, L. Janssen, H. S. J. van der Zant, and G. A. Steele, *Deterministic transfer of two-dimensional materials by all-dry viscoelastic stamping*, 2D Materials **1**, 011002 (2014).
- [10] C. Casiraghi, A. Hartschuh, H. Qian, S. Piscanec, C. Georgi, A. Fasoli, K. S. Novoselov, D. M. Basko, and A. C. Ferrari, *Raman spectroscopy of graphene edges*, Nano Letters **9**, 1433.

- [11] A. Das, S. Pisana, B. Chakraborty, S. Piscanec, S. K. Saha, U. V. Waghmare, K. S. Novoselov, H. R. Krishnamurthy, A. K. Geim, A. C. Ferrari, and A. K. Sood, *Monitoring dopants by Raman scattering in an electrochemically top-gated graphene transistor*, Nature Nanotechnology **3**, 210 (2008).
- [12] A. C. Ferrari, J. C. Meyer, V. Scardaci, C. Casiraghi, M. Lazzeri, F. Mauri, S. Piscanec, D. Jiang, K. S. Novoselov, S. Roth, and A. K. Geim, *Raman spectrum of graphene and graphene layers*, Physical Review Letters **97**, 187401 (2006).
- [13] A. C. Ferrari, *Raman spectroscopy of graphene and graphite: Disorder, electron-phonon coupling, doping and nonadiabatic effects*, Solid State Communications **143**, 47 (2007).
- [14] L. M. Malard, M. A. Pimenta, G. Dresselhaus, and M. S. Dresselhaus, *Raman spectroscopy in graphene*, Physics Reports **473**, 51 (2009).
- [15] A. C. Ferrari and D. M. Basko, *Raman spectroscopy as a versatile tool for studying the properties of graphene*, Nature Nanotechnology **8**, 235 (2013).
- [16] P. Venezuela, M. Lazzeri, and F. Mauri, *Theory of double-resonant raman spectra in graphene: Intensity and line shape of defect-induced and two-phonon bands*, Physical Review B **84**, 035433 (2011).
- [17] V. Sidorkin, E. van der Drift, and H. Salemink, *Influence of hydrogen silsesquioxane resist exposure temperature on ultrahigh resolution electron beam lithography*, Journal of Vacuum Science & Technology B **26**, 2049 (2008).
- [18] B. H. Schneider, S. Etaki, H. S. J. van der Zant, and G. A. Steele, *Coupling carbon nanotube mechanics to a superconducting circuit*, Scientific Reports **2**, 599 (2012).
- [19] V. Singh, B. H. Schneider, S. J. Bosman, E. P. J. Merkx, and G. A. Steele, *Molybdenum-rhenium alloy based high-Q superconducting microwave resonators*, Applied Physics Letters **105**, 222601 (2014).
- [20] V. E. Calado, *Graphene nanodevices*, Ph.D. Thesis, Technische Universiteit Delft (2013).

5

MODIFICATION OF ENCAPSULATED GRAPHENE BY HIM

In this chapter, we study helium-ion-beam induced defects in graphene that is encapsulated by hexagonal boron nitride (h-BN). By comparing Raman spectra from different sandwich configurations, we examine the influence of the primary ions and the environment on the nature of the induced defects. We observe a high tolerance of the sp^2 -bonds in encapsulated graphene to helium-ion-beam exposure, up to a dose of 1×10^{16} ions cm^{-2} , whereas unprotected graphene becomes highly defective already at 5×10^{14} ions cm^{-2} . We show for the first time the autonomous behavior of the D' Raman peak: in contrast to the D defect peak, the D' defect peak strongly depends on the environment; saturating with dose in the encapsulated graphene. Finally, we made one-dimensional edge contacts to the BN-encapsulated graphene. Electrical measurements reveal n-type behavior, already at low ion doses at which the G and 2D Raman peaks are still unaffected. We conclude that unbound atoms (interfacials) between the sp^2 -layers of h-BN and graphene promote self-healing of the beam induced lattice damage and that nitrogen-carbon exchange between the graphene and the boron nitride lead to n-doping. This work demonstrates that h-BN encapsulation in combination with focused He^+ beam exposure is a promising technique to achieve controlled modification of graphene for device applications.

Parts of this chapter have been published in Nano Letters **15** (6), 4006-4012 (2015) [1].

5.1. INTRODUCTION

BECAUSE of its exceptional electrical[2, 3], mechanical[4], and optical properties [5], graphene has been investigated extensively over the past decade. However, the absence of a bandgap in normal graphene thwarts its potential for applications in electronic devices. Many different approaches have been explored to realize a bandgap in graphene, for instance by nanoribbon formation [6], doping[7, 8], or by inducing strain[9, 10]. Nanoribbon formation by oxygen plasma etching[6], chemical synthesis[11], and focused ion beam milling[12–16] usually degrades its electrical properties. An alternative means of tuning the electrical properties in graphene is by controlling the doping level and modulating carrier transmission probability with p-n junctions[17, 18]. After its introduction in 2006[19], the helium ion microscope (HIM) with its focused helium ion beam of 1 nm in diameter, became a promising instrument to structure graphene[13, 15, 16, 20–22]. Here, the ion beam is scanned over an area to remove C atoms via atomic collisions. Several attempts have been made to ion mill graphene into nanoribbons with a focused He⁺ beam[13, 15, 16, 20–22], but the devices made on disordered SiO₂ suffered seriously from beam induced contamination[13], extensive vacancy defects, and uncontrolled charged impurity doping[23]. Obviously, vacancies and dopants modify the electronic structure of graphene[24], but control of the modification is essential for device applications. The excess of damage induced by the ions to bare or unprotected graphene precluded fabrication of graphene devices by focused-helium-ion-beam milling. In order to optimize controlled modification and minimize collateral damage, protection of graphene might provide a solution. Several recent studies appeared on ion beam induced defect formation in graphene[21, 22, 25–30], but missing are studies focusing on the role of graphene's direct local environment during the ion bombardment. It has been found recently that hexagonal boron-nitride (h-BN), an insulator with the same lattice structure as graphene with only a 1.7% lattice mismatch, is ideal for achieving minimal environmental sensitivity and high mobility in graphene[31]. In addition, two recent studies have demonstrated significant reduction of electron-beam damage in MoS₂ by encapsulation in graphene [32, 33]. These studies suggest that BN-encapsulated graphene is a serious candidate for structuring with a 1-nm focused He⁺ beam. In order to achieve controlled modification, one must study the correlation between the type and behavior of beam induced defects and the physical and chemical processes in graphene with various local environments. In this chapter, we report the defect behavior of graphene in different sandwich configurations, exposed to a focused He⁺ beam and studied with Raman spectroscopy. Finally, the effect of He⁺ beam exposure on the charge transport in BN-encapsulated graphene is measured.

5.2. SAMPLE PREPARATION

Four different types of samples were prepared: (1) SiO₂ covered by exfoliated graphene (SG); (2) SiO₂ covered by h-BN and then by graphene (SBG); (3) SiO₂ covered by graphene and then by h-BN (SGB); and (4) SiO₂ covered by graphene encapsulated between two h-BN layers (SBGB). The last three types of samples were made by similar stack-transfer and van der Waals pick-up techniques as reported by Dean *et al.*[31] and by Wang *et*

al.[34], respectively. Our procedure is described in the sample preparation section of Chapter 4. AFM images of all the four samples are shown in Figure 5.1.

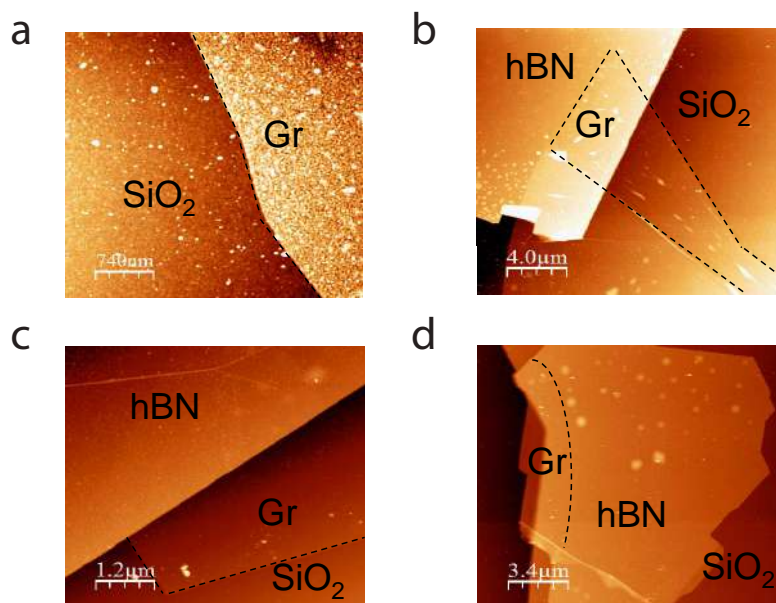


Figure 5.1: AFM images of some samples used in this study. (a) Single-layer graphene on a silicon oxide surface (an SG sample), (b) Single-layer graphene on an h-BN substrate (an SBG sample), (c) Single-layer graphene partially covered by h-BN (an SGB sample), (d) Graphene sandwiched between two h-BN flakes (an SBGB sample).

5.3. HELIUM ION BEAM EXPOSURES

Helium ion beam exposures were performed in a Carl Zeiss OrionTM Plus scanning helium ion microscope (HIM). The chamber pressure during the exposures was around 4×10^7 mbar. A 30-keV He^+ beam at normal incidence and a $5\text{-}\mu\text{m}$ aperture were used for all exposures. The beam current of 0.4-0.5 pA was maintained by regulating the helium gas pressure in the source. An internal pattern generator was used to expose areas of $1\text{-}2\ \mu\text{m}^2$ with a beam step size of 1 nm. Electrical leads were fabricated for all samples with e-beam lithography and Cr/Au lift off to facilitate beam navigation and to prevent image fading during ion microscopy caused by sample charging. Consequently, unintended exposures of the crucial sites were avoided. Many samples were prepared and for each dose between 5×10^{13} and 5×10^{16} ions cm^{-2} a fresh sample is used to avoid cross exposure.

5.4. DEFECT STUDY VIA RAMAN SPECTROSCOPY

5.4.1. RAMAN SPECTRA OF GRAPHENE

Raman spectroscopy measurements were performed in air at room temperature with a Renishaw inVia Raman microscope. This spectrometer is equipped with a 514-nm (2.41-eV) laser with a spot size of about 350 nm. A 100x objective was used for the spectroscopy measurements. The laser power is kept well below 1 mW to avoid sample heating. Micro-Raman spectra measurements of all the exposed sandwich structures as function of ion dose are shown in Figure 5.2. For each dose, at least two different samples were studied.

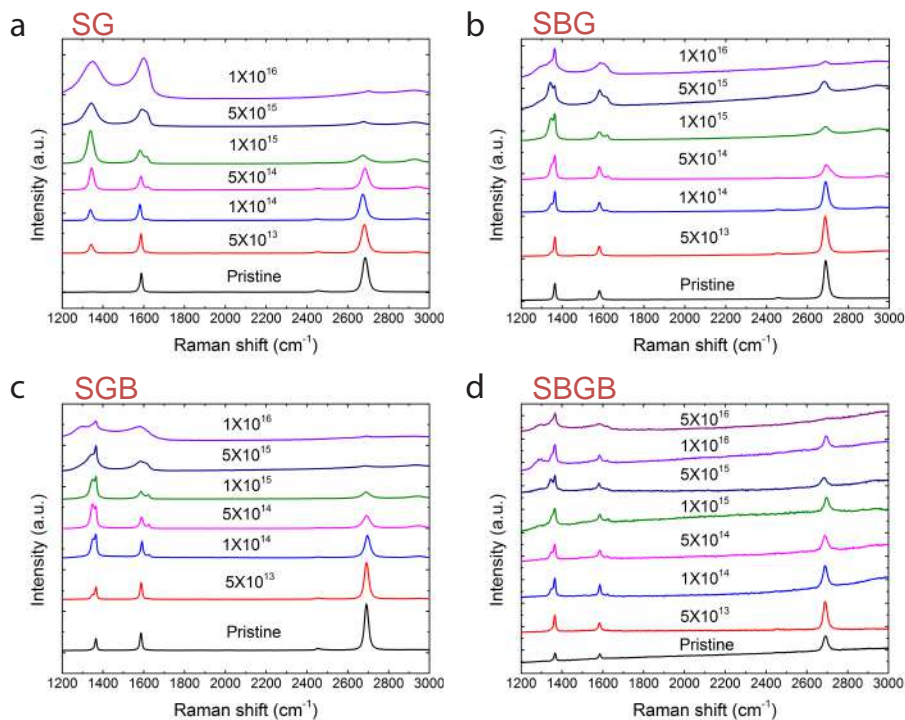


Figure 5.2: Raman spectra of graphene as function of ion dose for all sandwich structures. Doses mentioned are in ions cm^{-2} .

5.4.2. DEFECT DEPENDANCE ON THE SAMPLE TYPE

Figure 5.3 shows Raman spectra of pristine and exposed samples. The exposure dose was 1×10^{16} helium ions cm^{-2} , at which graphene is found to be seriously damaged by the loss of hexagonal rings[21, 22]. A significant increase in the intensity of the G peak is observed for the exposed SG, SBG, and SGB samples as compared to their pristine counterparts, with a simultaneous decrease in the intensity of the 2D peak (Figure 5.3a-c). In contrast, the G and 2D peak intensities for the SBGB sample remain almost unaffected

(Figure 5.3d). We note that the small changes in energy and direction of the primary ions in the top h-BN layer cannot explain the different behavior of the G and 2D peaks. A new peak has appeared at 1295 cm^{-1} , which we attribute to beam induced transformation of sp^2 -bonds in h-BN to sp^3 -bonds in c-BN [35, 36]. Implanted helium often becomes trapped in the substrate, leading to sample swelling if the helium atoms cannot diffuse out. Swelling can cause significant device failure and become a limiting factor in He^+ -beam processing[21, 37]. Interestingly, we did not observe swelling in any of our samples, even at the highest doses.

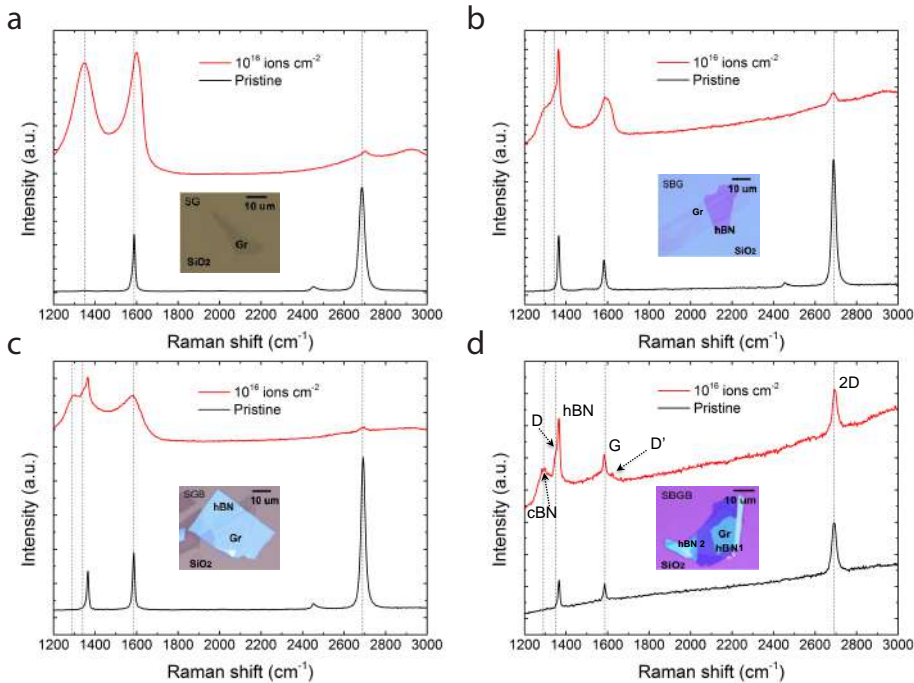


Figure 5.3: Raman spectra of graphene (G) in various sandwich configurations with silicon oxide (S) as substrate and boron nitride (B) as encapsulation. (a) SG, (b) SBG, (c) SGB, and (d) SBGB. Red spectra are for the samples exposed to $1 \times 10^{16}\text{ ions cm}^{-2}$ and the black ones for the pristine samples. Vertical dashed lines guide the eye.

Exposure to a beam of 30-keV helium ions induces vacancy defects and disorder in graphene[21, 22]. Beam induced disorder is often observed via the emergence of D and D' peaks in the Raman spectra, which initially increase continuously with ion dose. [25, 26, 38] They originate from single-phonon intervalley and intravalley processes, respectively, where defects provide the missing momentum[39–41]. Whereas the D peak is widely used to quantify the defects in graphene, the D' peak is generally considered to be proportional to the D peak and often discarded because of its low intensity. Figure 5.4 shows the Raman spectra of the SBGB sample near the G and D' peaks for various doses. These spectra are clearly different from those of the other samples, in which the D' peaks merge with the G peaks at a dose of $5 \times 10^{15}\text{ ions cm}^{-2}$, making it difficult to sep-

arate their individual contributions[30]. We have fitted each peak with a Lorentzian line shape to obtain values of their full-width-at-half-maximum Γ , position ω , and intensity I . The results are shown in Figure 5.5. For instance, Figure 5.5a shows the $I_{D'}/I_G$ peak intensity ratios. Interestingly, the ratio for the encapsulated sample saturates at a dose of 1×10^{15} ions cm^{-2} , whereas it continues to rise for the other samples. The I_D/I_G ratio is generally regarded as a measure of disorder in graphene [25, 26, 30, 38, 39, 42]. For the SG, SBG, and SGB samples, the I_D/I_G ratio has a maximum at 1×10^{15} ions cm^{-2} , but for the BN-encapsulated sample the maximum is lower and lies at a 5 times higher dose (Figure 5.5b). Lucchese *et al.*[26] found that the I_D/I_G ratio reflects two stages of disordering in ion-irradiated graphene. In stage 1, I_D/I_G is proportional to the defect density n_D : $I_D/I_G \propto n_D \propto 1/L_D^2$, where L_D is the average distance between neighboring defects. However, if L_D becomes less than the average distance an electron-hole pair travels before scattering with a phonon, then the contributions of separate defects do not add up anymore[40] and I_D/I_G starts to scale with L_D^2 . This is stage 2 disordering.

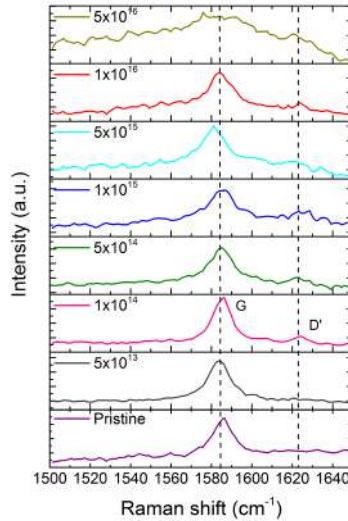


Figure 5.4: Raman spectra of the SBGB sample, showing the G and D' peaks as function of the ion dose (labels indicate the dose in ions cm^{-2}).

The value of L_D at the transition is around 3.5 nm, given by v_F/ω_D , where v_F is the Fermi velocity and ω_D the Debye cut-off frequency[21, 40, 43]. Note that in the low-energy Ar^+ irradiation study by Lucchese *et al.*[26], the defect density n_D and the ion dose σ are assumed to be equal. Fox *et al.*[22] showed that also defects in graphene induced by He^+ irradiation follows a two-stage process. However, the kinetic energy transfer from swift, light ions to atoms in a solid is much lower than that from slow, heavy ions. Indeed, the graphene in the latter study became highly defective only at 5×10^{14} He^+ ions cm^{-2} . Because of the similarities with the studies of Lucchese *et al.*[26] and Fox *et al.*[22], we regard the dose of the maximum in I_D/I_G (1×10^{15} cm^{-2}) as the transition between stage

1 and stage 2 disorder in our SG, SBG, and SGB samples.

According to Cançado *et al.*[25], the defect density n_D for stage 1 disorder and the Raman peak intensity ratio are related as

$$n_D = \alpha E_L^4 \frac{I_D}{I_G} \quad (5.1)$$

where α is $(7.3 \pm 2.2) \times 10^9 \text{ cm}^{-2} \text{ eV}^{-4}$ and E_L is the laser excitation energy. Accordingly, n_D in the SBGB sample increases from $0.7 \times 10^{11} \text{ cm}^{-2}$ at $5 \times 10^{13} \text{ ions cm}^{-2}$ to $4 \times 10^{11} \text{ cm}^{-2}$ at $5 \times 10^{15} \text{ ions cm}^{-2}$, see Figure 5.5b. Defect sites in graphene are very reactive and chemical reactions, *e.g.* with molecules adsorbed from the atmosphere or with the substrate material, can alter the *size* rather than the *density* of the defects[27]. However, the relation of Cançado *et al.*[25] does not consider the chemical state of the defects and we assume Equation 6.1 to be valid for all our samples. Because its I_D/I_G ratio stays below 1.5 and its G and 2D peak shapes are barely affected, we conclude that the encapsulated graphene does not reach stage 2 disorder up to $1 \times 10^{16} \text{ ions cm}^{-2}$ and that Equation 6.1 remains valid. Then, n_D has decreased slightly to $3 \times 10^{11} \text{ cm}^{-2}$, maybe due to healing of the lattice. If we further increase the dose to $5 \times 10^{16} \text{ ions cm}^{-2}$, the 2D peak almost completely disappears (Figure 5.2), indicating stage 2 disorder. Apparently, disintegration of the sp^2 -lattice of the protected graphene cannot be avoided at such a high ion dose.

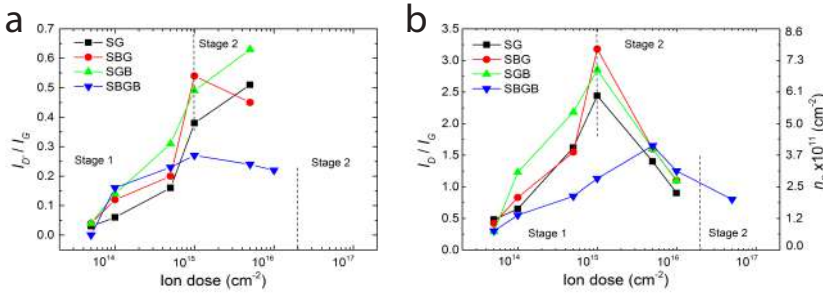


Figure 5.5: (a) D' to G peak intensity ratio as function of ion dose, (b) D to G peak intensity ratio (left vertical axis); the defect density n_D according to Equation 6.1 is given at the right vertical axis.

In various previous studies, the D and D' peaks were found to be proportional to each other in stage 1, both increasing proportionally with ion dose[30, 39]. Recently, Axel *et al.*[39] correlated the $I_{D'}/I_D$ ratio to the type of defects: the ratio being 1/13 for defects associated with sp^3 -hybridization, 1/7 for vacancy-like defects, and 1/3.5 for boundary-like defects. We observe a weak increase of the $I_{D'}/I_D$ ratio in the SG, SBG, and SGB samples and a clear decrease for the BN-encapsulated one, see Figure 5.6. For the latter Figure, we have taken the transition to be at $1 \times 10^{15} \text{ ions cm}^{-2}$ for the SG, SBG, and SGB samples and $2 \times 10^{16} \text{ ions cm}^{-2}$ for the SBGB one. We can explain the observation (Figure 5.5a, Figure 5.6) of the limited change of the D' peak in the SBGB sample with the model of Venezuela *et al.*[44]. The Fourier transform of the Coulomb potential has a maximum close to the Γ point in the Brillouin zone and decays as q^{-1} , where q is the phonon momentum. The D peak is due to phonons near the K point at relatively large

q [44, 45]. Consequently, the contribution of Coulomb (or charged) impurities to the D peak is small. In contrast, the D' peak is due to phonon scattering near the Γ point, making it sensitive to Coulomb defects, *e.g.* atmospheric water or hydrocarbons, adatoms, polymer residues, and relocated atoms from the SiO₂ substrate. If graphene is encapsulated in h-BN, charged impurities due to atmospheric or other external contaminations are absent after the ion bombardment. We relate the appearance of the D' peak in Figure 5.4 to relocated C, N, and B atoms near the BN-graphene interface. In the SGB sample, where graphene is protected only from the top, charged impurities can reside at the SiO₂-graphene interface and form sp³-bonds with the vacancies created by the ion beam. Moreover, charged adsorbents and oxide electric fields facilitate charge transfer to unprotected (SG) or partially protected graphene (SBG and SGB), causing the continuing growth and alteration of the D' peak.[46, 47]

Das *et al.*[48] have shown that electron and hole doping has a direct influence on the frequency ω_G of the G peak and the I_G/I_{2D} ratio: both increase with doping.[34, 48, 49] The I_G/I_{2D} ratio increases with ion dose for the SG, SBG, and SGB samples, but not for the SBGB sample (Figure 5.7c). Note that the inverse of the I_G/I_{2D} ratio is a measure of the quality of graphene[34]. The 2D peak is doubly electronically resonant and, hence, sensitive to the dynamics of photo-excited electron-hole pairs: all resonant electronic scattering states decrease the intensity of the 2D peak[30, 34, 39, 40]. In our experiments, the I_G/I_{2D} ratio of the encapsulated graphene is constant up to 1×10^{16} ions cm⁻² (Figure 5.7c), indicating that stage 2 disorder is unlikely below this dose. Figure 5.7d shows the frequency shift of the G peak. Once again, the changes for the SBGB sample are considerably less than for the other three samples.

Lattice disorder has a direct impact on the width Γ of the G and 2D peaks[25, 39]. The width Γ_G of the Raman G peak for the SG, SBG, and SGB samples increases by 40 to 65 cm⁻¹ (Figure 5.7a), but for the encapsulated sample only by ~ 10 cm⁻¹. The 2D peak in Figure 5.7b shows the same trend, albeit that it becomes unobservable above 1×10^{15} ions cm⁻² for the SG, SBG, and SGB samples.

5.5. SRIM SIMULATIONS

In order to elucidate details of the energy transfer and collision processes in the sandwich structures, we performed SRIM calculations[50]. In a 15-nm top h-BN layer, 30-keV helium ions lose about 2.1 keV by electronic collisions and 0.1 keV by nuclear collisions. The corresponding beam broadening is less than 1 nm (Figure 5.8). Hence, the ions pass the graphene layer in all samples with about the same energy and in the same direction. Note that for heavier ions, such as Ga⁺ or Ar⁺, deflections and energy loss by nuclear collisions are huge and mainly concentrated in the top h-BN layer, unless the ion's energy is much higher. Beams of light ions are, thus, better suited for structuring BN-protected graphene. The SRIM simulation also shows that 2% of the helium ions passing a single layer of graphene displace a C atom (Figure 5.8c), thus producing a defect, consisting of a vacancy and a temporary unbound C atom. Also in each h-BN sp²-layer 2% of the ions displace a B or N atom. Due to the impact of the collision, these C, B, and N atoms travel typically 1 nm before coming to rest. At a dose of *e.g.* 1×10^{15} ions cm⁻², 2×10^{13}

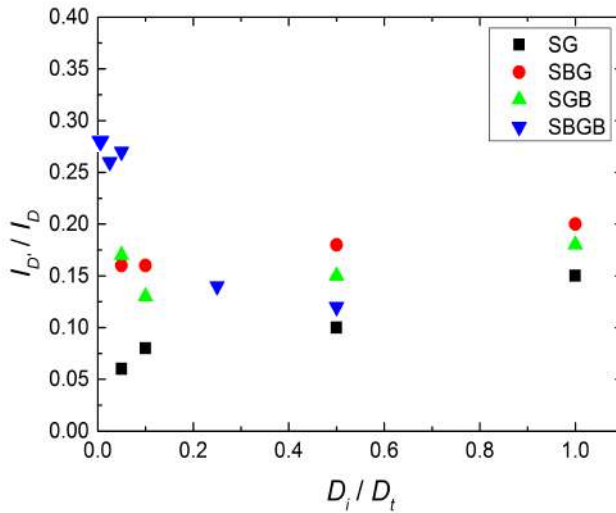


Figure 5.6: $I_{D'}/I_D$ ratio versus normalized dose in stage 1, where D_i is the ion dose and D_t is the dose at the transition between stage 1 and stage 2 disorder. The $I_{D'}/I_D$ ratio shows a weak increase for the SG, SBG, and SGB samples and a clear decrease for the SBGB one.

cm^{-2} C atoms are displaced, corresponding to an average distance of 2.2 nm between neighboring defects.

5.6. ELECTRICAL MEASUREMENTS

The gate-voltage dependence of the resistance of the BN-encapsulated graphene can provide insight into the influence of the ion bombardment and the self-healing on the material's electrical properties. For this purpose, we made one-dimensional electrical contacts along the edges of the SBGB sample by electron beam lithography, etching, and thermal deposition of Cr and Au. Figure 5.9a shows the measured resistance as a function of the back-gate voltage for a pristine sample and two irradiated samples. The charge neutrality point in the pristine graphene lies at zero gate-voltage, indicating the absence of doping.[7] Increasing dose shifts the charge neutrality point, consistent with previous studies[7, 17] and revealing n -type conduction. Substitutional N atoms in graphene are electron-donating (n -type) dopants and substitutional B atoms p -type dopants.[8, 51] The bond length of C-N is 1.40 Å, similar to that of C-C in graphene (1.41 Å)[8]. Hence, N atoms can be substitutionally incorporated in graphene without distortion of the planar lattice. In contrast, the bond length of C-B is 1.48 Å and, therefore, substitutional B incorporation causes lattice distortion and is, thus, less likely. The schematic of this process is shown in Figure 5.9c. In a He^+ -atom collision, C, B, and N atoms can be displaced and subsequently bind to existing defects, thus forming new, stable configurations. Gong *et al.*[52] studied the chemical graphene-BN conversion and

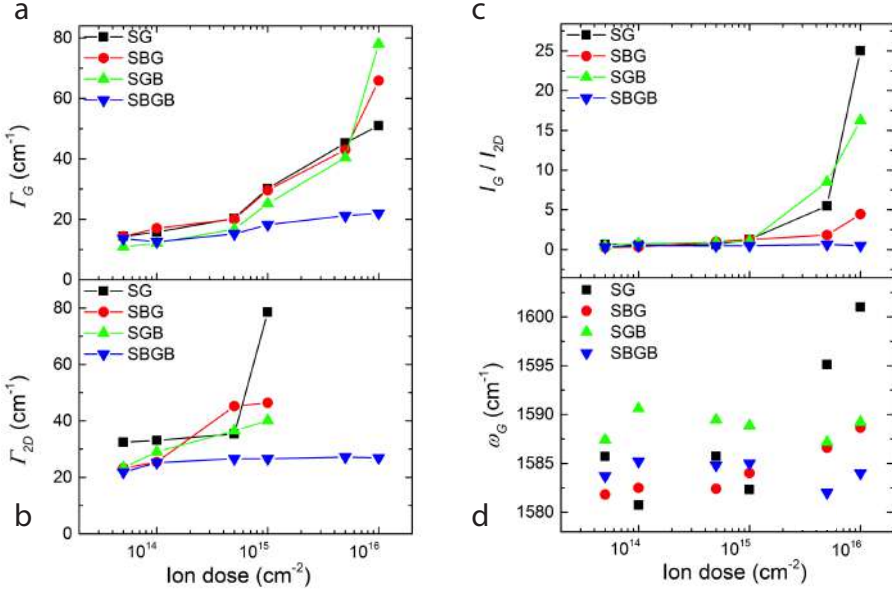


Figure 5.7: (a) Raman peak widths Γ_G , (b) Γ_{2D} , (c) Peak intensity ratios I_G/I_{2D} , and (d) Peak positions ω_G as functions of the ion dose.

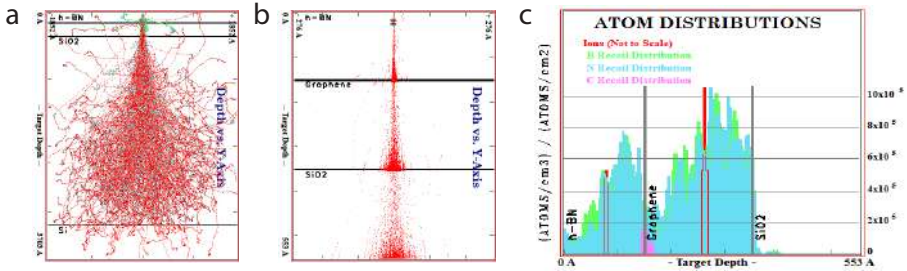


Figure 5.8: SRIM simulation results for the SBGB structure (both BN layers are 15 nm thick and the graphene 0.3 nm). (a) Full trajectories of 500 30-keV He ions (lateral and depth ranges of the plot are both 370 nm), (b) Ion trajectories in the top layers, showing the beam spread in the BN-graphene-BN stack (lateral and depth ranges are 55 nm; the drop in track density at the interfaces is an artefact of the plotting), (c) Distribution of displaced atoms for 1000 He ions.

found that nitrogen atoms are favored over boron atoms in substituting carbon atoms. The *n*-doping of our SBGB sample is, thus, consistent with this observation of Gong *et al.*. The substitutional nitrogen doping suppresses the density of states of graphene near the Fermi level, thus opening a gap between the valence and conduction bands[7]. Nevertheless, more experimental and theoretical investigations are needed to better understand the substitutional doping by helium-ion-beam irradiation and its influence on the band structure of BN-encapsulated graphene.

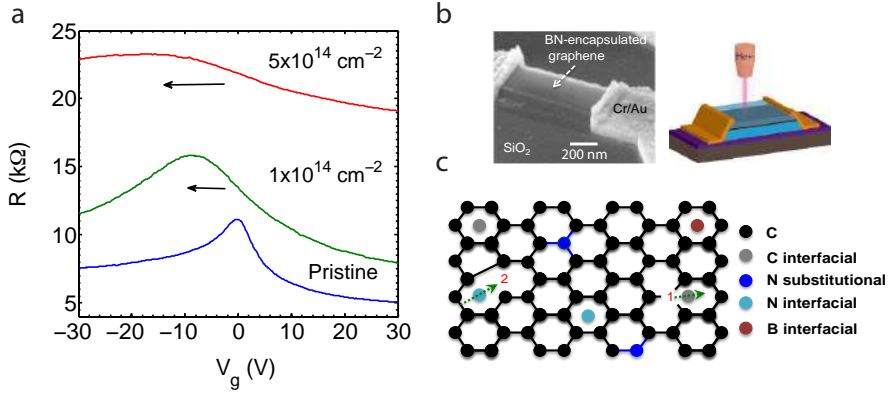


Figure 5.9: (a) Resistance (R) versus gate-voltage (V_g) of a pristine device and two devices exposed to the 30-keV helium ion beam, (b) SEM image of an edge-contacted and h-BN encapsulated graphene device, (c) Schematic representation of (1) a displaced C atom becoming an interfacial and (2) an interfacial N atom becoming substitutional.

5.7. DISCUSSION AND CONCLUSION

In the defect model of Lucchese *et al.*[26] the transition from stage 1 to stage 2 occurs at a defect distance of 3.5 nm. Because we do not observe the transition up to a dose of 1×10^{16} ions cm^{-2} , we conclude that most unbound atoms and vacancies in the encapsulated graphene are short-lived. The interlayer distances of graphene and h-BN are almost the same[53], about 1.34 nm[54]. The surface diffusion barrier of carbon adatoms on bare graphene is 0.4 eV [54–56] and on h-BN 0.68 eV[57]. Since the graphene is sandwiched between h-BN layers, we expect the diffusion barrier to be similar or slightly higher for the atoms in the interface between the graphene and the boron nitride and we conclude that atoms in the interface can move in the same manner as adatoms on graphene. And, hence, unbound C atoms can diffuse relatively easily here. We call these mobile atoms "interfacials", being an intermediate species between interstitials and surface adatoms. Interfacials diffuse until they are captured, most likely by a vacancy. If the vacancy is in the graphene, the capture implies healing of the defect. This healing mechanism is in accordance with two related studies. Xu *et al.*[58] observed self-healing of electron-beam induced point defects in graphene at 600 °C. However, if a high electron intensity is used, several adjacent C atoms are knocked out and the graphene lattice can no longer self-heal. Kalbac *et al.*[27] observed similar effects for 100-keV Ar^+ irradiation of isotopically labeled bi-layer graphene. The C interfacials recombine preferably with vacancies in the bottom layer, resulting in a reduction of the radiation damage. If an interfacial B or N atom is captured in a graphene vacancy, a doping defect is formed. Of course, interfacial C atoms can also be captured in the BN layer, but there they do not affect the Raman peaks of graphene. Continued exposure to the ion beam produces new interfacials and vacancies, leading to faster healing. This mechanism, we think, explains the saturation and maybe also the slight reduction of the defect peak intensities in Fig-

ure 5.5. Obviously, the protection of the encapsulated graphene excludes or minimizes formation of many notorious types of defects, such as charged impurity and doping defects from the oxide. Nevertheless, also extended vacancy or defect complexes can be formed during the ion-beam irradiation. However, the continuous energy influx during the exposure, the high-energy state of these complexes, and the scarcity of chemically stable configurations slow down the disintegration of the encapsulated graphene. This suggests that the vacancies created by the passing ions can only arrange themselves into simple polygons (Stone-Wales defects[55]) or disappear by capture of C, B, or N interfacials, leading to either healing or doping of the defected graphene. At a dose of 5×10^{16} ions cm^{-2} , healing cannot prevent amorphization of the graphene anymore despite the retardation in defect accumulation. In conclusion, we presented a systematic analysis of helium-ion-beam irradiation of graphene that is encapsulated between h-BN flakes. A comparison is made between four different sandwich configurations to elucidate the roles of the primary ions and the environment on defect formation and annealing in irradiated graphene. Raman measurements showed that radiation defects in graphene do not simply reflect the original disorder created by the collisions of the primary He^+ ions. Instead, the disorder evolves after termination of the collision process; this evolution is strongly influenced by the graphene's environment. If the graphene is fully encapsulated in h-BN, lattice healing and nitrogen doping occur, possibly stimulated by the continuing ion bombardment itself. We observed healing among others as a retarded growth of the D and a saturating growth of the D' Raman defect peaks and as a delay in the onset of stage 2 lattice disorder. In contrast, if the irradiated graphene is in contact to a substrate oxide or the atmosphere, defects can form stable sp^3 -bonds, hindering lattice self-healing. In addition, this study shows unequivocally that the D' peak is not a miniature copy of the D peak: it has a different origin, shows independent behavior, and is presumably sensitive to Coulomb defects.

So far, all ion-beam-irradiation studies were conducted on unprotected graphene and, hence, stable defects dominated the electrical behavior of the irradiated material. Our electrical measurements on the encapsulated graphene showed n -type behavior after He^+ irradiation, probably caused by the collisional substitution of carbon atoms by nitrogen atoms. We surmise that defect self-annealing and n -doping of irradiated encapsulated graphene could prove to be essential for various important applications, such as the realization of graphene-based p - n junction devices.

REFERENCES

- [1] G. Nanda, S. Goswami, K. Watanabe, T. Taniguchi, and P. F. A. Alkemade, *Defect control and n -doping of encapsulated graphene by helium-ion-beam irradiation*, *Nano Lett.* **15**, 4006 (2015).
- [2] Y. Zhang, Y. Tan, H. L. Stormer, and P. Kim, *Experimental observation of the quantum Hall effect and Berry's phase in graphene*, *Nature* **438**, 201 (2005).
- [3] K. S. Novoselov, A. K. Geim, S. V. Morozov, D. Jiang, M. I. Katsnelson, I. V. Grigorieva,

- S. V. Dubonos, and A. A. Firsov, *Two-dimensional gas of massless Dirac fermions in graphene*, Nature **438**, 197 (2005).
- [4] I. W. Frank, D. M. Tanenbaum, A. M. van der Zande, and P. L. McEuen, *Mechanical properties of suspended graphene sheets*, Journal of Vacuum Science & Technology B **25**, 2558 (2007).
- [5] R. R. Nair, P. Blake, A. N. Grigorenko, K. S. Novoselov, T. J. Booth, T. Stauber, N. M. R. Peres, and A. K. Geim, *Fine structure constant defines visual transparency of graphene*, Science **320**, 1308 (2007).
- [6] M. Y. Han, B. Özyilmaz, Y. Zhang, and P. Kim, *Energy band-gap engineering of graphene nanoribbons*, Physical Review Letters **98**, 206805 (2007).
- [7] D. Wei, Y. Liu, Y. Wang, H. Zhang, L. Huang, and G. Yu, *Synthesis of n-doped graphene by chemical vapor deposition and its electrical properties*, Nano Letters **9**, 1752 (2009).
- [8] P. Rani and V. K. Jindal, *Designing band gap of graphene by B and N dopant atoms*, RSC Advances **3**, 802 (2013).
- [9] Z. H. Ni, T. Yu, Y. H. Lu, Y. Y. Wang, Y. P. Feng, and Z. X. Shen, *Uniaxial strain on graphene: Raman spectroscopy study and band-gap opening*, ACS Nano **11**, 2301 (2008).
- [10] G. Gui, J. Li, and J. Zhong, *Band structure engineering of graphene by strain: First-principles calculations*, Physical Review B **78**, 075435 (2008).
- [11] J. Cai, P. Ruffieux, R. Jaafar, M. Bieri, T. Braun, S. Blankenburg, M. Muoth, A. P. Seitsonen, M. Saleh, X. Feng, K. Müllen, and R. Fasel, *Atomically precise bottom-up fabrication of graphene nanoribbons*, Nature **466**, 470 (2010).
- [12] D. Pickard and L. Scipioni, *Graphene nano-ribbon patterning in the Orion plus*, Zeiss Application Note .
- [13] M. C. Lemme, D. C. Bell, J. R. Williams, L. A. Stern, B. W. H. Baugher, P. Jarillo-Herrero, and C. M. Marcus, *Etching of graphene devices with a helium ion beam*, ACS Nano **3**, 2674 (2009).
- [14] Y. Zhang, C. Hui, R. Sun, K. Li, K. He, X. Ma, and F. Liu, *A large-area 15 nm graphene nanoribbon array patterned by a focused ion beam*, Nanotechnology **25**, 135301 (2014).
- [15] D. C. Bell, M. C. Lemme, L. A. Stern, J. R. Williams, and C. M. Marcus, *Precision cutting and patterning of graphene with helium ions*, Nanotechnology **20**, 455301 (2009).
- [16] A. N. Abbas, G. Liu, B. Liu, L. Zhang, H. Liu, D. Ohlberg, W. Wu, and C. Zhou, *Patterning, characterization, and chemical sensing applications of graphene nanoribbon arrays down to 5 nm using helium ion beam lithography*, ACS Nano **8**, 1538 (2014).

- [17] B. Guo, Q. Liu, E. Chen, H. Zhu, L. Fang, and J. R. Gong, *Controllable n-doping of graphene*, *Nano Letters* **10**, 4975 (2010).
- [18] B. H. Seo, J. Youn, and M. Shim, *Direct laser writing of air-stable p-n junctions in graphene*, *ACS Nano* **8**, 8831 (2014).
- [19] B. Ward, J. A. Notte, and N. Economou, *Helium ion microscope: a new tool for nanoscale microscopy and metrology*, *Journal of Vacuum Science & Technology B* **24**, 2871 (2006).
- [20] N. Kalhor, S. A. Boden, and H. Mizuta, *Sub-10 nm patterning by focused He-ion beam milling for fabrication of downscaled graphene nano devices*, *Microelectronic Engineering* **114**, 70 (2014).
- [21] S. Hang, Z. Moktadir, and H. Mizuta, *Raman study of damage extent in graphene nanostructures carved by high energy helium ion beam*, *Carbon* **72**, 233 (2014).
- [22] D. Fox, Y. B. Zhou, A. O'Neill, S. Kumar, J. J. Wang, J. N. Coleman, G. S. Duesberg, J. F. Donegan, and H. Z. Zhang, *Helium ion microscopy of graphene: beam damage, image quality and edge contrast*, *Nanotechnology* **24**, 335702 (2013).
- [23] S. Ryu, L. Liu, S. Berciaud, Y. Yu, H. Liu, P. Kim, G. W. Flynn, and L. E. Brus, *Atmospheric oxygen binding and hole doping in deformed graphene on a SiO₂ substrate*, *Nano Letters* **10**, 4944 (2010).
- [24] R. Faccio, L. Fernández-Werner, H. Pardo, C. Goyenola, O. N. Ventura, and A. W. Momburu, *Electronic and structural distortions in graphene induced by carbon vacancies and boron doping*, *Journal of Physical Chemistry C* **114**, 18961 (2010).
- [25] L. G. Cançado, A. Jorio, E. H. M. Ferreira, F. Stavale, C. A. Achete, R. B. Capaz, M. V. O. Moutinho, A. Lombardo, T. S. Kulmala, and A. C. Ferrari, *Quantifying defects in graphene via Raman spectroscopy at different excitation energies*, *Nano Letters* **11**, 3190 (2011).
- [26] M. M. Lucchese, F. Stavale, E. H. M. Ferreira, C. Vilani, M. V. O. Moutinho, R. B. Capaz, C. A. Achete, and A. Jorio, *Quantifying ion-induced defects and Raman relaxation length in graphene*, *Carbon* **48**, 1592 (2010).
- [27] M. Kalbac, O. Lehtinen, A. V. Krasheninnikov, and J. Keinonen, *Ion-irradiation-induced defects in isotropically-labeled two layered graphene: Enhanced in-situ annealing of the damage*, *Advanced Materials* **25**, 1004 (2013).
- [28] O. Lehtinen, J. Kotakoski, A. V. Krasheninnikov, A. Tolvanen, K. Nordlund, and J. Keinonen, *Effects of ion bombardment on a two-dimensional target: Atomistic simulations of graphene irradiation*, *Physical Review B* **81**, 153401 (2010).
- [29] B. S. Archanjo, B. Fragneaud, L. G. Cançado, D. Winston, F. Miao, C. A. Achete, and G. Medeiros-Ribeiro, *Graphene nanoribbon superlattices fabricated via helium ion lithography*, *Applied Physics Letters* **104**, 193114 (2014).

- [30] A. Eckmann, A. Felten, I. Verzhbitskiy, R. Davey, and C. Casiraghi, *Raman study of defective graphene: effect of the excitation energy, type, and amount of defects*, Physical Review B **88**, 035426 (2013).
- [31] C. R. Dean, A. F. Young, I. Meric, C. Lee, L. Wang, S. Sorgenfrei, K. Watanabe, T. Taniguchi, P. Kim, K. L. Shepard, and J. Hone, *Boron nitride substrates for high quality graphene electronics*, Nature Nanotechnology **5**, 722 (2010).
- [32] G. Algara-Siller, S. Kurasch, M. Sedighi, O. Lehtinen, and U. Kaiser, *The pristine atomic structure of MoS₂ monolayer protected from electron radiation damage by graphene*, Applied Physics Letters **103**, 203107 (2013).
- [33] R. Zan, Q. M. Ramasse, R. Jalil, T. Georgiou, U. Bangert, and K. S. Novoselov, *Control of radiation damage in MoS₂ by graphene encapsulation*, ACS Nano **7**, 10167 (2013).
- [34] L. Wang, Z. Chen, C. R. Dean, T. Taniguchi, K. Watanabe, L. E. Brus, and J. Hone, *Negligible environmental sensitivity of graphene in a hexagonal boron nitride/graphene/h-BN sandwich structure*, ACS Nano **6**, 9314 (2012).
- [35] E. Aradi, R. M. Erasmus, and T. E. Derry, *Formation of c-BN nanoparticles by helium, lithium and boron ion implantation*, Nuclear Instruments and Methods in Physics Research Section B: Beam Interactions with Materials and Atoms **272**, 57 (2012).
- [36] R. Machaka, R. M. Erasmus, and T. E. Derry, *Formation of c-BN nanocrystals by He⁺ implantation into h-BN*, Diamond Related Materials **19**, 1131 (2010).
- [37] Y. Wang, S. A. Boden, D. M. Bagnall, H. N. Rutt, and C. H. de Groot, *Helium ion beam milling to create a nano-structured domain wall magnetoresistance spin valve*, Nanotechnology **23**, 395302 (2012).
- [38] A. C. Ferrari, J. C. Meyer, V. Scardaci, C. Casiraghi, M. Lazzeri, F. Mauri, S. Piscanec, D. Jiang, K. S. Novoselov, S. Roth, and A. K. Geim, *Raman spectrum of graphene and graphene layers*, Physical Review Letters **97**, 187401 (2006).
- [39] A. Eckmann, A. Felten, A. Mishchenko, L. Britnell, R. Krupke, K. S. Novoselov, and C. Casiraghi, *Probing the nature of defects in graphene by Raman spectroscopy*, Nano Letters **12**, 3925 (2012).
- [40] A. C. Ferrari and D. M. Basko, *Raman spectroscopy as a versatile tool for studying the properties of graphene*, Nature Nanotechnology **8**, 235 (2013).
- [41] C. Thomsen and S. Reich, *Double resonant Raman scattering in graphite*, Physical Review Letters **85**, 5214 (2000).
- [42] E. H. M. Ferreira, M. V. Moutinho, F. Stavale, M. M. Lucchese, R. B. Capaz, C. A. Achete, and A. Jorio, *Evolution of the Raman spectra from single-, few-, and many-layer graphene with increasing disorder*, Physical Review B **82**, 125429 (2010).
- [43] C. Casiraghi, A. Hartschuh, H. Qian, S. Piscanec, C. Georgi, A. Fasoli, K. S. Novoselov, D. M. Basko, and A. C. Ferrari, *Raman spectroscopy of graphene edges*, Nano Letters **9**, 1433 (2009).

- [44] P. Venezuela, M. Lazzeri, and F. Mauri, *Theory of double-resonant Raman spectra in graphene: Intensity and line shape of defect-induced and two-phonon bands*, Physical Review B **84**, 035433 (2011).
- [45] E. H. Hwang and S. D. Sarma, *Single-particle relaxation time versus transport scattering time in a two-dimensional graphene layer*, Physical Review B **77**, 195412 (2008).
- [46] R. Decker, Y. Wang, V. W. Brar, W. Regan, H. Z. Tsai, Q. Wu, W. Gannett, A. Zettl, and M. F. Crommie, *Local electronic properties of graphene on a BN substrate via scanning tunneling microscopy*, Nano Letters **11**, 2291 (2011).
- [47] H. Pinto, R. Jones, J. P. Goss, and P. R. Briddon, *Mechanisms of doping graphene*, Physica Status Solidi A **207**, 2131 (2010).
- [48] A. Das, S. Pisana, B. Chakraborty, S. Piscanec, S. K. Saha, U. V. Waghmare, K. S. Novoselov, H. R. Krishnamurthy, A. K. Geim, A. C. Ferrari, and A. K. Sood, *Monitoring dopants by Raman scattering in an electrochemically top-gated graphene transistor*, Nature Nanotechnology **3**, 210 (2008).
- [49] N. Jung, N. Kim, S. Jockusch, N. J. Turro, P. Kim, and L. Brus, *Charge transfer chemical doping of few layer graphenes: charge distribution and band gap formation*, Nano Letters **9**, 4133 (2009).
- [50] J. F. Ziegler, J. P. Biersack, and M. D. Ziegler, *Stopping and range of ions in matter*, (Chester, MD: SRIM Co.) .
- [51] P. Lazar, R. Zbořil, M. Pumerab, and M. Otyepka, *Chemical nature of boron and nitrogen dopant atoms in graphene strongly influences its electronic properties*, Phys. Chem. Chem. Phys. **16**, 14231 (2014).
- [52] Y. Gong, G. Shi, Z. Zhang, W. Zhou, J. Jung, W. Gao, L. Ma, Y. Yang, S. Yang, G. You, R. Vajtai, Q. Xu, A. H. MacDonald, B. I. Yakobson, J. Lou, Z. Liu, and P. M. Ajayan, *Direct chemical conversion of graphene to boron- and nitrogen- and carbon-containing atomic layers*, Nature Communications **5**, 3193 (2014).
- [53] O. Hod, *Graphite and hexagonal boron-nitride have the same interlayer distance. why?* J. Chem. Theory Comput. **8**, 1360 (2012).
- [54] A. Ishii, M. Yamamoto, H. Asano, and K. Fujiwara, *DFT calculation for adatom adsorption on graphene sheet as a prototype of carbon nanotube functionalization*, Journal of Physics: Conference Series **100**, 052087 (2008).
- [55] F. Banhart, J. Kotakosk, and A. V. Krasheninnikov, *Structural defects in graphene*, ACS Nano **5**, 26 (2011).
- [56] P. O. Lehtinen, A. S. Foster, A. Ayuela, A. Krasheninnikov, K. Nordlund, and R. M. Nieminen, *Magnetic properties and diffusion of adatoms on a graphene sheet*, Physical Review Letters **91**, 01722 (2003).

- [57] V. O. Özçelik and S. Ciraci, *Self-assembly mechanisms of short atomic chains on single-layer graphene and boron nitride*, *Physical Review B* **86**, 155421 (2012).
- [58] Q. Xu, M. Wu, G. F. Schneider, L. Houben, S. K. Malladi, C. Dekker, E. Yucelen, R. E. Dunin-Borkowski, and H. W. Zandbergen, *Controllable atomic scale patterning of freestanding monolayer graphene at elevated temperature*, *ACS Nano* **7**, 1566 (2013).

6

ELECTRONIC TRANSPORT IN HELIUM-ION-BEAM ETCHED ENCAPSULATED GRAPHENE NANORIBBONS

In this chapter, we report the etching and electrical transport in nanoribbons of graphene sandwiched between atomically flat hexagonal boron nitride (h-BN). The etching of ribbons of varying width was achieved with a focused beam of 30 keV He⁺ ions. Using in-situ electrical measurements, we established a critical dose of 7000 ions nm⁻² for creating a 10 nm wide insulating barrier between a nanoribbon and the rest of the encapsulated graphene. Subsequently, we measured the transport properties of the ion-beam etched graphene nanoribbons. Conductance measurements at 4 K show an energy gap, that increases with decreasing ribbon width. The narrowest ribbons show a weak dependence of the conductance on the Fermi energy. Furthermore, we observed power-law scaling in the measured current-voltage (I-V) curves, indicating that the conductance in the helium-ion-beam etched encapsulated graphene nanoribbons is governed by Coulomb blockade.

6.1. INTRODUCTION

Graphene-based research has seen significant developments in the past decade, thanks to its unique band structure and extremely high mobilities[2, 3]. Despite the high mobilities, graphene is a semi-metal without a bandgap which precludes applications in post-silicon electronics. Nevertheless, one can modify the electronic band structure by trimming graphene into nanoribbons. Under this geometrical constriction, quantum confinement and edge effects lead to a finite source-drain gap or a transport gap [4, 5]. In their review paper, Bischoff *et al.* [5] noted that a stern distinction has to be made between a *source-drain gap*—*i.e.*, the suppression of conductance in a limited source-drain voltage range—and a *transport gap*—*i.e.*, the suppression in a limited gate voltage range. Also, it is known that the gap is greatly influenced by the presence of disorder in the graphene nanoribbons (GNRs) themselves [5, 6]. Numerous techniques have been developed to create nanoribbons in graphene, such as plasma etching[5, 7–10], chemical synthesis[11–13], electron beam etching[14–16], and ion beam etching [17–21]. It is not straightforward, however, to make near-defect-free nanoribbons using the aforementioned techniques and, hence, it remains unclear how much the conductance and the presence of a gap are affected by edge effects, quantum confinement, and disorder[5].

Graphene devices are often fabricated on oxidized silicon substrates (SiO_2), which unfortunately lowers the mobility due to the presence of electron-hole puddles[22], charged impurity scattering[23], and contamination[18]. These adverse issues can be suppressed by encapsulating the graphene in hexagonal boron nitride (h-BN)[24]. As a consequence, the mobility in encapsulated graphene is typically an order of magnitude higher, in fact comparable to that in suspended graphene[3, 25, 26]. Because of its short de-Broglie wavelength, its sub-nanometer probe size, and the small beam spreading in materials[18, 27, 28], the focused ion beam (FIB) of a helium ion microscope (HIM) is an attractive tool for precise etching of encapsulated graphene devices. Moreover, the 30 keV helium ions used in this microscope can easily pass through the covering BN layer[29], typically tens of nanometers thick[24], and etch the buried graphene with still good resolution.

A recent experiment by Abbas *et al.* [21] with a He-FIB has shown indications of bandgap opening in arrays of 5 nm wide graphene ribbons. Also, Nakaharai *et al.* [30] have shown, by conductance tuning, bandgap opening in narrow graphene channels, etched with a He^+ beam. However, these measurements show very low conductance ($\sim 10,000$ times higher resistivity than for pristine graphene), likely due to extensive ion beam damage. Since the paper by Kalhor *et al.* [31] it is known that exposure of graphene to helium ions leads to collateral damage in the non-exposed adjacent areas and to ion beam induced surface contamination[18]. A recent study by Nanda *et al.* [24] has shown that encapsulation of graphene in h-BN, with a ≤ 15 nm top h-BN layer, slows down the built-up of He^+ beam damage in the exposed graphene and precludes detrimental effects due to beam induced surface contamination. Moreover, this material shows *n*-doping and self-healing. However, fabrication of encapsulated graphene devices via focused He^+ beam etching requires a good understanding of graphene's response to ion-beam bombardment and, thus, proper optimization of ion exposure doses. This understanding and process optimization are still wanting.

In this chapter we present transport properties of He^+ beam etched encapsulated GNRs (graphene nanoribbons). The sub-nanometer He^+ beam allows us to precisely control the size of the etched areas and in-situ electrical probes in the helium ion microscope enable us to determine quickly the minimal dose needed to isolate different parts of the graphene. The low-temperature measurements show an energy gap opening in narrow GNRs. We conclude that the gap arises due to the beam induced disorder, leading to Coulomb blockade; the transport is governed by hopping between randomly distributed charged islands and localized states in the GNRs. We fabricated boron nitride/graphene/boron nitride sandwiches by stacking h-BN and graphene flakes via the van-der-Waals pick-up technique[24, 32]. Ribbons were cut with a focused helium ion beam and devices were made by e-beam lithography, plasma etching, and Cr/Au deposition.

6.2. RESULTS AND DISCUSSION

6.2.1. DEVICE MILLING AND CHARACTERIZATION

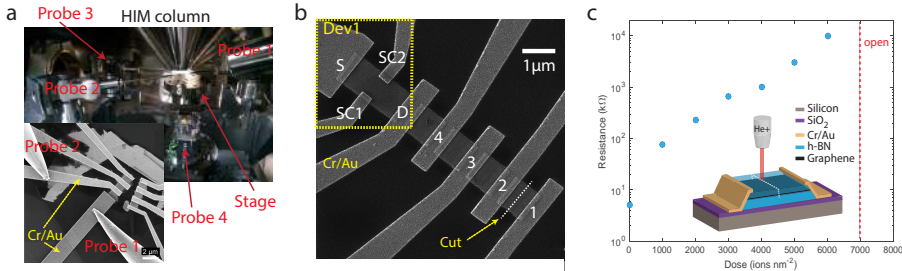


Figure 6.1: (a) Optical image of four micro-manipulators used to electrically probe the sample in the helium ion microscope (HIM) chamber. The inset shows a helium ion micrograph of the probes contacting the Cr/Au leads of the sample, (b) He^+ micrograph of multiple graphene devices fabricated in a h-BN/graphene/h-BN sandwich, stacked via the van-der-Waals pick-up technique. The probes are applied to pairs of contacts (e.g. 1-2 or 2-3), and the resistance between them is measured by applying a voltage across the contacts, (c) In-situ dose optimization in the HIM. The resistance between the two leads increases as a function of dose until an open circuit is reached at $7000 \text{ ions nm}^{-2}$. The inset depicts the device during line cutting.

Figure 7.1a shows an optical image of the HIM chamber with micro-probes for the in-situ electrical measurements. The inset is a HIM micrograph of a number of devices with two probes in contact with one of them. The in-situ probes allow direct measurement of the relation between the ion dose and the electrical conductivity. Figure 7.1b is a HIM micrograph of an array of encapsulated graphene devices, most of them $1 \mu\text{m} \times 1 \mu\text{m}$ in size. In all our samples the thickness of the top h-BN is 15 nm or less. The devices were exposed to line doses ranging from 1000 to 10,000 ions nm^{-2} with simultaneous monitoring of the resistance. One example of a $1.2 \mu\text{m}$ long and 10 nm wide cut is depicted in Figure 7.1b and 7.1c as a white dotted line. The pristine devices had resistances between 5 and 10 k Ω , corresponding to resistivities between 5 and 10 k Ω/\square . Several independent measurement series were conducted on different samples and we observed good reproducibility in the resistance.

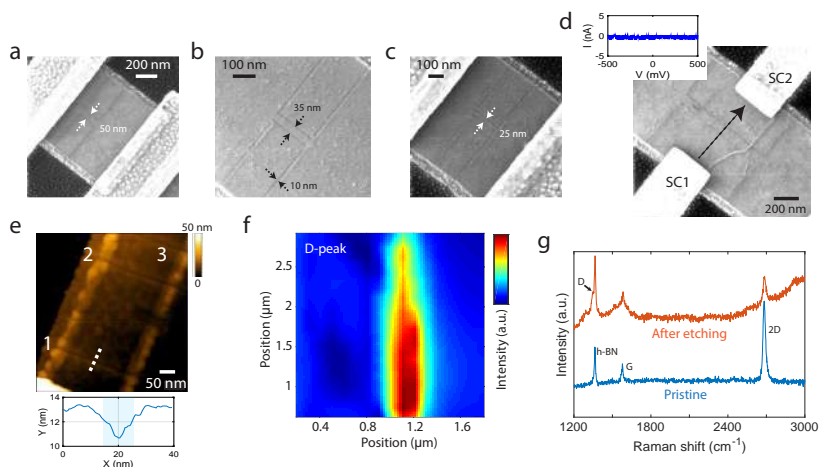


Figure 6.2: (a-c) Helium ion micrographs of nanoribbons with widths of 50, 35, and 25 nm, respectively, (d) Blow-up of the yellow box in Figure 7.1b. A source-drain bias is applied between side contact 1 (SC1) and side contact 2 (SC2). The inset shows the measured source-drain current. A 10 nm wide line cut with a dose of 7000 helium ions nm^{-2} is sufficient to create an insulating barrier, (e) AFM images of three 10 nm line exposures with 7000 ions nm^{-2} . The lower figure shows the line profile across cut 1, (f) D-peak Raman map of the 10 nm line cut region, (g) Raman spectra of the pristine sample and of the 25 nm wide etched nanoribbon device.

The resistance vs. ion dose is plotted in Figure 7.1c. One sees that the resistance increased almost exponentially up to a critical dose of 7000 ions nm^{-2} , where the circuit became open. In this regard, the in-situ measurements provide a unique knob to monitor the end-point detection and dose determination of the encapsulated graphene devices. Subsequently, we used this critical dose to etch nanoribbons in encapsulated graphene of 200 nm in length and with widths of 90, 70, 50, 35, 25, and 10 nm. Figures 7.2a-c show helium ion micrographs of various GNRs. Figure 7.2d shows a device (Dev1), also shown in Figure 7.1b, where a dose of 7000 ions nm^{-2} is applied to make a 35 nm wide ribbon. The two side contacts (SC1 and SC2) are used to check that there is no residual conductivity between the isolated regions. The inset shows that indeed no measurable current flowed between SC1 and SC2; the resistance is >1 G Ω . Figure 7.2e shows an AFM image of two 10 nm line exposures with 7000 ions nm^{-2} . The full-width-at-half-maximum (FWHM) of the etched line is 10 nm, see the AFM profile. Note that the widths of the etch line in the HIM image (Fig. 2b) and in the AFM profile are both equal to the designed line width of 10 nm.

We performed Raman mapping around the etched line to investigate the lateral damage in the exposed graphene. Ion induced defects in single-layer graphene can be studied via the evolution of the D-peak in the Raman spectrum[33–35]. The Raman map of the D-peak is shown in Figure 7.2f. Because of the narrow and localized interaction volume of the He^+ beam in the outermost few dozens of nanometers[24, 29, 36], most of the ion beam damage is expected to be concentrated in the 10 nm etched lines. Yet, the measured D-peak intensity decays up to ~ 200 nm on both sides of the exposure area. This result is, however, limited by the relatively large laser spot size (~ 350 nm) of our

Raman spectrometer. Figure 7.2g shows Raman spectra before and after etching. Before etching, the signature of single-layer graphene is clearly discernible; in particular the 2D peak intensity is ~ 4 times higher than that of the G peak and a D peak is absent, both are signs of high-quality graphene. After etching, a small but significant D-peak is visible as a shoulder on the h-BN peak at 1345 cm^{-1} , thus indicating atomic disorder[24, 34]. The 2D peak is still visible, which indicates that the crystalline structure of graphene is still partly intact within the probe size ($\sim 350\text{ nm}$) of the Raman beam.[24, 37]

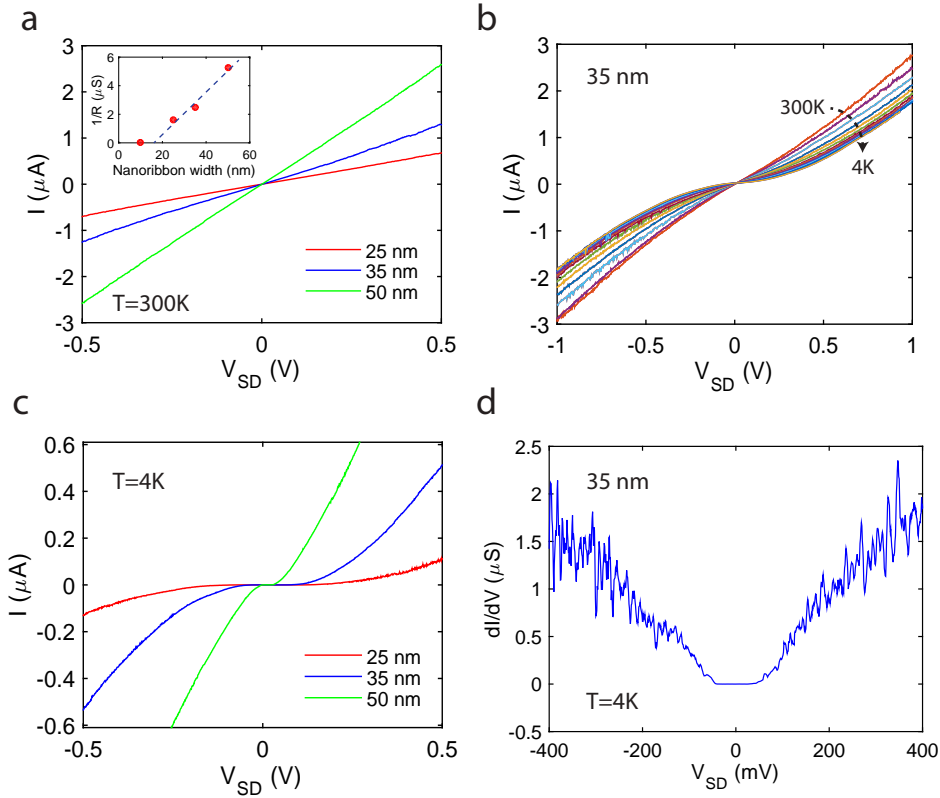


Figure 6.3: (a) Source-drain bias (V_{SD}) dependence of the drain current (I_{SD}) at room temperature in the nanoribbons. The inset shows the relation between nanoribbon width and the conductance ($1/R$), (b) V_{SD} dependence of the I_{SD} for the 35 nm ribbon as a function of temperature, (c) V_{SD} dependence of the I_{SD} for the 25, 35, and 50 nm ribbons at 4 K, (d) Differential conductance (dI/dV) as a function of V_{SD} for the 35 nm ribbon, showing zero conductance near zero source-drain bias. The back gate bias (V_{BG}) for all figures is zero.

6.2.2. LOW-TEMPERATURE TRANSPORT IN GNRs

To characterize the electronic properties of the GNRs, transport measurements were conducted. The room temperature current-voltage (I - V) characteristics in Figure 7.3a show a linear behavior in the 35 and 50 nm wide ribbons and a slight non-linearity in the

25 nm ribbon. The room temperature resistivity of the 50 nm wide ribbon is $\sim 50 \text{ k}\Omega/\square$. The inset shows the conductance ($1/R$) of the 10-50 nm wide ribbons, which were all made from the same stack, as a function of the ribbon width. Except for the smallest ribbon, the conductance increases more or less linearly with the width, suggesting a ~ 8 nm inactive layer at both edges of the ribbons. As we cool the samples to 4 K, non-linearity clearly appears, see Figure 7.3b for the 35 nm ribbon. The non-linearity in the I - V characteristics depends on the ribbon width, see Figure 7.3c. Figure 7.3d shows the differential conductance (dI/dV) of the 35 nm wide ribbon at 4 K as a function of the bias voltage V_{SD} ; approaching zero in the ~ 100 mV range around zero bias voltage. The appearance of non-linear I - V characteristics is an indication of an energy gap (E_{gap}) in the GNRs[15, 38]. Non-linear I - V characteristics have recently been reported for He^+ beam etched ribbons in supported graphene[30] and for electron beam etched ribbons in suspended graphene[15, 16].

Figure 7.4 shows dc-conductance measurements at 4 K. We studied the influence of the voltage applied to the bottom gate (V_{BG}) on the source-drain current (I_{SD}). Note that the I_{SD} of the narrowest ribbons is low because of their high resistance; therefore we applied a higher V_{SD} bias for the 25 and 35 nm ribbons. One can clearly see that the position of the minimum current shifts to more negative V_{BG} with decreasing width, thus indicating a higher electron doping level in the narrower ribbons. This effect is due to beam induced n -doping of graphene, likely by collision induced C-N exchange[24]. Apparently, the strong n -doping of the 25 nm ribbon is due to the close proximity of the central region of the ribbon to the heavily damaged regions near its edges.

From the dc-conductance as a function of gate bias (V_{BG}) and source-drain bias (V_{SD}), one can estimate the energy of the source-drain gap[7–9]. Previous bias spectroscopy measurements in narrow ribbons have shown the formation of overlapping Coulomb diamonds, signifying suppression in conductance by Coulomb blockade (CB)[5, 7–9]. The Coulomb blockade is caused by the interaction between charge carriers and localized charges, *e.g.* of islands, impurities or defects[5]. Therefore, the energy gap is related to the voltage of the largest diamond (V_{SD}^*) as $E_{gap} = eV_{SD}^*$ [7–9](see the arrow in Figure 7.3b). The 90 nm ribbon shows a small source-drain gap (< 5 meV) which is gate dependant. As the width of the ribbon decreases, E_{gap} increases, reaching a maximum of 180 meV in the 25 nm wide ribbon. Also, one can notice that the gate response of the 25 nm ribbon is very weak. The E_{gap} in our 25 nm ribbon is larger than the gap reported by Han *et al.* [7] for 25 nm ribbons made by plasma etching, in fact, it is close to the value for their 15 nm ribbons. This discrepancy could be due to extra beam induced damage near the edges of our GNRs. As mentioned before, there is an inactive strip of ~ 8 nm wide at the edges of the ribbons, see the inset of Figure 7.3a.

In contrast, Evaldsson *et al.* [4] inferred that not Coulomb blockade but Anderson-type localization, induced by edge disorder, is responsible for the energy gap in plasma-etched GNRs. Naitou *et al.*[39] have observed a metal-insulator transition in supported graphene for a He^+ beam dose of 120 ions nm^{-2} . They also related this transition to Anderson-type localization caused by beam induced disorder; they estimated the localization length to lie between 20 and 50 nm. The beam induced disorder near the edges of our ribbons was very high and, therefore, we expect a finite region in the GNR to be non-conducting

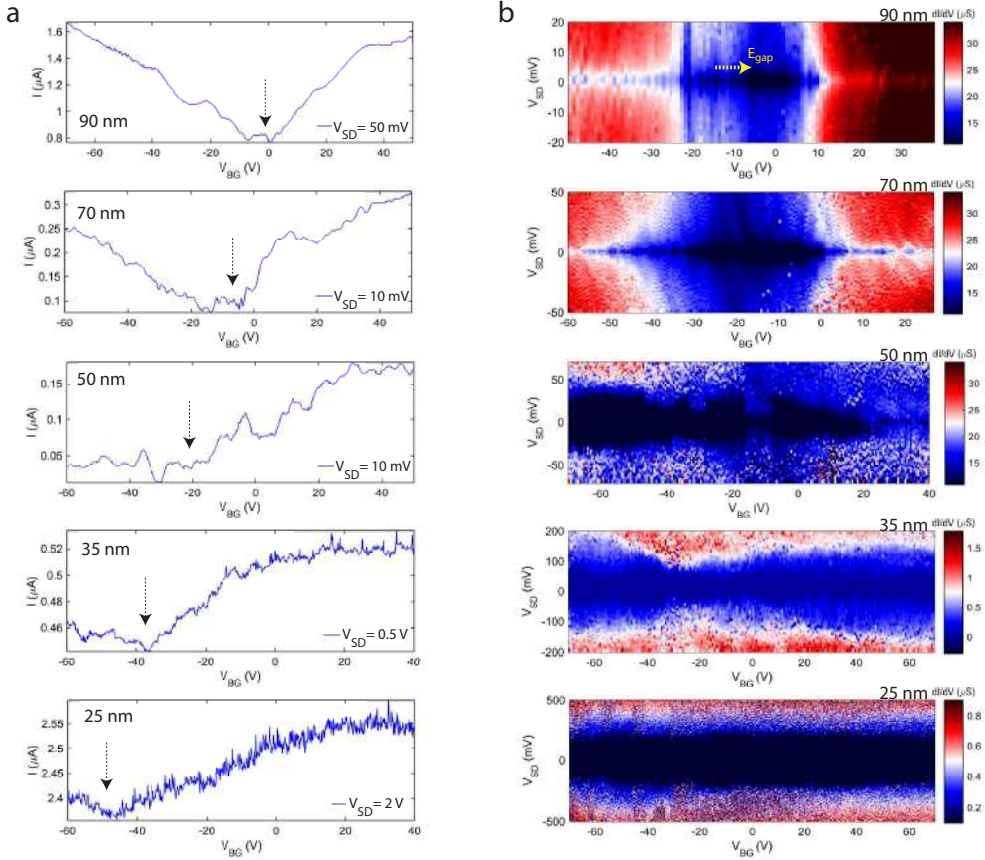


Figure 6.4: (a) Back-gate bias (V_{BG}) dependence of the drain current (I_{SD}) for fixed source-drain bias (V_{SD}). The onsets of the charge neutrality point are marked with arrows, (b) Color plots of the source-drain current (I_{SD}) as a function of V_{BG} and V_{SD} for nanoribbons with a length of 200 nm and a width of 25, 35, 50, 70, and 90 nm. The yellow arrow in the plot of the 90 nm ribbon refers to the V_{SD}^* of the largest diamond. It determines the energy gap ($=eV_{SD}^*$). All measurements were taken at 4 K.

(discussed later in Figure 7.5). Indeed, our 10 nm wide ribbons did not show any conductance and the other ribbons had an inactive region of ~ 8 nm at each edge. This value is in reasonably good agreement with the disorder radius of at least 10 nm, *i.e.* half the minimal localization length, found by Naitou *et al.*[39]. Moreover, it is only slightly larger than that of the GNRs of Han *et al.* [7]: 7 nm at each edge in conductance measurements at 1.7 K.

6.2.3. MODEL FOR DEFECT INDUCED TRANSPORT IN GNRs

The disorder arising from beam induced defects breaks the ideal two-dimensional (2-D) lattice of graphene down into isolated islands, causing inhomogeneities in the charge

distribution and in conductance when voltages are applied[40]. A sketch illustrating the presumed damage extent in our graphene exposed to the etching He^+ beam is shown in Figure 7.5a. In general, focused ion beams have a Gaussian shape with finite tails[41]. For our He^+ beam, unfortunately, of unknown width and intensity. We assume that the lateral extent of the damage in our encapsulated graphene is determined by ions from the beam tail, by beam broadening in the top h-BN layer, by defect diffusion, and by edge modification via C-N exchange. The He^+ beam broadening in h-BN encapsulated graphene has been studied previously by Nanda *et al.* [24] using SRIM simulations; it is less than 1 nm in 15 nm h-BN. The extent of the other mechanisms is largely unknown, but obviously they are relatively more severe for the smaller ribbons. Figure 7.5b shows a sketch of islands and defect sites in a narrow (upper) and a wide GNR (lower), inspired by a similar figure in Ref.[42]. The transport through the narrow GNR is predominantly governed by charge hopping between the islands and the defects, showing up as Coulomb blockade. The wide GNRs have also a central region with a low defect density, allowing charge carriers to reach the drain electrode with or without scattering.

For our smaller GNRs (25 and 35 nm), diamonds of suppressed conductance overlap (see Figure 7.4b), similarly as described by Gallagher *et al.* for quantum dots in GNRs[9]. To provide more evidence of the presence of localized states in our GNRs, we analyzed the I - V characteristics using the model of Middleton and Wingreen (MW)[43], who have studied the transport in arrays of metallic dots. In their work, the current I scales as:

$$I \sim \left[\frac{V_{SD}}{V_t} - 1 \right]^\zeta \quad (6.1)$$

where ζ is a power-law exponent and V_t is the threshold voltage below which the current is virtually absent. Above V_t , the applied source-drain bias is large enough to populate the islands with electrons or holes, causing the current to flow through the entire nanoribbon. Previous experiments have shown this scaling behavior in arrays of metallic islands[44], in graphene quantum dot arrays[40], in disordered MoS_2 nanoflakes[42], and in a quantum dot lattice in GaAs[45]. Figure 7.5c shows the measured current in our narrower ribbons on a log-log scale, obeying indeed the scaling law of Equation 6.1. The curves for different ribbon widths have different values of V_t . Nevertheless, they exhibit a reasonably clear collapse into a single trace with $\zeta \approx 1.3$. The larger values for V_t of the narrower ribbons indicate that the islands in these ribbons are relatively small. According to the MW model, the characteristic exponent ζ is determined by the dimensionality of the conducting channels. For a 1-D system, with only one dominant path or with a small number of preferred paths, ζ equals 1, whereas for a 2-D system it is between 1.6 and 2[42, 43]. Since $\zeta \approx 1.3$ in our nanoribbons, we conclude that the transport is mediated by multiple hops of the charge carriers between localized states and islands, mainly dispersed along the ribbon length. The corresponding transport mechanism in our ribbons is sketched in Figure 7.5b.

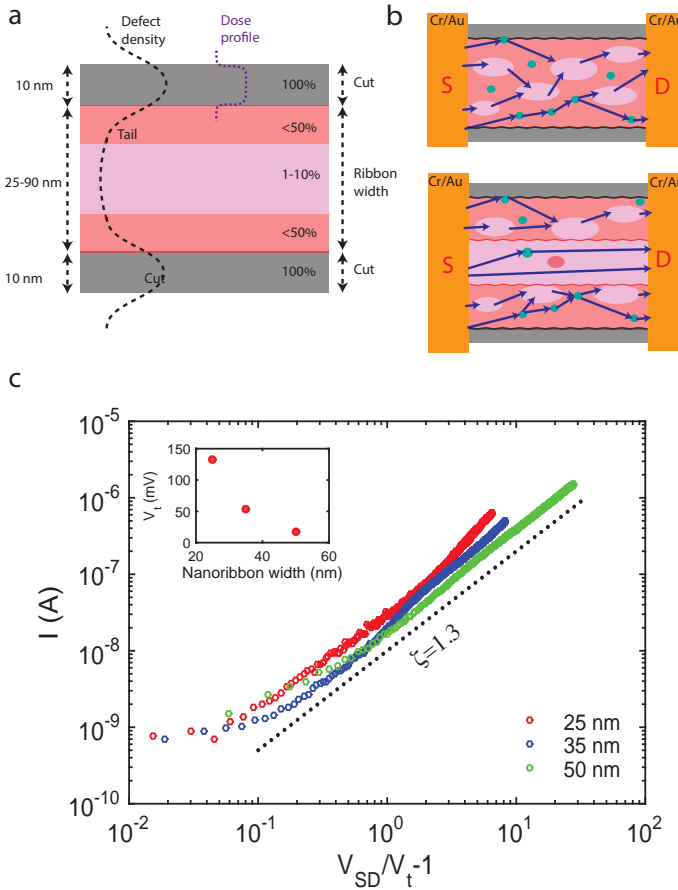


Figure 6.5: (a) Sketch showing the defect density in graphene, built-up during etching with a focused He^+ beam. The assumed defect density decays within a few nanometers outside the actual 10 nm wide etch cut. The center of the ribbon between the two cuts has a low but finite defect density caused by beam tails, by beam broadening in the material, and by defect diffusion. In reality, the boundaries between the various regions are rough, (b) Sketch illustrating a few possible paths of carrier transport in a narrow (upper) and a wide (lower) GNR; in contrast to 5a, the roughness of the boundaries is taken into account. The light purple regions represent relatively intact graphene (either charged islands or a continuous strip) and the green circles are defect sites. The dark blue solid arrows depict examples of carrier transport through charged islands and defect sites, (c) Measured current as a function of $V_{SD}/V_t - 1$ on a log-log plot showing power-law scaling (same data as in Figure 7.3c). The dotted line is a curve with $\zeta = 1.3$. The inset shows the variation of the threshold voltage (V_t) with nanoribbon width.

6.3. CONCLUSION

We have demonstrated the successful fabrication of nanoribbon devices in h-BN encapsulated graphene via etching with a focused He^+ beam. We have measured the conductance of graphene nanoribbons (GNRs) with widths between 25 and 90 nm. At room temperature and without gate bias, the resistivity of the wider ribbons (>50 nm) was

typically $\sim 50 \text{ k}\Omega/\square$, about 5 to 10 times higher than that of the pristine graphene. The bias spectroscopy measurements of the wider ribbons show Coulomb diamonds in a limited gate-voltage range. However, for the narrow ribbons, Coulomb diamonds had merged and formed a broad band with an almost constant energy gap, independent of the Fermi energy. At 4 K, we found an energy gap (E_{gap}) of 180 meV for the 25 nm wide ribbon. The narrower ribbons exhibited higher resistivities and a higher E_{gap} , likely due to the influence of ~ 8 nm wide inactive layers at their edges. Unfortunately, our Raman spectrometer cannot resolve the disorder radius; for that purpose tip-enhanced Raman spectroscopy (TERS) might be suited. Moreover, the I - V characteristics of the GNRs follow power-law scaling with an exponent ζ of 1.3, confirming that Coulomb blockade determines the charge transport [40, 43, 44]. In our understanding, the quantum dots, responsible for the Coulomb blockade, are generated by beam induced disorder.

In conclusion, the transport in our FIB-etched encapsulated GNRs is best described in terms of a series of overlapping quantum dots, in which the current suppression is due to Coulomb blockade. Finally, we note that the in-situ current probes in the helium ion microscope are very useful for efficient dose optimization and end-point detection during focused ion beam etching. We expect that the findings of this study are crucial for focused ion beam nano-patterning of 2-D materials for the realization of e.g. electronic and spintronic nanodevices.

6

REFERENCES

- [1] G. Nanda, G. Hlawacek, S. Goswami, K. Watanabe, T. Taniguchi, and P. F. A. Alkemade, *Electronic transport in helium-ion-beam etched encapsulated graphene nanoribbons*, Carbon **119**, 419 (2017).
- [2] K. S. Novoselov, A. K. Geim, S. V. Morozov, D. Jiang, M. I. Katsnelson, I. V. Grigorieva, S. V. Dubonos, and A. A. Firsov, *Two-dimensional gas of massless Dirac fermions in graphene*, Nature **438**, 197 (2005).
- [3] L. Wang, I. Meric, P. Y. Huang, Q. Gao, Y. Gao, H. Tran, T. Taniguchi, K. Watanabe, L. M. Campos, D. A. Muller, J. Guo, P. Kim, J. Hone, K. L. Shepard, and C. R. Dean, *One-dimensional electrical contact to a two-dimensional material*, Science **342**, 614 (2013).
- [4] M. Evaldsson, I. V. Zozoulenko, H. Xu, and T. Heinzel, *Edge-disorder-induced anderson localization and conduction gap in graphene nanoribbons*, Physical Review B **78**, 161407 (2008).
- [5] D. Bischoff, A. Varlet, P. Simonet, M. Eich, H. C. Overweg, T. Ihn, and K. Ensslin, *Localized charge carriers in graphene nanodevices*, Applied Physics Reviews **2**, 031301 (2015).
- [6] F. Molitor, A. Jacobsen, C. Stampfer, J. Güttinger, T. Ihn, and K. Ensslin, *Transport gap in side-gated graphene constrictions*, Physical Review B **79**, 075426 (2009).

- [7] M. Y. Han, B. Özyilmaz, Y. Zhang, and P. Kim, *Energy band-gap engineering of graphene nanoribbons*, Physical Review Letters **98**, 206805 (2007).
- [8] C. Stampfer, J. Güttinger, S. Hellmüller, F. Molitor, K. Ensslin, and T. Ihn, *Energy gaps in etched graphene nanoribbons*, Physical Review Letters **102**, 056403 (2009).
- [9] P. Gallagher, K. Todd, and D. Goldhaber-Gordon, *Disorder-induced gap behavior in graphene nanoribbons*, Physical Review B **81**, 115409 (2010).
- [10] Y. Lu, B. Goldsmith, D. R. Strachan, J. H. Lim, Z. Luo, and A. T. C. Johnson, *High-on/off-ratio graphene nanoconstriction field-effect transistor*, Small **6**, 2748 (2010).
- [11] X. Li, X. Wang, L. Zhang, S. Lee, and H. Dai, *Chemically derived, ultrasmooth graphene nanoribbon semiconductors*, Science **319**, 1229 (2008).
- [12] T. Shimizu, J. Haruyama, D. C. Marcano, D. V. Kosinkin, J. M. Tour, K. Hirose, and K. Suenaga, *Large intrinsic energy bandgaps in annealed nanotube-derived graphene nanoribbons*, Nature Nanotechnology **6**, 45 (2011).
- [13] D. V. Kosynkin, A. L. Higginbotham, A. Sinitskii, J. R. Lomeda, A. Dimiev, B. K. Price, and J. M. Tour, *Longitudinal unzipping of carbon nanotubes to form graphene nanoribbons*, Nature **458**, 872 (2009).
- [14] B. Sommer, J. Sonntag, A. Ganczarczyk, D. Braam, G. Prinz, A. Lorke, and M. Geller, *Electron-beam induced nano-etching of suspended graphene*, Scientific Reports **5**, 7781 (2015).
- [15] Q. Wang, R. Kitaura, S. Suzuki, Y. Miyauchi, K. Matsuda, Y. Yamamoto, S. Arai, and H. Shinohara, *Fabrication and in situ transmission electron microscope characterization of free-standing graphene nanoribbon devices*, ACS Nano **10**, 1475 (2016).
- [16] J. A. Rodríguez-Manzo, Z. J. Qi, A. Crook, J. H. Ahn, A. T. C. Johnson, and M. Drndić, *In situ transmission electron microscopy modulation of transport in graphene nanoribbons*, ACS Nano **10**, 4004 (2016).
- [17] D. Pickard and L. Scipioni, *Graphene nano-ribbon patterning in the Orion plus*, Zeiss Application Note (2009).
- [18] M. C. Lemme, D. C. Bell, J. R. Williams, L. A. Stern, B. W. H. Baugher, P. Jarillo-Herrero, and C. M. Marcus, *Etching of graphene devices with a helium ion beam*, ACS Nano **3**, 2674 (2009).
- [19] Y. Zhang, C. Hui, R. Sun, K. Li, K. He, X. Ma, and F. Liu, *A large-area 15 nm graphene nanoribbon array patterned by a focused ion beam*, Nanotechnology **25**, 135301 (2014).
- [20] D. C. Bell, M. C. Lemme, L. A. Stern, J. R. Williams, and C. M. Marcus, *Precision cutting and patterning of graphene with helium ions*, Nanotechnology **20**, 455301 (2009).

- [21] A. N. Abbas, G. Liu, B. Liu, L. Zhang, H. Liu, D. Ohlberg, W. Wu, and C. Zhou, *Patterning, characterization, and chemical sensing applications of graphene nanoribbon arrays down to 5 nm using helium ion beam lithography*, ACS Nano **8**, 1538–1546 (2014).
- [22] J. Martin, N. Akerman, G. Ulbricht, T. Lohmann, J. H. Smet, K. von Klitzing, and A. Yacoby, *Observation of electron–hole puddles in graphene using a scanning single-electron transistor*, Nature Physics **4**, 144 (2008).
- [23] J. H. Chen, C. Jang, S. Adam, M. S. Fuhrer, E. D. Williams, and M. Ishigami, *Charged-impurity scattering in graphene*, Nature Physics **4**, 377 (2008).
- [24] G. Nanda, S. Goswami, K. Watanabe, T. Taniguchi, and P. F. A. Alkemade, *Defect control and n-doping of encapsulated graphene by helium-ion-beam irradiation*, Nano Letters **15**, 4006 (2015).
- [25] X. Du, I. Skachko, A. Barker, and E. Y. Andrei, *Approaching ballistic transport in suspended graphene*, Nature Nanotechnology **3**, 491 (2008).
- [26] C. R. Dean, A. F. Young, I. Meric, C. Lee, L. Wang, S. Sorgenfrei, K. Watanabe, T. Taniguchi, P. Kim, K. L. Shepard, and J. Hone, *Boron nitride substrates for high quality graphene electronics*, Nature Nanotechnology **5**, 722 (2010).
- [27] M. Ananth, L. Stern, D. Ferranti, C. Huynh, J. Notte, L. Scipioni, C. Sanford, and B. Thompson, *Creating nanohole arrays with the helium ion microscope*, Proceedings of SPIE **8036**, 8036M (2011).
- [28] G. Hlawacek, V. Veligura, R. van Gastel, and B. Poelsema, *Helium ion microscopy*, Journal of Vacuum Science & Technology B **32**, 020801 (2014).
- [29] D. Cohen-Tanugi and N. Yao, *Superior imaging resolution in scanning helium-ion microscopy: A look at beam-sample interactions*, Journal of Applied Physics **104**, 063504 (2008).
- [30] S. Nakaharai, T. Iijima, S. Ogawa, S. Suzuki, S. L. Li, K. Tsukagoshi, S. Sato, and N. Yokoyama, *Conduction tuning of graphene based on defect-induced localization*, ACS Nano **7**, 5694 (2013).
- [31] N. Kalhor, S. A. Boden, and H. Mizuta, *Sub-10 nm patterning by focused he-ion beam milling for fabrication of downscaled graphene nano devices*, Microelectronic Engineering **114**, 70 (2014).
- [32] V. E. Calado, S. Goswami, G. Nanda, M. Diez, A. R. Akhmerov, K. Watanabe, T. M. K. T. Taniguchi, and L. M. K. Vandersypen, *Ballistic Josephson junctions in edge-contacted graphene*, Nature Nanotechnology **10**, 761 (2015).
- [33] A. C. Ferrari, J. C. Meyer, V. Scardaci, C. Casiraghi, M. Lazzeri, F. Mauri, S. Piscanec, D. Jiang, K. S. Novoselov, S. Roth, and A. K. Geim, *Raman spectrum of graphene and graphene layers*, Physical Review Letters **97**, 187401 (2006).

- [34] A. C. Ferrari, *Raman spectroscopy of graphene and graphite: Disorder, electron-phonon coupling, doping and nonadiabatic effects*, Solid State Communications **143**, 47 (2007).
- [35] A. C. Ferrari and D. M. Basko, *Raman spectroscopy as a versatile tool for studying the properties of graphene*, Nature Nanotechnology **8**, 235 (2013).
- [36] J. Buchheim, R. M. Wyss, I. Shorubalko, and H. G. Park, *Understanding the interaction between energetic ions and freestanding graphene towards practical 2d perforation*, Nanoscale **8**, 8345 (2016).
- [37] L. G. Cançado, A. Jorio, E. H. M. Ferreira, F. Stavale, C. A. Achete, R. B. Capaz, M. V. O. Moutinho, A. Lombardo, T. S. Kulmala, and A. C. Ferrari, *Quantifying defects in graphene via Raman spectroscopy at different excitation energies*, Nano Letters **11**, 3190 (2011).
- [38] M. W. Lin, C. Ling, L. A. Agapito, N. Kioussis, Y. Zhang, M. M. C. Cheng, W. L. Wang, E. Kaxiras, and Z. Zhou, *Approaching the intrinsic band gap in suspended high-mobility graphene nanoribbons*, Physical Review B **84**, 125411 (2011).
- [39] Y. Naitou and S. Ogawa, *Anderson localization of graphene by helium ion irradiation*, Applied Physics Letters **108**, 171605 (2016).
- [40] D. Joung, L. Zhai, and S. I. Khondaker, *Coulomb blockade and hopping conduction in graphene quantum dots array*, Physical Review B **83**, 115323 (2011).
- [41] R. L. Kubena and J. W. Ward, *Current density profiles for a Ga⁺ ion microprobe and their lithographic implications*, Applied Physics Letters **51**, 1960 (1987).
- [42] S. T. Lo, O. Klochan, C. H. Liu, W. H. Wang, A. R. Hamilton, and C. T. Liang, *Transport in disordered monolayer MoS₂ nanoflakes—evidence for inhomogeneous charge transport*, Nanotechnology **25**, 375201 (2014).
- [43] A. A. Middleton and N. S. Wingreen, *Collective transport in arrays of small metallic dots*, Physical Review Letters **71**, 3198 (1993).
- [44] A. J. Rimberg, T. Ho, and J. Clarke, *Scaling behavior in the current-voltage characteristic of one- and two-dimensional arrays of small metallic islands*, Physical Review Letters **74**, 4714 (1995).
- [45] S. Goswami, M. A. Aamir, C. Siegert, M. Pepper, I. Farrer, D. A. Ritchie, and A. Ghosh, *Transport through an electrostatically defined quantum dot lattice in a two-dimensional electron gas*, Physical Review B **86**, 119904 (2012).

7

HELIUM ION BEAM INDUCED GROWTH OF HAMMERHEAD AFM PROBES

In this chapter, we report the direct-write growth of hammerhead AFM probes by He⁺ beam induced deposition of platinum-carbon. In order to grow a thin nano-needle on top of a conventional AFM probe, we move a focused He⁺ beam during exposure to a PtC precursor gas. In the final growth stage, a perpendicular movement of the beam results in the required 3D (hammerhead) shape. The diameter of the needle depends on the ion beam dose, beam dwell time, and speed of the beam movement. A nano-needle radius below 10 nm and a hammerhead smaller than 35 nm have been achieved. This fabrication process is robust and enables precise control over the three-dimensions of the hammerhead AFM probe. Finally, we test the capabilities of the fabricated AFM probes for 2D metrology of sidewall angles and line-edge roughness of trenches and shark-fins in silicon.

7.1. INTRODUCTION

Atomic force microscope (AFM) is increasingly being used for high precision profiling and metrology in semiconductor processing, such as for the measurement of roughness and height of trenches made in photoresist. However, measurements of undercut, sidewall roughness, and critical dimensions (CD) have not yet been optimized in accordance to the International Technology Roadmap for Semiconductors (ITRS) recommendations [2]. A limiting factor is the extension of the probe-resist interaction region when the tip of an AFM probe is inserted into a trench. The conventional conical or parabolic-shaped AFM tip is incapable of resolving undercuts and sidewall roughness due to the lack of access of the tip to these features of the trenches. In order to improve the probe-surface interaction and, hence, to truly resolve 3D structures, a 3D-AFM probe is needed. For a CD measurement the tip must have a lateral protrusion in order to measure the sidewalls and angles with sufficient accuracy [3, 4]. The first demonstration of such a probe was reported by Martin *et al.* [3] for CD measurements, where a 3D-AFM with a hammerhead or boot tip shape is scanned in CD mode and in deep-trench (DT) mode. Later, these 3D probes have been applied for the critical dimension metrology by Dixson *et al.* [4, 5] and Foucher *et al.* [6, 7]. However, still lacking is a one-step fabrication method to grow such probes with high reproducibility. Various attempts have been made to grow or to shrink the size of these probes by electron beam induced deposition (EBID) followed by plasma etching [6–8]. However, EBID with a stationary electron beam usually gives relatively thick needles due to the scattering of primary and secondary electrons (SEs) in the growing material [9]. One way to minimize the scattering is to use a horizontal growth mode, *i.e.* using a horizontally moving beam during EBID. This mode usually results in needles of around 18–100 nm in diameter [10]. In this work, we use a focused He⁺ beam to make a 3D probe with a hammerhead tip. The main advantage of a He⁺ beam is that the interacting volume of the helium ions is smaller than that for an electron beam or a gallium focused ion beam (Ga-FIB) at the same acceleration voltage [11]. Because of the small interaction volume, the helium ion microscope has been used as a nanofabrication tool in recent years, *e.g.* for the modification of graphene [12, 13], for lithography [14], and for ion beam induced deposition (IBID) [15]. Using a stationary He⁺ beam, *et al.* [9] fabricated 36-nm wide PtC pillars. Moreover, we expect the dimensions to be even smaller when using the horizontal growth mode. Therefore, the aim of our present work is to explore the use of He⁺ IBID in the horizontal growth mode for making high-aspect 3D-AFM probes.

7.2. EXPERIMENTAL SECTION

The experiments are performed in a Carl Zeiss OrionTM Plus scanning helium ion microscope, equipped with an omniGIS system from Omniprobe. A nozzle with a 500- μm wide opening is positioned around 150–200 μm above the sample during the deposition. The nozzle is at an angle of 25° to the surface normal. The working distance is 9.2 mm. The precursor gas (CH₃)₃Pt(C_pCH₃) is used, mixed with N₂ carrier gas in the ratio of 1:10. The background pressure in the microscope is around 5 × 10⁻⁷ mbar, rising to 8 × 10⁻⁶ mbar during deposition. Tapping-mode silicon AFM probes from Nanoand-

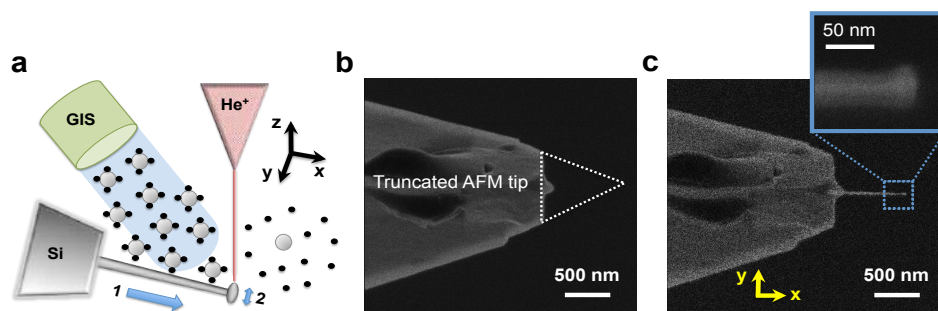


Figure 7.1: Fabrication of a PtC AFM probe with a hammerhead using $(\text{CH}_3)_3\text{Pt}(\text{C}_p\text{CH}_3)$ precursor decomposition with a focused He^+ beam at 0.3 pA and 30 keV. (a) Sketch of the last step of the hammerhead growth. In the presence of the precursor gas, the beam is slowly moved from left to right (1); in the last step, the beam is moved in the perpendicular direction (2). HIM images of the growth, (b) Original AFM probe with removed apex before tip growth, where dotted lines show the removed part, (c) The same probe after growth of the nano-needle with a hammerhead shape (inset shows the hammerhead).

more GmbH are used as the base material. There is a possibility that during the AFM measurement the grown needle breaks or buckles[10], leading to unintentional scanning with the standard AFM probe. To eliminate this possibility, we cut the top of the conventional silicon AFM probe using Ga-FIB milling, see Figure 7.1b. Thereafter, the AFM probe is cleaned gently with acetone and isopropanol and then mounted vertically in the helium ion microscope such that the truncated probe of the cantilever is perpendicular to the incident beam. The He^+ beam is aimed onto the edge of the cantilever and then slowly moved horizontally away from the edge into the vacuum, such that a continuous needle-like structure grows, see the schematic of this process in Figure 7.1a. Next, the beam is moved in the perpendicular horizontal direction to form two lateral protrusions. The exposure of the very end of the tip to the helium ions should be minimized to avoid sputtering of silicon. Therefore, we start with focusing the beam at the edge of the cantilever and then we move the beam slowly towards the tip. Before the actual growth, we perform a test deposition nearby to make sure the beam conditions are optimal. We performed plasma cleaning of the chamber before loading the sample. After cleaning, we performed several deposition tests without the precursor gas and did not observe any deposition. We used an Elphy Plus (Raith GmbH) pattern generator, 1-nm beam step size, and a beam current below 1 pA. The Raith pattern generator is programmed such that the nano-needle is grown in one continuous process. The current is set by regulating the helium gas pressure in the source. In order to optimize the growth of freestanding nano-needles, we varied the beam dwell time between 1 and 20 ms. The grown nano-needles are imaged by subsequent HIM imaging with a 0.3 pA beam current. To test the hammerhead AFM probes, 2D AFM scans are carried out using a Bruker FastScan AFM system on trenches made in silicon. These trenches are made by e-beam lithography and chlorine-based reactive ion etching.

7.3. HAMMERHEAD NANO-NEEDLE FABRICATION

7.3.1. HEIBID GROWTH MECHANISM

For the nano-needle growth, 30-keV beam energy and 0.35 ± 0.05 pA current are used. For a step size of 1 nm, the flux is 1.25×10^{20} ions $\text{cm}^{-2} \text{s}^{-1}$.

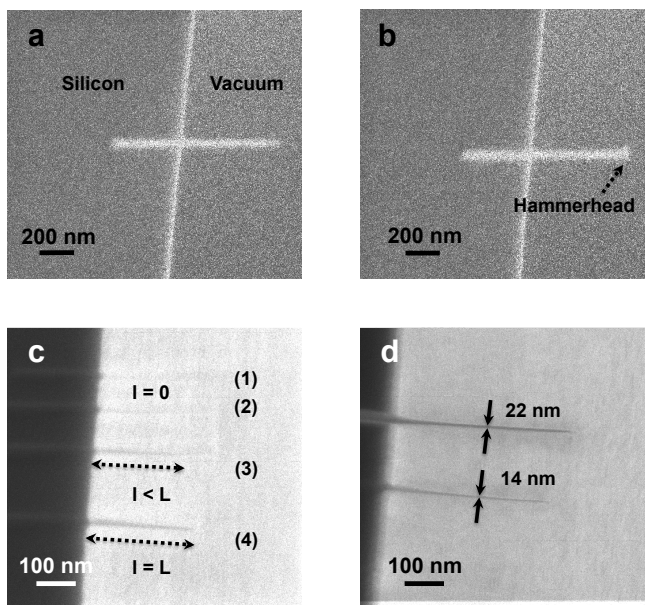


Figure 7.2: HIM images of nano-needles grown by He-IBID, where l is the grown length and L is the designed length of the nano-needle. (a) Nano-needle grown beyond the edge of a silicon sample via the horizontal growth mode, (b) needles with a 3D hammerhead grown at the apex via the perpendicular growth mode, (c) growth for various dwell times for a fixed current; (1,2) no growth, here the dwell time was too short to form a free-standing needle, (3) precursor-limited growth, here the grown needle is shorter than the designed length, and (4) successful growth, where the needle has the designed length, (d) two needles, grown with different dwell times.

Figure 7.2b shows the cutting of the standard AFM probe by Ga-FIB milling, followed by the successive growth of the hammerhead nano-needle by He-IBID, Figure 7.1c. Figure 7.2 shows HIM images of the nano-needle grown on the edge of the truncated silicon cantilever. The beam is moved from left to right (Figure 7.2a-d), extending beyond the edge of the silicon. We found that below the critical dose of 5×10^{17} ions cm^{-2} , no horizontal growth beyond the edge took place ($l = 0$). Apparently, the dwell time is then too short to complete 1-nm (*i.e.* the step size) growth at the apex, see (1,2) in Figure 7.2c. At 5×10^{17} ions cm^{-2} , a thin needle of ~ 14 nm in diameter extending from the edge into the vacuum is obtained. The apex of the growing needle is supplied with precursor molecules via direct adsorption and via surface diffusion from the substrate edge[16]. Due to the increasing distance, the diffusion of precursor molecules from the substrate edge decreases and, hence, needles become thinner near the apex, see Figure 7.2c-d.

Apparently, the amount of deposited material progressively reduces while the horizontal beam shift proceeds[17]. At some point, the beam shift outruns the precursor supply and the growth stops. As a result, the final needle is shorter than designed ($l < L$), see (3) in Figure 7.2c. Thus, at short dwell times, nano-needles are short and have very sharp ends. The observed behavior suggests that the horizontal growth is influenced by the transition from an ion-limited growth mode to a precursor-limited growth mode[16]. For dwell times of 6 ms and longer, nano-needles are grown with the desired length ($l = L$), see (4) in Figure 7.2c.

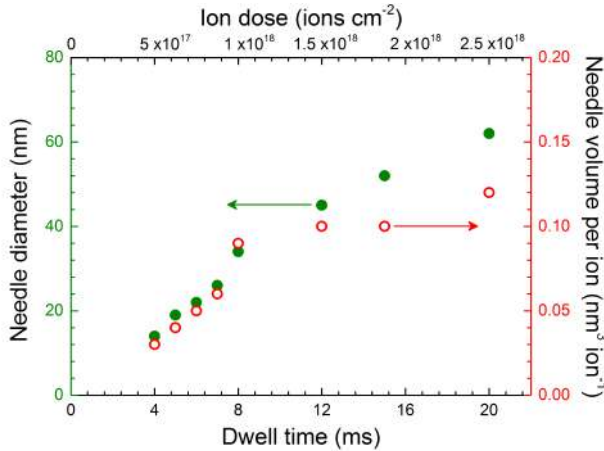


Figure 7.3: Nano-needle diameter at half-length as a function of dwell time or ion dose. No needles did grow at dwell times less than 4 ms. Red open circles show the deposition efficiency as a function of beam dwell time.

For increasing dose above 5×10^{17} ions cm^{-2} , the nano-needles thicken, see Figure 7.3. They reach a diameter of 62 nm at 2.5×10^{18} ions cm^{-2} . Smith *et al.*[18], Chen *et al.*[9], and Fujita *et al.*[19] have demonstrated that for a stationary ion beam the vertical growth is dominated by the decomposition of precursor molecules by primary ions and SEs. The initial nano-needle is widened by the forward scattered ions that exit the vertical needle from the side. In contrast, our moving helium ion beam passes through the apex of the growing horizontal nano-needle. As a consequence, the nano-needles remain much thinner.

7.3.2. VARIATION OF NEEDLE DIAMETER WITH ION DOSE

Figure 7.3 shows the needle diameter as a function of the dwell time or dose. With the increase in dose, we obtain a thicker needle. The deposition efficiency (V_{ion}), *i.e.* the needle volume per incident ion, is given by:

$$V_{ion} = \frac{\pi D^2 s e}{4 \tau_{dwell} i} \quad (7.1)$$

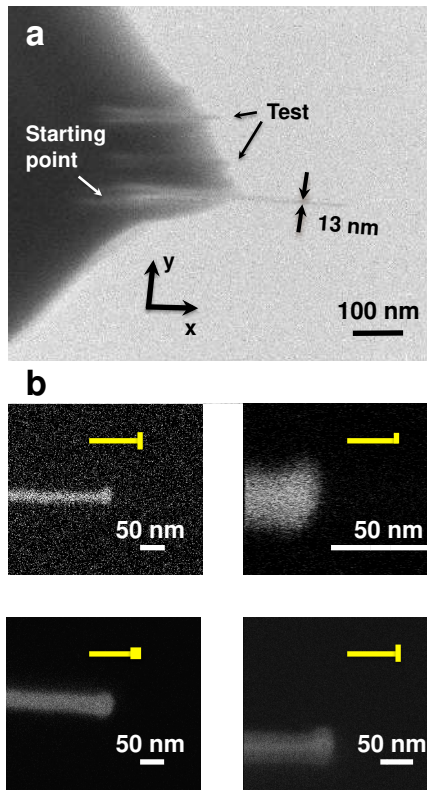


Figure 7.4: (a) Nano-needle grown on the gallium FIB modified AFM probe. Two test needles are grown before the actual needle growth to ensure the focus and beam conditions are optimal, (b) tips grown with various beam movements, as shown in the yellow insets.

where D is the needle diameter, s is the beam step size (1 nm in our experiment), i is the beam current, and τ_{dwell} is the dwell time. The deposition efficiency V_{ion} is $0.03 \text{ nm}^3 \text{ ion}^{-1}$, comparable to $0.04 \text{ nm}^3 \text{ ion}^{-1}$ for the stationary He^+ beam at the same current, although at a lower beam energy of 25 keV.[9] The needle volume per ion versus τ_{dwell} at different regimes can be distinguished: (1) the nucleation regime (0-4 ms in Fig. 3) where no significant growth takes place; (2) an intermediate regime (4-8 ms) characterized by a fast increase of the needle volume per ion; (3) and the saturation regime (beyond 12 ms) where the needle volume per ion attains a more or less constant value. The primary helium beam traverses the tip apex and generates secondary electrons (SEs), which are emitted from a volume larger than the beam diameter. The SEs dissociate adsorbed molecules and, hence, material is being deposited.[16] The mean free path (or escape distance) of the SEs and the geometrical spreading of the SE flux determine the diameter of the growing material. If the dwell time τ_{dwell} is increased, more SEs are being generated and a larger volume is grown. Obviously, the growth in the x-direction during τ_{dwell} must be equal to the beam step size of 1 nm. The additional volume growth for increased dwell times is, thus, in the y- and z-directions. If the needle width becomes larger than the mean free path of the SEs (a few nanometers[16, 18]) the broadening in the y-direction saturates.

Assuming a density of 11 PtC_4 molecules nm^{-3} [9], ~ 3 molecules are decomposed per ion for the thinnest needle, most likely by SEs generated by the primary beam[9, 16]. Figure 7.4a shows a 13-nm nano-needle grown on a truncated conventional AFM probe. The depositions were started ~ 200 nm from the edge, see Figure 7.4a. The figure demonstrates that the process with the moving He^+ ion beam enables us to fabricate needles with a diameter down to 13 nm and a length up to ~ 700 nm. Needles have been grown on various days under slightly varying conditions. In all attempts, we reduced the dwell time slowly until no or a too-short needle appeared. We have made at least 10 series of needles on the edges of a silicon sample and on the truncated AFM tips with currents ranging from 0.3 to 0.6 pA. We observed that the diameter of the narrowest successful hammerhead needle was always 13-14 nm, independent of the actual current. This procedure to produce hammerhead AFM probes is, thus, robust. Figure 7.4b shows HIM images of hammerhead tips grown with slightly different final beam movements, see the yellow insets. Single spot exposure (lower left in Fig. 4b) gives a spherical head because of the higher number of isotropically emitted SEs. When the beam is moved in the +y-direction (upper right in Fig. 4b), an elliptical or hook-like shape is obtained. Two small protrusions are grown by moving the beam in the +y and -y directions (upper left and lower right in Fig. 4b), giving the needle a hammerhead shape. Schematics of these movements are shown in Figure 7.4b. The growth mechanism of the nano-needle can be further explained by the following Equation[20, 21]:

$$Y_{net} = Y_D - S \quad (7.2)$$

Where Y_{net} is the net deposition rate, Y_D is the decomposition rate, and S is the sputtering rate. Since most of the helium ions penetrate through the 13 nm needle without any significant scattering, we do not expect sputtering by helium ions to be vigorous, and therefore, the net growth rate is mainly determined by the decomposition rate of the precursor molecules induced by the primary helium ions and SEs. The ions of the

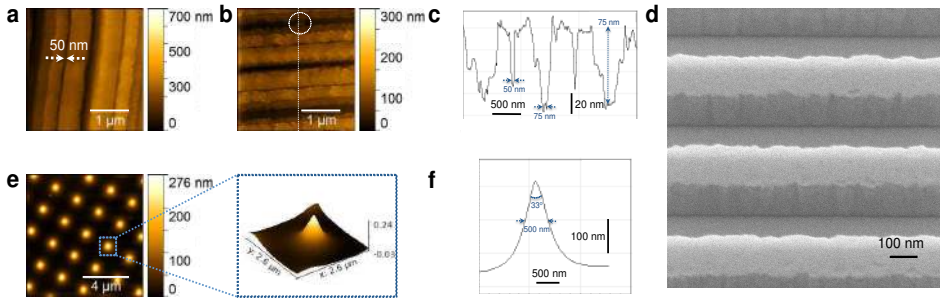


Figure 7.5: (a-b) AFM images of trenches in silicon obtained with 35-nm hammerhead probes. Sidewall roughness are clearly seen along the trenches, (c) shows the profile along the dotted line of the structure in (b), (d) HIM image of the trenches in silicon (the sample is 40° tilted), (e) 2D-scan of a shark-fin sample, (f) shows the line profile across the shark-fin.

helium beam do not only contribute to needle growth via precursor decomposition, but also to needle break-down by sputtering. However, the sputtering yield for He^+ ions is low, typically less than 0.1 atoms ion^{-1} [22]. Hence, the net growth yield is mainly determined by precursor decomposition, in contrast to growth via heavy-ion beam induced deposition [20, 21].

7.4. AFM MEASUREMENTS

Finally, 2-D AFM measurements are carried out to illustrate the usefulness of the hammerhead probe. For this purpose, trenches in silicon with varying pitch and shark-fin sample structures are measured. Figure 7.5a-b shows AFM images of the trenches. The measured depth of the silicon trenches in 5b-c is $\sim 75\text{nm}$, in good agreement with the designed depth of $75 \pm 5\text{nm}$ using plasma etching. Discrepancies in the measured profile are most likely due to re-deposited particles on the trench bottom and tilting over of the trench edges; whereas the V-shape is either due to partial isotropy in the etching or to the needle shape. These AFM measurements are taken with an AFM probe with a 35-nm hammerhead. Fine details are observable along the trench sidewalls and some particles can be seen on the trench bottom, see the dotted circle in Figure 7.5b. Thus, we conclude that the hammerhead probe is effective and can resolve small geometrical features. For comparison Figure 7.5d shows a HIM image of similar trenches but with a slightly different pitch. Figure 7.5e show AFM images of the shark-fin sample. Interestingly, the 35-nm hammerhead probe can resolve the sharp apex of the shark-fin, see Figure 7.5e-f. The measured tip angle of the shark-fin is $\sim 33^\circ$, in good agreement with the nominal value of $\sim 30^\circ$. The nominal height of the shark-fin is ~ 300 nm. Each tip is used for several AFM measurements over a period of at least one month. We have not observed any variation in the obtained morphology of the trenches or any buckling. This reproducibility demonstrates the probe's stability during deep-trench measurements. We note that the scanning system of our standard 2D-AFM is only capable of measuring the tip's z-mo-

tion. Therefore, it is not possible to scan the vertical trench edges; for that purpose one needs a 3D-AFM. Full characterization of these probes could include stiffness and stability tests during AFM scanning and TEM study of the thickness (*i.e.* in the *z*-direction) of the probes, the length of the overhang, and the radius of the hammerhead edges, all as function of the growth conditions.

7.5. CONCLUSION

Silicon-based AFM probes suffer from strong limitations with regard to tip width, length, and shape to fulfill ITRS recommendations for 3D critical dimension (CD) metrology. In this chapter, we have investigated the capabilities of He⁺ beam processing (He-IBID) for the growth of thin needles with hammerhead tips as probes for 3D AFM measurements. The He-IBID grown probes have distinct merits because of their high aspect ratio and the possibility for relatively easy customization. The lateral movement of the ion beam during growth determines the 3D probe shape. This one-step process enables precise control over the tip shape and length. We have grown PtC 3D-AFM probes with a minimum diameter of 13 nm and with 35-nm wide hammerheads. The main factors that enable the small width of our nano-needles are the sub-nm ion-beam size, the negligible scattering of primary and secondary particles, negligible ion-beam sputtering, and a balance between the beam movement speed and the needle growth rate. Our 2D AFM measurements show that the probes can be used for AFM measurements without any noticeable wear. We conclude that this one-step He-IBID process to grow 3D AFM probes is an important step towards meeting the requirements of CD metrology.

REFERENCES

- [1] G. Nanda, E. van Veldhoven, D. Maas, H. Sadeghian, and P. F. A. Alkemade, *Helium ion beam induced growth of hammerhead AFM probes*, J. Vac. Sci. Technol. B **33**, 06F503 (2015).
- [2] G. Dai, M. Heidelmann, C. Kübel, R. Prang, J. Fluegge, and H. Bosse, *Reference nano-dimensional metrology by scanning transmission electron microscopy*, Measurement Science and Technology **24**, 085001 (2013).
- [3] Y. Martin and H. K. Wickramasinghe, *Method for imaging sidewalls by atomic force microscopy*, Applied Physics Letters **64**, 19 (1994).
- [4] R. Dixon and A. Guerry, *Reference metrology using a next-generation CD-AFM*, Proceedings of SPIE **5375**, 633 (2004).
- [5] R. Dixon, N. G. Orji, J. Fu, M. Cresswell, R. Allen, and W. Guthrie, *Traceable atomic force microscope dimensional metrology at NIST*, Proceedings of SPIE **6152**, 61520P (2006).

- [6] J. Foucher, E. Pargon, M. Martin, S. Reyne, and C. Dupré, *Paving the way for multiple applications for the 3D-AFM technique in the semiconductor industry*, Proceedings of SPIE **6922**, 69220F (2008).
- [7] J. Foucher, P. Filippov, C. Penzkofer, B. Irmer, and S. W. Schmidt, *Manufacturing and advanced characterization of sub-25 nm diameter CD-AFM probes with sub-10 nm tip edges radius*, Proceedings of SPIE **8681**, 86811I (2013).
- [8] M. Wendel, H. Lorenz, and J. P. Kotthaus, *Sharpened electron beam deposited tips for high resolution atomic force microscope lithography and imaging*, Applied Physics Letters **67**, 25 (1995).
- [9] P. Chen, E. van Veldhoven, C. A. Sanford, H. W. M. Salemink, D. J. Maas, D. A. Smith, P. D. Rack, and P. F. A. Alkemade, *Nanopillar growth by focused helium ion-beam-induced deposition*, Nanotechnology **21**, 455302 (2010).
- [10] J. D. Beard and S. N. Gordeev, *Fabrication and buckling dynamics of nanoneedle AFM probes*, Nanotechnology **22**, 175303 (2011).
- [11] D. C. Bell, M. C. Lemme, L. A. Stern, and C. M. Marcus, *Precision material modification and patterning with He ions*, Journal of Vacuum Science & Technology B **27**, 2755 (2009).
- [12] N. Kalhor, S. A. Boden, and H. Mizuta, *Sub-10 nm patterning by focused He-ion beam milling for fabrication of downscaled graphene nano devices*, Microelectronic Engineering **114**, 70 (2014).
- [13] G. Nanda, S. Goswami, K. Watanabe, T. Taniguchi, and P. F. A. Alkemade, *Defect control and n-doping of encapsulated graphene by helium-ion-beam irradiation*, Nano Letters **15**, 4006 (2015).
- [14] V. Sidorkin, E. van Veldhoven, E. van der Drift, P. Alkemade, H. Salemink, and D. Maas, *Sub-10-nm nanolithography with a scanning helium beam*, Journal of Vacuum Science & Technology B **27**, L18 (2009).
- [15] P. F. A. Alkemade, E. M. Koster, E. van Veldhoven, and D. J. Maas, *Imaging and nanofabrication with the helium ion microscope of the van Leeuwenhoek laboratory in delft*, Scanning **34**, 90 (2012).
- [16] P. F. A. Alkemade, P. Chen, E. van Veldhoven, and D. Maas, *Model for nanopillar growth by focused helium ion-beam-induced deposition*, Journal of Vacuum Science & Technology B **28**, C6F22 (2010).
- [17] G. C. Gazzadi, S. Frabboni, and C. Menozzi, *Suspended nanostructures grown by electron beam-induced deposition of Pt and TEOS precursors*, Nanotechnology **18**, 445709 (2007).
- [18] D. A. Smith, D. C. Joy, and R. P. D., *Monte carlo simulation of focused helium ion beam induced deposition*, Nanotechnology **21**, 175302 (2010).

- [19] J. Fujita, M. Ishida, T. Ichihashi, Y. Ochiai, T. Kaito, and S. Matsui, *Carbon nanopillar laterally grown with electron beam-induced chemical vapor deposition*, Journal of Vacuum Science & Technology B **21**, 2990 (2003).
- [20] Y. H. Kahng, J. Choi, K. Jeong, B. C. Park, D. H. Kim, J. Lyou, J. J. Lee, H. Lee, T. Lee, and S. J. Ahn, *Fabrication of ball-shaped atomic force microscope tips by ion-beam-induced deposition of platinum on multiwall carbon nanotubes*, Ultramicroscopy **110**, 82 (2009).
- [21] A. D. Dubner and A. Wagner, *The role of gas adsorption in ion-beam-induced deposition of gold*, Journal of Applied Physics **66**, 870 (1989).
- [22] M. Stepanova and S. Dew, *Nanofabrication*, Springer-Verlag Wien (2012).

8

BALLISTIC JOSEPHSON JUNCTIONS IN EDGE-CONTACTED GRAPHENE

Hybrid graphene-superconductor devices have attracted much attention since the early days of graphene research. So far, these studies have been limited to the case of diffusive transport through graphene with poorly defined and modest quality graphene-superconductor interfaces, usually combined with small critical magnetic fields of the superconducting electrodes. In this chapter, we show graphene based Josephson junctions with one-dimensional edge contacts of Molybdenum Rhenium. The contacts exhibit a well defined, transparent interface to the graphene, have a critical magnetic field of 8 Tesla at 4 Kelvin and the graphene has a high quality due to its encapsulation in hexagonal boron nitride. This allows us to study and exploit graphene Josephson junctions in a new regime, characterized by ballistic transport. We find that the critical current oscillates with the carrier density due to phase coherent interference of the electrons and holes that carry the supercurrent caused by the formation of a Fabry-Pérot cavity. Furthermore, relatively large supercurrents are observed over unprecedented long distances of up to 1.5 μm . Finally, in the quantum Hall regime we observe broken symmetry states while the contacts remain superconducting. These achievements open up new avenues to exploit the Dirac nature of graphene in interaction with the superconducting state.

Parts of this chapter have been published in Nature Nanotechnology **10**, 761-764 (2015) [1].

8.1. INTRODUCTION

The chiral nature of the charge carriers in graphene is predicted to give rise to specular Andreev reflection[2], and the conventional quantum Hall effect can be markedly different due to the interaction between edge states and the superconductor[3, 4]. Such systems also provide a unique way to probe valley-polarized edge states[5], topological confinement in bilayer graphene[6], the interplay between superconductivity and quantum confinement or ballistic two-dimensional Josephson junctions and their response to phase coherent interference effects.

There are two important prerequisites that must be satisfied in order to observe any of these phenomena experimentally. First, the graphene-superconductor interface should be transparent and well defined. Secondly, the graphene must be of high electronic quality. In addition, for some of the above effects, a superconductor with a large upper critical field, H_{c2} , is required. While significant technological progress has been made in improving the quality of graphene by either suspending graphene[7] or encapsulating it in hexagonal boron nitride (hBN) [8, 9], the main challenge has been to combine such low-scattering graphene with a (large H_{c2}) superconductor. All reports on graphene-superconductor devices to date involved superconducting contacts deposited directly on the graphene surface, and diffusive transport through the device. In addition to the modest electronic quality, the use of top contacts leaves ambiguity in where exactly Andreev reflection takes place and under what spectral conditions. *I.e.* it is not clear how far electrons travel beneath the contact before entering the superconductor.

To realise high quality graphene-superconductor junctions we encapsulate graphene between two hBN crystals using the van der Waals pick-up method [9]. This method ensures that the graphene is never in contact with any polymer during the stacking and thereafter. Electrical contact is made by metal deposition onto areas where the stack has been etched through. Unlike earlier work[9], where metal deposition is done in a separate lithography step, we start by etching only the region to be contacted, followed immediately by metal deposition. This has the following advantages: (i) our contacts are self-aligned, thereby minimizing redundant metal overlap above the graphene and reducing the screening of electric and magnetic fields and (ii) combining the etching and deposition in one step minimizes resist residues at the contact interface, which is necessary for transparent contacts. Instead of a normal metal, we sputter an alloy superconductor MoRe, which is attractive in several respects. First, MoRe is a type-II superconductor with a critical temperature $T_c \approx 8\text{K}$ and an upper critical field $H_{c2} \approx 8\text{T}$ (at 4.2 K), which should easily allow for the observation of quantum Hall states while the MoRe remains predominantly superconducting. Secondly, it has been shown that MoRe makes good electrical contact to carbon-based materials such as carbon nanotubes[10]. Considering the fact that edge-contact resistance can vary by an order of magnitude depending on the choice of metal[9], it is critical to select a superconductor which makes good electrical contact to graphene. This is particularly important in the context of superconductor (S) graphene (G) JJs, where the transparency of the S-G interface directly affects the Andreev reflection. Furthermore, unlike surface contacts, such one-dimensional edge contacts ensure that the Andreev reflection occurs at a well-defined location, at the edge

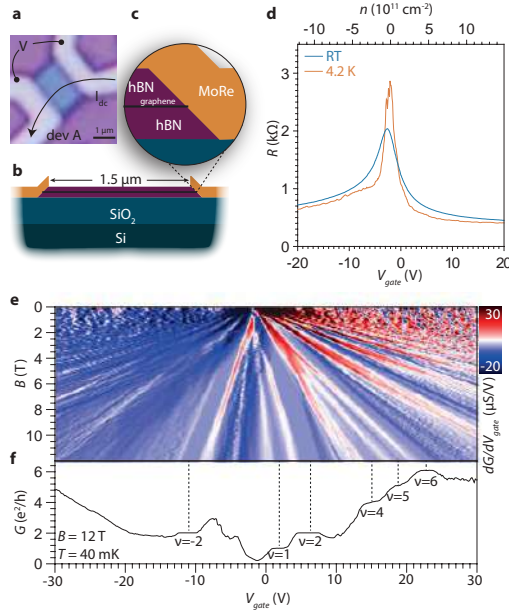


Figure 8.1: (a) An optical image of device *A*. A graphene/hBN sandwich (blue) is contacted on both sides from the edge with MoRe contacts (yellow). The contacts are split further in two, which allows a (quasi-) four probe measurement with minimal series lead resistance, (b-c) A schematic cross-section of the device, (d) The measured resistance, R , as a function of gate voltage, V_{gate} , at room temperature and at 4.2 K. The carrier density, n , is extracted from Shubnikov-de-Haas oscillations, (e) Differentiated conductance, dG/dV_{gate} , as a function of gate voltage and magnetic field, taken at 40 mK, (f) The conductance, G , as a function of gate voltage at $B = 12 T$ and $T = 40$ mK, showing the symmetry broken states.

of the graphene, where it contacts with the 3-dimensional bulk superconductor. After the deposition of the superconducting electrodes, we etch the stack into the desired geometry.

An optical image and a cross-sectional schematic of device *A* are shown in Figure 8.1a-c. The graphene is etched to a $L = 1.5 \mu m$ long and $W = 2.0 \mu m$ wide rectangle, with MoRe edge contacts on either side. All measurements described here are performed in a (dc) four point geometry, as shown in Figure 8.1a. The MoRe leads are arranged such that the lead series resistance is minimized and the measured resistance is effectively the two-probe graphene resistance, irrespective of whether the MoRe is normal or superconducting. This is important since disordered superconductors such as MoRe have a large normal-state resistivity, potentially confusing the interpretation of the measurements when the electrodes turn normal.

8.2. RESULTS AND DISCUSSION

Figure 8.1d shows the measured resistance, R , versus back gate voltage, V_{gate} , at room temperature and 4.2 K. A clear electron-hole asymmetry is visible with the resistance in

the hole doped (p) regime being somewhat larger than that in the electron doped (n) regime. We attribute this to contact-induced n -type doping, which leads to the formation of pn junctions close to the contacts when the bulk of the graphene is p doped. Such n -type doping effects from normal edge contacts have also recently been reported [11]. Figure 8.1e shows the Landau fan diagram recorded up to $B = 12T$. The high electronic quality of the graphene is evident from the emergence of broken symmetry states above $B = 5T$, which are well developed at $B = 12T$ (Figure 8.1f). To our knowledge, this is the first observation of broken symmetry states in graphene with superconducting contacts. The plateaus on the electron side are better developed than those on the hole side, presumably a consequence of doping near the contacts.

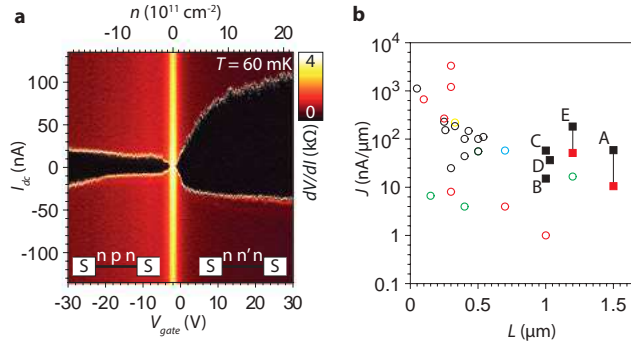


Figure 8.2: (a) The differential resistance, dV/dI , is plotted as a function of applied dc current bias, I_{dc} , and gate voltage, V_{gate} , at $60mK$. (b) Critical current density, J , plotted as a function of device length, L . Squares are the side contacted MoRe graphene devices A–E reported here. Black (red) squares correspond to a temperature of $50mK$ ($700mK$). More details about the temperature dependence can be found in Figure 8.5. Circles are data points taken from the literature[18–25]. Colors indicate different superconductors used: Black circles refer to Al, green circles to Nb/NbN/NbTiN, blue ReW, red Pb/PbIn and yellow Pt/Ta.

8

At zero magnetic field we observe a gate-tunable supercurrent through the device. In Figure 8.2a we plot the differential resistance, dV/dI , as a function of gate voltage, V_{gate} , and the current bias, I_{dc} . Evidently, the critical current, I_c , vanishes at the charge neutrality point, but reaches values in excess of $100nA$ at $V_{gate} = 30V$. The individual $I_{dc} - V$ curves are hysteretic, as is evident from the asymmetry about $I_{dc} = 0$ (see Figure 8.5). On the hole side I_c is considerably smaller, consistent with the formation of the conjectured $n p n$ junctions. In Figure 8.2b we plot the critical current density per unit length, J , versus the JJ length, L , with data obtained from previous reports of graphene JJs (circles) along with the present MoRe edge-contacted devices (squares). The black squares show the critical current density at $50mK$, whereas the red squares are taken at $700mK$. We point out that the critical current density depends on the temperature and the graphene carrier density, which vary from study to study. Despite this, it is clear that our MoRe edge-contacted devices stand out in relative magnitude compared to the previous data. We find large supercurrent densities (up to $\sim 200nA/\mu m$) over significantly longer distances ($\sim 1.5\mu m$). The observation of large supercurrents over an unprecedented long distance of $1.5\mu m$ indicates a high quality of both the graphene itself and of the 1D graphene-superconductor interfaces.

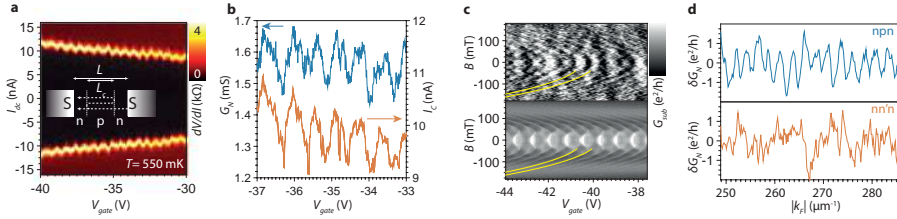


Figure 8.3: (a) The differential resistance, dV/dI , is plotted as a function of the applied dc current bias, I_{dc} , and gate voltage, V_{gate} , at $T = 550\text{mK}$. At 60mK , statistical fluctuations in I_c make the effect much less visible. Inset: A schematic of a cavity formed between pn -junctions due to doping near the contacts. Interference occurs due to reflections at the pn -junctions, (b) The normal state conductance, G_N , and the critical current, I_c , plotted as a function of gate voltage, V_{gate} , (c) (upper panel) The conductance measured as a function of the magnetic field and gate voltage with $I_{dc} = 100\text{nA}$. The dispersion of the Fabry-Pérot interferences follows a 4th-order polynomial, see Equation 8.1, plotted in yellow. See Figure 8.6 for a similar dispersion in device D . (lower panel) simulated conductance for a cavity size of $L = 1.3\mu\text{m}$ and $W = 2\mu\text{m}$, (d) (upper panel) The conductance δG in the npn regime as function of absolute wavenumber $|k_F|$ in the central part of the device ($|k_F|$ is determined from the carrier density). δG_N is obtained after subtraction of a slowly varying background (see Figure 8.7). In the lower panel we plot δG_N in the $nn'n$ regime for the same wavenumber range. Here we attribute the fluctuations to UCE.

In addition, we find unambiguous signatures of ballistic Josephson transport in this 2D geometry. As shown in Figure 8.3a, we observe for the first time clear oscillations in the critical current and the retrapping current when we vary the gate voltage, indicative of Fabry-Pérot (FP) interferences in the supercurrent through the junction. The transmission probability of electrons and holes that carry the supercurrent is the result of interference of trajectories that travel ballistically from one contact to the other with multiple reflections close to or at the edges of the graphene flake. As the gate voltage is varied, the Fermi wavelength changes, constructive and destructive interference alternate, leading to modulations in the critical current. One may expect the graphene-superconductor interfaces to form the walls of the cavity. However, we observe the I_c oscillations only on the hole-doped side and not on the electron-doped side (see Figure 8.3d and the discussion below). This suggests that in the presence of n -doped regions near the MoRe-graphene interface the relevant cavity is instead formed by pn junctions near the contacts (see inset Figure 8.3a). This gives rise to a reduced cavity length L_c . This length can be directly inferred from the period of the oscillations, extracted via a Fourier analysis (see Figure 8.7c) of these oscillations over many periods. A cavity length of $L_c = 1.3\mu\text{m}$ is found, which is smaller than the etched device length ($L = 1.5\mu\text{m}$). A similar difference between device size and inferred cavity length was seen in device D (see Figure 8.7). This difference may arise from screening of the back gate near the contacts in combination with the presence of the n -doped regions at the MoRe-graphene interfaces in both devices.

The interpretation of the oscillations in I_c in terms of FP interference, is further supported by comparing them with the oscillations in the normal state conductance, G_N , measured at currents just above I_c . The oscillations of I_c with gate voltage clearly match the oscillations in G_N , (see Figure 8.3b), as expected for Josephson junctions. In the case of normal state transport, we can apply a weak magnetic field perpendicular to

the graphene, to apply a Lorentz force to the trajectories of electrons and holes. This is expected to give a characteristic shift of the FP resonances due to the accumulation of extra field-dependent phases. Indeed in the measurements shown in Figure 8.3c, we find that as B increases the main resonance features shift to higher density, following a characteristic dispersion. To enhance the visibility, we plot the quantity G_{sub} , which was obtained after subtracting a gate dependent (but field independent) modulation of the background conductance. We compare the data with the results of numerical simulations of the device conductance (see SI for further details) in the ballistic regime and with npn junctions for the exact geometry of the measured device (Figure 8.3c lower panel). Simulation and experiment show an almost identical dispersion of the FP resonances with magnetic field. It is also possible to obtain a semiclassical expression for the resonance condition by considering all the phases accumulated in the n -region of the npn junction:

$$\frac{L_c}{\lambda_F(V_{gate})} = n_m + \frac{1}{2} + \frac{1}{6n_m} \left(\frac{L_c^2 e B}{h} \right)^2, \quad (8.1)$$

with n_m a specific integer mode, $\lambda_F(V_{gate})$ the Fermi wavelength which is tuned by the backgate ($V_{gate} \sim 1/\lambda_F^2$), L_c the cavity size, e the electron charge and h Planck's constant. The yellow curves in Figure 8.3d are calculated using Equation 8.1 for modes $n_m = -121, -120$ and show an excellent agreement with the measured and simulated results. This provides strong evidence that the observed oscillations, both in I_c and G_N , arise from Fabry-Pérot interference, which implies phase-coherent ballistic transport. While such oscillations due to FP interference have been reported before in a variety of systems including high-quality graphene with normal contacts [12, 13], here we provide evidence for phase coherent FP interference in the supercurrent, which has not been observed before in any 2D geometry.

8

In order to better understand the microscopic details of our device, we compare the conductance in the npn regime with that in the $nn'n$ regime (Figure 8.3d). Whereas in the npn regime (upper panel), we observe periodic oscillations as a function of absolute wave number, $|k_F|$, we observe universal conductance fluctuations (UCF) in the $nn'n$ case (lower panel). We attribute these fluctuations to diffuse boundary scattering at or close to the graphene-MoRe interface. This diffuse scattering should also be present on the hole-side but does not dominate the transport due to the presence of the pn junctions. Using the ballistic limit, L much larger than the mean free path, where all resistance is from the contact interface, we can estimate a lower bound on the contact transparency, T via $G = \frac{T}{2} \frac{4e^2}{\pi h} k_F W$. From the conductance in the $nn'n$ regime (see Figure 8.7) we find a contact transparency of $T > 0.2$. In the npn case, the conductance is dominated by the pn barriers. In this case, we can estimate the sharpness, d , of the p to n transition regions via $G_{npn} = \frac{e^2}{\pi h} \sqrt{\frac{k_F}{d}} W$. We find a sharpness of $d \sim 70nm$, which is a plausible value considering the device dimensions.

Since the DC Josephson effect is observed in these graphene devices over micron scale distances, we can also explore the magnetic field dependence of the critical current for unusual geometries. Earlier reports concerned graphene Josephson junctions with lengths much shorter than their width. In this case, the magnetic field dependence of

I_c is expected to follow the standard Fraunhofer diffraction pattern observed in tunnel junctions[14]. In the present devices, in contrast, the aspect ratio is close to 1, which has two consequences. First, unlike in tunnel junctions, the phase difference across the junction must be integrated along both interfaces. Furthermore, contributions involving reflections off the side of the junction must be included, especially when transport is ballistic[15–17]. The main prediction in this case is that the periodicity of I_c with magnetic flux becomes larger than a single flux quantum, $\Phi_0 = h/2e$. Despite significant differences across the patterns measured on the various devices, we consistently find a period larger than Φ_0 , as seen in Figure 8.4 for device *A* (and in the Figure 8.9 for devices *B* and *C*). In contrast, earlier reports on graphene Josephson junctions all show flux periods smaller than Φ_0 [18–25] before corrections to account for the London penetration depth.

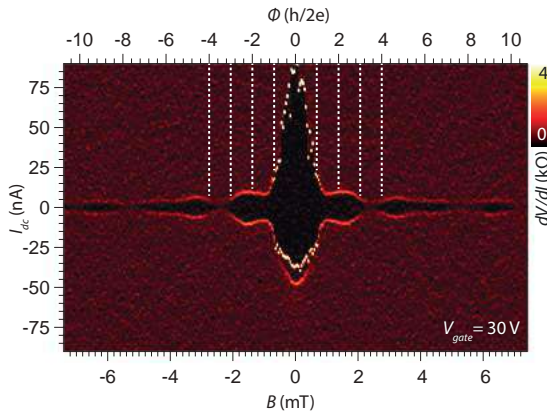


Figure 8.4: The differential resistance (dV/dI) is plotted as a function of applied current bias, I_{dc} , and magnetic field, B , at a gate voltage of 30V. We observe a separation between minima that clearly exceeds the flux quantum, $h/2e$.

8.3. CONCLUSION

In conclusion, we observe gate-tunable supercurrents over distances as long as $1.5 \mu\text{m}$. The ballistic and phase coherent transport in these devices causes the switching current to oscillate periodically with the Fermi wave number, thus providing clear evidence of a ballistic Josephson junction. The Fabry P erot oscillations in the critical current and the anomalous Fraunhofer diffraction patterns are mutually consistent and provide strong evidence of ballistic effects in superconducting transport through graphene. Furthermore, the large critical field of MoRe allows us to resolve several broken symmetry states in the quantum Hall regime, while the MoRe remains superconducting. We believe that this is the first unambiguous demonstration of a ballistic JJ in graphene.

8.4. SUPPLEMENTARY INFORMATION

8.4.1. TIGHT-BINDING SIMULATION

The FP oscillations in the npn junction are simulated by a tight-binding calculation using the Kwant software package[26]. A $1.5\mu\text{m} \times 2.0\mu\text{m}$ hexagonal lattice is discretized with a lattice constant of $a = 2\text{nm}$, with metallic leads on the $2.0\mu\text{m}$ wide sides. The contact induced doping near both leads is modeled by a 100nm region with a fixed chemical potential. The width of the transition region from the n to the central p region is set to 50nm and modelled by $\tanh[(x - x_0)/25\text{nm}]$. A finite contact resistance is imposed by reducing the transparency between the central strip and the leads to 60%. Finally we calculate the transmission as a function of the Fermi wavenumber $k_F(\mu_p)$ and magnetic field B , resulting in the dispersion given in Figure 8.3d.

8.4.2. CURRENT-VOLTAGE CHARACTERISTICS AND TEMPERATURE DEPENDENCE

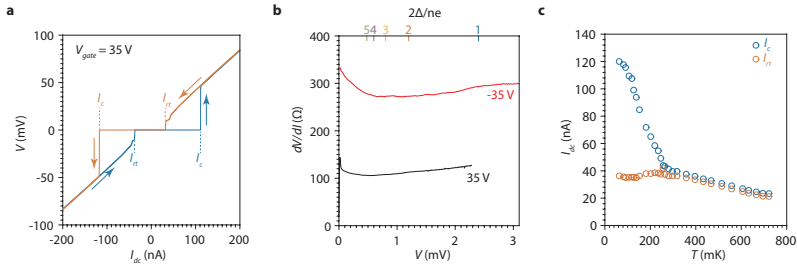


Figure 8.5: (a) A current-voltage curve (in device A) at 50 mK and large n-doping showing a characteristic hysteresis. Such hysteresis is often attributed to the existence of an underdamped Josephson junction. An alternative explanation for such hysteresis lies in non-equilibrium or heating effects in the JJ. In this scenario increasing the current results in an increased power fed through the JJ, Joule heating, and an increased electron temperature compared to the temperature of the reservoirs. Both these processes could be at play in our graphene JJs, and one would require further detailed studies to determine the origin of the hysteresis, (b) Bias spectroscopy (device E) shows no discernable features associated with multiple Andreev reflections (MAR). Top axis shows the expected positions of these features. There can in principle be several reasons for the absence of discernable MAR features in the differential resistance, such as extremely low (or high) transparency or the presence of residual inelastic scattering. To resolve this question we need more data from a range of devices, a more accurate determination of the contact transparency, and a more mature theoretical model for ballistic graphene-superconductor devices, (c) Temperature dependence of I_c and I_{rl} for device A. We can compare this data with the behavior predicted by either the Eilenberger equations (for clean SNS junctions) or the Usadel equations (for diffusive junctions). Both models predict a smooth variation of I_c with temperature, so the pronounced kink around 300 mK requires a separate explanation.

8.4.3. FABRY-PÉROT INTERFERENCE IN DEVICE D

8.4.4. POWER SPECTRAL DENSITY FROM FABRY-PÉROT OSCILLATIONS

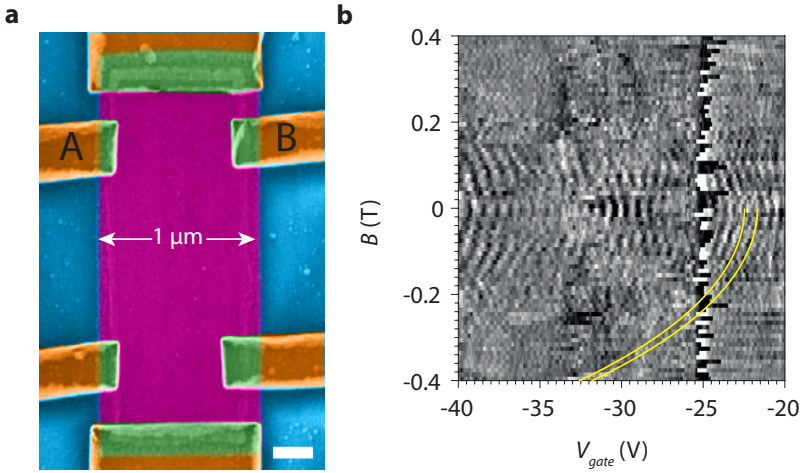


Figure 8.6: (a) Scanning electron microscope image of device D with MoRe contacts. The measurements in panel (b) are recorded between the contacts indicated in the figure. The distance between the contacts is $1\mu\text{m}$ and the contact width is 360nm , (b) The conductance G between the contacts indicated in panel (a) plotted as function of magnetic field B and gate voltage. Here we observe a very similar parabolic dispersion as in Figure 8.3c. The yellow lines are calculated via Equation 8.1 for $L = 0.8\mu\text{m}$ and $n_m = -56, -55$. These results imply that the transport across the Hall bar device is ballistic.

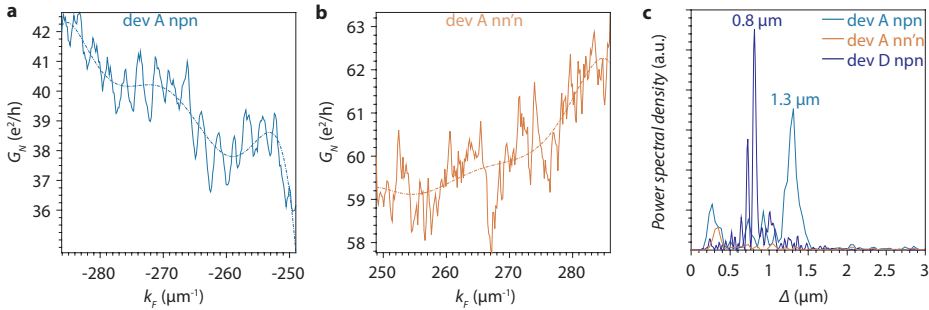


Figure 8.7: (a) The normal state conductance G_N measured in the $n\text{pn}$ regime as a function of number k_F . The dashed line is the slowly varying background, defined here by a 6^{th} -order polynomial fit, (b) The normal state conductance G_N in the $nn'n$ regime as a function of wavenumber k_F , with the dashed line the slowly varying background. By taking the discrete Fourier transform $\mathcal{F}\{\delta G_N(k_F)\} = Y(\Delta)$ of the conductance fluctuations in (a) and (b) (after subtracting the steep background, see also Figure 8.3d), we can obtain the power spectral density $PSD(\Delta) = Y(\Delta)Y^*(\Delta)$, (c) The power spectral density PSD for device A in the $n\text{pn}$ and $nn'n$ regime and for device D in the $n\text{pn}$ regime as a function of length $\omega/2$. Device A and D have a designed length of $L_A = 1.5\mu\text{m}$ and $L_D = 1.0\mu\text{m}$, respectively. From the peak positions in the PSD we extract a cavity size of $L_A^{FP} = 1.3\mu\text{m}$ and $L_D^{FP} = 0.8\mu\text{m}$. We attribute the difference of $\sim 200\text{nm}$ to two effects. Firstly, the size of the graphene/hBN is most likely slightly smaller than the designed size due to the etching process. Secondly, the cavity is formed between the pn junctions, where the n -region is caused by doping from the contact and has a finite length. This would mean the n -doped region is about $\sim 100\text{nm}$ on each side. The fact that the pn junctions act as the cavity walls leading to FP interference, is further supported by the fact that PSD in the $nn'n$ regime shows no predominant period.

8.4.5. EFFECT OF LEAD SWITCHING ON MAGNETO-TRANSPORT

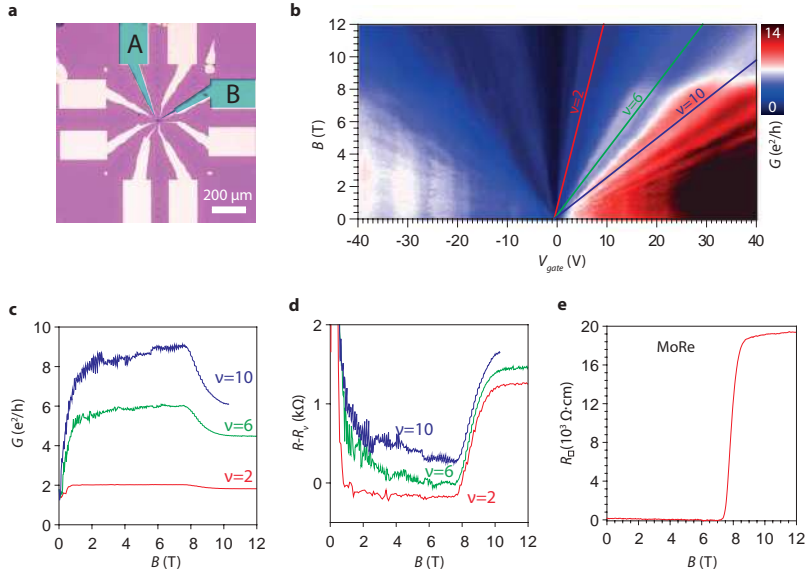


Figure 8.8: (a) An optical image of the die of device *D*. In this device, transport is measured between contacts *A* and *B* in a two-terminal configuration. In the normal state, the MoRe leads have a non-negligible resistance. This causes artifacts in the measurement when switching between the superconducting and normal state of the MoRe. Such artifacts from the lead resistance are minimized in the quasi four-terminal configuration used in device *A*, see Figure 8.1a, (b) Landau fan diagram of Device *D* (shown also in Figure 8.6a), showing the conductance as a function of magnetic field *B* and gate voltage V_{gate} . Above the critical field of MoRe $H_{c2} \sim 8T$, the MoRe leads switch to the normal state, causing a jump in the two-terminal conductance, (c) The conductance G in units of e^2/h for filling factors $\nu = 2, 6$ and 10 as a function of magnetic field B , (d) When plotting resistance instead of conductance, it becomes clear that there is a fixed resistance increase when the MoRe leads turn normal. To facilitate comparison, we plot $R - R_\nu$, where $R_\nu = \frac{h}{\nu e^2}$ is the ideally expected resistance for filling factor ν , (e) The square resistance R_\square of the MoRe sheet measured using a Hall bar as a function of the magnetic field B . We observe again the upper critical field of MoRe of about $H_{c2} \sim 8T$.

8.4.6. ANOMALOUS FRAUNHOFER DIFFRACTION PATTERNS

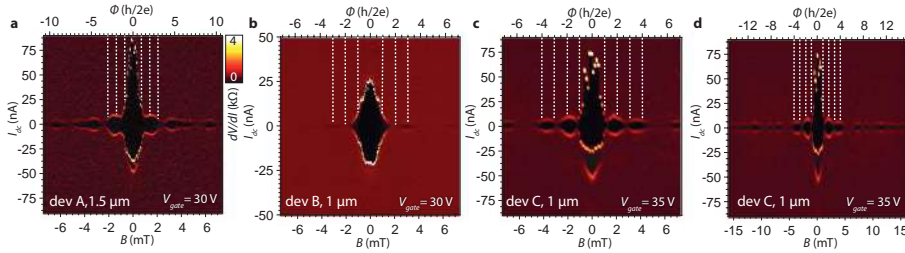


Figure 8.9: (a) The differential resistance (dV/dI) as a function of applied current bias, I_{dc} , and magnetic field, B at a gate voltage of $30V$, for device A. This is the same plot as in Figure 8.4, (b-c) Similar plots for devices B and C, (d) The same measurement as in (c), but shown over a larger magnetic field range. The lobes persist up to at least 20 mT which corresponds to about 9-10 periods. In general, the dependence of I_c on B shows a wide range of behaviors, seen through the various Fraunhofer diffraction patterns in the four panels. An important question is what kind of variations in our samples contribute to the variation in the Fraunhofer response. For instance, we do not know a priori whether the edge contacts have uniform transmission over the full width of the contact. Despite the variations, we consistently observe that (1) when deducing the flux periodicity from the first lobe, the flux periodicity is larger than one flux quantum Φ_0 and (2) the minima in I_c do not reach zero between the lobes.

REFERENCES

- [1] V. E. Calado, S. Goswami, G. Nanda, M. Diez, A. R. Akhmerov, K. Watanabe, T. Taniguchi, T. M. Klapwijk, and L. M. K. Vandersypen, *Ballistic Josephson junctions in edge-contacted graphene*, Nature Nanotechnology **10**, 761 (2015).
- [2] C. W. J. Beenakker, *Specular Andreev reflection in graphene*, Physical Review Letters **97**, 067007 (2006).
- [3] H. Hoppe, U. Zülicke, and G. Schön, *Andreev reflection in strong magnetic fields*, Physical Review Letters **84**, 1804 (2000).
- [4] N. M. Chtchelkatchev and I. S. Burmistrov, *Conductance oscillations with magnetic field of a two-dimensional electron gas-superconductor junction*, Physical Review B **75**, 214510 (2007).
- [5] A. R. Akhmerov and C. W. J. Beenakker, *Detection of valley polarization in graphene by a superconducting contact*, Physical Review Letters **98**, 157003 (2007).
- [6] I. Martin, Y. M. Blanter, and A. F. Morpurgo, *Topological confinement in bilayer graphene*, Physical Review Letters **100**, 036804 (2008).
- [7] X. Du, I. Skachko, A. Barker, and E. Y. Andrei, *Approaching ballistic transport in suspended graphene*, Nature Nanotechnology **3**, 491 (2008).
- [8] C. R. Dean, A. F. Young, I. Meric, C. Lee, L. Wang, S. Sorgenfrei, K. Watanabe, T. Taniguchi, P. Kim, K. L. Shepard, and J. Hone, *Boron nitride substrates for high-quality graphene electronics*, Nature Nanotechnology **5**, 722 (2010).

- [9] L. Wang, I. Meric, P. Y. Huang, Q. Gao, Y. Gao, H. Tran, T. Taniguchi, K. Watanabe, L. M. Campos, D. A. Muller, J. Guo, P. Kim, J. Hone, K. L. Shepard, and C. R. Dean, *One-dimensional electrical contact to a two-dimensional material*, *Science* **342**, 614 (2013).
- [10] B. H. Schneider, S. Etaki, H. S. J. van der Zant, and G. A. Steele, *Coupling carbon nanotube mechanics to a superconducting circuit*, *Scientific Reports* **2**, 599 (2012).
- [11] P. Maher, L. Wang, Y. Gao, C. Forsythe, T. Taniguchi, K. Watanabe, D. Abanin, Z. Papić, P. Cadden-Zimansky, J. Hone, P. Kim, and C. R. Dean, *Tunable fractional quantum hall phases in bilayer graphene*, *Science* **345**, 61 (2014).
- [12] A. F. Young and P. Kim, *Quantum interference and Klein tunnelling in graphene heterojunctions*, *Nature Physics* **5**, 222 (2009).
- [13] A. Varlet, M.-H. Liu, V. Krueckl, D. Bischoff, P. Simonet, K. Watanabe, T. Taniguchi, K. Richter, K. Ensslin, and T. Ihn, *Fabry-Pérot interference in gapped bilayer graphene with broken anti-Klein tunneling*, *Physical Review Letters* **113**, 116601 (2014).
- [14] M. Tinkham, *Introduction to superconductivity*, Dover, New York, 2nd edition (2004).
- [15] J. P. Heida, B. J. van Wees, T. M. Klapwijk, and G. Borghs, *Nonlocal supercurrent in mesoscopic Josephson junctions*, *Physical Review B* **57**, R5618 (1998).
- [16] U. Ledermann, A. L. Fauchère, and G. Blatter, *Nonlocality in mesoscopic Josephson junctions with strip geometry*, *Physical Review B* **59**, R9027 (1999).
- [17] D. E. Sheehy and A. M. Zagoskin, *Theory of anomalous magnetic interference pattern in mesoscopic superconducting/normal/superconducting Josephson junctions*, *Physical Review B* **68**, 144514 (2003).
- [18] H. B. Heersche, P. Jarillo-Herrero, J. B. Oostinga, L. M. K. Vandersypen, and A. F. Morpurgo, *Bipolar supercurrent in graphene*, *Nature* **446**, 56 (2007).
- [19] X. Du, I. Skachko, and E. Y. Andrei, *Josephson current and multiple Andreev reflections in graphene SNS junctions*, *Physical Review B* **77**, 184507 (2008).
- [20] C. Ojeda-Aristizabal, M. Ferrier, S. Guéron, and H. Bouchiat, *Tuning the proximity effect in a superconductor-graphene-superconductor junction*, *Physical Review B* **79**, 165436 (2009).
- [21] J.-H. Choi, H.-J. Lee, and Y.-J. Doh, *Above-gap conductance anomaly studied in superconductor-graphene-superconductor Josephson junctions*, *Journal of the Korean Physical Society* **57**, 149 (2010).
- [22] D. Jeong, J.-H. Choi, G.-H. Lee, S. Jo, Y.-J. Doh, and H.-J. Lee, *Observation of supercurrent in PbIn-graphene-PbIn Josephson junction*, *Physical Review B* **83**, 094503 (2011).

- [23] U. C. Coskun, M. Brenner, T. Hymel, V. Vakaryuk, A. Levchenko, and A. Bezryadin, *Distribution of supercurrent switching in graphene under proximity effect*, Physical Review Letters **108**, 097003 (2012).
- [24] M. Popinciuc, V. E. Calado, X. L. Liu, A. R. Akhmerov, T. M. Klapwijk, and L. M. K. Vandersypen, *Zero-bias conductance peak and Josephson effect in graphene-NbTiN junctions*, Physical Review B **85**, 205404 (2012).
- [25] K. Komatsu, C. Li, S. Autier-Laurent, H. Bouchiat, and S. Gueron, *Superconducting proximity effect through graphene from zero field to the quantum Hall regime*, Physical Review B **86**, 115412 (2012).
- [26] C. W. Groth, M. Wimmer, A. R. Akhmerov, and X. Waintal, *Kwant: a software package for quantum transport*, New Journal of Physics **16**, 063065 (2014).

9

GATE-TUNABLE QUANTUM INTERFERENCE DEVICES OF BALLISTIC GRAPHENE

In this chapter, we report the fabrication and operation of dc-superconducting quantum interference devices (SQUIDs) composed of two gate-tunable Josephson junctions (JJs) with graphene weak links incorporated into a Molybdenum-Rhenium (MoRe) loop. Under a perpendicular magnetic field, periodic oscillations of the critical current due to the flux quantization in SQUID are observed. The supercurrent in this device can be modulated independently by two top gates. By independently controlling the critical current of each graphene JJ, the SQUID can be electrostatically tuned from a symmetric configuration to a highly-asymmetric one, where the critical current of one JJ is significantly larger than the other. We observed clear Fabry–Pérot interferences in both the junctions, which is due to the partial reflections of electron waves. Moreover, the low-inductance and the gate-tunability of our SQUID can be used to probe current-phase relation (CPR) in graphene-based JJs.

9.1. INTRODUCTION

THE ballistic propagation of Dirac fermions and proximity-induced superconductivity in graphene has sparked significant interest in the past few years, leading to the observation of phase-coherent interference of charge carriers[1, 2], specular Andreev reflections[3], supercurrent in quantum Hall regime[4], and predictions of Majorana particles[5–8]. Although the theory of ballistic graphene Josephson junctions (JJs) has been previously established several years ago[9], experimentally the micron scale ballistic transport has only recently been attained[1, 2], opening the possibility to explore intriguing new physics. Calado *et al.*[1] and Shalom *et al.*[2] have shown that high-quality graphene (encapsulated in hexagonal boron nitride) contacted with superconductors (SCs) can give rise to ballistic Josephson junctions (JJs). We use two such JJs to create the first fully gate-tunable superconducting quantum interference device (SQUID) in graphene. By independently controlling the critical current of each graphene JJ, the SQUID can be electrostatically tuned from a symmetric configuration to a highly asymmetric one, where the critical current of one JJ is significantly larger than the other. The symmetric SQUID produces typical flux-periodic oscillations in the critical current with a large modulation amplitude. The modulation of critical current in a dc-SQUID is determined by the relative phase difference between the junctions that is set by the flux (Φ) threading the loop according to $\Phi_1 - \Phi_2 = 2\pi\Phi/\Phi_0$, where Φ_0 is the magnetic flux quantum. It blends two quantum properties of superconductivity, *i.e.* flux quantization in a superconducting loop and the tunneling of phase coherent Cooper pairs between corresponding macroscopic wavefunctions, where the amplitude of supercurrent can be controlled via individual top gates.

In this chapter, we demonstrate fabrication and measurements of the dc-SQUIDs consisting of two Josephson junctions with BN-encapsulated graphene as a weak link. We show that the supercurrent in this device can be modulated by two individual top gates and, therefore, a symmetric and highly asymmetric configurations can be achieved.

9.2. EXPERIMENTAL SECTION

We designed the first fully gate-tunable graphene-SQUID device as presented in Figure 9.1a. The superconducting SQUID loop consists of two SC/graphene/SC junctions connected in parallel on a superconducting loop made of MoRe, which has a critical temperature $T_c = 8$ K. A schematic cross-section of the device is shown in Figure 9.1b. Each junction is designed to be $3 \mu\text{m}$ wide and $1 \mu\text{m}$ long. The superconducting coherence length (ξ) is estimated to be ≈ 548 nm using $\xi \sim v_f \hbar / \Delta$, where $\Delta \approx 1.2$ meV is the superconducting energy gap of MoRe and v_f is the fermi velocity. Therefore, the junction length (L) is greater than the superconducting coherence length (ξ) and present links are in the long-junction limit. The loop area of the resulting SQUID is $200 \mu\text{m}^2$, which is expected to give around $10.3 \mu\text{T}$ period ($B = h/2e/A$) oscillation of the critical current. The d.c. measurements were performed in a Leiden Cryogenics MCK-50 3He/4He dilution fridge equipped with a superconducting magnet coil which can sustain fields up to 12 T. Each JJ of the graphene SQUID was fabricated using van der Waals pick-up technique,

which has been described previously[1].

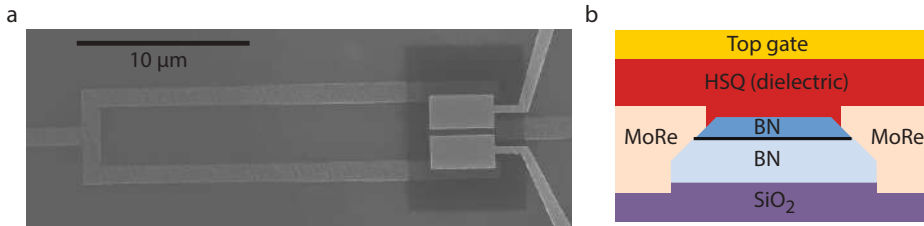


Figure 9.1: (a) Scanning electron microscope image of a superconducting quantum interference device made with h-BN encapsulated graphene, (b) Shows the schematic cross-section of one of the Josephson junctions.

9.3. SQUID OPERATION

Below the transition temperature of the MoRe contacts ($T_c \approx 8$ K), proximity effect can occur in the graphene weak links. Figure 9.2a-c show the electrical transport measurements for graphene SQUIDs at 4 K. The strength of the critical current in each JJ can be tuned via gate voltages; V_L and V_R . The 2-D color plot in Figure 9.2b shows the charge neutrality point (CNP) of both the junctions where the highest resistance point coincides. The resistance vs gate voltage curves for both the junctions are plotted in Figure 9.2c. The red curve is taken while keeping the right gate to its CNP and the blue curve is taken while keeping the left gate to its CNP. If we zoom on the hole side of the red curve in 1b, one can see periodic oscillations, indication of the partial reflection of electron waves from the p-n junction created near the contacts.[1, 2] This creates a Fabry-Pérot (FP) interferences in the resistance, meaning the junctions are ballistic. We calculated the length of the FP cavity from the period of the oscillations using the formula: $\Delta n = 2k_F/L_{cavity}$, [10] where $k_F = \sqrt{n\pi}$ and n is the density of charge carriers. This yields an effective cavity length of ≈ 950 nm, in good agreement with the designed length ($1 \mu\text{m}$) of our graphene junction. At 40 mK and at zero magnetic field, a gate-tunable supercurrent is observed in our SQUID device, see Figure 9.2d. The critical current I_c reaches a value in excess of $1.7 \mu\text{A}$ at $V_{TG} = 10\text{V}$. The I_c vanishes at zero gate voltage and a finite supercurrent is observed away from the CNP. We see that the I_c is smaller in the hole side, consistent with the previous observation of the ballistic Josephson junctions by Calado *et al.*[1].

The SQUIDs were DC biased above the critical currents and the voltages were measured. The current-voltage ($I-V$) characteristics of graphene SQUIDs exhibit dissipationless current flow between the junctions and demonstrates Josephson coupling in the device. From these $I-V$ curves we can extract the critical current I_c , defined as the average of the maximum switching current for positive and negative bias. Under a perpendicular magnetic field, constructive and destructive interference between the superconducting wavefunction along the arms of the loop are observed, giving rise to the periodic oscillations in the I vs Φ/Φ_0 curves. When the critical current of two junctions is equal,

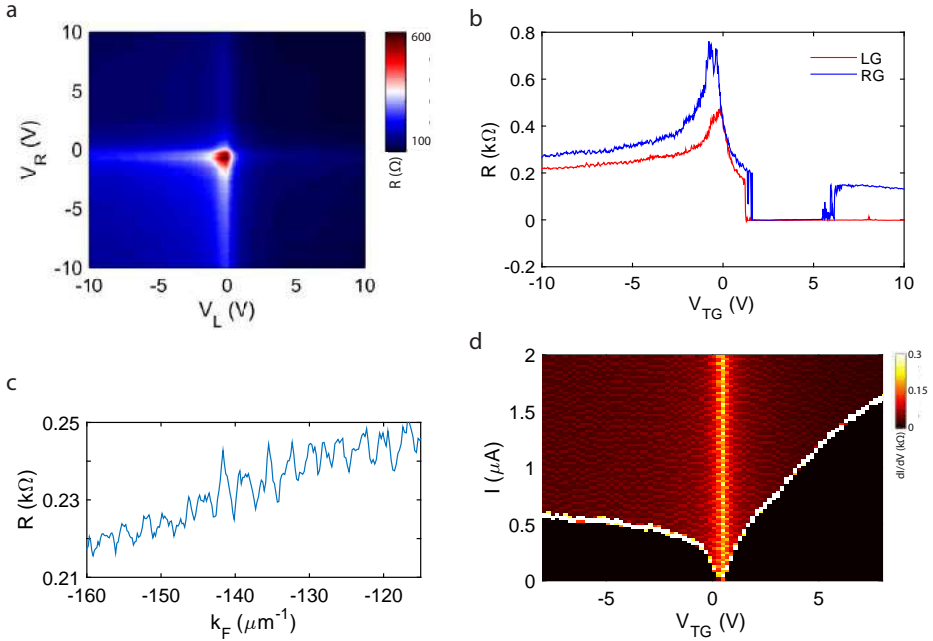


Figure 9.2: (a) Differential resistance dV/dI vs V_L and V_R , demonstrating independent control of carrier type and density in left and right JJ, respectively, (b) Resistance vs gate voltage plot for V_L (V_R) while keeping V_R (V_L) fixed at CNP, (c) Resistance in the n-p-n regime as a function of wavenumber k_F (k_F is determined from the carrier density), (d) Differential resistance dV/dI as a function of applied d.c. current bias I and top gate voltage V_{TG} , at 40 mK.

a symmetric configuration is achieved, which is shown in the middle curve of Figure 9.3b. However, when the critical current of one of the junction is relatively high compared to the other junction, the modulation depth is strongly reduced (typically by 20-90%), shown as the upper and lower curves of Figure 9.3b. The modulation depth or $V_{is} = (I_{cmax} - I_{cmin})/I_{cmax}$ is limited by two factors, asymmetry in the critical currents of two JJs and screening parameter $\beta_L = 2\pi I_0 L_s / \Phi_0$, where L_s is the self inductance of the SQUID loop. One can see that even in the symmetric configuration the modulation depth is not 100% (see Figure 9.3b). The modulation depth can be different depending on the β_L . There are two factors which could influence the modulation depth; large inductance of the SQUID loop or the presence of higher harmonics in the current phase relation of the graphene JJs[11]. This will be studied later in Chapter 10. We calculated the SQUID behaviour for two different values of β_L using RCSJ model and presented in Figure 9.3c along with the experimental data. One can see that the calculated modulation depth of 100% is achieved when the β_L is close to zero (black curve in Figure 9.3c). This means the junctions have very low inductance. However, by changing the values of β_L , one can obtain the real value of the β_L from the theoretical and experimental curves (red curve in Figure 9.3c). This gives an upper bound on the inductance. The calculations of the inductance, RCSJ model, and the higher harmonics will be discussed in

Chapter 10.

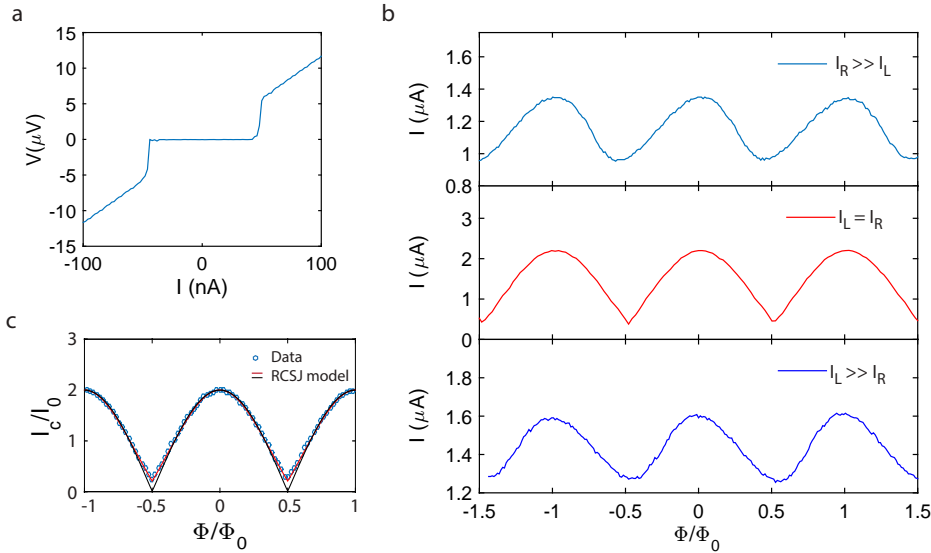


Figure 9.3: (a) A current-voltage curve at 4 K and large n-doping, (b) Shows the I_c vs Φ in MoRe/graphene/MoRe junctions by tuning the critical current of the junctions to an asymmetric situation. SQUID can be tuned to forward or backward skewness, depending on which JJ has the higher critical current. Top and bottom curves show the forward and backward skewness, respectively. The middle curve is when both the junction are tuned to similar values of I_c , (c) Comparison of the symmetric SQUID with RCSJ model. Note that the curves do not hit zero, even when the critical currents of the both the junctions are equal.

When the magnetic field is applied perpendicular to the SQUID loop, gradual changes in the current-voltage ($I-V$) characteristic curves at $T=4$ K are shown in Figure 9.4a, where Josephson supercurrent flowing through SGS junction is observed. With increasing magnetic flux (Φ), periodic oscillations, whose period is about $10.33 \mu\text{T}$ can be seen where I_c is maximum at $\Phi = 0$ and absent at $\Phi_0/2$, where $\Phi_0 = h/2e$ is the magnetic flux quantum, h is Planck's constant and e is the elementary charge. In this case, we tune both the Josephson junctions to a region with similar critical current such that we observe almost 100% modulation depth. We see that at 4 K, 100% modulation depth is restored. Hence, one could say that the lower modulation at 40 mK is not related to the inductance of the SQUID loop. Under the assumption of negligible self-inductance of the loop, I_c is given by:

$$I_c = \sqrt{(I_{c1} - I_{c2})^2 + 4I_{c1}I_{c2}\cos^2\frac{\pi\Phi}{\Phi_0}} \quad (9.1)$$

where I_{c1} and I_{c2} are the critical currents of each JJ At $T = 40$ mK, I_{c1} and I_{c2} are obtained by fitting Equation 9.1 to the experimental data (see Figure 9.4b). Here, $I_{c1} = (I_{cmax} + I_{cmin})/2$, $I_{c2} = (I_{cmax} - I_{cmin})/2$ and $I_0 = (I_{c1} + I_{c2})/2$ is an average critical current. It is inferred that when two JJ in the SQUID is almost identical with $I_{c2}/I_{c1} = 1$.

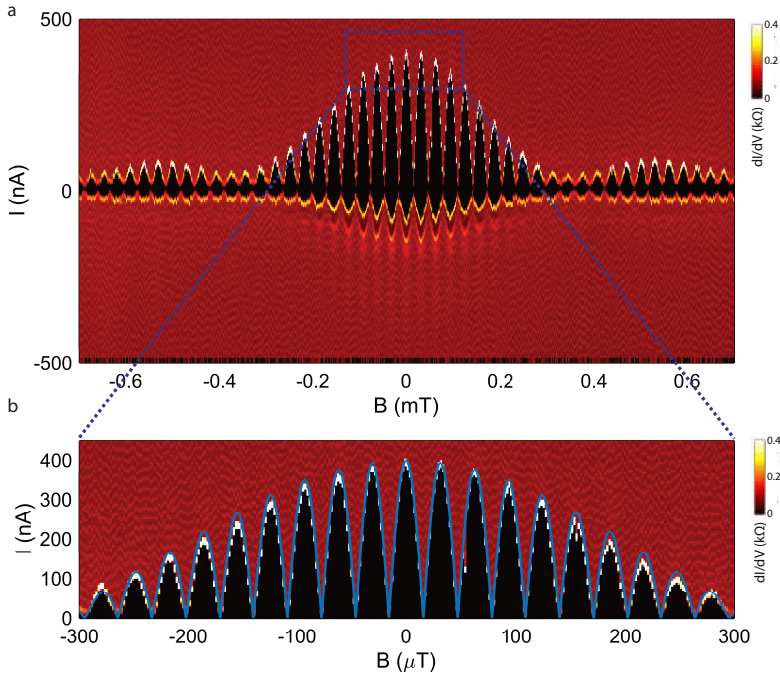


Figure 9.4: Shows SQUID oscillations bound by a Fraunhofer (FH) envelope corresponding to the single-junction diffraction pattern of the symmetric SQUID. The differential resistance dI/dV of the junction is represented in red, as a function of the bias current I and the magnetic field B . The black regions correspond to the superconducting regions in which the SQUID resistance, $R = 0\Omega$ while the white and red areas correspond to a finite resistance state.

9.4. CONCLUSION

In conclusion, we have presented the first fully gate-tunable dc-SQUID composed of two ballistic graphene Josephson junctions. By tuning the critical currents in each junction, the SQUID can be tuned from a symmetric situation to a highly asymmetric one. We see that even in a symmetric situation, full modulation at 40 mK is not achieved. We concluded that the critical current is not fully suppressed to zero and the modulation depth of the critical current is not 100%. We believe these devices exhibit an ideal platform to study novel phenomenon's, such as current-phase relation in graphene Josephson junctions.

REFERENCES

- [1] V. E. Calado, S. Goswami, G. Nanda, M. Diez, A. R. Akhmerov, K. Watanabe, T. M. K. T. Taniguchi, and L. M. K. Vandersypen, *Ballistic Josephson junctions in edge-contacted graphene*, Nature Nanotechnology **10**, 761 (2015).

- [2] M. B. Shalom, M. J. Zhu, V. I. Fal'ko, A. Mishchenko, A. V. Kretinin, K. S. Novoselov, C. R. Woods, K. Watanabe, T. Taniguchi, A. K. Geim, and J. R. Prance, *Quantum oscillations of the critical current and high-field superconducting proximity in ballistic graphene*, Nature Physics **12**, 318–322 (2016).
- [3] D. K. Efetov, L. Wang, C. Handschin, K. B. Efetov, J. Shuang, R. Cava, T. Taniguchi, K. Watanabe, J. Hone, C. R. Dean, and P. Kim, *Specular interband Andreev reflections at van der Waals interfaces between graphene and NbSe₂*, Nature Physics **12**, 328 (2016).
- [4] F. Amet, C. T. Ke, I. V. Borzenets, J. Wang, K. Watanabe, T. Taniguchi, R. S. Deacon, M. Yamamoto, Y. Bomze, S. Tarucha, and G. Finkelstein, *Supercurrent in the quantum Hall regime*, Science **352**, 966 (2016).
- [5] L. Fu and C. L. Kane, *Superconducting proximity effect and Majorana fermions at the surface of a topological insulator*, Physical Review Letters **100**, 096407 (2008).
- [6] C. W. J. Beenakker, *Search for Majorana fermions in superconductors*, arXiv **Preprint**, arXiv:1112.1950 (2011).
- [7] X. L. Qi and S. C. Zhang, *Topological insulators and superconductors*, Reviews of Modern Physics **83**, 1057 (2011).
- [8] P. San-Jose, J. L. Lado, R. Aguado, F. Guinea, and J. Fernández-Rossier, *Majorana zero modes in graphene*, Physical Review X **5**, 041042 (2015).
- [9] M. Titov and C. W. J. Beenakker, *Josephson effect in ballistic graphene*, Physical Review B **74**, 041401 (2006).
- [10] P. Rickhaus, M.-H. L. R. Maurand, M. Weiss, K. Richter, and C. Schönenberger, *Balistic interferences in suspended graphene*, Nature Communications **4**, 2342 (2013).
- [11] Ç. Girit, V. Bouchiat, O. Naaman, Y. Zhang, M. F. Crommie, A. Zettl, and I. Siddiqi, *Current–phase relation in graphene and application to a superconducting quantum interference device*, Physica Status Solidi B **246**, 2568 (2009).

10

CURRENT-PHASE RELATION OF BALLISTIC GRAPHENE JOSEPHSON JUNCTIONS

The current-phase relation (CPR) of a Josephson junction (JJ) determines how the supercurrent evolves with the superconducting phase difference across the junction. Knowledge of the CPR is essential in order to understand the response of a JJ to various external parameters. Despite the rising interest in ultra-clean encapsulated graphene JJs, the CPR of such junctions remains unknown. In this chapter, we use a fully gate-tunable graphene superconducting quantum interference device (SQUID) to determine the CPR of ballistic graphene JJs. Each of the two JJs in the SQUID is made with graphene encapsulated in hexagonal boron nitride. By independently controlling the critical current of the JJs, we can operate the SQUID either in a symmetric or asymmetric configuration. The highly asymmetric SQUID allows us to phase-bias one of the JJs and thereby directly obtain its CPR. The CPR is found to be skewed, deviating significantly from a sinusoidal form. The skewness can be tuned with the gate voltage and oscillates in anti-phase with Fabry-Pérot resistance oscillations of the ballistic graphene cavity. We compare our experiments with tight-binding calculations which include realistic graphene-superconductor interfaces and find a good qualitative agreement.

10.1. INTRODUCTION

THE past few years have seen remarkable progress in the study of graphene-superconductor hybrids. This surge in interest has primarily been driven by the ability to combine high-quality graphene with superconductors via clean interfaces, and has led

Parts of this chapter have been accepted for publication in Nano Letters (2017) [1].

to several experimental breakthroughs. These include the observation of specular Andreev reflection [2], crossed Andreev reflections [3], and superconducting proximity effects in ballistic graphene Josephson junctions (JJs) [4–8]. In a majority of these studies the device comprises of graphene encapsulated in hexagonal boron nitride (BN) contacted along the edge by a superconductor. The encapsulation in BN keeps the graphene clean, while the edge contacting scheme provides transparent interfaces. In particular, ballistic JJs fabricated in this manner have been central to recent studies of novel Andreev bound states in perpendicular magnetic fields [5], edge-mode superconductivity [6], and supercurrents in the quantum Hall regime [7]. However, to date there have been no measurements of the Josephson current phase relation (CPR) in these systems.

The CPR is arguably one of the most basic properties of a JJ, and provides information about the Andreev bound state (ABS) spectrum in the junction. While typical superconductor-insulator-superconductor (SIS) JJs exhibit a sinusoidal CPR, deviations from this behavior can be present in superconductor-normal-superconductor (SNS) junctions. Examples of this include JJs with high transmission such as nanowires [9] and atomic point contacts [10, 11], where the CPR contains significant higher frequency components. Furthermore, the periodicity of the CPR itself can be different from 2π for more exotic systems such as topological JJs [12]. For graphene JJs there have been several numerical estimates of the CPR which take into account its linear dispersion relation [13–16]. More recently, ballistic graphene JJs operated in large magnetic fields have been predicted to undergo a topological transition [17] which should be detectable via direct CPR measurements. However, the experimental determination of the CPR in graphene has been restricted to junctions which are either in the diffusive limit [18] or in a geometry which does not allow gate control of the junction properties [19].

In this chapter, we use a dc superconducting quantum interference device (SQUID) to directly determine the CPR in encapsulated graphene JJs. These graphene SQUIDs stand out from previous studies [20, 21] in two important ways. Firstly, the superconducting contacts are made with Molybdenum Rhenium (MoRe), which allows us to operate the SQUID up to 4.2 K. More importantly, our SQUID consists of graphene JJs which are ballistic and independently tunable, thereby allowing full electrostatic control over the SQUID response. By applying appropriate gate voltages we can continuously tune from a symmetric to an asymmetric SQUID. We show that the asymmetric configuration allows us to directly extract the CPR from flux periodic oscillations in the critical current of the SQUID. The CPR is found to be non-sinusoidal, displaying a prominent forward skewing. This skewness can be tuned over a large range with the gate voltage and shows correlations with Fabry-Pérot (FP) resistance oscillations in the ballistic cavity. We complement our experiments with tight-binding simulations which go beyond the short junction limit and explicitly take into account realistic graphene-superconductor interfaces.

10.2. RESULTS AND DISCUSSION

Figure 10.1a shows a scanning electron micrograph and cross-sectional schematic of a device. It consists of two encapsulated graphene JJs contacted with MoRe, incorporated in a SQUID loop. The fabrication strategy is similar to earlier work [4] and further de-

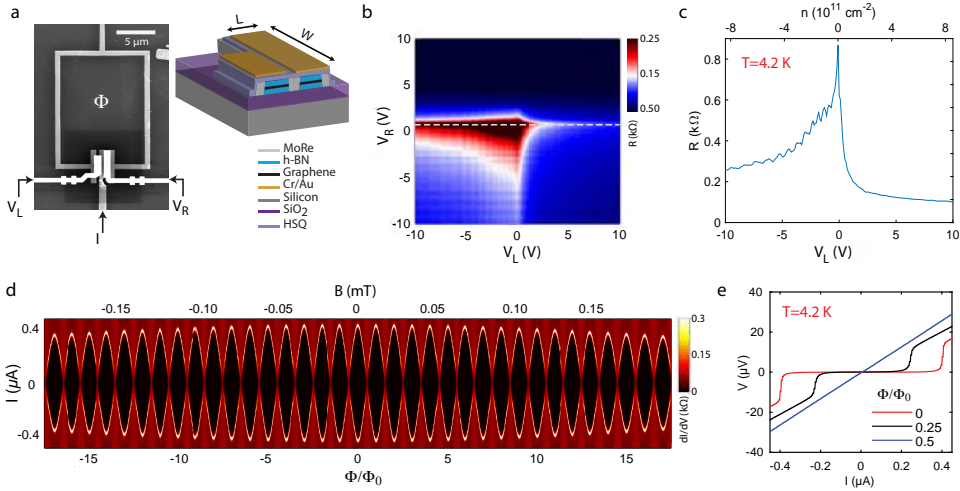


Figure 10.1: (a) Scanning electron micrograph of the graphene dc-SQUID (Dev1) along with a cross-sectional schematic. Gate voltages V_L and V_R independently control the carrier density of the left and right junction respectively, (b) Resistance R across the SQUID vs V_L and V_R , demonstrating independent control of carrier type and density in the JJs, (c) Line trace taken along the dashed white line in (b) showing Fabry-Pérot oscillations in the hole-doped regime, (d) Differential resistance dV/dI as a function of dc current bias I and magnetic field B , with the SQUID operated in a symmetric configuration ($V_L=+10$ V and $V_R=+2.5$ V). Flux-periodic oscillations are clearly visible with a slowly decaying envelope arising from the interference pattern of a single JJ, (e) $V-I$ plots (extracted from (d)) for different values of magnetic flux Φ showing a nearly 100 % modulation of the critical current. All measurements shown here are performed at $T = 4.2$ K.

tails are provided in the Supplementary Information (SI). The left (L-JJ)/right (R-JJ) JJs can be tuned independently by applying voltages (V_L/V_R) to local top gates. The junctions are intentionally designed to have a geometrical asymmetry, which ensures that the critical current of R-JJ (I_{cR}) is larger than that of L-JJ (I_{cL}) at the same carrier density. We report on two devices (Dev1 and Dev2) both of which have the same lithographic dimensions ($L \times W$) for L-JJ ($400 \text{ nm} \times 2 \text{ } \mu\text{m}$). The dimensions of R-JJ for Dev1 and Dev2 are $400 \text{ nm} \times 4 \text{ } \mu\text{m}$ and $400 \text{ nm} \times 8 \text{ } \mu\text{m}$ respectively. All measurements were performed using a dc current bias applied across the SQUID, in a dilution refrigerator with a base temperature of 40 mK.

Figure 10.1b shows the variation in the normal state resistance (R) of the SQUID with V_L and V_R at $T = 4.2$ K. The device was biased with a relatively large current of 500 nA, which is larger than the critical current of the SQUID for most of the gate range. Figure 10.1c shows a single trace taken along the white dashed line of Figure 10.1b, where R-JJ is held at the charge neutrality point (CNP). We see clear FP oscillations on the hole (p) doped region due to the formation of $n-p$ junctions at the superconductor-graphene interfaces [4, 5]. Furthermore, the criss-cross pattern seen in the lower left quadrant of Figure 10.1b indicates that both graphene junctions are in the ballistic limit and that there is no cross-talk between the individual gates. We note that when $V_R > 3$ V the critical current of the SQUID (I_c) is larger than the applied current bias, and a zero-resistance state is thus visible even at 4.2 K. Having established the fact that our JJs are in the ballis-

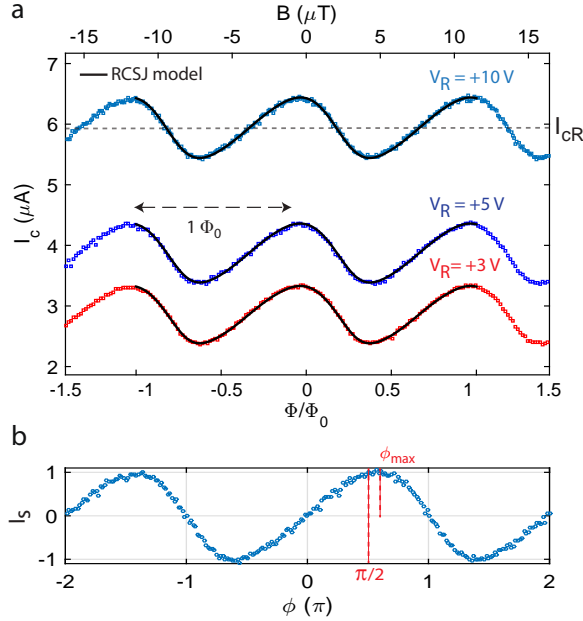


Figure 10.2: (a) Variation of I_c with Φ for $V_L = -4\text{V}$ and $V_R = +10\text{V}$, $+5\text{V}$ and $+3\text{V}$ at 40 mK. Solid black lines are results from RCSJ simulations of the SQUID, (b) Variation of supercurrent I_s with phase ϕ extracted from the top curve in (a). ϕ_{max} indicates the phase at which I_s reaches a maximum, and is noticeably different from $\pi/2$, indicating a forward skewed CPR.

tic regime, we now look in more detail at the behavior of the SQUID. At $T = 4.2\text{ K}$ we first tune the gate voltages ($V_L = +10\text{ V}$, $V_R = +2.5\text{ V}$) such that the SQUID is in a symmetric configuration and $I_{cR} = I_{cL}$. Figure 10.1d shows the variation in differential resistance dV/dI with current bias I and magnetic field B , where we observe clear oscillations in I_c with magnetic flux. In this configuration, the modulation in I_c is nearly 100 %, as seen by the individual $V - I$ traces in Figure 10.1e. The slow decay in the maximum value of I_c arises due to the (Fraunhofer) magnetic field response of a single junction. The devices were designed such that this background was negligible around $B = 0$ (*i.e.*, the SQUID loop area was kept much larger than the JJ area). Minimizing this background is important for a reliable determination of the CPR, as we will see below.

We now turn our attention to the flux-dependent response of a highly asymmetric SQUID ($I_{cR} \gg I_{cL}$), a condition which can be readily achieved by tuning the gate voltages appropriately. To outline the working principle of the device, we start with the assumption that both JJs have a sinusoidal CPR (a more general treatment can be found in the SI). So, the critical current of the SQUID can be written as $I_c = I_{cL} \sin\theta + I_{cR} \sin\delta$, where θ (δ) is the phase drop across L-JJ (R-JJ). When an external magnetic flux (Φ) threads through the SQUID loop, the flux and phase are related by $\delta - \theta = 2\pi\Phi/\Phi_0$, assuming the loop inductance is negligible. Now, when $I_{cR} \gg I_{cL}$ the phase difference across R-JJ is very close to $\pi/2$. Thus, $I_c(\Phi) \approx I_{cR} + I_{cL} \sin(2\pi\Phi/\Phi_0 + \pi/2)$ and the flux-dependence of I_c directly

represents the CPR of L-JJ, *i.e.*, $I_c(\Phi) \approx I_{cR} + I_s(\phi)$, where I_s is the supercurrent through L-JJ and ϕ is the phase drop across it. This principle of using an asymmetric SQUID to probe the CPR has been employed in the past for systems such as point contacts [10, 11] and vertical graphene JJs [19], where an SIS junction (with a well known sinusoidal CPR) was used as the reference junction. In our case, the reference junction is also a graphene JJ, where the CPR is not known a priori. We show (see SI) that this does not affect our ability to probe the CPR, provided time reversal symmetry is not broken, meaning that the CPR satisfies the condition $I_s(\phi) = -I_s(-\phi)$ [22]. Throughout the remainder of the text we use R-JJ as the reference junction (larger critical current), and L-JJ is the junction under study (smaller critical current).

Figure 10.2a shows the typical magnetic response of the asymmetric SQUID at $T = 40$ mK, with $V_L = -4$ V (fixed) and different values of V_R . For the most asymmetric configuration ($V_R = +10$ V) I_c oscillates around a fixed value of roughly $6 \mu\text{A}$ (I_{cR}) with an amplitude of about 500 nA (I_{cL}). Using the arguments described above, this $I_c(\Phi)$ curve can be converted to $I_s(\phi)$, as shown in Figure 10.2b. Here I_s is the normalized supercurrent defined as $(I_c - I_{cR})/I_{cL}$. We note that there is an uncertainty (less than one period) in the exact position of zero B . This, combined with the unknown CPR of the reference graphene JJ, makes it important to do this conversion carefully, and we describe the details in the SI. The CPR shows a clear deviation from a sinusoidal form, showing a prominent forward skewing (*i.e.*, I_s peaks at $\phi > \pi/2$). We define the skewness of the CPR as $S = (2\phi_{max}/\pi) - 1$ [18], where ϕ_{max} is the phase for which the supercurrent is maximum.

To be certain that we are indeed measuring the CPR of L-JJ, we perform some important checks. We keep I_{cL} fixed and reduce I_{cR} (by reducing V_R). Figure 10.2a shows that reducing I_{cR} merely shifts the $I_c(\Phi)$ downwards and therefore does not affect the extracted CPR, as one would expect. Furthermore, we use the experimentally determined CPR (from Figure 10.2b), the junction asymmetry, and loop inductance as inputs for the resistively and capacitively shunted junction (RCSJ) model to compute the expected SQUID response (see SI for details of the simulations). These plots (solid lines) show an excellent agreement between simulations and experiment, thus confirming that the asymmetry of our SQUID is sufficient to reliably estimate the CPR of L-JJ. Furthermore, it shows that there are no significant effects of inductance in our measurements, which could potentially complicate the extraction of the CPR from $I_c(\Phi)$ in an asymmetric SQUID [23].

To study the gate dependence of the CPR we fix V_R at $+10$ V (to maximize I_{cR}) and study the change in S with V_L (Figure 10.3a) for Dev1 and Dev2. For both devices we find that S is larger on the n-side as compared to the p-side, showing a dip close to the CNP. We note that Dev2 allows us to probe the CPR up to a larger range on the n-side due to its larger geometric asymmetry (see SI for other measurements on Dev2). We expect the skewness to depend strongly on the total transmission through the graphene JJ, which should depend on (a) the number of conducting channels in the graphene, as well as (b) the transparency of the graphene-superconductor interface. The gate voltage V_L obviously changes the Fermi wave vector, but it also changes the contact resistance [24], which plays a significant role in determining S . This can be seen most clearly for Dev2 for high n-doping, where S saturates, despite the fact that I_{cL} continues to increase up to the largest measured density (see inset). At large p-doping S also seems to saturate,

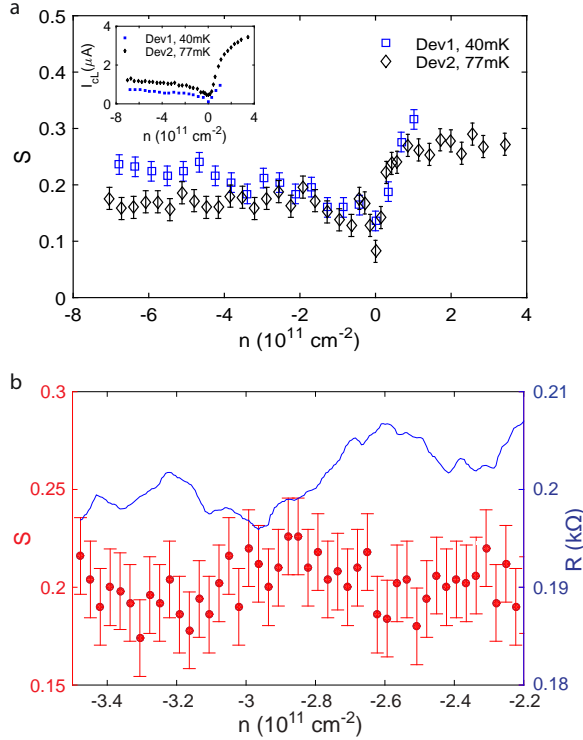


Figure 10.3: (a) Variation of skewness S as a function of carrier density n for Dev1 and Dev2. The larger geometric asymmetry of Dev2 (see text) allows one to reliably probe the CPR up to higher n -doping. Inset shows the variation of I_{cL} with density, (b) S oscillates with carrier density in the p-doped regime in anti-phase with Fabry Péro oscillations in the resistance.

but a closer look (Figure 10.3b) shows that S oscillates in anti-phase with the FP oscillations in resistance. This clearly indicates that in this regime the CPR is modulated by phase coherent interference effects similar to the FP oscillations which affect the total transmission.

We complement our measurements with a minimal theoretical model by solving the corresponding Bogoliubov-de Gennes (BdG) equations to calculate the CPR in graphene JJs. To set the stage, we note that SNS junctions can be characterized by the quasiparticle mean free path l_f in the normal (N) region and the coherence length $\xi_0 = \hbar v_F / \Delta$, where v_F is the Fermi velocity in N. In our devices $L \ll l_f$, *i.e.*, they are in the ballistic regime, and therefore we neglect impurity scattering in our calculations. Taking $v_F \approx 10^6$ m/s for graphene and $\Delta \approx 1.2$ meV for MoRe, one finds $\xi_0 = 548$ nm, which means that in our junctions $L \lesssim \xi_0$, *i.e.*, they are not in the strict short junction limit $L \ll \xi_0$. Consequently, the Josephson current is carried not only by discrete Andreev bound states (ABSs), but also by states in the continuum (CONT) [25–27]. To this end we numerically solve the BdG equations using a tight-binding (TB) model (see Figure 10.4a) and a recently developed numerical approach [16, 28] which handles the ABSs and states in

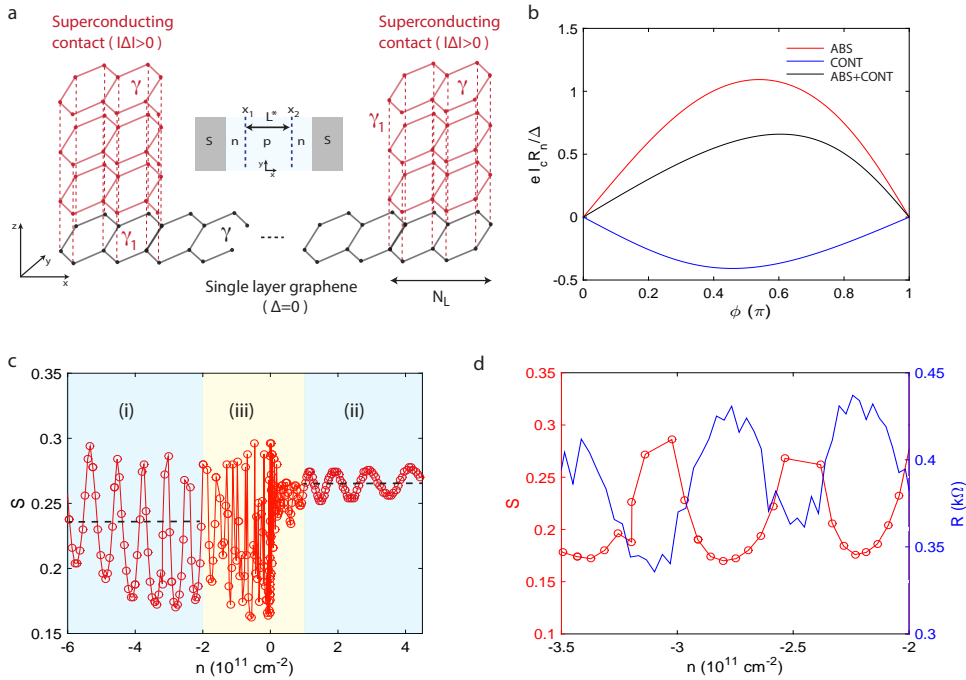


Figure 10.4: (a) The geometry of the system used in the calculations. The superconducting leads are attached in a top-contact geometry to the normal graphene sheet. A periodic boundary condition is applied in the y direction. (Inset) Top view of the system. Due to doping from the S contacts, the normal graphene region is assumed to be n -doped up to a distance x_1 (x_2) from the left (right) contact. The distance $L^* = x_2 - x_1$ is the effective cavity length which depends on the gate voltage applied to the junction, (b) The contribution of the ABSs (red) and continuum CONT (blue) to the total supercurrent (black) as a function of the phase difference for an n -doped junction, (c) The skewness S as a function of doping of the junction. The regimes i-iii indicated by the rectangles are further discussed in the text. Dashed lines show the average S in the p and n doped regime, (d) The skewness (red circles, left axis) and normal state resistance (blue, right axis) vs doping for strong p -doping of the junction.

the continuum on equal footing. The description of both the normal region and the superconducting terminals is based on the nearest-neighbor TB model of graphene [29]. The on-site complex pair-potential Δ is finite only in the superconducting terminals and changes as a step-function at the N-S interface. The results presented here are calculated using the top-contact geometry (Figure 10.4a), a model with perfect edge contacts is discussed in the SI. As observed experimentally, we take into account n -doping from the superconducting contacts (see Figure 10.4b). If the junction is gated into hole-doping, a FP cavity is formed by the two $n-p$ junctions in the vicinity of the left and right superconducting terminals. The length L^* of this FP cavity depends on the gate voltage [5], for stronger hole-doping the $n-p$ junctions shift closer to the contacts. For further details of the model see SI.

Turning now to the CPR calculations, Figure 10.4b shows separately the contribution of the ABS and the continuum to the supercurrent. Since $L \lesssim \xi_0$, the latter contribution is

not negligible and affects both the value of the critical current and the skewness of the CPR. In Figure 10.4c we show the calculated skewness S as a function of the doping of the junction at zero temperature. We consider three regimes: (i) strongly p -doped junction; (ii) large n -doping, (iii) the region around the CNP. We start with the discussion of (i). It is well established that in this case the p - n junctions lead to FP oscillations in the normal resistance as well as in the critical current [4, 5] of graphene JJs. Our calculations, shown in Figure 10.4d, indicate that due to FP interference the skewness also displays oscillations as a function of doping around an average value of $S \approx 0.23$. As already mentioned, similar oscillations are present in the normal state resistance R , however, we find that R oscillates in antiphase with the skewness. Compared to the measurements (Figure 10.3b), our calculations therefore reproduce the phase relation between the oscillations of the skewness and R and give a qualitatively good agreement with the measured values of the skewness. In the strong n -doped regime (case ii) the calculated average skewness of $S = 0.27$ is larger than for p -doped junctions, and very close to the measured values. Small oscillations of S are still present in our results and they are due to the n - n' interfaces, *i.e.*, the difference in the doping close to the contacts (for $x < x_1$ and $x > x_2$) in Figure 10.4a and the junction region ($x_1 < x < x_2$), which enhances backscattering. Our calculations therefore predict smaller skewness for p -doped than for n -doped junctions. The enhancement of S in the n -doped regime can be clearly seen in the measurements of Figure 10.3a. We note that previous theoretical work [15], which calculated the spatial dependence of the pairing amplitude self-consistently, predicted a skewness of $S \approx 0.15$ for n -doped samples with $L < \xi_0$, while a non-self-consistent calculation which took into account only the contribution of the ABS yielded $S \approx 0.42$ [15]. The comparison of these results to ours, and to the measurements, suggest that the skewness may depend quite sensitively on the S-N interface as well as on the L/ξ_0 ratio and that our approach captures the most important effects in these junctions. Finally, we briefly discuss the case (iii), where the measurements show a suppression of the skewness as the CNP is approached. The measured values of $S \sim 0.1$ are similar to those found in diffusive junctions [18], but significantly lower than the theoretical prediction of $S = 0.26$ in the short junction limit [13] at the CNP. This suppression of S is not reproduced in our calculations, instead, we find rapid oscillations as the CNP is approached from the p -doped regime. This discrepancy is likely to be due to effects that are not included in our ballistic model, such as charged scatterers which are poorly screened in this regime, or scattering at the edges, which is more relevant at low densities when only a few open channels are present.

Finally, we study the effect of temperature on the CPR of these JJs. In Figure 10.5a, we compare the CPR in the n -doped regime ($V_R = +1$ V; $n = 0.9 \times 10^{11}$ cm⁻²) at 40 mK and 4.2 K. One clearly sees that at 4.2 K the CPR is sinusoidal. This is consistent with our observation that the critical current modulation of the SQUID is nearly 100 % at 4.2 K (Figure 10.1d), a condition which can only be achieved if the CPR is sinusoidal. Figure 10.5b shows the full temperature dependence of S for two representative values of electron and hole doping. The reduction in skewness with temperature is a consequence of the fact that the higher frequency terms in the CPR arise due to the phase coherent transfer of multiple Cooper pairs and involve longer quasiparticle paths [30], thereby making them more sensitive to temperature. As a result, their amplitude decreases quickly with

increasing temperature [14–16, 18]. Numerical estimates show the same qualitative behavior, however the experimentally determined skewness reaches zero (sinusoidal CPR) faster than the numerics. At this point it is difficult to ascertain the exact reason for this discrepancy, but one possible explanation for this is that the induced superconducting gap in the graphene is somewhat smaller than the bulk MoRe gap, resulting in a faster decay.

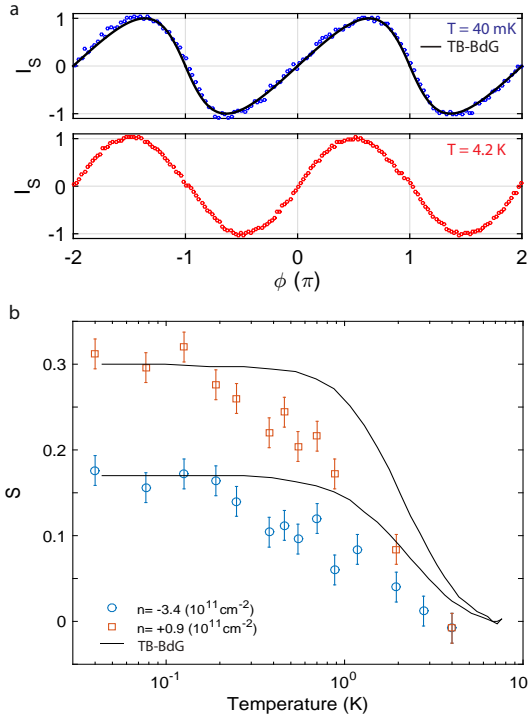


Figure 10.5: (a) CPR for $V_L = +1$ V ($n = 0.9 \times 10^{11}$ cm $^{-2}$) at 40 mK (upper curve) and 4.2 K (lower curve). Solid line shows the calculated CPR. A forward skewness is clearly seen in the curve at 40 mK but is absent at 4.2 K, (b) Variation of S with temperature for electron and hole doping. Increasing the temperature suppresses higher harmonics in the CPR, thereby reducing S until it vanishes near 4.2 K and the curves become sinusoidal. Black lines show the results of tight-binding simulations.

10.3. CONCLUSION

In conclusion, we have used a fully gate-tunable graphene based SQUID to provide measurements of the current-phase relation in ballistic Josephson junctions made with encapsulated graphene. We show that the CPR is non-sinusoidal and can be controlled by a gate voltage. We complement our experiments with tight-binding simulations to show that the nature of the superconductor-graphene interface plays an important role in determining the CPR. We believe that the simplicity of our device architecture and measurement scheme should make it possible to use such devices for studies of the CPR

in topologically non-trivial graphene Josephson junctions.

10.4. SUPPLEMENTARY INFORMATION

10.4.1. DEVICE FABRICATION

Graphene flakes are exfoliated onto silicon chips with 90 nm SiO_2 . Next, h-BN is exfoliated separately on a glass slide covered by a 1-cm² piece of PDMS coated with an MMA/MAA copolymer layer. This glass slide is baked for 20 minutes on a hot plate at 120°C, prior to h-BN exfoliation. The glass slide is mounted on a micromanipulator in a home-built set-up (similar to Ref [31]) equipped with a heating stage. Next, a h-BN flake on the slide is aligned with the target graphene and the substrate is heated to 90°C. The flakes are brought into contact, after which the glass slide is released smoothly such that the graphene flake is picked up by the h-BN flake on the glass slide. Finally, the graphene/h-BN stack is transferred onto another h-BN flake (exfoliated onto a silicon chip with 285 nm SiO_2), at a temperature of 80°C.

The fabrication flow is outlined in Figure 10.6. First MoRe contacts are made to the stack via an etch fill technique [4] using standard e-beam lithography. The sample is plasma-etched for 1 min in a flow of 40/4 sccm CHF_3/O_2 with 60 W power, and 80 μbar pressure. After etching, we immediately sputter ~ 70 nm MoRe using a DC plasma with a power of 100 W in an Argon atmosphere. Next, the MoRe lift-off is completed in hot (54°C) acetone for about 3-4 hours. The two JJs are shaped using another e-beam lithography in which the intended graphene geometry is defined via a PMMA/HSQ mask, followed by CHF_3/O_2 etching. In order to isolate the contacts from the top gate, we use ~ 170 nm of HSQ as a dielectric. Finally, top gates are fabricated by e-beam evaporation of 5nm Cr + 120 nm Au, and subsequent lift off in hot acetone.

10.4.2. BALLISTIC TRANSPORT IN DEV2

10.4.3. MAGNETIC FIELD TO PHASE CONVERSION

In the main text we pointed out that one must take care in converting the flux-periodic oscillations of the critical current of the SQUID $I_c(\Phi)$ to the CPR of L-JJ $I_s(\phi)$. Figure 10.8

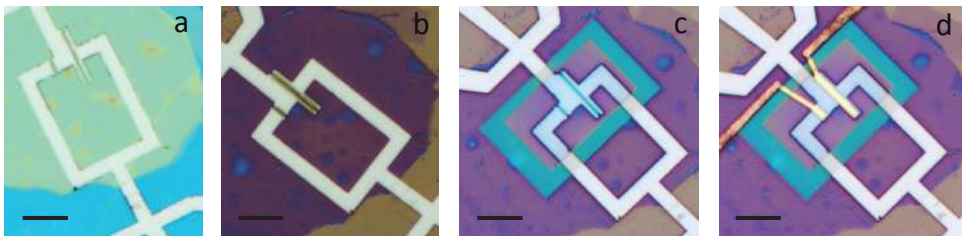


Figure 10.6: Optical images of device after (a) MoRe deposition, (b) shaping of the graphene, (c) dielectric (HSQ) deposition, and (d) deposition of top gates. The scale bar for all images is 5 μm .

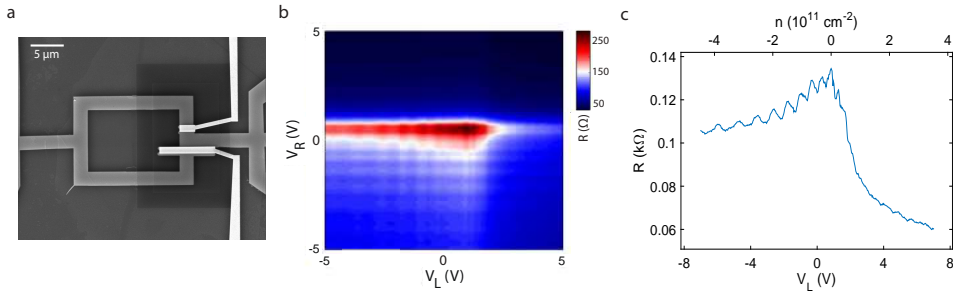


Figure 10.7: (a) Scanning electron micrograph of Dev2. The left junction (L_{JJ}) is $0.4 \mu\text{m}$ long (L) and $8 \mu\text{m}$ wide (W), while the right junction (R_{JJ}) is $0.4 \mu\text{m}$ long and $2 \mu\text{m}$ wide, (b) Resistance map as a function of V_L and V_R at 4.2 K, demonstrating independent control of carrier type and density in left and right JJ, respectively, (c) Resistance vs V_L (while keeping V_R fixed at CNP of R-JJ) showing Fabry-Pérot oscillations in resistance.

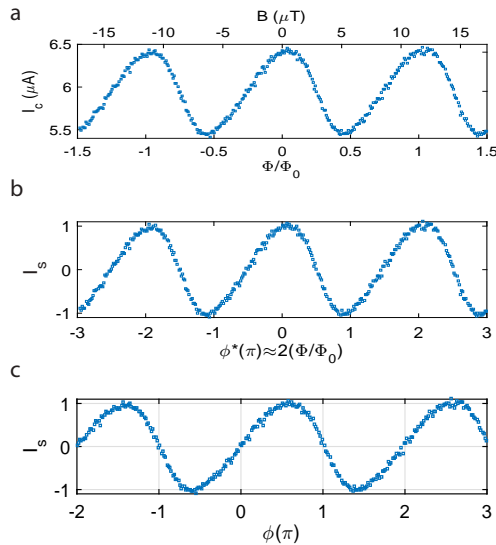


Figure 10.8: (a) The variation of I_c as a function of magnetic field B for $V_L = -4 \text{ V}$ and $V_R = +10 \text{ V}$, (b) The curve in (a) replotted after converting flux Φ to phase ϕ^* , and rescaling I_c to $I_s = (I_c - I_{cR})/I_{cL}$. (c) Curve in (b) offset along the ϕ^* -axis to ensure that $I_s(0) = 0$, thus giving the true phase ϕ axis.

shows how this is done. We start with the upper plot in Figure 10.2a, which is shown here again for convenience (Figure 10.8a). We then subtract a constant background (I_{cR}) about which the curve oscillates and normalize it with respect to the oscillation amplitude (I_{cL}). Also, the flux is converted to phase by $\phi^* \rightarrow 2\Phi/\Phi_0$. This is not the true phase ϕ for two important reasons. Firstly, the zero of the magnetic field is not known precisely. Secondly, the flux to phase conversion is only possible up to a constant offset, which is determined by the CPR of R-JJ (which is a-priori unknown). In order obtain the CPR we then offset the curve in Figure 10.8b along the ϕ^* axis such that the supercurrent at zero phase difference is zero, which finally gives us the CPR. We note that this procedure is

only valid for systems where $I_s(\phi) = -I_s(-\phi)$ and $I_s(0) = 0$, both of which are reasonable assumptions for our graphene JJs.

10.4.4. ELIMINATING INDUCTANCE EFFECTS

In an asymmetric SQUID inductance effects can give rise to skewed $I_c(\Phi)$ curves. It is therefore important to establish that such effects do not dominate the response of the SQUIDS described in this study. To do so, we first provide some qualitative arguments which make it evident that the skewness arises only from a non-sinusoidal CPR. Furthermore, we extract the loop inductance of our SQUID, use it as an input for the RCSJ model and confirm that (within our experimental resolution) the inductance does not play an important role in determining the shape of the $I_c(\Phi)$ curves, and hence does not affect our ability to measure the CPR.

10.4.5. LARGE ASYMMETRY

We have shown that for large asymmetry (*i.e.*, $I_{cR} \gg I_{cL}$), we probe the CPR of L-JJ. We define the asymmetry parameter $a_i = (I_{cR} - I_{cL}) / (I_{cR} + I_{cL})$. Figure 10.9a shows three traces at $T = 40$ mK, where $I_{cL} \approx 0.5 \mu\text{A}$ is kept fixed and I_{cR} is varied from $6 \mu\text{A}$ (black trace, $a_i \approx 0.83$) to $2.8 \mu\text{A}$ (red trace, $a_i \approx 0.78$). Figure 10.9b shows that all three curves collapse despite the fact that the maximum critical current ($I_{max} = I_{cR} + I_{cL}$) changes by a factor of two. If the skewness was dominated by inductance effects, we would have not expected this collapse, since the screening parameter $\beta_L = I_{max}L / \Phi_0$ increase by a factor

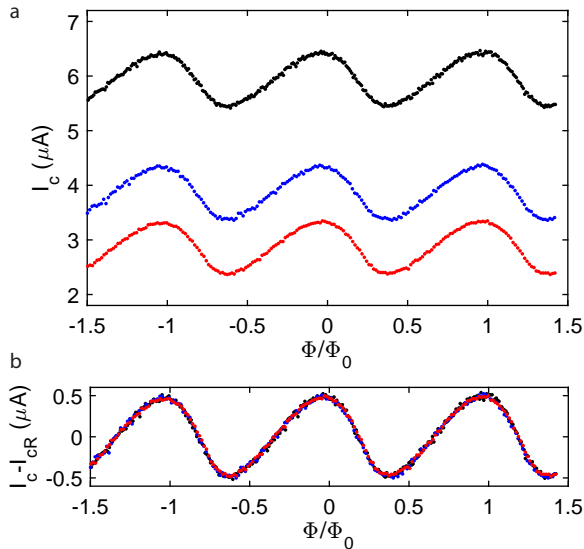


Figure 10.9: (a) $I_c(\Phi)$ plots with fixed I_{cL} , but varying I_{cR} , as shown earlier in Figure 10.2a, (b) The curves in (a), now plotted as $(I_c - I_{cR})$ vs. Φ . Collapse of the curves shows that the skewness does not depend on I_c , and hence represents the CPR of L-JJ.

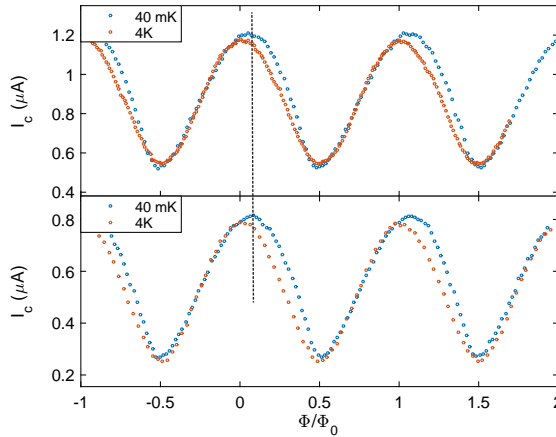


Figure 10.10: $I_c(\Phi)$ plots at $I_{max} \approx 1.2 \mu\text{A}$ (upper) and $\approx 0.8 \mu\text{A}$ (lower) for low asymmetries of $a_i = 0.45$, $a_i = 0.33$ respectively. The curves at 40 mK are skewed (indicated by position of dashed line), while those at 4.2 K are not.

of two (going from the red trace to the blue trace). In other words, the combined effect of large asymmetry and inductance should have resulted in a larger skewing of the black trace (maximum β_L and a_i) as compared to the red one.

10.4.6. INTERMEDIATE ASYMMETRY

We have shown in Figure 10.5 that the skewness of the CPR decreases with increasing temperature, resulting in a sinusoidal CPR at 4.2 K. One might argue that this is consistent with inductance effects, whereby an increase in temperature reduces the critical currents and hence β_L . To eliminate this possibility, we compare $I_c(\Phi)$ at 40 mK and 4.2 K. Figure 10.10a,b show two such data sets. In each case the gate voltages were tuned such that both I_{max} and a_i were roughly the same for both temperatures. We see that at 40 mK the curves are noticeably skewed as compared to 4.2 K. The asymmetry here is not sufficient to directly extract the CPR, but it clearly demonstrates that the non-sinusoidal CPR also manifests itself in skewed $I_c(\Phi)$ curves at intermediate asymmetry. We note that this argument is made stronger by the fact that the inductance at 4.2 K should in fact be larger than that at 40 mK, since the inductance of the MoRe loop is dominated by kinetic inductance, which increases at higher temperatures. In other words, one would expect inductance related effects to be enhanced at higher temperatures, rather than become suppressed.

10.4.7. ESTIMATING THE LOOP INDUCTANCE

Figure 10.11a shows $I_c(\Phi)$ measurements of an asymmetric SQUID at 4.2 K, where we have established that the CPR is sinusoidal. The position of maximum I_c for positive and negative current bias are offset along the flux axis due to self-flux effects [32]. This

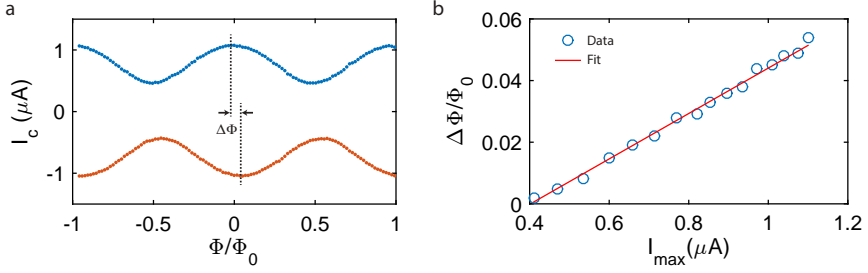


Figure 10.11: (a) $I_c(\Phi)$ curves for an asymmetric SQUID, (b) Variation of $\Delta\Phi$ with I_{max} . Here I_{cL} is kept fixed, while I_{cR} is varied. Blue circles are the experimentally obtained values of $\Delta\Phi$ and the red line is a linear fit to the data.

shift is given by: $\Delta\Phi = 2L(I_{cR} - I_{cL})$, where I_{cR} and I_{cL} are the critical current of right and left junction respectively. Figure 10.11b shows the variation of $\Delta\Phi$ with I_{max} . These values are obtained by keeping $I_{cL} \approx 0.2 \mu\text{A}$ fixed and varying I_{cR} from $0.2 \mu\text{A}$ (symmetric configuration) to $0.9 \mu\text{A}$ (highly asymmetric). Since $\partial\Delta\Phi/\partial I_{cR} = L$, a linear fit (red line) allow us to extract $L \approx 152 \text{ pH}$. Since MoRe is a highly disordered superconductor, its inductance is dominated by the kinetic inductance and the low temperature inductance $L(0) = L(T)[1 - (T/T_c)^2]$, giving $L \approx 110 \text{ pH}$ at $T = 40 \text{ mK}$. We use this inductance to compare our experiments with the RCSJ simulations described below.

10.4.8. RCSJ MODEL

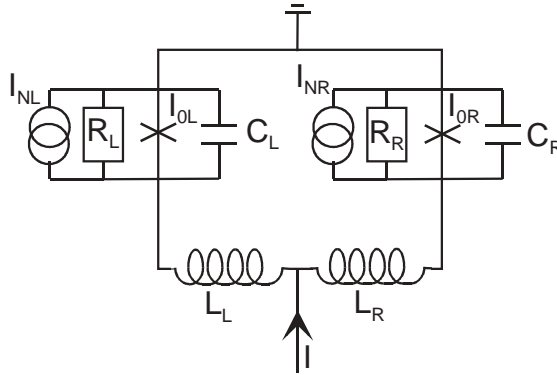


Figure 10.12: Circuit diagram of the asymmetric SQUID.

To model the asymmetric SQUID we consider the circuit shown in Figure 10.12. The Josephson junctions are described by the resistively and capacitively shunted junction (RCSJ) model[33, 34] by Josephson currents with phases δ_L and δ_R and amplitudes $I_{cL} = I_c(1 - a_i)$ and $I_{cR} = I_c(1 + a_i)$, resistors R_L and R_R , and capacitors C_L and C_R . The Josephson currents are given by $I_L = I_c(1 - a_i) \cdot f_L(\delta_L)$ and $I_R = I_c(1 + a_i) \cdot f_L(\delta_L)$, where

$f_i(\delta_i)$ are the normalized current-phase relations of the left and right JJ, respectively. The Nyquist noise arising from the two resistors is described by two independent current noise sources I_{NL} and I_{NR} having white spectral power densities $4k_B T/R_L$ and $4k_B T/R_R$, respectively. The two arms of the SQUID loop have inductances L_L and L_R . The total inductance L is the sum of the geometric (L_g) and the kinetic (L_k) inductance. The loop is biased with a current I , and a flux Φ is applied to the loop.

In the following we are interested only in static solutions and normalize currents by I_c . The currents i_L and i_R through the left (right) arm of the SQUID are then given by:

$$i_R = (1 + a_i) \cdot f_R(\delta_R). \quad (10.1)$$

$$i_L = (1 - a_i) \cdot f_L(\delta_L). \quad (10.2)$$

Assuming for simplicity that $L_L = L_R$ (a reasonable assumption based on our device geometry) the normalized circulating current j is given by:

$$j = \frac{i_R - i_L}{2} = \frac{1}{\beta_L} \left(\frac{\delta_L - \delta_R}{\pi} - 2\Phi/\Phi_0 \right). \quad (10.3)$$

and the maximum current across the SQUID is $i_{cR} + i_{cL}$. From Equation 10.3 we obtain

$$\delta_L = 2\pi\Phi/\Phi_0 + \delta_R + \pi\beta_L \frac{i_R - i_L}{2}. \quad (10.4)$$

Let us consider the case $a_i \gg 0$, *i.e.*, the right junction has a much larger critical current than the left one. As we will see, in this case the modulation of the SQUID critical current reflects the CPR of the left junction, provided that $\beta_L \ll 1$.

$$i = i_R + i_L = (1 + a_i) \cdot f_R(\delta_R) + (1 - a_i) \cdot f_L(\delta_L). \quad (10.5)$$

From Equation 10.4, for $\beta_L \ll 1$, we obtain $\delta_L \approx 2\pi\Phi/\Phi_0 + \delta_R$. Thus

$$i = i_R + i_L = (1 + a_i) \cdot f_R(\delta_R) + (1 - a_i) \cdot f_L(2\pi\Phi/\Phi_0 + \delta_R). \quad (10.6)$$

Let us assume that $i > 0$. Then the task is to maximize i with respect to δ_R , to obtain $i_{c,SQUID}$ vs Φ/Φ_0 . If the critical current of the right JJ is much bigger than the critical current of the left JJ, the value of δ_R will be close to the value δ_R^0 where the CPR of the right JJ has its maximum. We thus Taylor expand:

$$f_R(\delta_R) \approx f_R(\delta_R^0) + \frac{1}{2} \frac{d^2 f_R}{d\delta_R^2} \Big|_{\delta_R^0} (\delta_R - \delta_R^0)^2 + \dots \quad (10.7)$$

Note that in Equation 10.7 the first derivative of f_R is zero, because we look for the maximum of this CPR. If the second derivative (< 0) is reasonably peaked, δ_R will be very close to δ_R^0 and we obtain:

$$i_{c,SQUID} \approx (1 + a_i) \cdot f_R(\delta_R^0) + (1 - a_i) \cdot f_L(2\pi\Phi/\Phi_0 + \delta_R^0) = const + (1 - a_i) f_L(2\pi\Phi/\Phi_0 + \delta_R^0). \quad (10.8)$$

That means that $i_{c,SQUID}$ vs. Φ/Φ_0 probes the CPR of the left JJ up to a phase shift δ_R^0 . f_L can be evaluated further if one assumes that $f_L = 0$ at $\delta_L = 0$ and that $\min(f_L) = -\max(f_L)$.

In Figure 10.2a we have compared our experiments with a full RCSJ simulation, as described above. These simulations involve no free parameters since we use the experimentally determined inductance, asymmetry (a_i), and CPR of L-JJ $f_L(\delta_L)$ as input parameters. For simplicity, the numerical plots were generated assuming a sinusoidal CPR for the reference junction R-JJ, shown as the blue curve in the Figure 10.13a. The red curve shows how $I_c(\Phi)$ changes when R-JJ is assumed to have a non-sinusoidal CPR (with a functional form similar to that extracted for L-JJ). The only effect this has is to offset the simulated curves along the flux axis. This is a consequence of the fact that δ_R^0 (as described above) is different for the two cases. However, we see in Figure 10.13b that these two cases perfectly overlap with an appropriate offset along the flux axis. This confirms the fact that an incomplete knowledge of the CPR of R-JJ is (in practice) equiv-

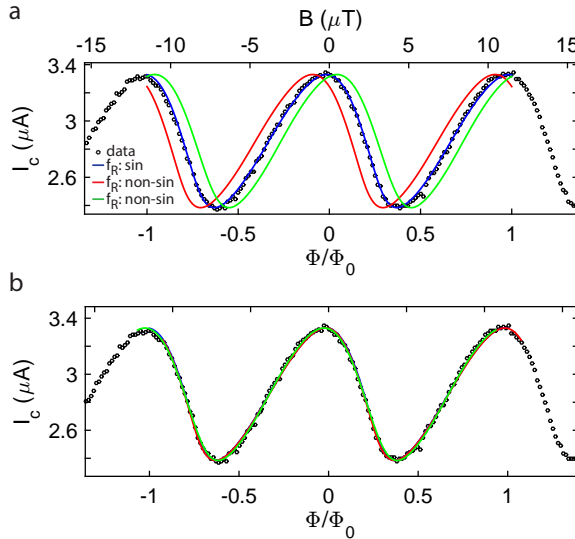


Figure 10.13: (a) Experimental $I_c(\Phi)$ (black) along with RCSJ simulations for a SQUID with $a_i = 0.83$. The blue (red) curve corresponds to a sinusoidal (non-sinusoidal) CPR f_R for the reference junction R-JJ, with the experimentally determined $\beta_L = 0.34$. The green curve shows the result for $\beta_L = 0.01$. The data has been offset along the flux axis to match the blue curve, (b) Same as (a), but with the red and green curves shifted along the flux axis.

alent to an unknown offset in magnetic field, and therefore does not affect our ability to accurately determine the functional form of the CPR of L-JJ. The green curve in Figure 10.13a is a simulation with $\beta_L = 0.01$ (*i.e.*, in the limit where the loop inductance is negligible). Looking carefully at Figure 10.13b shows that this $I_c(\Phi)$ has a slightly different shape as compared to the blue/red curves. However, this difference is well within the error bars for our estimation of the skewness, and we can conclude that the functional form of the $I_c(\Phi)$ curves is not dominated by the inductance effects, but by the non-sinusoidal CPR of L-JJ. This is in agreement with the conclusions drawn from more qualitative arguments presented in the previous section.

10.4.9. TIGHT-BINDING BOGOLIUBOV-DE GENNES CALCULATIONS

10.4.10. DETAILS OF THE THEORETICAL MODEL

In this Section we provide further details of the theoretical model that we used in our numerical calculations. As it will be clear from the following discussion, we found that in order to obtain a good qualitative agreement with the measurements, a realistic and detailed model of the Josephson junction, especially the interface between the superconductor and the normal regions, is needed.

We assume that the graphene flake which serves as a weak link is perfectly ballistic and scattering processes only occur at the interfaces between regions of different doping in the normal part of the junction or between the superconductor and the normal region. The normal (N) and superconducting (S) regions are of the same width in our calculations. This allows us to use periodic boundary conditions perpendicular to the transport direction. The transverse momentum q_n is a good quantum number and the DC Josephson current can be calculated as a sum over all q_n :

$$I_J(\Delta\phi) = \sum_n I_J(q_n, \Delta\phi), \quad (10.9)$$

where $I_J(q_n, \Delta\phi)$ is the momentum resolved Josephson current calculated for a specific transverse momentum q_n via the contour integral method developed recently in Reference [16]. For wide junctions and high dopings, when there are many transverse momenta, the exact form of the boundary conditions is not important and therefore we used the infinite mass boundary condition to obtain q_n : $q_n = (n + \frac{1}{2}) \frac{\pi}{W}$, where $n = 0, 1, 2, \dots$ and W is the width of the junction.

The description of both the N region and the S terminals is based on the nearest-neighbour tight-binding model of graphene[29]

$$\hat{H} = \sum_i U_i c_i^\dagger c_i - \sum_{\langle ij \rangle} \gamma c_i^\dagger c_j + h.c. \quad (10.10)$$

where U_i is the on-site energy on the atomic site i , $\gamma = 2.97$ eV is the hopping amplitude between the nearest-neighbor atomic sites $\langle ij \rangle$ in the graphene lattice, and c_i^\dagger (c_i) is a creation (annihilation) operator for electrons at site i . We considered two junction geometries. Most of our results were obtained using the top-contact geometry, which

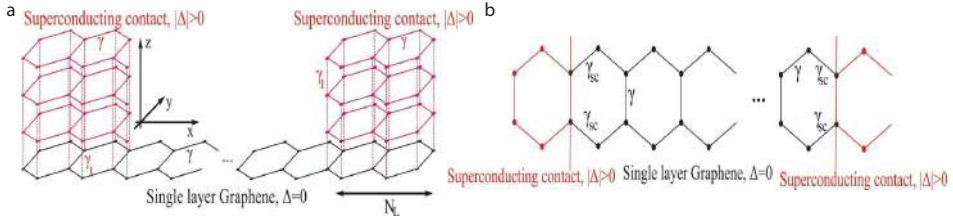


Figure 10.14: (a) The geometry of the top contacted superconductor-graphene-superconductor junction. N_L is the number of unit cells under the superconducting contacts in the x direction, (b) The side-contacted geometry. The interface resistance between the S and regions is modelled by a hopping $\gamma_{sc} < \gamma$. In both geometries the lattice is translational invariant in the y direction

is shown in Figure 10.4a and for convenience repeated here in Figure 10.14(a). The S terminals are described by vertically stacked graphene layers (AA stacking) where the inter-layer hopping is given by $\gamma_1 = 0.6\text{eV}$. The same inter-layer hopping γ_1 was also used between the S terminals and the N region. The S leads are coupled to the normal graphene sheet over N_L unit cells. The result do not depend strongly on the exact value of N_L , therefore we used $N_L = 10$ in our calculations.

To mimic metallic leads with many open channels, the S terminals are highly n -doped. This is described by an on-site potential U_n and we used $U_n = 350\text{meV}$ in our calculations. For high n -doping of the N region we calculated an average transparency of $Tr = 0.82$ for the junction, see the Supplementary of Reference [5] for the precise definition of Tr . We find that the calculated Tr does not depend very sensitively on the precise value U_n and γ_1 because most of the backscattering taking place at the interface of the S leads and the N region is due to a “geometric” effect: the electron trajectories have to turn at right angle to arrive from the lead into the N region. Moreover, we find that for $Tr = 0.82$ the calculated dependence of the normal state resistance R_n on the doping of the N region agrees qualitatively well with the measurements where the right JJ was kept at the charge neutrality point (Figure 10.1c and Figure 10.17a below). (We did not try to achieve quantitative agreement for R_n because in the experiments the resistance of the two junctions are always measured in parallel, whereas we used single junctions in the calculations.)

As shown in Figure 10.14b and discussed further later on, we have also made calculations using the side-contact geometry. For both geometries we used open boundary conditions for the leads in the transport direction (which is the z direction in top-contacted geometry and the x direction in the side-contacted one, see Figure 10.14).

In contrast to the S leads, which are always n -doped in our calculations, the normal region of the JJ can be either n or p doped depending on the gate voltage. This is modeled by a doping potential U_p . Experimentally, it was shown that the superconducting terminals n -dope the normal region of the JJ [4, 5]. This n -doped region extends to a distance x_1 ($L_0 - x_2$) from the left (right) terminal, where L_0 is the distance between the two S leads. The potential profile in the junction can be therefore either $n p n$ or $n n' n$. The exact value of the x_1 and x_2 , and hence the cavity length $L^* = x_2 - x_1$, however, depends

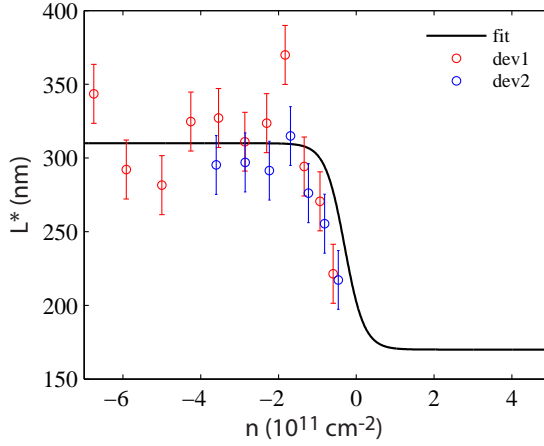


Figure 10.15: The experimental cavity length L_{exp}^* vs doping (symbols) and the fitting function used to obtain the L^* in our calculations (solid line).

on the gating of the JJ. In the npn regime, where clear FP oscillations can be measured in the normal state resistance R_n in our devices, we extracted the experimental cavity length using the relation $L_{exp}^* \approx 2\sqrt{\pi n}/\delta n$, where δn is the density difference between consecutive peaks in R_n [35].

The results of this analysis are summarized in Figure 10.15. We find that $L_{exp}^* \approx 310$ nm is roughly constant for $n < -1.8 \times 10^{11} \text{ cm}^{-2}$, but it decreases for densities approaching the CNP. In order to extract the theoretical cavity length L^* for $n > -1.8 \times 10^{11} \text{ cm}^{-2}$, we fitted the experimental results by the function

$$L^*(U_p) = \frac{L_{exp}^* - L_{nn'n}}{1 + \exp[\beta(n - n_0)]} + L_{nn'n}. \quad (10.11)$$

Here $L_{nn'n}$ is the cavity length for strongly n doped junctions which could not be determined from the R_n measurements, therefore we used $L_{nn'n} = 170$ nm. As mentioned above, a good qualitative agreement between the calculated and measured normal state resistance is achieved using this value of $L_{nn'n}$. We have also checked that for $L_{nn'n} \gtrsim 160$ nm the calculation results do not depend strongly on the exact value of $L_{nn'n}$. The two fitting parameters in Eq. (10.11) are β and n_0 and we found $\beta = 4.0$ and $n_0 = -0.3$, see Figure 10.15. Once L^* is determined, the parameters x_1 and x_2 are given by $x_1 = \frac{L_0 - L^*(U_p)}{2}$ and $x_2 = L_0 - x_1$. The total potential profile along the junction, which describes the smooth transition between the highly doped regions ($x < x_1$ and $x > x_2$) and the central part of the junction ($x_1 \leq x \leq x_2$) is modeled by

$$U(x) = U_n + \frac{U_p - U_n}{2} \left(\tanh\left(\frac{x - x_1}{l_{tr}}\right) - \tanh\left(\frac{x - x_2}{l_{tr}}\right) \right). \quad (10.12)$$

where the parameter l_{tr} controls the smoothness of the transition. We used $l_{tr} = \frac{2}{5}x_1$ in our calculations corresponding to a relatively sharp transition. Larger values of l_{tr} would

effectively mean that the leads n dope the N region of the junction and the doping there would therefore not be determined by U_p .

Finally, superconductivity in the S terminals is modelled by a on-site, complex pair-potential Δ which goes to zero as a step-function at the S-N interface. We made sure that the Fermi-wavelengths λ_N and λ_S in the N and S regions, respectively, satisfy $\lambda_S \ll \lambda_N$. This ensures that the exact spatial dependence of the superconducting pair potential at the N-S interface is not very important in the calculations[13].

10.4.11. SOFT VS HARD SUPERCONDUCTING GAP

Following Reference [36], we also considered the effect of quasiparticle broadening in the superconducting terminals by introducing a complex energy shift $E \rightarrow E + i\eta$ in the self-energy calculations. Such a broadening, described by the parameter η , can arise due to scattering with phonons or other electrons or due to other effects leading to quasiparticle poisoning.

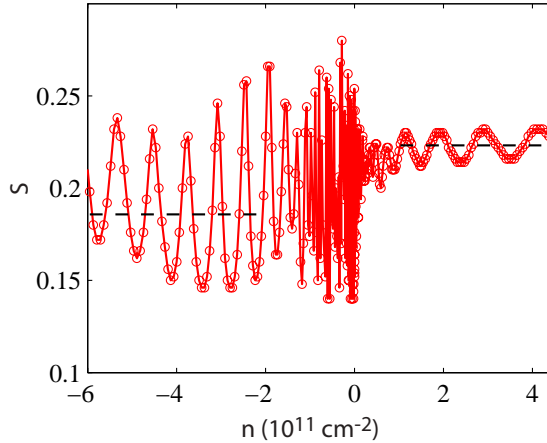


Figure 10.16: The calculated skewness vs doping for soft superconducting gap, *i.e.*, $\eta = 0.17\Delta$.

We find that a finite η can considerably affect the value of the calculated critical current I_c . Since I_c is not the main focus of this work, we do not discuss the details here. Instead, we present results to illustrate the effect of η on the skewness. We repeated the calculations using $\eta = 0.17\Delta$ and the results are shown in Figure 10.16. Comparing Figure 10.4d and Figure 10.16, one can notice that the results are qualitatively very similar, but for $\eta = 0$ the average skewness is larger for both npn and $nn'n$ doping than for $\eta \neq 0$. We note that in the $nn'n$ regime the calculated average skewness $\bar{S} = 0.27$ for $\eta = 0$ is closer to the measured one $S_{exp} \approx 0.28$ than the result $\bar{S} = 0.22$ for $\eta = 0.17\Delta$. The opposite is true in the npn regime, where the calculations with $\eta = 0.17\Delta$ ($\eta = 0$) yielding $\bar{S} = 0.19$ ($\bar{S} = 0.22$) give better agreement with the measurements ($S_{exp} \approx 0.2$). We were not able to achieve an equally good agreement in both the npn and $nn'n$ regimes using a single value of η . This may indicate that η depends on the doping of the junction, but one

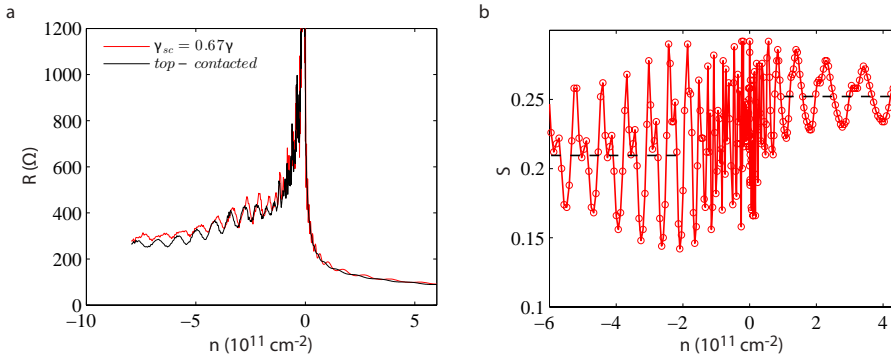


Figure 10.17: (a) Comparison of the calculated normal state resistance vs doping for top- and side-contacted junctions, (b) Skewness vs doping calculated in the side-contact geometry. Dashed lines indicate the average skewness in the n and p doped regime.

would need a more microscopic understanding of the processes that contribute to η . We emphasize, however, that η is not the only parameter which can affect the value of the skewness. Generally, the value of the skewness depends on the interface between the S and N regions. Calculations not shown here indicated that the presence/absence of a smooth transition between the highly doped leads and the normal graphene region (the parameter l_{tr} in Eq.10.12) and the value of the hopping amplitude γ_{sc} in Figure 10.14(b) between the S and N regions can also affect the results. However, we fixed the value of the parameters describing the junction such that we obtain a qualitatively good agreement for R_n (as discussed previously) and did not change these parameters in the skewness calculations.

10.4.12. CALCULATIONS USING THE SIDE CONTACT GEOMETRY

We also performed calculations using the side-contact geometry, which is shown in Figure 10.14(b). This contact geometry has recently been employed, *e.g.*, in Reference [37] to model diffusive graphene JJs both in the short and in the long junction regime. The most important results of our calculations are shown in Figure 10.17. We have used the same doping profile $U(x)$ along the junction as in the top-contact geometry. As it can be seen in Figure 10.17(a), by choosing $\gamma_{sc} = 0.67\gamma$, the doping dependence of the normal state resistance is qualitatively very similar for both models. One can notice, however, that the amplitude of the R_n oscillations for $nn'n$ doping is larger in the side-contact geometry. In the npn regime the amplitude of the FP oscillations is somewhat different, but the oscillations are in the same phase, except for large p doping.

The skewness calculation for the side contact geometry is shown in Figure 10.17(b). We used the same Δ and $\eta = 0.17\Delta$ as for the corresponding calculation in the top-contact geometry. The result are qualitatively similar to those shown in Figure 10.16 and Figure 10.4c. In particular, the average skewness is different in the npn and $nn'n$ doping regime, but the obtained \bar{S} values are larger than the ones calculated in the top-contact

geometry for $\eta = 0.17\Delta$. However, the amplitude of the skewness oscillations is larger in the side-contact geometry, especially for $nn'n$ doping, where they are three times larger than in Figure 10.4c. Such large oscillations are not present in the experimental data and for this reason we find a better overall agreement between the experiments the the calculations using the top-contact geometry. Finally, we briefly note in the vicinity of the CNP one can see large oscillations in the skewness and therefore both models fail to reproduce the experimental results in this regime.

REFERENCES

- [1] G. Nanda, J. L. Aguilera-Servin, P. Rakyta, A. Kormányos, R. Kleiner, D. Koelle, K. Watanabe, T. Taniguchi, L. M. K. Vandersypen, and S. Goswami, *Current-phase relation of ballistic graphene Josephson junctions*, Nano Letters (2017).
- [2] D. K. Efetov, L. Wang, C. Handschin, K. B. Efetov, J. Shuang, R. Cava, T. Taniguchi, K. Watanabe, J. Hone, C. R. Dean, and P. Kim, *Specular interband Andreev reflections at van der Waals interfaces between graphene and NbSe₂*, Nature Physics **12**, 328 (2016).
- [3] G. H. Lee, K. F. Huang, D. K. Efetov, D. S. Wei, S. Hart, T. Taniguchi, K. Watanabe, A. Yacoby, and P. Kim, *Inducing superconducting correlation in quantum Hall edge states*, arXiv:1609.08104 (2016).
- [4] V. E. Calado, S. Goswami, G. Nanda, M. Diez, A. R. Akhmerov, K. Watanabe, T. M. K. T. Taniguchi, and L. M. K. Vandersypen, *Ballistic Josephson junctions in edge-contacted graphene*, Nature Nanotechnology **10**, 761 (2015).
- [5] M. B. Shalom, M. J. Zhu, V. I. Fal'ko, A. Mishchenko, A. V. Kretinin, K. S. Novoselov, C. R. Woods, K. Watanabe, T. Taniguchi, A. K. Geim, and J. R. Prance, *Quantum oscillations of the critical current and high-field superconducting proximity in ballistic graphene*, Nature Physics **12**, 318 (2016).
- [6] M. T. Allen, O. Shtanko, I. C. Fulga, A. R. Akhmerov, K. Watanabe, T. Taniguchi, P. Jarillo-Herrero, L. S. Levitov, and A. Yacoby, *Spatially resolved edge currents and guided-wave electronic states in graphene*, Nature Physics **12**, 128 (2016).
- [7] F. Amet, C. T. Ke, I. V. Borzenets, J. Wang, K. Watanabe, T. Taniguchi, R. S. Deacon, M. Yamamoto, Y. Bomze, S. Tarucha, and G. Finkelstein, *Supercurrent in the quantum Hall regime*, Science **352**, 966 (2016).
- [8] I. V. Borzenets, F. Amet, C. T. Ke, A. W. Draelos, M. T. Wei, A. Seredinski, K. Watanabe, T. Taniguchi, Y. Bomze, M. Yamamoto, S. Tarucha, and G. Finkelstein, *Ballistic graphene Josephson junctions from the short to the long regime*, Physical Review Letters **117**, 237002 (2016).
- [9] A. Murani, A. Kasumov, S. Sengupta, Y. Kasumov, V.T.Volkov, I. Khodos, F. Brisset, R. Delagrèe, A. Chepelianskii, R. Deblock, H. Bouchiat, and S. Guéron,

- Ballistic edge states in bismuth nanowires revealed by SQUID interferometry*, arXiv:1609.04848 (2016).
- [10] H. Miyazaki, A. Kanda, and Y. Ootuka, *Current-phase relation of a superconducting quantum point contact*, *Physica C* **437-438**, 217 (2006).
- [11] M. L. D. Rocca, M. Chauvin, B. Huard, H. Pothier, D. Esteve, and C. Urbina, *Measurement of the current-phase relation of superconducting atomic contacts*, *Physical Review Letters* **99**, 127005 (2007).
- [12] J. Wiedenmann, E. Bocquillon, R. S. Deacon, S. Hartinger, O. Herrmann, T. M. Klapwijk, L. Maier, C. Ames, C. Brüne, C. Gould, A. Oiwa, K. Ishibashi, S. Tarucha, H. Buhmann, and L. W. Molenkamp, *4π -periodic Josephson supercurrent in HgTe-based topological Josephson junctions*, *Nature Communications* **7**, 10303 (2016).
- [13] M. Titov and C. W. J. Beenakker, *Josephson effect in ballistic graphene*, *Physical Review B* **74**, 041401 (2006).
- [14] I. Hagymási, A. Kormányos, and J. Cserti, *Josephson current in ballistic superconductor-graphene systems*, *Physical Review B* **82**, 134516 (2010).
- [15] A. M. Black-Schaffer and J. Linder, *Strongly anharmonic current-phase relation in ballistic graphene Josephson junctions*, *Physical Review B* **82**, 184522 (2010).
- [16] P. Rakyta, A. Kormányos, and J. Cserti, *Magnetic field oscillations of the critical current in long ballistic graphene Josephson junctions*, *Physical Review B* **93**, 224510 (2016).
- [17] P. San-Jose, J. Lado, R. Aguado, F. Guinea, and J. Fernández-Rossier, *Majorana zero modes in graphene*, *Phys. Rev. X* **5**, 041042 (2015).
- [18] C. D. English, D. R. Hamilton, C. Chialvo, I. C. Moraru, N. Mason, and D. J. V. Harlingen, *Observation of non-sinusoidal current-phase relation in graphene Josephson junctions*, *Physical Review B* **94**, 115435 (2016).
- [19] G. H. Lee, S. Kim, S. H. Jhi, and H. J. Lee, *Ultimately short ballistic vertical graphene Josephson junctions*, *Nature Communications* **6**, 6181 (2015).
- [20] Ç. Girit, V. Bouchiat, O. Naaman, Y. Zhang, M. F. Crommie, A. Zettl, and I. Siddiqi, *Tunable graphene dc superconducting quantum interference device*, *Nano letters* **9**, 198 (2008).
- [21] Ç. Girit, V. Bouchiat, O. Naaman, Y. Zhang, M. F. Crommie, A. Zettl, and I. Siddiqi, *Current-phase relation in graphene and application to a superconducting quantum interference device*, *Physica Status Solidi B* **246**, 2568 (2009).
- [22] A. A. Golubov, M. Y. Kupriyanov, and E. Il'ichev, *The current-phase relation in Josephson junctions*, *Reviews of Modern Physics* **76**, 411 (2004).
- [23] T. A. Fulton, L. N. Dunkleberger, and R. C. Dynes, *Quantum interference properties of double Josephson junctions*, *Physical Review B* **6**, 855 (1972).

- [24] L. Wang, I. Meric, P. Y. Huang, Q. Gao, Y. Gao, H. Tran, T. Taniguchi, K. Watanabe, L. M. Campos, D. A. Muller, J. Guo, P. Kim, J. Hone, K. L. Shepard, and C. R. Dean, *One-dimensional electrical contact to a two-dimensional material*, *Science* **342**, 614 (2013).
- [25] A. V. Svidzinsky, T. N. Antsygina, and E. N. Bratus, *Concerning the theory of the Josephson effect in pure SNS junctions*, *Journal of Low Temperature Physics* **10**, 131 (1973).
- [26] D. Giuliano and I. Affleck, *Topological superconductor–Luttinger liquid junctions*, *Journal of Statistical Mechanics*, P02034 (2013).
- [27] E. Perfetto, G. Stefanucci, and M. Cini, *Equilibrium and time-dependent Josephson current in one-dimensional superconducting junctions*, *Physical Review B* **80**, 205408 (2009).
- [28] *The numerical calculations were performed with the EQUUs software*, see <http://eqt.elte.hu/equus/home>.
- [29] K. Wakabayashi, M. Fujita, H. Ajiki, and M. Sigrist, *Electronic and magnetic properties of nanographite ribbons*, *Physical Review B* **59**, 8271 (1999).
- [30] T. T. Heikkilä, J. Särkkä, and F. K. Wilhelm, *Supercurrent-carrying density of states in diffusive mesoscopic Josephson weak links*, *Physical Review B* **66**, 184513 (2002).
- [31] A. Castellanos-Gomez, M. Buscema, R. Molenaar, V. Singh, L. Janssen, H. S. J. van der Zant, and G. A. Steele, *Deterministic transfer of two-dimensional materials by all-dry viscoelastic stamping*, *2D Materials* **1**, 011002 (2014).
- [32] S. Goswami, E. Mulazimoglu, A. M. R. V. L. Monteiro, R. Wölbling, D. Koelle, R. Kleiner, Y. M. Blanter, L. M. K. Vandersypen, and A. D. Caviglia, *Quantum interference in an interfacial superconductor*, *Nature Nanotechnology* **11**, 861 (2016).
- [33] D. E. McCumber, *Effect of ac impedance on dc voltage-current characteristics of superconductor weak-link junctions*, *Journal of Applied Physics* **39**, 3113 (1968).
- [34] W. C. Stewart, *Current-voltage characteristics of Josephson junctions*, *Applied Physics Letters* **12**, 277 (1968).
- [35] P. Rickhaus, M. H. L. R. Maurand, M. Weiss, K. Richter, and C. Schönenberger, *Balistic interferences in suspended graphene*, *Nature Communications* **4**, 2342 (2013).
- [36] S. Takei, B. M. Fregoso, H. Y. Hui, and A. M. L. S. D. Sarma, *Soft superconducting gap in semiconductor Majorana nanowires*, *Physical Review Letters* **110**, 186803 (2013).
- [37] C. Li, S. Guéron, A. Chepelianskii, and H. Bouchiat, *Full range of proximity effect probed with superconductor/graphene/superconductor junctions*, *Physical Review B* **94**, 115405 (2016).

11

OUTLOOK

This chapter is intended to give an insight into the current trends and future directions of helium ion microscopy and graphene research. Although both are completely different subjects, they are core ingredients of this thesis. I will briefly discuss the current trends in the aforementioned research areas along with the related work elsewhere. This chapter ends with a discussion on the future directions and some technical challenges.

11.1. SUMMARY OF THE STUDIES IN THIS THESIS

11.1.1. MODIFICATION OF GRAPHENE USING HIM

The first two chapters of this thesis are concentrated on the modification of boron nitride encapsulated graphene devices using a focused helium beam. I sub-divided that study into two parts: the first part is the evolution of beam induced defects in encapsulated graphene, and the second part is the fabrication of nanoribbon devices. We observed experimentally the evolution of the D' Raman peak in the defected graphene, by which the influence of the environment is studied. This study confirmed self-healing of graphene, which has also been observed during high energy electron beam bombardment, but at an elevated temperature[1].

Because of self-healing and beam induced N-C exchange, the bombarded graphene became n-doped. There is significant interest in the controlled n-doping of graphene via chemical and physical methods. This is so far the only demonstration of n-doping via an ion beam.

The second part entails the fabrication of graphene nanoribbon devices using the helium beam. Although we see the source-drain gap in the fabricated narrow ribbons, the devices suffered strongly from the beam induced disorder. This led to the conclusion that multiple quantum dots in the ribbon are present. For the narrow ribbons, Coulomb diamonds had merged and formed a broad band with an almost constant energy gap, independent of the Fermi energy. In our understanding, the quantum dots, responsible for the Coulomb blockade, are generated by beam induced disorder.

11.1.2. HELIUM ION BEAM INDUCED DEPOSITION

Chapter 6 of this thesis slightly deviates from the graphene-based research, which constitutes the core of this thesis. In a quest to explore other applications of the helium ion microscope, we used beam induced chemical processes to fabricate 3D AFM probes. These probes can be an essential element of the AFM technology for future critical dimension metrology. We optimized the probe growth using a moving beam, instead of the standard stationary beam to make pillars or deposits. The essence of this process lies in the minimal scattering of the ions of the moving helium beam. Consequently, the probe diameter can be made much smaller than, for example, with an electron beam. This technique shows a potential in making smaller structures for fundamental and applied research.

11.1.3. GRAPHENE-BASED JOSEPHSON JUNCTIONS

Graphene–superconductor devices have been explored since the first observation by Heersche *et al.*[2] of proximity-induced superconductivity in graphene. However, all measured devices so far were in the diffusive regime with low critical currents. Thanks to the recent technical advancements in the fabrication techniques of graphene-based devices, we made the first observation of ballistic graphene Josephson junctions with

large critical currents up to a distance of $1.5 \mu\text{m}$. We find that the critical current oscillates with the carrier density due to the phase-coherent interference of the electrons and holes that carry the supercurrent. The phase-coherent interferences are caused by the formation of a Fabry–Pérot cavity. Our observations revived significant interest in graphene-superconductor hybrid systems, opening the possibility to explore intriguing new physics. Recent examples include the phase-coherent interference of charge carriers[3, 4], specular Andreev reflections[5], supercurrent in quantum Hall regime[6], and predictions of Majorana particles[7–10]. More specifically, the recent theoretical[11, 12] and experimental[3, 4, 6, 13] studies on ballistic graphene Josephson junctions (JJs) are primarily focused on the scaling of the critical current with temperature, Fermi energy, magnetic field, and junction length.

Moreover, these technical advancements led to our study on the Josephson current-phase relation (CPR), which has so far eluded experimental observation. We tried to understand the influence of the ballistic propagation on the CPR of the graphene junction. For this purpose, we used a SQUID geometry with two geometrically asymmetric JJs with top gates to individually tune the critical current density in each JJ. More interestingly, we show that the highly asymmetric configuration allows one to directly obtain the current-phase relation (CPR) of these ballistic graphene JJ. The CPR shows a clear non-sinusoidal behavior, deviating significantly from the standard sinusoidal form. Moreover, we show how the CPR depends on the Fermi energy and temperature in the ballistic limit.

11.2. FUTURE DIRECTIONS

11.2.1. HELIUM ION MICROSCOPY RESEARCH

Helium ion microscopy has undoubtedly emerged as a new technique for high-resolution imaging and nanofabrication. Although it has been explored for many different applications in this thesis and elsewhere, the material-sample interactions have not been studied in sufficient detail. Fundamental understanding of the interactions of ions with the sample is important for the use of this technology in various applications. Some of these applications include fabrication of nanoribbons in graphene, pores in graphene for water filtration, and high-resolution structuring. This understanding is essential to realize various new applications. Some are briefly discussed in the following subsections, giving an overview and future directions.

HELIUM ION BEAM PATTERNING

The helium ion beam has already made various contributions to the advancement of nanofabrication processes, thanks to its sub-nanometer probe size and high-resolution patterning capabilities. However, because of the lower mass and the low sputter rate of helium ions, practical applications of this technology are limited. For example, the implantation of helium ions in silicon is an issue for its applications in the semiconductor industry. Another important application, *i.e.* lamella preparation for the transmission electron microscopy (TEM) studies, can greatly benefit from its high resolution. How-

ever, it suffers from the low sputtering rate, making it extremely time-consuming and therefore often not useful.

To overcome these issues, Zeiss has made available a new microscope with helium and neon ions. This is definitely a valuable addition to the HIM. Although the probe size of a neon ion beam is slightly larger than of a helium ion beam, typically around 1-2 nm, neon has several advantages. Some of the advantages include high sputter rate (30x higher than helium), and a shallower penetration depth. This translates into less sub-surface damage. It would be interesting to use neon for various applications, for which the helium beam was initially suggested. Such studies include plasmonic bowtie devices, an array of nanopores, structuring silicon, TEM lamella preparation, and ion beam lithography. For instance, the neon beam lithography is 1000x more efficient than using 30 keV electrons[14], but the resist dissociation process has not been studied in sufficient detail. Also, a comparison of helium and neon beams for structuring sensitive samples, such as graphene, would be of interest.

HELIUM ION BEAM INDUCED DEPOSITION

Helium ion beam induced deposition (HeBID) is still in its infancy compared to electron beam induced deposition (EBID), which has been explored for decades. There has been considerable work done with platinum, but in order to truly use this technique for applications, one must try to improve the metal content in the deposits. One has seen some recent improvements in metal content in EBID using plasma cleaning[15], in-situ heating[16], and laser cleaning[17]. These techniques can potentially be utilized for HeBID as well. In addition, other precursor gases need to be explored, such as gold, phenanthrene, cobalt etc. In particular, phenanthrene is an ideal precursor gas to further shrink the size of the nanoneedles discussed in Chapter 7. To make them stiffer, post-processing of grown phenanthrene needles can provide tips with presumably a smaller width and a higher density of the diamond-like core[18]. This would enhance the lifetime and the reproducibility of AFM data acquired by these tips.

BUBBLE FORMATION

One must take into account the inevitable sub-surface damage caused by the helium beam when it is used for imaging, milling, or ion-induced modification purposes. This damage becomes more important when studying sensitive samples, like graphene. Livenood *et al.*[19] and Veligura *et al.*[20] studied the sub-surface damage by the helium ion beam as a function of beam energy, dosage, and dose delivery rate in silicon, copper, and gold. Helium ions create a lot of surface damage in silicon via bubble formation. This phenomenon is discussed in Chapter 3.

In an experiment by Rudneva *et al.*[21], it is shown that by heating silicon and SrTiO₃ samples at 600 °C, the out-diffusion of helium during ion bombardment is sufficiently large to preclude bubble formation. This study is, however, limited to crystalline samples. For amorphous samples such as SiO₂, the helium ions can move through the amorphous network of silicon and oxygen. Thus, the out-diffusion of helium becomes relatively easy, which prevents the creation of bubbles. Nevertheless, it is unclear whether

the crystallinity of the samples is responsible for bubble formation. The bubble formation can also be circumvented when using thin membranes of thickness less than 50 nm. However, for most of the practical applications, the use of underlying substrates cannot be avoided.

Studies on a variety of amorphous and crystalline samples could provide further insight into the physical processes of out-diffusion and the bubble formation. In particular, the influence of beam current, dose, and energy needs to be clearly studied in detail before a conclusion can be made.

IN-SITU MODIFICATION

As discussed in the bubble formation subsection, it would be useful to construct an in-situ heater for the HIM to counteract subsurface damage. In-situ heating would be a nice addition to control the milling of crystalline samples. This technique could also be used to etch graphene at elevated temperature, which heals defects[1]. The heater used by Rudneva *et al.*[21] has a few holes in a SiN membrane. The graphene samples are laid down over these holes via a dry or a wet transfer technique. Next, a focused gallium beam is used to etch out the unwanted graphene. This gallium beam milling step induces damage to the graphene lattice. So far, only a free-standing graphene sheet can be placed over these heaters, which remain suspended. The devices prepared on the SiO₂ or h-BN substrate cannot be placed directly over the heaters, which limits the use of these heaters for the modification of actual devices. One would need to make a similar heater compatible with heating actual devices. This would open up many possibilities to modify nanomaterials at elevated temperatures.

11.2.2. GRAPHENE RESEARCH

Graphene research has seen significant advancements over the past decade and graphene has potential applications in many fields. So, considering the scope of this thesis, I limit this discussion to the topics studied in this thesis.

P-N JUNCTION IN GRAPHENE USING A FOCUSED HELIUM BEAM

As discussed in Chapters 5 and 6, direct writing with a helium beam can be used to control the doping levels in graphene. By adjusting the irradiation dose, one can vary the degree of n-type doping. The proposed experiment can be realized by combining the capabilities of the narrow interaction volume of a focused helium beam, at most tens of nanometer in the material, and the encapsulation of the graphene in a h-BN sandwich.

With the ability to direct-write, the helium beam irradiation can induce spatially controllable *p-n* junctions in graphene devices without the need of additional structures, such as extra local gates, and chemical dopants. This approach of spatial modulation of the doping profile in graphene may provide easily accessible routes to a variety of novel fundamental studies, including Veselago lens[22], Klein tunneling[23].

CROSSED ANDREEV REFLECTIONS IN GRAPHENE

When an electron is injected from a normal metal into a superconductor, the electron can be reflected as a hole (Andreev reflection) and a Cooper Pair is induced in the superconducting region. Consider two normal metal contacts N_1 and N_2 separated by a distance $L \leq \xi$ from a superconductor. Under a perpendicular magnetic field (B), the incoming electrons from N_1 can either reach N_2 directly, or it can be reflected as a hole from the superconductor and collected at N_2 as an Andreev reflected hole. The former is called electron transfer (ET) process and the latter crossed Andreev reflection (CAR). These processes are schematically shown in Figure 11.1.

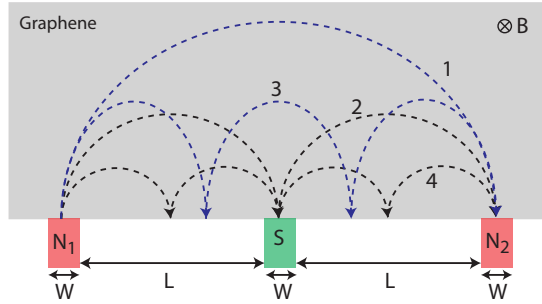


Figure 11.1: Schematic Illustration of focused crossed Andreev reflection (CAR). When the separation between N_1 and N_2 is an even integer multiple of the cyclotron diameter (black dotted trajectories), electron focusing enhances CAR and leads to a negative non-local conductance. However, when the separation is an odd multiple, electron transfer (ET) (blue dotted trajectory) is enhanced and we expect a positive peak in the non-local conductance. 1, 2, 3, and 4 indicate electron trajectories at different perpendicular B fields. The figure is adapted from Ref.[24]

The electron focusing between the normal contacts occur when the distance $2L$ between N_1 and N_2 is a multiple of the cyclotron diameter, $2L = nd_c$, where n is a positive integer. For odd values of n , ET is dominant, while CAR will be observed for even values of n . The magnetic field dependence of the motion of electrons with momentum k_F and cyclotron diameter d_c is given as[24]:

$$d_c = \frac{2\hbar k_F}{eB_{focus}} \quad (11.1)$$

To realise this effect, two essential conditions should be met: (1) ballistic transport over the entire length of the device, (2) clean and transparent interfaces. With the new pick-up technique, e.g. utilized in Chapters 9 and 10 and an optimized etching recipe, one can easily make $10 \mu\text{m}$ long ballistic graphene channels. For the proposed experiments, if we make $L = 10 \mu\text{m}$ and set the device to a density of $5 \times 10^{11} \text{ cm}^{-2}$, a critical focusing field of $\sim 16.5 \text{ mT}$ is required to observe the first CAR. With the current technical advancements in the sample making process, this is attainable. Therefore, one could easily study CAR and ET in the ballistic graphene devices.

CPR IN SHORT BALLISTIC JUNCTIONS

As we have seen in Chapter 10, the current phase relation (CPR) shows a clear non-sinusoidal behavior. We have studied the junction in the intermediate regime. However, it would be interesting to study the evolution of the CPR as a function of channel width; mainly in the short junction and long junction regime. One could make the short junction using aluminium. For the short junction in the ballistic limit with high transmission, a saw-tooth behavior is expected[11]. Another possibility is to study the edge-contacted junctions in the diffusive limit. For this, one could make the devices directly on SiO₂ with h-BN capping on top. These experiments would give further insight into the Andreev processes at the graphene-superconductor interface.

11.2.3. TECHNICAL CHALLENGES

HELIUM ION BEAM RESEARCH

A drawback we experienced in the course of the work described in this thesis was the downtime of the instrument used. This imposed a limit on our advancements in helium ion beam research. The Delft instrument was one of the first ever built; this circumstance might have made the instrument less reliable. Although HIM provides extremely high-resolution patterning capabilities, the low sputtering rate of the helium ions imposes another problem. For certain applications, such as for making an array of nanoholes in SiN membranes for DNA sequencing, high-resolution patterning and faster milling rates are required. For such applications, it would be useful to combine the capabilities of HIM with other ions, such as neon.

For milling, ion-induced doping, and imaging applications, there has been a growing interest in developing other ion sources in the past few years. Recent developments include a new kind of ion source, known as magneto-optical trap ion source (MOTIS) or ultracold ion source (UCIS)[25]. This ion source makes use of photoionized and laser-cooled gases to generate a focused beam of ions, such as lithium and chromium. The main advantages of such ion sources are high brightness, low energy spread, and a wide choice of ionic species. The high brightness is made possible by keeping the source at extremely low temperatures ($\sim \mu\text{K}$) attained via laser cooling. However, this technology is still in the prototype stage, and it would take at least a few years before a first commercial tool is made available. The advancements of these technologies are definitely important, but their availability and the practical uses are still unclear.

GRAPHENE RESEARCH

Thanks to the recent technical advancements and the new specimen pick-up technique, it has become easier to make clean devices in graphene. However, for the practical use of graphene, a few challenges must be tackled. Some of them include direct growth of graphene on a wafer, polymer-free clean transfer, low-cost production, and isolation from the environment on a large scale. Encapsulating graphene in h-BN flakes could be the first step toward this goal, but large scale encapsulation is extremely difficult to achieve. It would be a great solution if one could develop a recipe to grow wafer-scale

encapsulated graphene via CVD or other synthetic methods. Moreover, it is worth mentioning that graphene-based research in a laboratory setup suffers a great deal from air bubbles formed during the stacking process. This limits the usable area on the stack for making clean devices, thus reducing the throughput. These bubbles, that typically cover up to 70% area of a BN-graphene-BN stack, needs to be completely avoided. This will be an important step towards making clean devices of the order of a few hundred microns.

REFERENCES

- [1] Q. Xu, M. Y. Wu, G. Schneider, L. Houben, S. Malladi, C. Dekker, E. Yucelen, R. E. Dunin-Borkowski, and H. W. Zandbergen, *Controllable atomic scale patterning of freestanding monolayer graphene at elevated temperature*, ACS Nano **7**, 1566 (2013).
- [2] H. B. Heersche, P. Jarillo-Herrero, J. B. Oostinga, L. M. K. Vandersypen, and A. F. Morpurgo, *Bipolar supercurrent in graphene*, Nature **446**, 56 (2007).
- [3] V. E. Calado, S. Goswami, G. Nanda, M. Diez, A. R. Akhmerov, K. Watanabe, T. M. K. T. Taniguchi, and L. M. K. Vandersypen, *Ballistic Josephson junctions in edge-contacted graphene*, Nature Nanotechnology **10**, 761 (2015).
- [4] M. B. Shalom, M. J. Zhu, V. I. Fal'ko, A. Mishchenko, A. V. Kretinin, K. S. Novoselov, C. R. Woods, K. Watanabe, T. Taniguchi, A. K. Geim, and J. R. Prance, *Quantum oscillations of the critical current and high-field superconducting proximity in ballistic graphene*, Nature Physics **12**, 318–322 (2016).
- [5] D. K. Efetov, L. Wang, C. Handschin, K. B. Efetov, J. Shuang, R. Cava, T. Taniguchi, K. Watanabe, J. Hone, C. R. Dean, and P. Kim, *Specular interband Andreev reflections at van der Waals interfaces between graphene and NbSe₂*, Nature Physics **12**, 328 (2016).
- [6] F. Amet, C. T. Ke, I. V. Borzenets, J. Wang, K. Watanabe, T. Taniguchi, R. S. Deacon, M. Yamamoto, Y. Bomze, S. Tarucha, and G. Finkelstein, *Supercurrent in the quantum Hall regime*, Science **352**, 966 (2016).
- [7] L. Fu and C. L. Kane, *Superconducting proximity effect and Majorana fermions at the surface of a topological insulator*, Physical Review Letters **100**, 096407 (2008).
- [8] C. W. J. Beenakker, *Search for Majorana fermions in superconductors*, arXiv **Preprint**, arXiv:1112.1950 (2011).
- [9] X. L. Qi and S. C. Zhang, *Topological insulators and superconductors*, Reviews of Modern Physics **83**, 1057 (2011).
- [10] P. San-Jose, J. L. Lado, R. Aguado, F. Guinea, and J. Fernández-Rossier, *Majorana zero modes in graphene*, Physical Review X **5**, 041042 (2015).
- [11] I. Hagymási, A. Kormányos, and J. Cserti, *Josephson current in ballistic superconductor-graphene systems*, Physical Review B **82**, 134516 (2010).

- [12] P. Rakyta, A. Kormányos, and J. Cserti, *Magnetic field oscillations of the critical current in long ballistic graphene Josephson junctions*, Physical Review B **93**, 224510 (2016).
- [13] C. T. Ke, I. V. Borzenets, A. W. Draelos, F. Amet, Y. Bomze, G. Jones, M. Craciun, S. Russo, M. Yamamoto, S. Tarucha, and G. Finkelstein, *Critical current scaling in long diffusive graphene-based Josephson junctions*, Nano Letters **16**, 4788 (2016).
- [14] D. Winston, V. R. Manfrinato, S. M. Nicaise, L. L. Cheong, H. Duan, D. Ferranti, J. Marshman, S. McVey, L. Stern, J. Notte, and K. K. Berggren, *Neon ion beam lithography (NIBL)*, Nano Letters **11**, 4343 (2011).
- [15] D. Belić, M. M. Shawrav, M. Gavagnin, M. S. ger Pollach, H. D. Wanzenboeck, and E. Bertagnolli, *Direct-write deposition and focused-electron-beam-induced purification of gold nanostructures*, ACS Applied Materials & Interfaces **7**, 2467 (2015).
- [16] A. Botman, J. J. L. Mulders, R. Weemaes, and S. Mentink, *Purification of platinum and gold structures after electron-beam-induced deposition*, Nanotechnology **17**, 3779 (2006).
- [17] M. G. Stanford, B. B. Lewis, J. H. Noh, J. D. Fowlkes, N. A. Roberts, H. Plank, and P. D. Rack, *Purification of nanoscale electron-beam-induced platinum deposits via a pulsed laser-induced oxidation reaction*, ACS Applied Materials & Interfaces **6**, 21256 (2014).
- [18] M. Wendel, H. Lorenz, and J. P. Kotthaus, *Sharpened electron beam deposited tips for high resolution atomic force microscope lithography and imaging*, Applied Physics Letters **67**, 3732 (1995).
- [19] R. Livengood, S. Tan, Y. Greenzweig, J. Notte, and S. McVey, *Subsurface damage from helium ions as a function of dose, beam energy, and dose rate*, Journal of Vacuum Science & Technology B **27**, 3244 (2009).
- [20] V. Veligura, G. Hlawacek, R. P. Berkelaar, R. van Gastel, H. J. W. Zandvliet, and B. Poelsema, *Digging gold: keV He⁺ ion interaction with Au*, Beilstein Journal of Nanotechnology **4**, 453 (2013).
- [21] M. Rudneva, E. van Veldhoven, S. K. Malladi, D. Maas, and H. W. Zandbergen, *Novel nanosample preparation with a helium ion microscope*, Journal of Materials Research **28**, 1013 (2013).
- [22] V. V. Cheianov, V. Fal'Ko, and B. L. Altshuler, *The focusing of electron flow and a Veselago lens in graphene p-n junctions*, Science **315**, 1252 (2007).
- [23] A. F. Young and P. Kim, *Quantum interference and klein tunnelling in graphene heterojunctions*, Nature Physics **5**, 222 (2009).
- [24] H. Haugen, A. Brataas, X. Waintal, and G. E. W. Bauer, *Focused crossed Andreev reflection*, Europhysics Letters **93**, 67005 (2011).
- [25] B. Knuffman, A. V. Steele, and J. J. McClelland, *Cold atomic beam ion source for focused ion beam applications*, Journal of Applied Physics **114**, 044303 (2013).

A

DEVICE FABRICATION RECIPE

This appendix provides a step-by-step guide to the devices fabricated in this thesis. Two methods were designed and optimized to contact graphene. These methods are discussed separately. The appendix ends with a few tips on the bonding of the devices.

A.1. SI/SiO₂ CLEANING

STEP 1: REMOVING ORGANIC CONTAMINANTS

- Insert in a H₂SO₄ bath for 5 minutes with continuous sonication
- Rinse with deionized (DI) water
- Rinse with Acetone Rinse with isopropyl alcohol (IPA)

STEP 2: REMOVING ORGANIC ADSORBATES AND SURFACE ACTIVATION

- Clean in oxygen plasma for 2 minutes
- Plasma conditions: 500 W and 200 sccm of oxygen

NOTE:

- Clean wafers just prior to exfoliation

A.2. BITMARKERS

Bitmarkers are made on the entire chip to locate the desired flake. E-beam lithography markers are also made in this step. These e-beam lithography markers are used to align the beam during the lithography process.

STEP 1:

- Spin PMMA 495K A4 at 4000 rpm
- Bake for 15 mins on the hotplate at 175 °C
- Spin PMMA 950K A3 at 4000 rpm
- Bake for 15 mins on the hotplate at 175 °C
- E-beam exposure (100 keV) at a dose of 1400 $\mu\text{C cm}^{-2}$
- Develop in MIBK:IPA (1:3) solution for 90 seconds
- Rinse in IPA for 30 seconds
- Blow dry with a N₂ gun

STEP 2:

- 5 nm chromium (Cr) at 0.5 A s⁻¹ followed by 60 nm gold (Au) at 1 A s⁻¹ is evaporated
- Blow dry with a N₂ gun

STEP 3:

- Liftoff is completed overnight in a warm acetone at 54 °C
- Use syringe to rinse off access metal
- Rinse in IPA for 30 seconds
- Blow dry with a N₂ gun

A.3. CONTACTING GRAPHENE

There are two ways by which one could make contacts to the encapsulated graphene. In Chapters 5, 6, and 8, the contacts are made to graphene using the first method (described below). For the devices studied in Chapters 9 and 10, a second method called "etch fill" is developed to contact graphene.

A.3.1. METHOD 1

ETCHING

STEP 1:

- Spin PMMA 495K A4 at 4000 rpm
- Bake for 15 mins on the hotplate at 175 °C
- Spin hydrogen silsesquioxane or HSQ:MIBK (1:1) at 10,000 rpm
- Bake for 2 minutes at 150 °C and then 2 minutes at 220 °C
- E-beam exposure (100 keV) at a dose of 950 $\mu\text{C cm}^{-2}$
- Develop in MF322 for 1 minute and MF322:H₂O (1:9) for 15 secs and then rinse in DI water for 15 secs
- Blow dry with a N₂ gun

STEP 2:

- Etch the BN/graphene/BN stack using 20 sccm O₂ at 60 W and 50 μbar for 1 minute
- Subsequently etch the stack in CHF₃:O₂ (40:4 sccm) at 60 W and 80 μbar for 1 minute
- Leave the sample in warm acetone (54 °C) for 30 minutes and then in cold acetone overnight

METALIZATION

- This step is exactly similar to the steps mentioned in bitmarkers section. However for the devices made in Chapter 8, Cr and Au are replaced by 80 nm of molybdenum rhenium (MoRe)
- The MoRe is deposited by a sputtering process using a DC plasma with a power of 100 W in argon atmosphere at a rate of 11 nm min^{-1}
- Leave the sample in warm acetone ($54 \text{ }^\circ\text{C}$) for 2 hours
- Use syringe to rinse off access metal
- Rinse in IPA for 30 seconds
- Blow dry with a N_2 gun

A.3.2. METHOD 2 (ETCH FILL)

STEP 1:

- Spin PMMA 495K A4 at 4000 rpm
- Bake for 15 mins on the hotplate at $175 \text{ }^\circ\text{C}$
- Spin PMMA 950K A3 at 4000 rpm
- Bake for 15 mins on the hotplate at $175 \text{ }^\circ\text{C}$
- E-beam exposure (100 keV) at a dose of $1400 \mu\text{C cm}^{-2}$
- Develop in MF322 for 1 minute and MF322:H₂O (1:9) for 15 secs and then rinse in DI water for 15 secs
- Blow dry with a N_2 gun

STEP 2:

- Etch the BN/graphene/BN stack in $\text{CHF}_3:\text{O}_2$ (40:4 sccm) at 60 W and $80 \mu\text{bar}$ for 1 minute

STEP 3:

- Deposit MoRe with a power of 100 W in argon atmosphere at a rate of 11 nm min^{-1}
- Leave the sample in warm acetone ($54 \text{ }^\circ\text{C}$) for 2 hours
- Use syringe to rinse off access metal
- Rinse in IPA for 30 seconds
- Blow dry with a N_2 gun

STEP 4:

- Repeat the two-step etching process to shape the device using HSQ (as described in the Etching section)

A.4. GATE DIELECTRIC

The top gate dielectric is made on the devices studied in Chapters 9 and 10. This step is needed to isolate the encapsulated graphene devices from the gate electrodes.

STEP 1:

- Spin HSQ (Concentrated) at 5000 rpm
- Bake the sample in an oven for 10 mins at 90 °C
- E-beam exposure (100 keV) at a dose of $950 \mu\text{C cm}^{-2}$
- Develop in MF322 for 1 minute and MF322:H₂O (1:9) for 15 secs and then rinse in DI water for 15 secs
- Blow dry with a N₂ gun

STEP 2:

- Repeat step 1
- The measured thickness of the top gate dielectric after step 1 and 2 is $\approx 175 \text{ nm}$

NOTE:

The designed area in this step should be smaller than the first step. This is needed to make sure the dielectric is not too thick for the metal to climb on

A.5. TOP GATE

The top gate is made using the recipe discussed in the bitmarkers section, except the total thickness is made 125 nm (5 nm Cr and 120 nm Au).

A.6. DEVICE BONDING

A final step of the fabrication is the bonding of device to the chip carrier. Bonding is a critical step and if not optimized carefully, it can lead to the device leakage.

- First, the sample is glued to the 32-pin PLCC chip carrier with silver paint
- Next, bond pads on the samples are bonded to the pads on the chip carrier via an aluminum wire

A

We found that bonding works nicely with MoRe pads. However, with Cr/Au pads, bonding is not straight forward and should be optimized for every new device. Often the pads are ripped off due to the higher ultrasonic power, time, or the force. So, all three parameters were optimized carefully. We found that force above 18 g tends to rupture the metal pads and the underlying 285 nm SiO₂ substrate. So, we kept the force below 18 g, mostly 16 or 17 g. One could make multiple metal layers in the successive processing steps. However, we found that it is extremely difficult to bond on the pads made of different metals. So, multiple layers of different metals should be avoided.

SUMMARY

This thesis describes the capabilities of the helium ion microscope (HIM) and that of graphene to explore fundamental physics and novel applications. While graphene offers superior electronic properties, the helium ion microscope allows us to combine imaging and modification of materials at the nanoscale. We used the capabilities of HIM to grow 3D-AFM probes, which can be used in the critical dimension semiconductor metrology. Moreover, we studied the ion-material interactions, needed to enable the fabrication of functional graphene nanoribbons. Similarly, we used the superior electronic properties of graphene to make ballistic Josephson junctions and studied the current-phase relation (CPR) of these junctions.

The core of this thesis is focused on the fabrication and electronic characterization of He^+ beam modified graphene, He^+ beam etched graphene nanoribbons, and graphene-based Josephson junctions (JJs). The graphene devices were prepared by a new polymer-free transfer "van der Waals pick-up" technique. The fabricated devices comprise graphene encapsulated in hexagonal boron nitride (BN) and contacted along the edge by either a normal metal (Cr/Au) or by a superconductor. The encapsulation in BN keeps the graphene clean and the edge contacting technique provides transparent interfaces. The thesis is divided into two main topics. In particular, the first three studies are dedicated to the research based on the helium ion microscope, and the next three are dedicated to the research based on boron nitride encapsulated graphene Josephson junctions.

Firstly, we conducted a thorough analysis of the consequences of He^+ beam irradiation of graphene. We showed that the Raman D' defect peak is sensitive to the local environment of the graphene. In particular, it saturates with ion dose in the encapsulated graphene. We observed that the evolution of the D and the D' peak in the BN-encapsulated graphene is retarded with respect to bare graphene. Moreover, exposure of the BN-encapsulated graphene to helium beam led to n-type conduction. This n-doping is probably caused by the collisional substitution of carbon atoms by nitrogen atoms. Next, we utilized the He^+ beam for making so-called "nanoribbons" in graphene. Despite excellent charge transport properties, graphene is a semi-metal with zero bandgap, which limits its potential use in electronic applications. By structuring graphene into nanoribbons, a bandgap can be induced. We used BN-encapsulated graphene for making nanoribbons. Since encapsulation mitigates some of the adverse issues related to the helium ion beam patterning of graphene, we used BN-encapsulated graphene for making the nanoribbons. The encapsulated graphene indeed proved to be suitable for the beam induced patterning. For that purpose, in-situ electrical measurements in a helium ion microscope were conducted to establish the critical ion dose for creating 10 nm wide insulating barriers between a nanoribbon and the rest of the encapsulated graphene. Subsequently, we measured the transport properties of the ion-beam etched

graphene nanoribbons. Conductance measurements at 4 K show an energy gap, that increases with decreasing ribbon width. The narrowest ribbons show a weak dependence of the conductance on the Fermi energy. Furthermore, we observed power-law scaling in the measured current-voltage ($I - V$) curves, indicating that the conductance in the helium-ion-beam etched encapsulated graphene nanoribbons is governed by Coulomb blockade.

Furthermore, nanostructures could also be realized based on the beam induced deposition capabilities of the microscope. Making use of this direct-write technique, we grew hammerhead atomic force microscope (AFM) probes of platinum-carbon on top of a conventional AFM probe. A minimum diameter of 13 nm and 35 nm wide hammerheads are achieved, thanks to the subnanometer ion-beam size and the negligible scattering of primary and secondary particles. Our fabrication process of these probes has distinct merits because of the probes' high aspect ratio and the possibility for relatively easy process customization. As a result, these probes with thin needles and a hammerhead tip can be used for critical dimension (CD) metrology.

Next, graphene devices in combination with a superconductor are fabricated to study proximity-induced superconductivity in graphene. The encapsulation and edge contacting technique provided clean and transparent interfaces which enabled us to operate these Josephson junction devices in the ballistic regime. We found that these Josephson junctions exhibit large supercurrents over distances of up to 1.5 μm . We observed oscillations in the relation between the critical current and the carrier density due to the phase-coherent interference of the electrons or holes that carry the supercurrent. The interference occurs because the molybdenum-rhenium superconductor induces n-doping near the contacts, leading to the partial reflection of electron or hole waves, thus creating a Fabry-Pérot cavity.

The ballistic propagation of charge carriers provided a unique platform to study these junctions in detail. The relatively simple fabrication method eases the incorporation of these junctions in a variety of device architectures. Following the work on graphene-based Josephson junctions, we next created the first fully gate-tunable dc quantum interference devices (SQUIDs) made of graphene. The supercurrent in this device is modulated independently by two top gates. By independently controlling the critical current of each graphene Josephson junction, the SQUID is electrostatically tuned from a symmetric configuration to a highly-asymmetric one, where the critical current of one Josephson junction is significantly larger than the other.

Finally, this gate-tunability of our asymmetric SQUIDs is utilized to probe the current-phase relation (CPR) in graphene Josephson junctions. The CPR is an essential component of the junction's properties, describing how the supercurrent evolves with the superconducting phase difference across the junction. The CPR is observed to be skewed, deviating significantly from the sinusoidal form. Moreover, the skewness can be controlled by a gate voltage. We found that the skewness oscillates in anti-phase with the Fabry-Pérot oscillations of the ballistic graphene cavity. Theoretical analysis of our results supported the validity of two important assumptions; (i) the skewness does not arise due to inductance effects, and (ii) the nature of the superconductor-graphene in-

terface plays an important role in the CPR.

SAMENVATTING

Dit proefschrift beschrijft de mogelijkheden van de heliumionenmicroscop (HIM) en van het materiaal grafeen voor zowel de beoefening van fundamentele natuurkunde als voor de verkenning van nieuwe toepassingen. Enerzijds heeft grafeen uitstekende elektronische eigenschappen, anderzijds geeft de heliumionenmicroscop ons de kans om materialen op nanometerschaal te bewerken en te bekijken. We hebben de mogelijkheden van de HIM gebruikt om 3D-AFM sondes te maken die kunnen worden toegepast voor kritische-dimensie metrologie in de chipfabricage. Daarnaast hebben we de interactie tussen versnelde ionen en materialen bestudeerd met als doel in grafeen functionele nanolinten te maken. Ook gebruikten we de superieure elektronische eigenschappen van grafeen om ballistische Josephson-juncties te vervaardigen en daarin de zogenaamde stroom-fase relatie (CPR) te onderzoeken.

De kern van dit proefschrift behelst de fabricage met een heliumbundel en de elektrische karakterisatie van vlak grafeen en van grafeen nanolinten alsook de bestudering van Josephson-juncties vervaardigd uit grafeen. De grafeen devices zijn via de nieuwe polymeervrije Van-der-Waals oppiktechniek gemaakt. Deze devices bestaan uit grafeen dat is ingebed in hexagonaal boornitride (BN) en dat via de randen contact maakt met een gewoon metaal (Cr/Au) of met een supergeleider. De inbedding in boornitride houdt het grafeen schoon en de randcontacten zorgden voor een elektrisch transparante overgang. Dit proefschrift heeft twee hoofdonderdelen. De eerste drie hoofdstukken zijn gericht op onderzoek gekoppeld aan de heliumionenmicroscop en de daaropvolgende drie hoofdstukken behandelen Josephson-juncties, gemaakt van grafeen dat is ingebed in boornitride.

Eerst hebben we een diepgaande analyse van de gevolgen van He^+ bestraling van grafeen verricht. We vonden dat de Raman D'-defectpiek gevoelig is voor de lokale omgeving van het grafeen. In het bijzonder bleek dat in BN-ingebed grafeen de groei van de defectpiek verzadigt bij hoge ionendosis. Ook zagen we dat de groei van de D en de D' defectpieken is vertraagd ten opzichte van de groei in onbedekt grafeen. Bovendien leidde de bestraling van het ingebedde grafeen tot n-type geleiding. De n-dotering is waarschijnlijk veroorzaakt door de vervanging van koolstofatomen door stikstofatomen als gevolg van botsingen van de He^+ ionen. Vervolgens gebruikten we de He^+ ionenbundel om nanolinten in grafeen te etsen. Hoewel grafeen uitstekende eigenschappen voor ladingstransport heeft, is het een halfmetaal zonder een bandafstand, wat de mogelijke toepassingen in de elektronica beperkt. Door het grafeen in de vorm van nanolinten te etsen, kan men toch een bandafstand creëren. Omdat inbedding een aantal nadelige bijkomstigheden van ionenbundel-patronering voorkomt, hebben we BN-ingebed grafeen gebruikt voor het maken van de nanolinten. Inderdaad bleek het ingebedde materiaal geschikt voor ionenbundel-patronering. Allereerst hebben we in-situ

elektrische metingen in de heliumionenmicroscopie uitgevoerd om de kritische ionendosis voor het etsen van 10 nm brede isolerende barrières tussen een nanolint en de rest van het ingebedde grafeen te bepalen. Vervolgens hebben we de transporteigenschappen van onze ionenbundel-geëtsde grafeen nanolinten onderzocht. Geleidingsmetingen bij 4 Kelvin tonen een bandafstand dat groter wordt met afnemende lintbreedte. De geleiding in de smalste linten vertoont een zwakke afhankelijkheid van de Fermi-energie. Daarnaast vonden we in de gemeten stroom-spanningscurves een schaling volgens een machtwet, wat suggereert dat Coulombblokkade de elektrische geleiding van onze heliumionenbundel-geëtsde grafeen nanolinten bepaalt.

Met de ionenmicroscopie kunnen nanostructuren ook worden gemaakt via bundel-geïnduceerde-depositie. Met deze directe schrijftechniek hebben we platina-koolstof sondes met een hamerkop gegroeid bovenop conventionele sondes voor atomaire-kracht microscopie (AFM). Dankzij de subnanometer bundelgrootte en de verwaarloosbare zwakke verstrooiing van primaire en secundaire deeltjes, kon een sondediameter van slechts 13 nanometer met een kopbreedte van 35 nm worden gerealiseerd. Ons fabricageproces van deze sondes heeft bijzondere voordelen vanwege de grote lengte-breedteverhouding van de sondes en de flexibiliteit van het proces. Hierdoor kunnen deze smalle sondes met hamerkop toegepast worden voor kritische-dimensie metrologie.

Vervolgens zijn devices gemaakt van grafeen in combinatie met een supergeleider om de nabijheidgeïnduceerde supergeleiding (proximity-induced superconductivity) in grafeen te bestuderen. De inbedding en de randcontacten garandeerden schone en elektrisch transparante overgangen in deze Josephson-junctie devices, wat het ons mogelijk maakte de juncties in het ballistische domein te laten werken. We vonden dat deze grafeen Josephson-juncties hoge superstromen vertonen over afstanden tot 1.5 μm . We namen oscillaties waar in het verband tussen de kritische stroom en de ladingdragerdichtheid, wat wordt veroorzaakt door fase-coherente interferentie van de elektronen of gaten die de superstroom dragen. De interferentie treedt op omdat het supergeleidende molybdeen-renium n-dotering nabij de contacten teweegbrengt, wat leidt tot gedeeltelijke weerkaatsing van de elektronen- of gatengolven en zo tot de vorming van een Fabry-Pérot trilholte.

De devices met daarin ballistische voortbeweging van de ladingdragers boden uniek materiaal om deze juncties in meer detail te bestuderen. De relatief eenvoudige fabricage vergemakkelijkt de inbouw van deze juncties in een veelheid van device-ontwerpen. Als vervolg op het werk met de grafeen Josephson-juncties hebben we een dc kwantuminterferentie device (SQUID) van grafeen gemaakt, die volledig instelbaar is via elektrodes. De superstromen in dit device zijn onafhankelijk regelbaar via twee top elektrodes. Door de kritische stroom in beide grafeen Josephson-juncties onafhankelijk te variëren, kon de SQUID elektrostatisch worden afgeregeld tussen een volledig symmetrische en een sterk asymmetrische configuratie waarin de kritische stroom in één junctie aanzienlijk hoger was dan in de andere.

Uiteindelijk is de gate-afhankelijkheid van de asymmetrische SQUIDS gebruikt om de stroom-faserelatie (CPR) in grafeen Josephson-juncties te meten. De stroom-faserelatie is een essentiële eigenschap van de junctie; het beschrijft hoe de superstroom afhangt

van het supergeleidende faseverschil over de junctie. De waargenomen CPR wijkt duidelijk af van een sinusvorm, met een scheefheid die met de elektrodes kon worden ingesteld. We vonden dat de scheefheid in tegenfase oscilleerde met de Fabry-Pérot trillingen in de ballistische grafeen trilholte. Theoretische analyse van onze resultaten bewezen twee belangrijke veronderstellingen: (i) de scheefheid ontstaat niet vanwege inductie en (ii) het karakter van de supergeleider-grafeen overgang speelt een belangrijke rol in de stroom-faserelatie.

CURRICULUM VITÆ

Gaurav NANDA

02-06-1988 Born in Hamirpur, India.

EDUCATION

2003–2006 High School
Silver Bells School, Hamirpur, India

2006–2012 B.Tech. & M.Tech. Nanotechnology
Amity University, India
Master Thesis: École Polytechnique de Montréal, Canada (2011)
Master Thesis: École Polytechnique Fédérale de Lausanne, Switzerland (2012)

2012–2016 Ph.D. Applied Physics
Delft University of Technology, The Netherlands

2017–Present Design Engineer - CD Metrology
ASML, The Netherlands

LIST OF PUBLICATIONS

7. **G. Nanda and J.L. Aguilera-Servin and P. Rakya and A. Kormányos and R. Kleiner and D. Koelle and K. Watanabe and T. Taniguchi and L.M.K. Vandersypen and S. Goswami**, *Current-Phase Relation of Ballistic Graphene Josephson Junctions*, *Nano Letters*, Accepted (2017).
6. **G. Nanda and G. Hlawacek and S. Goswami and K. Watanabe and T. Taniguchi and P.F.A. Alkemade**, *Electronic Transport in Helium-Ion-Beam Etched Encapsulated Graphene Nanoribbons*, *Carbon* **119**, 419-425 (2017).
5. **G. Nanda and E. van Veldhoven and D. Maas and H. Sadeghian and P.F.A. Alkemade**, *Helium Ion Beam Induced Growth of Hammerhead AFM Probes*, *Journal of Vacuum Science & Technology B* **33**, 06F503 (2015).
4. **G. Nanda and S. Goswami and K. Watanabe and T. Taniguchi and P.F.A. Alkemade**, *Defect Control and N-Doping of Encapsulated Graphene by Helium-Ion-Beam Irradiation*, *Nano Letters* **15**, 4006-4012 (2015).
3. **V.E. Calado and S. Goswami and G. Nanda and M. Diez and A. R. Akhmerov and K. Watanabe and T. Taniguchi and T. M. Klapwijk and L.M.K. Vandersypen**, *Ballistic Josephson Junctions in Edge-Contacted Graphene*, *Nature Nanotechnology* **10**, 761-764 (2015).
2. **S.S. Ghoreishizadeh and G. Nanda and S. Carrara and G. De Micheli**, *Empirical Study of Noise Dependence in Electrochemical Sensors*, *Advances in Sensors and Interfaces (IWASI)* **13698522**, 36-39 (2013).
1. **G. Tarabella and G. Nanda and M. Villani and N. Coppedè and R. Mosca and G.G. Malliaras and C. Santato and S. Iannotta and F. Cicoira**, *Organic Electrochemical Transistors Monitoring Micelle Formation*, *Chemical Science*, **3**, 3432-3435 (2012).

ACKNOWLEDGEMENTS

I would like to start by expressing my appreciation to my co-promotor and supervisor, Dr. Paul Alkemade, for giving me the opportunity to perform Ph.D. research at TU Delft. Much thanks for being a great supervisor, a wonderful teacher, and a very humble person. I could always go up to him to ask questions, ask suggestions, or have general discussions. His constant encouragements, valuable suggestions, and a sharp eye for details have significantly improved my efforts throughout the Ph.D. journey. Words cannot express all that I wish to say to my co-supervisor, Dr. Srijit Goswami, for insightful discussions, sharing ideas, useful suggestions, and helping with all the technical and scientific issues. He is a brilliant scientist with a deep understanding of physics. I have certainly learnt a lot from you. Special thanks to Prof. Lieven Vandersypen for giving me the opportunity to be a part of his graphene team and for being my promotor. This has contributed a lot to my personal and professional growth. I am grateful to Prof. Henny Zandbergen for his useful suggestions and ideas during the early days of my Ph.D. journey.

I cannot express enough thanks to TNO for providing technical support on the helium ion microscope, and for giving me a unique opportunity to do a traineeship. This traineeship was a wonderful experience; seeing how fundamental science helps technology innovate is just magical! This has certainly motivated me to join the fast-paced industrial setup after my Ph.D. Much thanks to Diederik Maas, Emile van Veldhoven, and Hamid Sadeghian for constant encouragements, technical help, and scientific discussions.

The work in this thesis could not have been completed without the technical expertise and support of Charles, Marc, Marco, Anja, Arnold, Roel, Ewan, Eugene, and Frank and all the members of Kavli Nanolab. The useful discussions that I have had with them, their support, fun times in and out of the cleanroom have made my stay very enjoyable. Thanks again for making time for me, always! Many thanks to Hozanna, Nima, and Anastasia for making my office a pleasant place to work, for insightful discussions, for useful suggestions, and for all the fun conversations. Hozanna, thanks for always helping me with Dutch, and answering all the general question I had about living in The Netherlands. To my colleagues and collaborators Gregor, Andor, Peter, Reinhold, Nandini, Adithya, Daniel, Stephanie, Leonardo, Shibabrata, Nima, Victor, Sumit, Kaveh, David, and Juan, thank you all from the bottom of my heart for your help, for fun times, and for useful discussions. I enjoyed working alongside each and every one of you. Gregor, I really appreciate all your help and support that you provided me with the helium ion microscope. Also, I want to thank my dear friends in The Netherlands, India, and other parts of the world for their unconditional support. Special thanks to Angad, Arjun, Greeshma, Aakriti, Ashish, Deepak, Rakesh, Ram, Varun, and Darwin. I greatly appreciate their friendship and their belief in me. It is not possible to mention names of all the

people who have made this journey possible, my apologies to those whose names I have missed.

I would like to take this opportunity to express my eternal gratitude to God, my beloved parents Ramesh and Suman, brother Anirudh, and the rest of my family for their everlasting love and support. I cannot express enough thanks to my wife, Silky, for all the happiness she has given me, which kept me motivated through the course of my Ph.D.

Finally, I thank Dutch Technology Foundation STW, which is part of The Netherlands Organization for Scientific Research (NWO), and the Ministry of Economic Affairs, for funding my research. A lot of thanks to the Delft University of Technology for hosting me and my research. It has been a fulfilling journey. Thanks everyone for making this journey so wonderful and memorable!

Gaurav Nanda
December 2016, Delft